UNIVERSITY OF CATANIA

Department of Chemical Sciences

Ph.D. course in Chemical Sciences

CYCLE XXXVIII

Development of Nanostructured Molecular Materials Based on Zinc(II) Metal Complexes as Optical and Electrical Chemosensors of Volatile Organic Compounds Vapors and Ammonia

Ph.D. Thesis

Ph.D. Candidate:
Agostino Attinà

Academic Tutor:
Prof. Santo Di Bella

Ph.D. Coordinator:
Prof. Salvatore Scirè

2022 - 2025

Development of Nanostructured Molecular Materials Based on Zinc(II) Metal Complexes as Optical and Electrical Chemosensors of Volatile Organic Compounds Vapors and Ammonia

Agostino Attinà

Doctoral thesis

Promoted by the SAMOTHRACE foundation

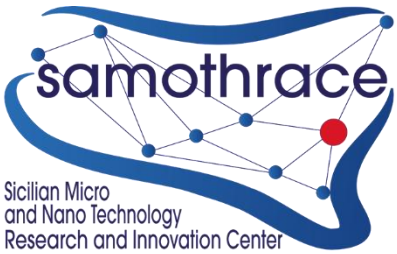

External reviewers:

Prof. Claude P. Gros, Université Bourgogne Europe (Dijon, France)

Prof. Laura R. Rodrìguez, Universitat de Barcelona (Barcelona, Spain)

Cover illustration:

Vapochromic paper-based films of Zn(salen)-type complexes for the optical detection of volatile organic compounds.

Acknowledgements

The present Ph.D. thesis covers the scientific work of my last three years at the University of Catania, a period filled with laboratory experiments conducted with curiosity and motivation. I feel like these three years have gone by too quickly, and every day I was very happy working with my supervisor and his coworkers.

For this reason, I would first like to sincerely thank my supervisor, Professor Di Bella, for all his patience with me, for his humanity, and for his invaluable guidance. I learned a lot under his supervision, not only scientifically, and for this reason I consider myself very fortunate to have met him during my academic studies. I would like to thank Professor Oliveri and Doctor Gaeta for their help during all my activities. They teach me a lot and I will remember all the funny moments with them, especially during our meals. I can truly consider them my friends inside and outside the workplace. I would also like to thank Professor Scirè, coordinator of the Ph.D. program in Chemical Sciences at the University of Catania, and all the members of the Teaching Board for their availability.

I would like to thank Professor Bouvet (Université Bourgogne Europe) for giving me the opportunity to work in his laboratory for a period of six months, during which I expanded my knowledge on a research topic that was completely new to me. Furthermore, I believe that other people I met while abroad, such as Dr. Ganesh Moorthy, Dr. Bečvár, Dr. Hruska, and Dr. Vachey, played an important role in my scientific growth and I can consider them friends despite the distance.

Since I began studying at the University of Catania, and especially during these last three years, my family has been with me, every time, and for this reason perhaps I don't have enough words to thank them: my parents, my aunts, my cousin Carmelo, my brother Pierluigi and his family. I consider them my irremovable point of reference for every decision I have made during these years. In the context of my family, I add a friend whom I consider like a brother, Vincenzo. I have to thank him for all the time we spent together by talking, eating, playing, listening to music, and so on. Also, during my Ph.D. I met a person who has become very special to me, Maria Luisa, and I am very happy to consider her part of my life and my family. I would also like to mention two very important friends to me, Giuseppe and Antonio, because despite the distance that separates us, we constantly text each other thanks to the friendship we built during my undergraduate and graduate degrees.

A special thanks also goes to Professor Lamia, who introduced me to chemistry when I was in high school with his lesson on radioactive decay of elements. From that moment on, I began to think about science, and chemistry in particular, in a completely different way.

Finally, I would like to thank the SAMOTHRACE Foundation for funding my doctoral studies, which I hope will enable me to achieve my personal goals in the future.

Contents

Abstract

In recent decades, the spread of industry has led to better living conditions for the human population, but as a consequence, an exponential increase in environmental pollution has also been observed. Numerous volatile compounds and gases are released into the environment from chemical plants, causing potentially hazardous conditions for human health. For this reason, there is great interest in developing new molecular chemosensors capable of ensuring rapid, highly selective and sensitive, low-cost and on-site detection of these compounds. Among these, optical and electrical chemosensors have received increasing attention for their advantages over classical sensing methods, such as simpler detection, fast response times, cheaper instrumentation, ease of fabrication, and on-site detection. Zn(salen)-type Lewis acid complexes have been extensively studied in recent years, providing insights into their aggregation/deaggregation processes and, more interestingly, their solid-state optical properties, suitable for the development of molecular sensors for the detection of air pollutants.

This Ph.D. thesis, promoted within the framework of the SAMOTHRACE project, deals with the development of novel molecular chemosensors for the selective and sensitive detection of vapors of nitrogen-containing volatile organic compounds (N-VOCs) and ammonia, and can be mainly divided in three parts: i) detection of mono- and diamine vapors, *n*-butylamine (BA) and ethylenediamine (EDA), using a vapochromic/ vapoluminescent Zn(salen)-type complex, **1**, on paper-based films (PBFs); ii) detection of pyridine (Py) vapors by PBFs of a vapochromic Zn(salen)-type complex, **2**; and iii) detection of NH_3 using conductometric sensors based on **1**/lutetium bis-phthalocyanine ($LuPc_2$) heterojunctions.

In the first part, the vapochromic/vapoluminescent response of **1**-PBFs towards vapors of different classes of VOCs is explored, to then achieve the selective and sensitive detection of BA vapors. To this end, the optimization of the **1**-PBFs fabrication procedure and the investigation of their appropriate storage conditions were first studied to achieve high repeatability and optical uniformity of the films, as a fundamental prerequisite for quantitative detection studies. Annealed **1**-PBFs are found to selectively detect BA vapors over all other VOCs involved, with a LOD down to 2.0 ppm, below the OSHA permissible exposure limit of 5 ppm. As-prepared and annealed **1**-PBFs also enabled detection of the IDLH (300 ppm) established by NIOSH for BA vapors. The high selectivity of **1**-PBFs was demonstrated by competitive experiments, in which the optical response of **1**-PBFs is found to be selective for BAs over other relevant primary aliphatic amines, especially at low concentrations (tens of ppm). The color change of **1**-PBFs detected with a smartphone-assisted color recognition app and appropriate RGB color analysis, including normalization to the rgb values and ΔE_{rgb} color difference, also enabled the quantification of BA vapors, useful for on-site detection studies. BA vapor leakage simulation experiments showed that both as-prepared and annealed **1**-PBF1s allow the detection of IDLH and PEL-C values, thus demonstrating their suitability for real-time detection of indoor amine contamination in semi-confined environments.

As-prepared and annealed **1**-PBFs also enabled discriminative and sensitive detection of volatile diamine vapors from those of monoamines, since their vapochromic and

vapoluminescent response is accompanied by distinct color changes and fluorescence quenching. Therefore, selective detection of EDA vapors, compared to other volatile diamines, allowed to estimate a LOD of 6.6 ppm, lower than the PEL value of 10 ppm. Overall, a sensing mechanism for the detection of EDA and BA vapors using **1**-PBFs was proposed, also based on XRD and TGA measurements.

In the second part, the vapochromic response of **2**-PBFs to various N-VOCs and oxygenated VOCs (O-VOCs) are explored. Analogously to the previous part, the optimization of the preparation procedure and storage conditions for **2**-PBFs was first studied. Selective detection of Py vapors, among all the other VOCs involved, results in peculiar color and optical absorption changes after exposure to Py vapors. The observed relevant color changes were exploited for the quantification of Py vapors also using a proper RGB color analysis of the films over a very broad concentration range, from tens to thousands of ppm, including the IDLH value (1000 ppm). A thorough study was conducted on the reliability of the RGB approach used, demonstrating that RGB color analysis for sensing applications using non-normalized RGB values can lead to unreliable and hardly repeatable results. Therefore, **2**-PBFs combined with smartphone-assisted RGB color analysis ensure high portability for on-site detection of Py vapors, and these features are unique among chemosensors for Py vapor detection.

The third part reports the preparation and characterization of conductometric sensors based on complex **1** in combination with a conductive material, such as $LuPc_2$. In particular, **1**/$LuPc_2$ bilayers and **1**:$LuPc_2$ mixed films were obtained on indium tin oxide interdigitated electrodes, and then morphological, optical and electrical characterizations of these films were performed. A different surface morphology characterizes bilayer and mixed films, as uniform rough surface and pillar-like or alveolar structure, respectively. Optical microscope images and related Raman spectra of **1**:$LuPc_2$ mixed films having a specific mass ratio show a uniform surface morphology, consistent with AFM results, and the presence of $LuPc_2$ domains. Annealed bilayer and mixed films, show interesting changes in both optical and electrical properties. The peculiar electrical properties of these films can be related to the different interface architecture, such as planar heterojunction for bilayers and bulk heterojunction for mixed films, as determined by electrochemical impedance spectroscopy. The potential application of these films as conductometric chemosensors for the gas-phase detection of NH_3 was also explored. Both bilayers and 1:2 mixed films can discriminate different NH_3 concentrations in a range from 10 to 90 ppm, resulting in improved sensing performance compared to starting materials **1** and $LuPc_2$, especially for the mixed films, thus highlighting the unique behavior of these heterojunction devices.

Abbreviations

AA	Acetaldehyde
ACE	Acetone
Ac_2O	Acetic anhydride
AcOEt	Ethylacetate
AcOH	Acetic acid
ACN	Acetonitrile
AFM	Atomic force microscopy
AN	Aniline
BA	*n*-Butylamine
BAs	Biogenic amines
BHJs	Bulk heterojunctions
BuSH	*n*-Butylthiol
Bz	Benzene
Cy	Cyclohexane
DCM	Dichloromethane
DAB	Diaminobutane
DAPe	Diaminopentane
DAPr	Diaminopropane
DEA	Diethylamine
DMF	N,N-dimethylformamide
EDA	Ethylenediamine
Et_2O	Ethylether
GBFs	Glass-based films
IDEs	Interdigitated electrodes
IDLH	Immediately dangerous to life or health
ITO	Indium thin oxide
LOD	Limit of detection
$LuPc_2$	Lutetium *bis*-phthalocyanine
MeOH	Methanol

NIOSH	National institute for occupational safety and health
N-VOCs	Nitrogen-containing volatile organic compounds
OSHA	Occupational safety and health administration
O-VOCs	Oxygenated volatile organic compounds
PBFs	Paper-based films
PEL	Permissible exposure limit
PHJs	Planar heterojunctions
ppm	parts per million by volume
Py	Pyridine
QE	Quenching efficiency
RH	Relative humidity
RR	Relative response
TEA	Triethylamine
TGA	Thermogravimetric analysis
THF	Tetrahydrofuran
VOCs	Volatile organic compounds
XRD	X-Ray diffraction

Chapter 1

Introduction

The last decades (after 1960) have been characterized by the growth of the human population (as never observed in other historical periods), with the consequent expansion of cities, the growth of industries and the development of new technologies. Industrial development has allowed this enormous expansion and population growth because it guarantees better living conditions, but one of the main problems caused by the spread of industries is the environmental pollution.

Environmental pollution is a generic expression that indicates the release into the environment of some substances, commonly called "pollutants" (such as solids, liquids or vapors/gases), that can modify the properties of ecosystems and, in some cases, lead to the death of animals or plants because of their toxicity.[1,2,3,4] Furthermore, various phenomena such as climate change, global warming, acid rain, eutrophication, the frequency of catastrophic events, *etc.*, can be related to the presence of these pollutants in the environment.[1,5,6] Pollutants do not only derive from anthropogenic activities, but also from biogenic origin. For example, heavy metals are intrinsic components of the soil, but the pollution associated with them is related with their high localized concentration caused by human activity (*e.g.*, extraction from mines, wastewaters of metallurgic industries, *etc.*).[7] Environmental pollutants can be found in soil, water and atmosphere.

Soil pollution is typically associated with the presence of pesticides, hydrocarbons, chemical solvents, fertilizers, heavy metals, particulate matter, plastics, *etc.* Some of these pollutants are introduced in the soil directly (*e.g.*, pesticides), while others arise mainly from improper treatment of urban and industrial wastes.[8,9] Through the soil, some of them can reach underground aquifers and become water contaminants. Their presence in high concentrations can represent a problem for plants, animals, and human health.[2]

Water pollution is associated with the presence of hydrocarbons, surfactants, chemical solvents, anions, heavy metals, insecticides, industries wastewaters, *etc.*,[10] and represents a relevant issue. Ingestion of contaminated water can cause some health problems such as headaches, nausea, diarrhea, cancer, *etc.*[11,12] Furthermore, the presence of nitrogen-containing compounds and phosphorus oxides in lakes can induce the phenomenon of eutrophication, which consists in the growth of microalgae on the water surface, resulting in the consumption of dissolved oxygen and the death of fish and algae.[5]

Air pollution is a widespread and dangerous type of pollution, also because air pollutants can travel long distances and enter in human and animal bodies through the respiratory system. The presence of air pollutants represents a problem for the human population because it can cause respiratory problems, cancer, headaches, asthma, irritation of throat, *etc.*[13] Volatile organic compounds (VOCs), particulate matter, carbon monoxide and dioxide, nitrogen oxides, sulphur oxides, polycyclic aromatic hydrocarbons, *etc.*, are known as air pollutants.

Among air pollutants, VOCs are a class of organic compounds that can easily volatilize at room temperature and atmospheric pressure from solid or liquid substances.[14] Their presence in the environment can derive from natural and/or anthropogenic sources. Natural sources of VOCs include forest fires, aerobic and anaerobic microbial processes, emission from plants, *etc.*, while VOCs derived from anthropogenic sources are mainly related to industrial emissions, the evaporation of organic solvents, tobacco smoke, the combustion of hydrocarbons, the use of pesticides, *etc.* Some VOCs are toxic for human health (*e.g.*, formaldehyde, chloroform, benzene, *etc.*)[14] and can be associated with carcinogenic effects, respiratory problems, allergic responses, *etc.*[15,16,17] Furthermore, these volatile substances are responsible for some environmental phenomena, such as climate change, photochemical smog (O_3 into the troposphere), depletion of stratospheric ozone, *etc.*[18]

VOCs can be classified on the basis of their volatility or chemical structure. In the first case, four different classes of VOCs can be distinguished as: very volatile organic compounds (VVOCs, b.p. < 50°C), VOCs (b.p. = 50 – 260°C), semi-volatile organic compounds (SVOCs, b.p. = 260 – 400°C), and particulate organic matter (POM, b.p. > 400°C).[18] In the second case, they can be distinguished based on their functional group into: halogenated VOCs (HVOCs), oxygenated VOCs (O-VOCs), nitrogen-containing VOCs (N-VOCs), volatile organic sulfur compounds (VOSCs), and non-methane VOCs (NMVOCs). Due to their volatility, organic solvents are mostly air pollutants and often fall into the category of VOCs.

Among N-VOCs, aliphatic and aromatic volatile amines are widely involved in chemical industries as reactants,[19,20] and some of them can be used as food freshness indicators in food industries.[21,22,23] Exposure to high concentrations of these substances can lead to several health diseases, from respiratory problems to carcinogenic effects.[24] To prevent serious health effects on workers, the permissible exposure limit (PEL) to amine vapors and/or other toxic substances in industries is strictly regulated worldwide by some institutions, such as the Occupational Safety and Health Administration (OSHA) in the United States. In addition to the negative effects on human health, the release of volatile amines during industrial chemical processes poses a serious risk of environmental contamination.[25,26,27,28] For all these reasons, their selective and sensitive detection is very important for human and environmental safety.

For these VOC pollutants, there are different standard procedures and analytical techniques that allow their detection. The most common techniques are GC-MS, ESI-MS, ICP-MS, HPLC, voltammetry, potentiometry, conductometry, *etc.*[29,30] These techniques offer good reproducibility and sensibility, low limit of detection (LOD), and good dynamic linear range of detection. However, they often require expensive instrumentation, time-consuming sample pretreatment, and skilled operators. Therefore, the development of detection methods, *e.g.*, chemosensors, that can directly detect VOCs of interest is highly desirable.

The term "chemosensors" refers to materials that exhibit a change in their chemical-physical properties in the presence of a specific analyte or class of analytes. The broad and growing interest in their study depends both on the search for new low-cost, portable, and reusable/disposable devices with selective and sensitive properties, and on the optimization of their performance, such as fast response times, simple, and on-site detection methods.[31,32,33,34] Depending on the chemical-physical property that changes after the interaction between sensor and analyte, chemosensors can be distinguished in

electrochemical,[35] optical,[36] piezoelectric,[37] *etc.*[31,32] Various molecular systems and/or nanomaterials have been widely investigated as chemosensors, for example organic molecules,[38] metal complexes,[39] polymers,[40] metal organic frameworks (MOFs),[41] carbon based materials,[42] *etc.*

Metal complexes of tetradentate Schiff bases show tunable spectroscopic properties useful for the development of new molecular materials for sensing pollutants and toxic substances.[43,44] In particular, Zn(II) complexes derived from salicylaldehyde, or its derivatives, and 1,2-diamines, namely Zn(salen)-type complexes, have been investigated for their interesting optical absorption/fluorescence properties. Their Lewis acidic character associated with the metal center, allows the facile interaction with Lewis bases, in solution and/or in the solid phase.[43] The significant changes in their structure and spectroscopic properties, upon coordination to the Zn(II) atom of Lewis bases, are useful to explore these molecular materials for the detection of VOCs, *e.g.*, volatile amines, having Lewis basicity.

The research activity reported in this doctoral thesis is focused on the development of optical/conductometric chemosensors, based on Zn(salen)-type complexes, for the sensitive and selective detection of VOCs and gases. All aspects such as the synthesis of the metal complexes used, film preparation, standardization of exposure methods, evaluation of detection performance under different conditions and validation of detection methods are discussed. A brief summary of the structure and contents of this thesis is given below.

Chapter 2 provides an overview of optical and electrical chemosensors, and their application for the detection of VOCs/gases, including properties of Zn(salen)-type complexes.

Chapter 3 reports all the experimental procedures used in this thesis, including the synthesis, film preparation, apparatus used for exposure to VOCs and ammonia, and the methods used.

Chapter 4 describes the vapochromic/vapoluminescent properties of glass- and paper-based films of a Zn(salen)-type complex, **1**, and its ability to detect specific volatile aliphatic mono- and diamines. Selective and sensitive detection of *n*-butylamine (BA) vapors using vapochromic and vapoluminescent optical changes as well as RGB color analysis is described. A detailed investigation of the effect of temperature, relative humidity, exposure time, and potential interfering factors on detection performance is also reported.

Chapter 5 describes the sensitive and selective detection of pyridine (Py) vapors using paper-based films of a Zn(salen)-type complex, **2**. The vapochromic response of the films is evaluated by UV-vis reflectance spectra and a detailed RGB color analysis.

Chapter 6 describes the preparation and characterization of conductometric sensors based on complex **1** and lutetium *bis*-phthalocyanine ($LuPc_2$), such as **1**/$LuPc_2$ bilayers and **1**:$LuPc_2$ mixed films. Evaluation of the morphological, optical, and electrical properties of the obtained heterostructures is reported, in addition to their potential application in NH_3 gas sensing.

All the research activity reported in this thesis was developed mainly at the University of Catania, with the exception of the results of Chapter 6, which are related to a six-month research activity at the "Institut de Chimie Moléculaire de l'Université de Bourgogne (ICMUB)" in Dijon (France).

Chapter 2

Chemosensors for Detection of Volatile Organic Compounds and Gases

Contents

2.1. Introduction

In recent years, there has been a growing interest in the development of chemical systems and devices for the detection of VOCs and gases, mainly for two reasons. First, several VOCs and gases are known as toxic substances that pose a relevant risk to human safety.[15,16,18] Secondly, the evolution of technologies has caused a widespread of industries and some changes in several industrial processes, which sometimes involve the use or production of these substances.[45,46] Consequently, they are also considered environmental pollutants due to their potential release into the environment from industries.[47] Therefore, rapid, simple and quantitative detection of VOCs and harmful gases is a very important topic in a wide range of applications, involving human and environmental safety.[15,47]

The most powerful technique for VOC/gas detection is clearly gas chromatography-mass spectrometry (GC-MS), which provides high sensitivity and specificity for the identification and detection of thousands of VOCs.[29,30,48,49] This technique is widely used in laboratory settings, but due to its bulky and expensive equipment, time-consuming operation, and the need for skilled operators, it is not suitable for portable VOC detection.[50]

An emerging approach for the detection of VOCs and gases is the development of materials called chemosensors.[31,34] The International Union of Pure and Applied Chemistry (IUPAC) define a chemosensor as "a device that transforms chemical information, ranging from the concentration of a specific sample component to total composition analysis, into an analytically useful signal".[51] In other words, the term chemosensor indicates a material that exhibits a change of its chemical-physical properties in the presence of specific analyte or class of analytes. Typically, a chemosensor consists of three basic parts, such as: i) a signaling unit, which transforms the chemical response into a physical signal; ii) a receptor unit, containing a binding site for the analyte; and iii) a mean of communication between them (Figure 2.1a).[52,53] Alternatively, chemosensors can be formed of an integrated system containing both receptor and signaling units (Figure 2.1b).[54]

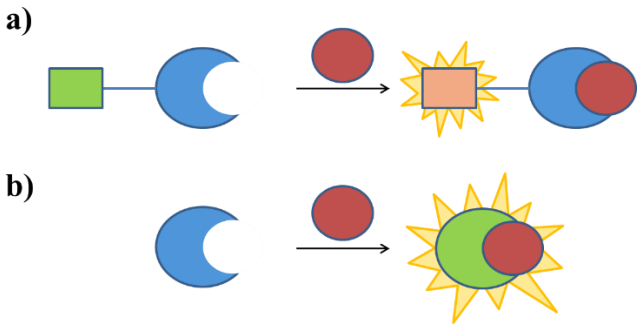

Figure 2.1. Schematic sketch of a chemosensor composed by **(a)** receptor (blue) and signaling (green) units and **(b)** an integrated system of these when interacting with an analyte (red).

The analytical signal obtained by the interaction between the receptor part and the analyte can derive from a physical, chemical or biochemical interaction.[52,54] Usually, physical interactions involved during physisorption processes are characterized by weak intermolecular interactions (van der Waals forces, hydrogen bonding, π−π interactions), and the analyte can be easily removed from the binding site of the receptor under specific conditions.[52,55] Thus, these non-covalent interactions may lead to a reversible or partially

reversible response of the chemosensor. On the other hand, chemical and/or biochemical interactions involve a chemical reaction resulting in the formation/breaking of chemical bonds that are responsible of the change in the analytical signal.[52,54] In this case, covalent bonds can provide high selectivity and sensitivity, and often leads to an irreversible response.

The specific type of interaction is determined by the chemical structure of the sensing material and the analyte. Thus, the sensing properties of a chemosensor, such as sensitivity, selectivity, and reversibility, can be modulated by a proper design of the involved molecular system and/or functionalization of the receptor/signaling unit.[54] Depending on the type of interaction involved, chemosensors are characterized by the formation of reversible interactions between the receptor and the analyte, while, if the interaction with the analyte is irreversible, they are called "chemodosimeters".[56]

Commonly, the classification of chemosensors is also based on the chemical-physical property that changes during the binding process between the sensor and analyte.[57] Thus, they can be distinguished in optical (*e.g.* colorimetric and fluorimetric),[36,58] mass sensitive (*e.g.* piezoelectric),[37,59] electrical (*e.g.* conductometric),[60,61,62,63] and electrochemical (*e.g.* amperometric and potentiometric).[35,64,65] Among these different categories of chemosensors, the growing interest in the development of electrical and optical sensors is paralleled by the development of simpler analytical tools, such as portable instruments for on-site detection of analytes,[50,66] which can enable their application in various fields such as medical diagnosis,[67,68] environmental safety,[69,70] and food quality monitoring.[23,71,72]

2.2. Optical Sensors

Optical chemosensors are characterized by a change in their optical properties in the presence of specific analytes. In general, several optical properties of a material such as color, absorbance, fluorescence, reflectance and refractive index are involved in the optical sensing of VOCs and gases.[58] In addition to simply comparing the absolute absorbance/fluorescence intensity values, *etc.* before and after interaction with the analyte, changes in other parameters such as fluorescence lifetime, light scattering, diffraction, resonance, polarization, *etc.* can also be useful for analyte recognition.[73]

The optical sensing of VOCs/gases involves three main components: i) a light source; ii) the pure chemosensor or a transducer functionalized with a VOC-sensitive material; and iii) a light detector. Different types of optical sensors can be distinguished on the basis of the physical parameter that changes upon the interaction with the analyte. For example, a change in the intensity of diffracted light in the presence of VOCs/gases can be detected for transducers based on a diffraction structure,[74] changes in interference patterns caused by the presence of VOCs (which introduce a difference in the phase of the two interfering beams) characterize interferometers,[75] variation in the polarization state of light passing through a transducer influenced by VOCs related to polarization-based sensors,[76] while the interaction with VOCs/gases influences the propagation of evanescent waves in optical fibers and plasmonic structures.[77,78,79] Among the different classes of optical sensors, a very wide interest is related to optical sensors based on materials that change their color/emission properties upon interaction with VOCs, and typically provide a visual response that can usually be observed even with the naked-eye.[80,81] In the latter case, the signaling unit is a

chromophore/fluorophore. It is therefore possible to distinguish two categories of optical chemosensors: colorimetric (or chromogenic) chemosensors and fluorometric (or fluorogenic) chemosensors. Depending on their molecular structure and the analyte involved, different detection mechanisms can be ascribed to these classes of chemosensors, resulting in peculiar optical responses.[73]

Compared to electrical sensors, optical sensors do not rely on electric fields or high-power inputs, and external factors such as humidity and temperature typically interfere less with the sensitive detection of analytes. Many optical chemosensors are immune to electromagnetic interference (*e.g.,* diffraction and fiber-based sensors), thus they can be implemented in industrial processes associated with strong electromagnetic fields. In relation to the high suitability of optical chemosensors in real-world applications, non-dispersive infrared (NDIR) sensors are predominant among commercial optical VOC sensors,[82] and enable the detection of these analytes by monitoring changes at specific wavelengths due to the unique absorption of VOC radiation, resulting in a reduction of the radiation reaching the detector.

Several types of chemosensors based on porphyrins,[83] hybrid materials,[84] polymers,[85,86] MOFs,[87] metal complexes,[88] perovskites,[89] *etc.*[90,91] are reported in literature for the development of optical chemosensors for the detection of VOCs/gases. In general, optical chemosensors are characterized by high selectivity, high sensibility, low cost, and fast response time.[73] In addition, many optical sensors can also provide real-time measurements and are suitable for remote sensing, which are crucial for continuous monitoring applications in industrial and environmental safety.[66,92] Optical sensors also offer significant potential for miniaturization, especially in the case of optical fibers and plasmonic structures, making them suitable for the development of portable and/or wearable devices.

A more detailed discussion about colorimetric and fluorometric optical sensors is reported in the following sections.

2.2.1. Colorimetric Sensors

Colorimetric sensors are a class of optical sensors involving a visible color change in the presence of analytes. The changes in optical absorption properties of these sensors are related to variations in energy levels involved in the chemisorption process. For example, in metal coordination complexes different mechanisms are involved to explain this behavior such as metal coordination, demetallation, metal-to-ligand charge transfer (MLCT), ligand-to-metal charge transfer (LMCT), *etc*.[91,93]

Colorimetric sensors are widely investigated in VOC/gas sensing mainly for their wide response to analytes, low cost, disposability, straightforward readability of their signal responses, high selectivity, and environmental tolerance,[81,94] making them highly attractive in a broad range of fields including clinical diagnosis, food safety, and environmental monitoring. In general, colorimetric sensors can provide intuitive detection for qualitative (*e.g.,* naked-eye observation) and quantitative (*e.g.,* UV–vis reflectance/absorbance or smartphone-based observation) sensing applications.[94] This clearly represents a great advantage over other detection platforms, as it enables direct and sensitive detection of analytes on-site, without the need for expensive instrumentation.[92] Common classes of

sensing materials for the development of colorimetric sensors include porphyrins and metalloporphyrins,[83] nanoparticles,[95] metal complexes,[88] polymers,[96] *etc.*

When the quantification of VOCs/gases involves optical absorption spectroscopy, the response of the colorimetric chemosensor can be evaluated on the basis of the Beer-Lambert Law:[97]

$$I = I_0 \exp(-\alpha l) \quad \textbf{(2.1)}$$

where I and I_0 are transmitted and incident light, respectively, α is the absorption coefficient of the sample and l is the optical length. A change in the values of I can be caused by changes of the absorption coefficient or in the optical length. The interaction between VOCs/gases and the sensing material, *e.g.* a layer, depends mainly on the architecture and design of the film, as well as the nature of the sensing material.[54]

The rich visual color changes of colorimetric chemosensors can also be estimated using methods that can quantitatively describe the color change using portable cameras or smartphones for detection of harmful analytes.[92,98,99,100] Recently, many examples have been reported in the literature on the evaluation of color changes using RGB (Red, Green, and Blue), HSV (Hue, Saturation, Value), or CIE (Commission Internationale de l'Eclairage) color models applied to colorimetric sensors.[100,101,102] Nowadays, the RGB color space is widely used in digital displays and allows the digitization of colors by combining three parameters as the intensity values of red, green and blue (ranging from 0 to 255 for each value). It also has several advantages over other color spaces, such as simplicity, compact data representation, ease of implementation in sensing systems, and direct mapping to device-specific color spaces.[101]

For example, Garcia *et al.* reported a new colorimetric chemosensor that enabled the detection of 14 different VOCs and hazardous gases.[103] In particular, the solid sensing material as an iron salt having formula $[Fe(H_2btm)_2(H_2O)_2]Cl_2$ (H_2btm = di(1*H*-tetrazol-5-yl)methane) was exposed to different common solvents, acids and amines, leading to peculiar color changes, detectable by naked eye, especially in the case of amine vapors. Very high sensitivity (0.58 ppm for NH_3, 0.62 ppm for hydrazine, 0.45 ppm for isobutylamine, and 0.71 ppm for diethylamine) and fast response (<2 min) to these analytes were achieved. The sensor response was also evaluated using RGB color analysis. In addition, the color changes after exposure to all the involved analytes were classified from the hierarchical cluster analysis (HCA).

Recently, there has been a growing interest in the development of sensor arrays composed of the combination of multiple colorimetric sensors with different response to specific analytes, with potential advantages of improved selectivity and sensitivity.[98]

For example, Aimiao *et al.* reported a paper-based colorimetric sensor array with an integrated smartphone to achieve visual detection of traces of H_2S, SO_2, and NO_2 gases.[104] Silver nanoparticles were synthesized, capped by long-chain hydrophobic molecules (Figure 2.2) and high-molecular hydrophilic polymer, and printed on a porous hydrophobic PVDF paper as substrate obtaining a 1×12 linear array pattern. The fabricated sensor array exhibits excellent fast response (5 min exposure) sensitivity to H_2S, SO_2, and NO_2 gases, with calculated LODs of 12.8 ppb for H_2S, 131.8 ppb for SO_2, and 23.1 ppb for NO_2, respectively. In all cases, the achieved LODs are below their respective permissible exposure limits. The

selectivity recognition ability of the sensor array was also evaluated considering 19 common VOCs/gases (acid, amines, aldehydes, ketones, alcohols, sulfur- containing, nitrogen-containing gases) as potential interferents. Among these, the sensor series showed a high selective colorimetric response towards H_2S, SO_2, and NO_2 gases, even in low concentrations (0.5 ppm). Additionally, the sensor array fabricated and integrated with the smartphone was tested by monitoring the freshness of chicken at room temperature for 24 hours.

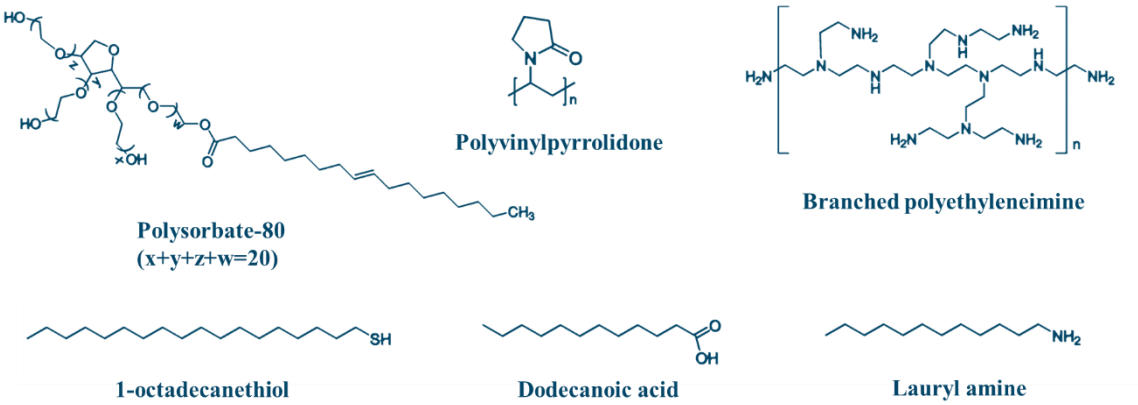

Figure 2.2. Molecular structures of capping agents used by Aimiao *et al.* Adapted from ref. 104.

Wang *et al*. described a wearable, readable colorimetric sensing system with a microchannel structure for *in-situ* detection of complex VOCs.[105] The highly gas-sensitive materials include eight dye/MOF composites that respond to various VOCs, and two Pd^{2+}/dye/MOF composites that are sensitive to ethylene. These materials were further deposited on an electrospun nanofiber membrane. The final wearable olfactory visualization system is formed by two adhesive layers, a PDMS microfluidic channel, the colorimetric sensing arrays, a PDMS cap, and an image processing marker. Five VOCs, namely *trans*-2-hexenal, benzaldehyde, 3-carene, ethanol, and ethyl acetate, were selected as characteristic VOCs due to their high concentration and significant variation in amounts during fruit ripening, and all detection parameters were optimized based on the response to the first analyte. The spots in the RGB difference became brighter as the concentration of *trans*-2-hexenal increased, and a linear dynamic response range from 5 to 500 ppm was observed, with a LOD of 5 ppm. The discriminative ability of the colorimetric sensor array was evaluated using principal component analysis (PCA) and HCA based on dataset obtained from RGB values. Finally, the sensor array was attached on the surface of different fruits (bananas, mangoes, and kiwis) to collect and monitor VOCs using the DenseNet classification method,[106] enabling *in-situ* detection and accurate classification of fruit ripeness.

Although RGB color analysis is a powerful tool for quantifying VOC/gas concentration using colorimetric sensors, its main limitations are its dependence on lighting conditions, difficult reproducibility of some color hues (*e.g.,* pastel and neon hues), and the difficulty of using color comparisons between different devices.

2.2.2. Fluorometric Sensors

Fluorometric chemosensors exhibit a change in fluorescence emission upon binding to a proper analyte. It is important to distinguish fluorescence and phosphorescence

phenomena. In both cases, photon emission is observed due to the change of state of an excited electron, but the fluorescence phenomenon is characterized by a shorter emission lifetime than phosphorescence.[107] Furthermore, the fluorescence emission process involves singlet states, while in the case of phosphorescence, an excited triplet transition state is involved.

In fluorometric sensors, the wavelength difference between the excitation (higher photon energy and lower wavelength) and emission (lower photon energy and higher wavelength) states is known as the Stokes shift, and the emission changes of the sensor can be useful to detect VOCs and gases.[39,80] The presence of these analytes can be observed with the aid of an UV lamp for qualitative detection, or with a fluorescence spectrometer for quantitative detection.[108] Typically, fluorogenic chemosensors are more sensitive than colorimetric chemosensors.

Analogously to colorimetric sensors, changes in the properties of fluorescent chemosensors are ascribed to the electronic interactions between the sensor and VOC/gas. In general, depending on the nature of the chemosensor-analyte interaction, four types of signals can be observed: i) shift of the emission peak; ii) fluorescence quenching; iii) fluorescence enhancement (or fluorescence turn-on); iv) resonance energy transfer (RET). Different mechanisms are interested in these processes, such as photoinduced electron transfer (PET), fluorescence resonance electron transfer (FRET), aggregation induced emission (AIE), chelation enhanced fluorescence (CHEF), intramolecular charge transfer (ICT), and electronic energy transfer (EET).[73,109]

A wide variety of sensing materials have been designed for VOC detection by monitoring their fluorescence response, such as metal complexes,[39] conjugated polymers,[40] MOFs,[110,111] supramolecular systems,[112] *etc.* Fluorescent chemosensors have a great potential in the detection of a wide range of analytes and are usually characterized by flexible synthesis, convenient processing, high sensitivity, good reproducibility, and biocompatibility.[113]

Sun *et al.* developed a fluorescent gas sensor (named CA-SCH_3) based on an indanonalkene structure for the quantitative detection of volatile amines.[114] Star shaped test papers were used as substrate and loaded with the molecular material by drop-casting of a CH_2Cl_2 solution. Initially the sensor is non-emissive under 365 nm irradiation, but a turn on of the fluorescence is obtained after exposure to NH_3 vapors (Figure 2.3) produced from its ammonium salt ($NH_3 \cdot H_2O$).

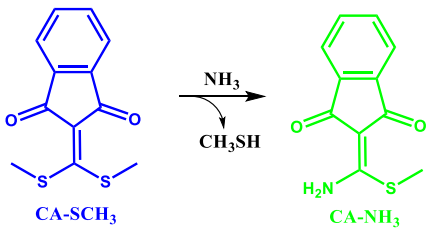

Figure 2.3. Sensing mechanism for the detection of NH_3 by CA-SCH_3. Adapted from ref. 114.

In particular, a moderate linearity in a concentration range of 0 – 624 ppm of NH_3 and a calculated LOD of 36 ppm are obtained. In addition to NH_3, an enhancement of in the emission of the system was also observed in the presence of different amines including

benzylamine, hydrazine, ethylamine, putrescine, 1,3-propylene diamine, cadaverine, trimethylamine and dimethylamine, while no response was obtained for aniline, *p*-bromoaniline, and histamine. Also, the real-world application of the sensor was tested by monitoring the spoilage of a cod fillet sealed in a plastic box and stored at 4 °C for 5 days.

A very interesting example in the application of a fluorometric sensor array was recently reported by Fang *et al.*[115] In particular, a column-shaped fluorometric sensor array was prepared using a capillary filled with fluorophore-loaded silica particles (~40 μm) compared to the commonly reported plane-shaped sensor arrays. Modified silica particles were loaded with four different fluorophores (Figure 2.4) dissolved in CH_2Cl_2, dried by heating, and arranged into a capillary (diameter 2.5 mm) at a fixed length (6 mm). Then the sensing and discrimination ability of the sensor array was evaluated by exposure to six alcohols: methanol, ethanol, isopropanol, *sec*-butanol, *tert*-butanol, and *tert*-amyl alcohol. Thanks to the different emission changes of the four fluorophores, the fluorometric array allowed the six tested alcohols to be distinguished as primary, secondary, or tertiary and to be identified individually. Furthermore, a better illustration of the sensor array responses towards these alcohols was also reported using absolute RGB values of the corresponding fluorescence changes taken from digital pictures of the array.

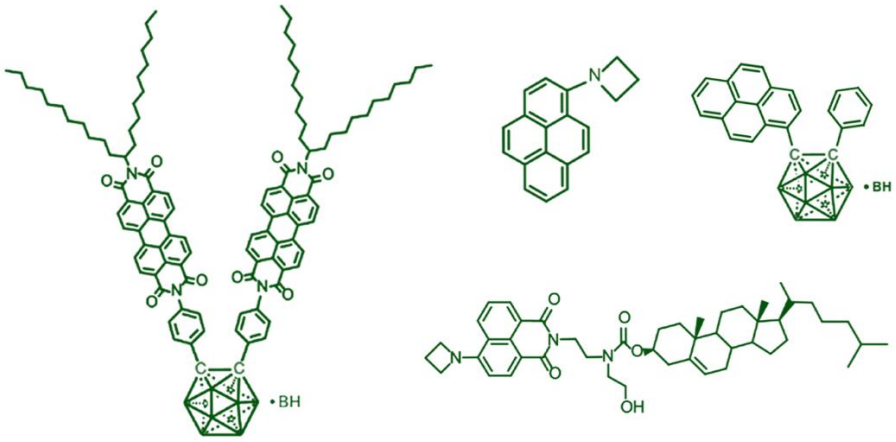

Figure 2.4. Molecular structure of the four fluorophores used by Fang *et al.* Adapted from ref. 115.

2.2.3. Vapochromic/Vapoluminescent Sensors

An interesting class of colorimetric/fluorometric chemosensors is represented by molecular systems having vapochromic behavior. The term "vapochromism" was introduced by Mann *et al.* in 1995 after the observation on the optical behavior of [Pt(aryl isonitrile)$_4$][Pd(CN)$_4$] salts in the presence of some organic solvents.[116] The same group also introduced the term "vapoluminescent" referring to an electronic nose transducer array based on platinum double salts.[117]

Generally, the term vapochromism refers to the reversible optical absorption and/or emission of a solid substance exposed to specific vapors and/or gases. The vapochromic/vapoluminescent response to these analytes is usually produced by a shift in an electronic absorption band of a molecule.[118] In particular, the vapochromic response of chemosensors towards VOCs/gases can be distinguished in two fundamental types of vapochromism: type I and type II vapochromism. In type I vapochromism, structural

changes in crystal packing and alterations in intermolecular interactions (such as metal−metal interactions, π-stacking, and hydrogen bonding) are involved, while direct interactions between the molecule and the analyte occurs in type II vapochromism.[118]

Many d^6, d^8, or d^{10} metal complexes containing strong-field coordination donors (*e.g.,* C, N, P, or S atoms) and/or extended π-system are characterized by a visible color/emission via intraligand (IL), metal-to ligand charge transfer (MLCT), ligand-to-metal charge transfer (LMCT) or ligand-to-ligand charge transfer (LLCT) transitions. Solid-state stacked structures of these metal complexes are characterized by strong intermolecular interactions such as metallophilic contacts, π–π stacking, and hydrogen bonding. These interactions can be perturbed incorporating vapor/gas molecules into the solid phase, thus inducing dramatic changes in color and/or emission intensity, easily observable by the naked-eye. Metallophilic interactions and/or π-stacking are common in many Pt(II) and Au(I) containing substances,[119,120,121] therefore the related vapochromism in the presence of vapors/gases falls under the type I vapochromism mechanism.

On the other hand, the occurrence of changes in the first coordination sphere, including the variation of both the coordination number and the coordination geometry, is common for several V(IV), Co(II), Ni(II), Cu(II), and Zn(II) metal complexes[122,123] and metalloporphyrins. In this case, the color/emission changes due to interaction with VOCs/gases can be attributed to type II vapochromism.

In general, in addition to the mentioned complexes, various molecular systems have also been reported in recent literature as vapochromic/vapoluminescent materials, such as supramolecular polymers[124] and organic molecular crystals.[125] Recent studies have also focused on development of vapochromic multifunctional systems that exhibit additional functions (*e.g.,* conductivity or magnetic properties) in order to expand the potential applications of vapochromic materials.[126]

A vapochromic sensor array based on MOFs characterized by distinct responses to VOCs and humidity has been developed by Park *et al*.[127] This sensor array consists of dicopper paddlewheel clusters and dimethylamine azobenzene as binary colorimetric sensing moieties. Monolayers of MOF crystals glass films were prepared using the liquid–air interfacial self-assembly technique and then transferred into a transparent cover glass substrate by simply lifting the substrate out of the water. After exposure to 14 different VOCs, the sensor displays a broad spectrum of colors, ranging from green to red, and exposure to different concentrations of THF vapor (range 50 – 200 ppm) results in a linear response and a LOD of 25 ppm for this substance obtained by quantifying the response using a smartphone camera.

Kato *et al.* reported a light-on sensor based on a coordinatively unsaturated Cu(I) complex (CuI(xantphos)) that could detect N-heteroaromatic vapors by luminescence changes.[128] First, the vapochromic properties of powders of the Cu(I) complex were evaluated in the presence of Py and 2-methylpyrazine (Mepyz) vapors, showing bright blue-green and yellow emissions, respectively (Figure 2.5). Then, a vapoluminescent thin film was fabricated using the Cu(I) complex and polyvinylpyrrolidone (PVP) via spin-coating. The response of the system to vapors is very fast (about 15 s) and, again, luminescence changes similar to those of the powder samples are observed after exposure to Py and Mepyz vapors.

Vapochromic/vapoluminescent materials certainly represent promising, but still little explored, chemosensors for VOCs and gases.

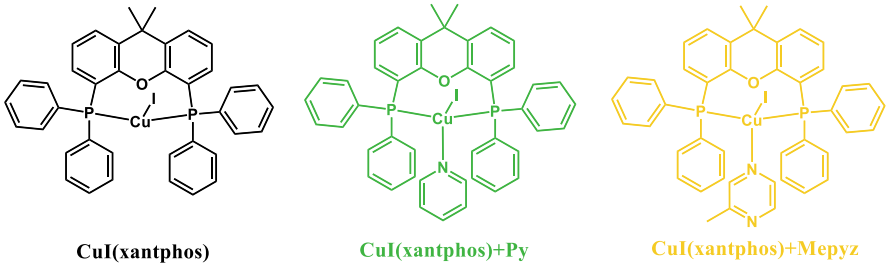

Figure 2.5. Molecular structure of Cu(I) complex used by Kato *et al.* and upon interaction with Py and Mepyz.

2.3. Electrical Sensors

Electrical sensors are characterized by a change of the electrical properties of the sensing material induced by the interaction with target analytes. These changes can be related to a few main physical parameters including electrical conductivity, work function, and permittivity.[129] The transduction process of these properties in a measurable electrical signal results in changes of current, capacitance, resistance/impedance, voltage, or electrical potential depending on the electronic components constituting the electrical sensor.[130] Further processing of these electrical signals including amplification, filtering, analysis, or display, which allows for information regarding the identification of the specific analyte and its quantification.[131]

A key role in determining the sensing properties of electrical devices such as sensitivity, selectivity, stability, and biocompatibility is related to the specific type of interaction between the sensing material and the target analyte, and the device architecture.[91] It is therefore possible to distinguish three different fundamental mechanisms responsible for the variations of one or more physical parameters in electrical sensors such as: i) Schottky barrier; ii) modulation of the doping level; and iii) formation of dipole and interfacial layer.

A Schottky barrier (rectifying contact) or an Ohmic contact can be generated at the interface between two materials characterized by different work functions.[132] The formation of a Schottky barrier is usually observed in electrical devices containing a metal – semiconductor junction because of the mismatch in their work functions. The height of the Schottky barrier depends on the work function difference of the two materials in electrical contact.[133] When a bias is applied to the junction, a bend of the barrier is observed on the semiconductor side, but this does not change the height of the barrier on the metal side. Thus, the Schottky barrier facilitates the unilateral flow of electrons. A change in the barrier height at the metal – semiconductor junction can be observed as a consequence of the adsorption of analytes at the semiconductor interface.[133] This event can cause a change in the doping level of the material, and consequently on its work function. On the other hand, an Ohmic junction is formed when the work function of the semiconductor is higher than the conducting component.[132] The Ohmic contact facilitates the flow of electrons between the metal and semiconductor materials in both forward and reverse-biased directions.

The doping process usually results in a change of the electrical properties of a semiconductor, and in an improved conductivity of the material due to the excess of electrons

(*n*-type) or holes (*p*-type) introduced. The doping level of a material can be defined as primary or secondary doping. The primary doping (inherent doping) involves the introduction of impurities, *e.g.* metal ions, in the lattice of a pure semiconductor.[134,135] This process is carried out during the synthesis of the semiconducting materials or during the chemical/electrochemical preparation processes.[135] On the other hand, in the interaction between the sensing material (semiconductor) and the analyte, the latter can act as an electron donor (*n*-type dopant) or acceptor (*p*-type dopant). This process is attributed as secondary doping of semiconducting sensing materials.[134] In both cases, modulation of the majority charge carriers through doping processes modify the density of states and the majority of charge carriers, and consequently the conductivity of the sensor.[136] Thus, changes in the conductivity of an electric sensing device due to a secondary doping process is closely related to the occupation of the sensing material surface by the analyte molecules. In this case, the sensing mechanism is described considering that the atoms on the surface of the sensing material can act as binding sites for molecular adsorption processes.[137]

Another possibility in the interaction of analytes with the semiconducting material can be the polarization or ionization of the analytes at the surface of the material.[129] In this case the redistribution of the electrical charges in the polarized/ionized layer (depletion region) causes the band bending at the material/metal interface.[138] The corresponding output signal, *e.g.* current, is related to the amount of the analyte adsorbed on the surface of the sensing material. This mechanism is evident in *n*-type metal oxide semiconductors under an oxygen−rich atmosphere because of the adsorption of oxygen molecules on the surface of the metal oxide.[139] Also, an equilibrium between the concentration of charge carriers at the material surface, and at the metal electrode/material interface is reached when an analyte is adsorbed on the surface of a semiconducting material. This result in the formation of an interfacial layer between the metal and semiconductor. Interactions with analytes can cause a modification of the barrier height, and consequently of the current flowing across the metal/semiconductor interface.[138] This will cause either an increase in the barrier height and an improvement in the rectification current-voltage behavior, or a reduction in the energy barrier and an improvement in the ohmic current-voltage behavior.[132] Furthermore, the interfacial layer should be able to support the transport of electrons or holes across the interface.

In general, electrical sensors offer several advantages over traditional analytical methods (*e.g.,* GC-MS), such as low cost, the possibility of miniaturization, intuitive reading, and low power consumption.[129] Many inorganic materials, like metal oxides,[140,141,142,143] are widely used for the fabrication of electrical devices, even for the development of commercially available electrical sensors,[82] but they present some problems. Typically, the preparation of inorganic devices requires very lengthy processes (*e.g.*, lithography) and expensive equipment, and then these devices require high working temperatures for gas sensing applications. In parallel, the development of organic semiconductors shows several advantages such as solution processability, mechanical flexibility, low cost, and multiple molecular designs.[144] All these features also have effects on the sensing performance of organic semiconductors such as fast response, high sensitivity, and good selectivity. Thanks to these advantages and their interesting electrical properties, molecular materials such as perylene diimide derivatives,[145] zeolite-based materials,[146] covalent organic frameworks,[147]

radical phthalocyanines,[144] semiconducting nanoparticles,[148] hybrid materials,[84] conductive polymers,[42] graphene-based materials,[149] *etc.*, have been widely studied for the development of VOC/gas sensing devices.[42,150,151,152]

The architectures of these chemical sensors, with few exceptions, fall into five categories: chemical diodes, capacitive sensors (or chemicapacitors), field−effect transistors (FETs), conductometric sensors (or chemiresistors), and electrochemical sensors.[129]

In the latter case, the working principle of electrochemical sensors is related to the oxidation/reduction of the target VOC/gas that occurs during the vapor/gas diffusion of the analyte to the working electrode interface inside an electrochemical cell containing a solid, liquid, or gaseous electrolyte or ionic conductor.[35,153] Such electrochemical reaction results in a charge transfer process and/or current flow change proportional to the VOC/gas concentration.[64] Several examples of such sensors are reported in literature involving their use in different fields such as safety and security,[154] air pollution,[155] food quality monitoring,[156] *etc.*

Electrochemical sensors include a wide variety of systems that can be classified on the basis of the measurable response involved in the presence of VOCs/gases in potentiometric, voltametric, amperometric, and impedimetric sensors.[153]

The following sections provide a discussion of the general configuration and working mechanism of electrical sensors that do not involve redox reactions (Figure 2.6).

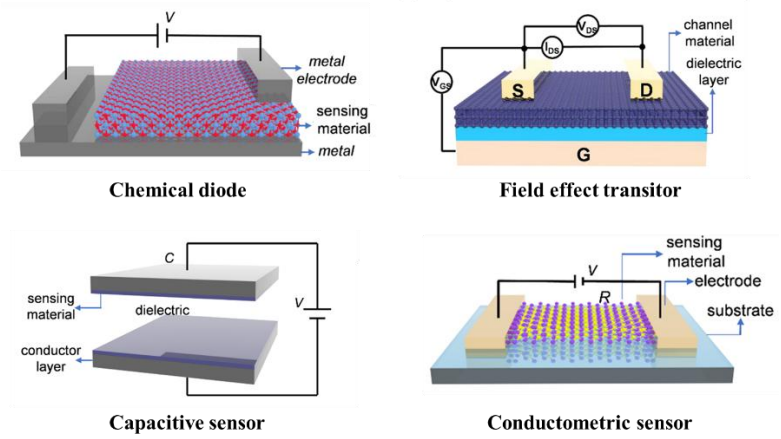

Figure 2.6. Schematic representation of electrical sensor architectures of chemical diodes, field effect transistors, capacitive sensors and conductometric sensors.

2.3.1. Chemical Diodes

A diode is a two−terminal electronic component characterized by a low resistance to the current flow in one direction, and a high resistance in the opposite direction. Two types of chemical diodes can be distinguished, such as Schottky diodes and p−n junction diodes.

Schottky diode sensors are composed of a *p*-type or *n*-type semiconducting material that is in electrical contact with the electrode.[157] Schottky diodes require simple fabrication procedures, without the need of high-temperature diffusion/oxidation steps or photolithographic processes. Typically, the electrical response of Schottky diode-based sensors towards vapors or gases is described by current-voltage (I – V) characteristics, but it is also possible to consider analogous current density – voltage (J – V) curves. The interaction

with the analyte results in an induced voltage shift at a given diode current I (or current density J) extracted from I – V characteristics.[157]

The current changes in Schottky diodes can be explained by a charge carrier transport mechanism described by the following equation:[136]

$$I = I_S \left[exp\left({}^{eV}/_{kT}\right) - 1\right] \quad \textbf{(2.2)}$$

where e is the fundamental charge, V is the forward bias voltage, k is the Boltzmann constant, T is temperature, and I_S is the reverse bias saturation current, and is defined as:

$$I_S = eN_C\mu_e E_{max}\, exp(-\frac{\Phi_b}{kT}) \quad \textbf{(2.3)}$$

where ϕ_b is the Schottky barrier height for an ideal contact between a metal and a semiconductor, e is the fundamental charge, k is the Boltzmann constant, T is temperature, N_C is the effective density of states in the conduction band of an inorganic semiconductor, μ_e is the electron mobility, and E_{max} is the maximum field strength at the metal/semiconductor interface.

The generation of an electric signal in Schottky barrier diodes in the presence of specific analytes originates from a Schottky barrier height change (Section 2.3) or by an alteration the built-in voltage in the device.[133] Thus, the sensing response can be due to either the formation of a dipole layer by adsorption of species at the surface of a metal that affects the interfacial polarization, or caused by the adsorption of analytes on the semiconductor (secondary doping), which changes its work function and, hence, the contact potential or built-in voltage of the diode. The former mechanism is usually encountered in Schottky barrier diodes based on inorganic semiconductors, while the latter is related to diodes based on organic semiconductors.[134]

As described in the previous section, usually electrical devices based on inorganic materials need high operating temperatures. However, Paily *et al.* developed a sensor based on a zinc oxide (ZnO) Schottky diode that can detect carbon monoxide (CO) at very low concentrations (as low as one ppm) at room temperature.[158] Three sensors were fabricated using a microcantilever printing system, changing the device channel system for the first two samples and using drop-casting of the ZnO ink on the silver nanoparticles (AgNP) electrodes for the third sensor. Different barrier heights characterize the three sensors, but all the sensors show a response after exposure to different concentrations of CO (from 1 up to 40 ppm) with a LOD between 549 and 608 ppb. The selectivity of the sensors towards CO compared to other gases and VOCs commonly present in breath was also tested, highlighting a lower response for all other gases and VOCs involved at a concentration of 40 ppm.

On the other hand, a p−n junction diode is formed by the combination of a *p*-type semiconductor (conduction by holes) with a *n*-type semiconductor (conduction by electrons).[159] When two different types of semiconductors are combined, band bending occurs at the interface between the two materials, and the electronic properties are changed at that interface. Considering inorganic materials, three different types of p−n junctions can be distinguished, such as straddling gap (type I), staggered gap (type II), and broken gap (type III) depending on the band alignment of the two materials. Again, the diode sensing response is related to the mechanisms described for Schottky barrier diodes.

Recently, Li *et al.* reported a very interesting diode-type gas sensor based on a two-dimensional MoS_2/black phosphorus (BP) heterojunction (Figure 2.7).[160] MoS_2 and BP nanoflakes were prepared from their bulk crystals and transferred on SiO_2/silicon wafers from viscoelastic PDMS stamps. Then, thermal evaporation was used to deposit Ti/Au (20/80 nm) contacts on the nanoflakes. Under a forward bias voltage, the sensor shows a high response and good selectivity to 100 ppm of NO_2 at room temperature, while in self-powered mode, it exhibits an open circuit voltage of 0.36 V, a fast recovery rate (27.3 s), and low power consumption (20 nW). Furthermore, the dynamic response of the sensor to different NO_2 concentrations in a range 1 – 100 ppm was evaluated, showing good response and recovery characteristics at 3 V bias voltage and 0 V under 405 nm illumination. A gas sensing mechanism was proposed on the basis of energy potential, photoluminescence, Raman spectra measurements, and the DFT calculations before and after exposure to NO_2.

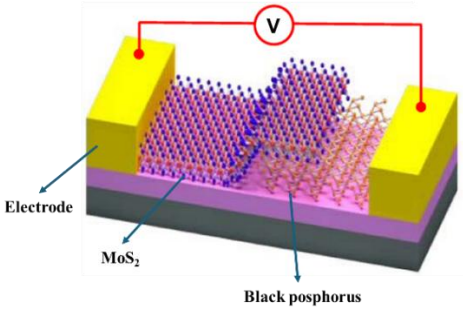

Figure 2.7. Device architecture of the p-n junction diode used by Li *et al.* Adapted from ref. 160.

In general, chemical diodes are effective sensors characterized by good sensitivity and low power consumption, but the electrical connection between the semiconductive material and the electrode must be precisely controlled, and their sensitivity depends on the applied voltage. The latter is the main disadvantage of chemical diodes because it requires semiconductor materials to be stable under higher bias voltages than other classes of electrical sensors, *e.g.* conductometric sensors.[129,161]

2.3.2. Capacitive Sensors

A capacitor is a device formed by two conducting electrodes separated by an insulating material, or in general by a non-conducting substance, called "dielectric".[162] In capacitive sensors (or chemicapacitors) the dielectric material is usually deposited or self-growth on the conducting electrodes, and act as the sensing layer involved in the detection of VOCs or gases.

In general, the capacitance value depends on the distance between the electrodes, the surface area of each plate, and the relative permittivity (or dielectric constant) of the sensing layer. In fact, the capacitance can be expressed in terms of geometry of the device and relative permittivity of the dielectric:[163]

$$C = \varepsilon_r \frac{\varepsilon_0 A}{d} \qquad \textbf{(2.4)}$$

where C is the capacitance in Faraday (F), ε_r is the relative static permittivity of the material between the plates, ε_0 represents the permittivity of free space (8.854×10^{-12} F/m), A is the area of each plate (m^2), and d corresponds to the separation distance of the two plates (m).

Changes in the capacitance of a capacitive sensor are related to adsorption and/or binding of analytes onto the dielectric material, which result in changes of the thickness and/or in the relative permittivity of the sensing material.[164] The relative permittivity of most inorganic gases (except H_2O) are very similar, thus chemical capacitors based on the change of dielectric constant are rarely applied to gas sensing applications. However, chemical capacitors characterized by changes in dielectric layer thickness are more frequently found in gas sensing.[165]

Gonçalves *et al.* reported a capacitive gas sensing system prepared using a MOF and Ionic Liquids (ILs).[166] First, ZIF-8 nanoparticles were synthesized and incorporated with ILs (Figure 2.8) using three different weight ratios as 1:0.1, 1:0.4 and 1:1. This results in ionic conductive materials ranging from solid porous inks to partially porous inks. Then ZIF-8 and ZIF-8/IL dispersions were spray-coated on the metallic contacts of a system composed of four flat parallel capacitors with a distance between terminals of 1 mm and 3 mm in length, to produce thirteen different capacitive sensors. The sensing performance of these sensors was evaluated in the presence of acetone, isopropanol, ethanol, and water vapor. A very fast (*ca.* 10 s to reach the 90% of the maximum response) and linear response was achieved for all ZIF-8/IL samples in a wide range of concentration (from 10^4 to 10^5 ppm), with calculated LOD around thousands of ppm for each VOC involved.

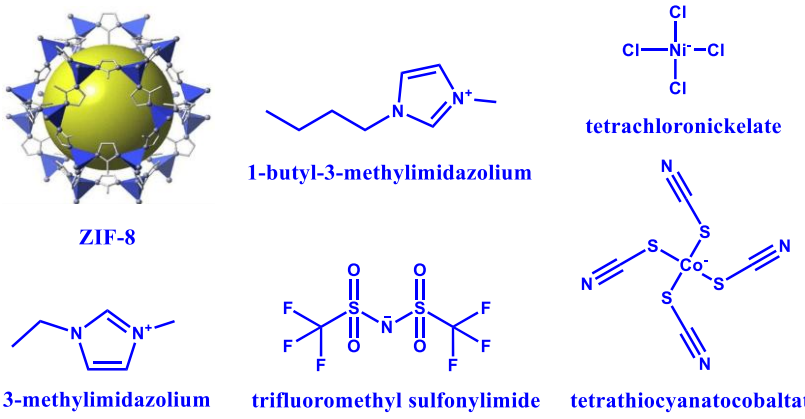

Figure 2.8. Structures of ZIF-8 and the cations and anions in ILs used by Gonçalves *et al.*

Capacitive sensors are characterized by a simple device configuration, ease of miniaturization, low cost, and good sensitivity to specific gas concentrations. In addition, the ideal non-dissipative sensing mechanism makes chemical capacitors suitable for their use in energy-constrained applications. However, chemical capacitors are generally less selective compared to other categories of electrical sensors, high concentrations of relative humidity can interfere with the gas sensing measurement because of the high dielectric constant of water.[167]

2.3.3. Field-Effect Transistors

Field−effect transistors (FETs) are characterized by the presence of two electrodes, called source and drain, connected by a semiconducting layer (channel), and an insulating gate oxide that separates the semiconducting material from a gate electrode.[168] In FET-based chemical sensors, the channel is composed of an inorganic or organic semiconducting material responsible of the sensitive detection of the analyte. In this type of electrical devices, the current flows from the source to the drain electrode through the semiconducting channel. The current intensity is regulated from an electric field originating between the gate electrode and the source by an applied voltage, that is perpendicular to the semiconducting layer. The intensity of the electric field regulates the number of mobile charge carriers in the semiconductor, and consequently, controls the current.[169] Thus, the conductivity of the channel is a function of the potential applied across the gate and source terminals, and the drain current (I_{DS}) is calculated from the following equation:

$$I_{DS} = \frac{C_i \mu W}{L} [\,(V_{GS} - V_{th}) - 0.5 V_{DS}\,] V_{DS} \qquad \textbf{(2.5)}$$

where C_i is the capacitance of the gate insulator, μ is the charge carrier mobility in the channel, W/L is the width to-length ratio of the channel, V_{GS} and V_{DS} are the applied gate−source and drain−source voltage, and V_{th} is the threshold voltage, defined as the minimum voltage required on the gate to create a layer of minority charge carriers under the insulating layer.

In FET-based chemical sensors the current change upon the adsorption of target analytes on the semiconducting layer is monitored. The semiconductor – analyte interaction can induce a change in the height of a Schottky barrier because of a secondary doping process, resulting in a change in the intensity of the current.[169] The electrical conductivity of the sensing material can be modulated by: i) type of the semiconducting sensing layer (*p*-type vs *n*-type); ii) morphology of the sensing material; iii) nature of the analyte (reducing *vs* oxidizing); and iv) geometry of the device. In fact, the sensing performance of FETs is governed by the intrinsic properties of the sensing layer, such as the work function, carrier mobility, and band gap.

FET-based chemical sensors can work in both gas and liquid environments, allowing detection of a wide range of analytes including gases, ions, and biomolecules. For example, Zhang *et al.* designed a carbon-based FET gas sensor with a dual-gate structure (Figure 2.9).[170] First the randomly arranged carbon nanotubes (CNTs) were distributed on a Si/SiO_2 substrate (creating the FET channel) using the soaking deposition technique, and then ultraviolet photolithography, reactive ion etching, and electron beam evaporation allowed the preparation of all the other components of the carbon-based FET.

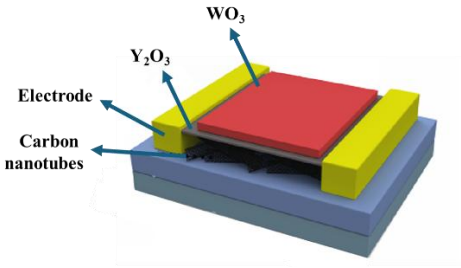

Figure 2.9. Device architecture of the carbon-based FET used by Zhang *et al.* Adapted from ref.170.

Gas sensing measurements showed a maximum of response for a gate voltage of -8 V for exposure to 10 ppm on NH_3. Using the same gate voltage, dynamic exposure experiments in a NH_3 concentration range of 40 – 100 ppb were performed, and a theoretical LOD of 14.29 ppb was calculated. Finally, the selectivity of the carbon-based FET towards NH_3 was demonstrated by comparing the sensing response after exposure to 10 ppm of other analytes as toluene, methane, sulfur hexafluoride, benzene, formaldehyde.

In addition to classical FETs, organic FETs (OFETs) are attracting considerable attention due to the intrinsic advantages of organic semiconductors (Section 2.3). In OFET-based sensors the interaction with the target analyte can occur at the interface, grain boundaries, or on the surface of the OFETs, depending on the different organic semiconductor morphology and device geometry.[171] Recently, Katz *et al.* reported OFET sensors based on diketopyrrolopyrrole (DPP)-based co-polymers.[172] In particular, seven different DPP-based co-polymers (Figure 2.10) were prepared and used for the successive preparation of XLPS/SiO_2 OFET sensors. The sensing response of these sensors was evaluated after exposure to different concentrations of acetone (5, 10, 20 and 50 ppm) in a gate voltage range from 0 to -50 V. LODs ranging from 43 ppb to 16 ppm were obtained depending on the DPP-based co-polymers involved. Also, the sensing performance of the OFET devices was evaluated for acetone, dimethyl carbonate, and acetic acid, in solution phases.

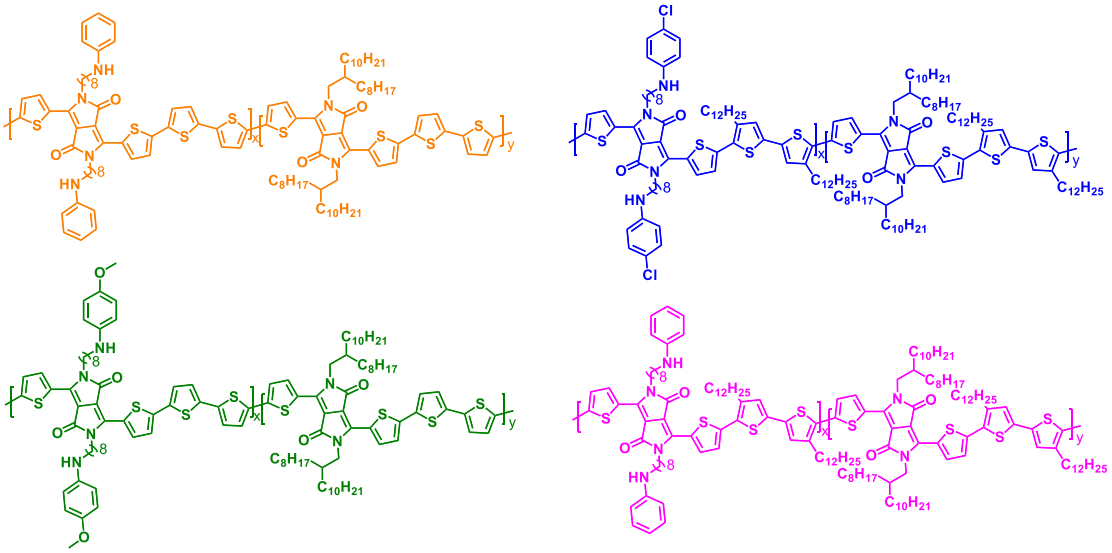

Figure 2.10. Molecular structure of some DPP-based co-polymers used by Katz *et al.* Adapted from ref. 172.

FET sensors possess high long-term stability and robustness, ease of miniaturization (microscale and/or nanoscale), high sensitivity, fast response and facile integration in electronic manufacturing processes. However, their fabrication is complex because the integration of materials into FET devices requires advanced techniques (*e.g.,* lithography) and a high degree of control over the material morphology.[173]

2.3.4. Conductometric Sensors

Conductometric (or chemiresistive) sensors consist of two electrodes connected by a chemiresistive material deposited onto an insulating support (*e.g.,* glass).[174] The sensing material used for the fabrication of conductometric sensors can be either semiconductive (*e.g.,* metal oxides) or metallic. The overall resistance of a conductometric sensor can be mainly divided into two components such as i) the resistance of the sensing material; and ii) the sum of contact resistance originating from the sensing material/electrode junction and from junctions generated within the sensing material (*e.g.,* between grains). In general, the conductivity of a material (σ) is given by the following equation:[175]

$$\sigma = e(\mu_e n_e + \mu_h n_h) \quad \textbf{(2.6)}$$

where e is the fundamental charge, μ_e and μ_h are the charge carrier mobility of electrons and holes, n_h and n_e are the electron and hole populations. The mobility of these carriers depends on the drift velocity under the influence of an electric field, while the population of charge carriers is related to the bandgap of the conductive material.

For conductometric sensors, a change in the conductivity (or its reciprocal called resistivity) of the sensing material can be observed due to a modification of the chemical surroundings induced by interactions with different analytes,[176] thus the concentration of the analyte can be evaluated by measuring the change in the recorded current or resistance of the sensor.[174]

Various processes may be involved on the surface of the sensing layer, such as chemisorption, surface adsorption (physisorption), redox reactions, catalytic decompositions, and direct charge transfer from analyte to surface, or vice versa,[177] depending on the chemical nature of the sensing material. The sensing process of chemiresistive devices after exposure to VOCs and/or gases can be due to the three main distinct mechanisms described in Section 2.3, such as i) modulation of Schottky barrier; ii) change of the doping level (secondary doping); and iii) modulation of the junction distance.

Considering semiconducting materials as the sensing layer, changes in the current (or resistance) after interaction with VOCs and/or gases are related to the type of the semiconductor (*p*- or *n*-type) and the chemical nature of the analyte. Classifying semiconductor materials based on their doping levels is critical when using conductometric sensors to detect VOCs and gases, because the chemical nature of the gas results in different variations in the electrical signal.[60,174] For example, exposure of a *p*-type semiconductor to electron donating analytes (*e.g.,* NH_3) results in a decrease in the concentration of the majority charge carriers (holes) due to an electron transfer from the analyte, resulting in a decrease in conductivity. On the other hand, exposing the same material to electron-absorbing analytes (*e.g.*, NO_2) results in an increase in hole concentration due to electron transfer from the *p*-type semiconductor material to the analyte and, consequently, an improvement in sensor conductivity. Obviously, the opposite behavior characterizes *n*-type semiconductors.

Recently, Ferlazzo *et al.* reported a conductometric sensors based on samarium oxide (Sm_2O_3).[178] Sm_2O_3nanorods were prepared from hydrothermal synthesis using cetyl trimethyl ammonium bromide (CTAB) as organic surfactant. Then, the gas sensor was fabricated by drop casting an aqueous suspension of nanorods onto an alumina support with dimensions

(6 × 3 mm) equipped with interdigitated Pt electrodes and a Pt heater located on the back side. The sensing properties of Sm_2O_3 nanorods at high temperatures (≥ 250 °C) towards some representative VOCs such as acetone, ethanol and formaldehyde, were evaluated. In particular, the sensor performance was tested at various concentrations of formaldehyde (from 25 to 400 ppm), acetone (from 1 to 40 ppm) and ethanol (from 10 to 400 ppm), resulting more responsive at low concentrations of acetone than those of ethanol and formaldehyde. Further investigations at low concentration of acetone (from 1 to 5 ppm) revealed good sensitivity and selectivity, and the response to 1 ppm of acetone was relatively fast (response and recovery times of 125 and 43 s, respectively).

Among the different categories of electrical sensors, conductometric sensors are the most widely used for sensing of VOCs and gases thanks to several advantages over the other device architectures such as simple fabrication, compatibility with conventional DC circuits, low cost, good sensitivity, good reproducibility, low power consumption, predictable electrical properties, and the ease of high precision measurement.[174]

2.4. Zn(salen)-Type Complexes as Optical Chemosensors

Among various classes of optical chemosensors, metal complexes of tetradentate Schiff bases are characterized by tunable spectroscopic properties that can be useful for the development of novel molecular materials for the detection of environmental pollutants (*e.g.,* VOCs) and toxic substances. In literature they have found applications as sensing materials,[44] catalysts,[179] fungicides,[180] anticancer agents,[181] *etc.* In particular, Zn(II) complexes of tetradentate Schiff bases derived from salicylaldehyde, or its derivatives, and 1,2-diamines, namely Zn(salen)-type complexes, have been extensively studied for their interesting spectroscopic properties arising from their peculiar Lewis acidic character.[44,182]

A more detailed discussion on their properties is reported in the following sections.

2.4.1. Lewis Acidic Character and Aggregation Properties

Commonly, the Zn(II) ion tends to form highly stable tetra-coordinated metal complexes with a tetrahedral geometry in the presence of monodentate or bidentate ligands (Figure 2.11). In the case of the tetradentate Schiff base ligands, however, the related Zn(II) complexes are characterized by a structure that constrains the Zn atom in a pseudo-planar coordination. As a result, in Zn(salen)-type complexes the metal center is coordinatively and electronically unsaturated.[183,184] Therefore, these complexes possess Lewis acidic character and can coordinate Lewis bases, leading to a penta-coordinated square pyramidal geometry, to saturate their Zn(II) coordination sphere.

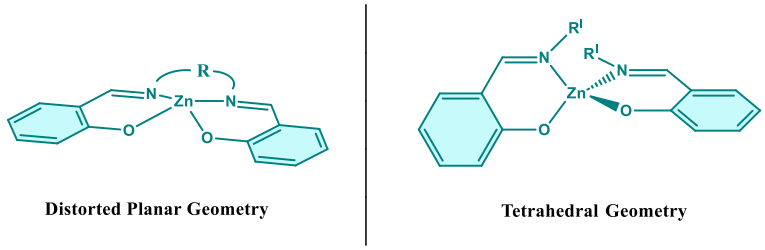

Figure 2.11. Distorted planar geometry and tetrahedral geometry of tetracoordinated Zn(II) complexes.

Zn(salen)-type complexes can be classified on the basis of the di-imine bridge as shown in Figure 2.12. Their Lewis acidic character is clearly an intrinsic property derived from their geometry, but it is also possible to tune the acidity by modifying the structure of the di-imine bridge. Di Bella *et al.* investigated a series of Zn(salen)-type complexes having different 1,2-diimine bridge structures[184] and, based on the calculated atomic charge on the Zn atom, it was found that the complexes having conjugated bridges possess a higher Lewis acidity than those having non-conjugated bridges. More recent studies based on DFT calculations have further supported these findings.[183]

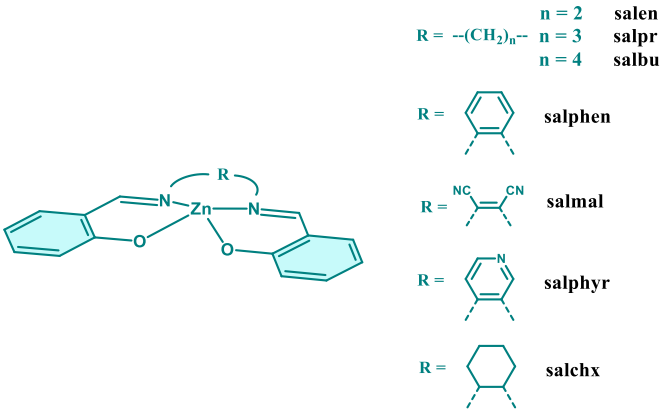

Figure 2.12. Chemical structure of Zn(salen)-type Schiff base complexes with different di-imine bridges.

Thanks to their Lewis acidic character, Zn(salen)-type complexes possess interesting aggregation properties both in solution[182] and in the solid state.[43] In the absence of Lewis bases (*e.g.,* in non-coordinating solvents) the metal center tends to fulfill a penta-coordination by intermolecular Zn····O axial interactions with the phenolic oxygen of another molecule, resulting in the formation of dimeric or aggregate species (Figure 2.13).[185] On the other hand, in coordinating solvents the Zn(II) center can be axially coordinated by the solvent itself, with the formation of monomeric adducts. Addition of Lewis bases to dimeric/aggregated species in non-coordinating solvents results in their disaggregation with formation of monomeric adducts.[186] Analogously, even in coordinating solvents, the presence of strong Lewis bases can induce the formation of monomeric adducts (Figure 2.13). In both cases, the adducts are characterized by a distorted square-pyramidal geometry.

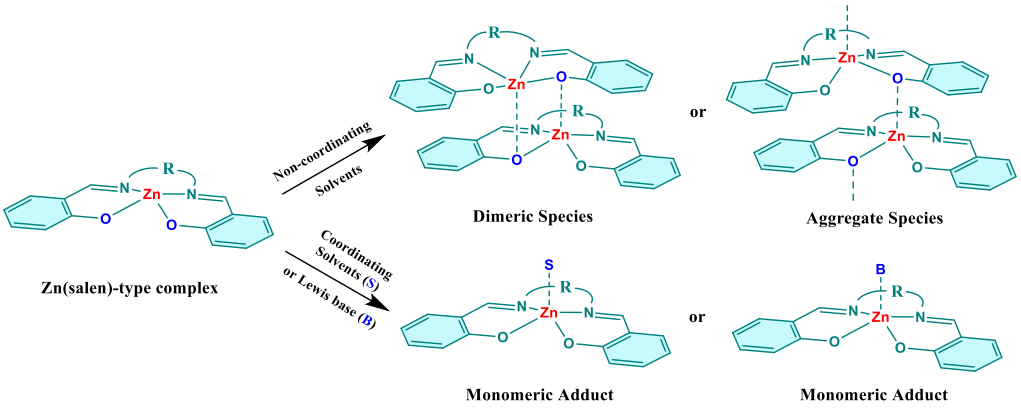

Figure 2.13. Behavior of Zn(salen)-type complexes in non-coordinating and coordinating solvents (S), and in the presence of Lewis bases (B).

Supramolecular structures and architectures can be observed in the presence of polytopic Lewis bases (*e.g.,* diamines),[187,188] or by the interaction with appropriate donor substituents present in the ligand framework, respectively (Figure 2.14a and Figure 2.14b).[189,190,191,192] There are very few exceptions to the penta-coordination mode related to the structure/stereochemistry of the 1,2-diimine bridge, but in the case of non-conjugated bridges it is possible to obtain structures with a tetrahedral coordination (Figure 2.14c).[193]

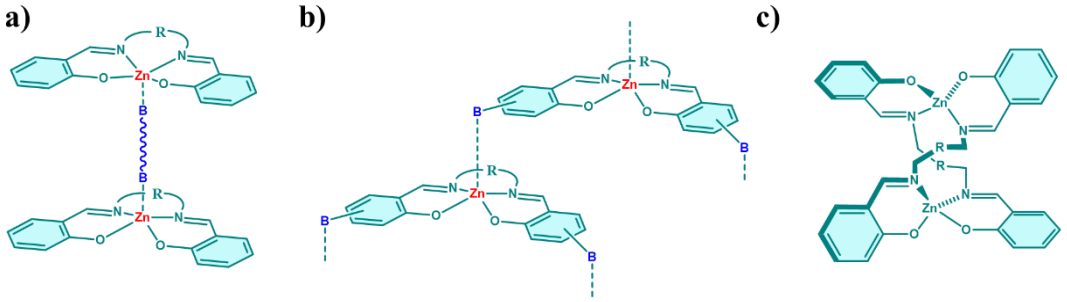

Figure 2.14. Structures of Zn(salen)-type complexes upon axial coordination of **a)** ditopic Lewis bases and **b)** donor substituents of the ligand framework. **c)** Tetrahedral coordination of Zn atom in a dinuclear complex with a helical structure. Adapted from ref. 43.

More interestingly, aggregated species and monomeric adducts possess different spectroscopic properties thanks to the different electronic environment around the metal center.[182] Therefore, the changes of the optical properties of these compounds are useful for the detection of analytes with Lewis basicity.

2.4.2. Optical Sensing of Lewis Bases

As anticipated, optical spectroscopic changes are observed for Zn(salen)-type complexes upon deaggregation. Several studies report the detection of various Lewis bases in non-coordinating solvents,[182] however several detection studies have also been conducted using coordinating solvents.[44,194,195,196] In both cases, the formation of monomeric adducts is observed. Several detection studies have been reported involving a disaggregation mechanism by the formation of adducts, including chiral species,[197,198,199] anions,[200] amines,[201,202] and amine derivatives.[203,204,205]

Interestingly, recent studies have reported a dinuclear Zn(salen)-type complex that act as a molecular tweezer upon interaction with ditopic diamines (Figure 2.15).[206] This system is characterized by a color change, from purple to magenta, and the appearance of a strong orange fluorescence upon the addition of stoichiometric amounts of histamine to CH_2Cl_2 solutions of the complex, in accordance with deaggregation of the monomeric intramolecular aggregates and the formation of 1:1 adducts.

Furthermore, a linear dynamic range from 0 to 10 μM was obtained from spectrophotometric/spectrofluorometric titrations performed by increasing the amount of histamine, with calculated LODs of 1.02 and 0.18 μM in the colorimetric and fluorometric detection modes, respectively. The high selectivity of the molecular tweezer was demonstrated by competitive experiments. Histamine quantification was also performed in a fish matrix (canned tuna), obtaining a good recovery rate, up to 77% and 82%, by optical absorption and fluorescence measurements, respectively.

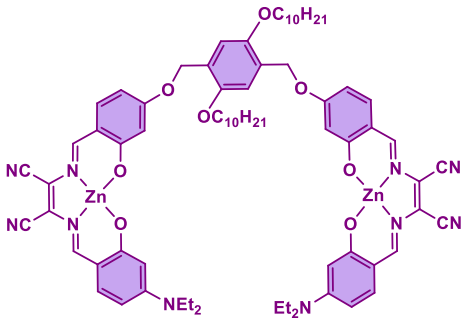

Figure 2.15. Molecular structure of a dinuclear Zn(salen)-type complex for the detection of ditopic bases.

Other sensing studies have involved anions detection, but in coordinating solvents. In this case, a solvent displacement mechanism was involved.[44] Obviously, the Lewis basicity of the anions involved must be higher than the basicity of the solvent, so these detection studies are usually performed in solvents with a weak Lewis basicity, such as acetone[207] or ethanol.[208,209]

Other studies have involved Zn(salen)-type complexes in aqueous solutions for the detection of ATP and ADP,[210] monohydrogensulfide,[211] α-aminoacids,[212] and anions.[213] In these cases, sensing mechanisms involving secondary interactions are proposed. Also, Zn(salen)-type complexes have been studied as optical probes for cell imaging,[214,215,216,217,218] thanks to their very good fluorescent properties.[219]

2.4.3. Optical Sensing of Metal Cations

Transmetalation allows the preparation of various organometallic complexes[220] and is also the key reaction in many important cross-coupling reactions.[221,222] Moreover, transmetallation reactions can also be useful in other fields, such as catalysis[223,224] and optical sensing.[225] In this regard, Zn(salen)-type Lewis base adducts in solution influence the ability of the Zn(II) ion to transmetalate with other metal ions. Recent studies reported by Di Bella *et al.* have demonstrated immediate and complete transmetalation with Cu^{2+} ions using Zn(salmal) complexes (Figure 2.16),[226,227] also involving selective and sensitive optical detection of Cu^{2+} ions in aqueous solutions.[228] In particular, from spectrophotometric and spectrofluorometric titrations performed by the progressive addition of Cu^{2+} to ACN solution of a Zn(salmal) complex, similar LOD values (0.60 and 0.90 μM, respectively) were obtained, resulting lower than the recommended concentration of Cu(II) in drinking water established by the European Union (about 30 μM), based on the World Health Organization (WHO) guidelines for water quality. The high selectivity of the Zn(salmal) complex towards Cu^{2+} was proven by competitive experiments in the presence of other potential interfering cations. The practical application of this complex for the sensitive detection of Cu^{2+} ions in real water samples was tested by spiking/recovery experiments.

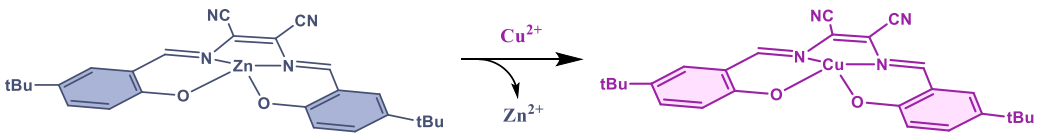

Figure 2.16. Detection of Cu^{2+} ions using a Zn(salen)-type complex through a transmetalation mechanism.

2.4.4. Responsive Solid-State Nanostructures

Non-mutual intermolecular Zn···O interactions lead to the formation of large aggregate species in Zn(salen)-type complexes which, in turn, can self-assemble into solid-state nanostructures.[43] Nanostructured Zn(salphen) complexes having alkoxy groups in the bridge[229,230,231] or in the salicylidene rings,[232,233,234] obtained from casting and/or solvent evaporation of solutions of these complexes in coordinating solvents are reported in literature. The presence of π–π stacking interactions between aromatic rings and interdigitation of alkyl side groups can contribute to the stabilization of Zn(salen)-type complexes nanostructures. The formation of columnar mesomorphic structures, characterized by fluorescent properties, has been reported for a series of Zn(salphen) and Zn(salen) complexes with 4,4′-*n*-alkoxysalicylidene substituents (*n* = 2, 12, 14, and 16).[233,235,236,237,238] Recently, Ramos *et al.* starting from a symmetrical dinuclear Zn(salphen) complex functionalized with phenyl groups, reported the formation of nanosized rings.[239]

These nanostructured self-assembled systems based on Zn(salen)-type complexes also represent emerging materials for the development of materials for sensing and optoelectronic applications.[44] In fact, because of the interesting photophysical properties of this class of metal complexes, responsive nanomaterials based on these molecular systems have also been reported. Figure 2.17 provides an overview of the Zn(salen)-type complexes reported in literature with known vapochromic properties.

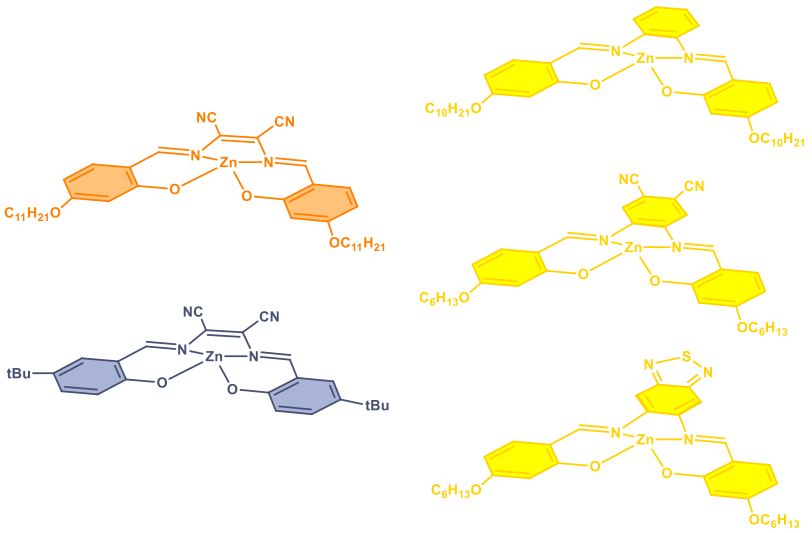

Figure 2.17. Molecular structure of Zn(salen)-type complexes with vapochromic properties.

For example, a Zn(salmal) complex, having 4,4′-alkoxy substituents in the salicylidene rings, shows marked vapochromic[240] and chemiresistive[241] properties upon interaction with vapors of volatile Lewis bases. The complex deposited onto interdigitated gold masks, characterized by a 2D nanostructure, shows a clear ohmic behavior in the range from -5 to 5 V, before and after exposure to amine vapors, with a marked decrease in resistance (from 130 to 17 GΩ), obtained from the I – V characteristics.

Analogously, vapochromic and chemiresistive properties were observed for a nanofibrillar molecular material composed of a Zn(salphen) complex derivative having 4,4′-decycloxy substituents as lateral groups.[242] Recently, the vapochromic properties of a

Zn(salmal) complex having the 5,5′-tert-butyl- bulky substituent on the salicylidene rings towards various VOCs have also been explored.[243] Other recent investigations reported a multi-responsive behavior of benzothiadiazole-bridging and phthalonitrile-bridging Zn(salphen) derivatives, with mechanochromic characteristics, in addition to their vapochromic properties.[244,245]

Overall, the Lewis acidic character of Zn(salen)-type complexes explored in solution is also reflected in their solid-state properties. The vapochromic and chemiresistive properties of these complexes represent a very good starting point for further investigations and development of optical/electrical chemosensors for volatile pollutants, such as VOCs and gases, having Lewis basicity.

Chapter 3

Materials and Methods

Contents

3.1. Chemicals

All chemicals used were purchased from Sigma-Aldrich (Merck) and used as received. All substances used as prototypes of different classes of VOCs were used as received, with the exception of pyrrole and pyrrolidine, which were purified over calcium hydride by fractional distillation at atmospheric pressure.

Cylinders of NH_3 in synthetic air (1000 ppm mol/mol) and synthetic air were purchased from Air Liquide, France, and used without further purification for gas exposure experiments.

3.2. Syntheses

The synthesis of $LuPc_2$ was achieved as previously reported.[246]

3.2.1. Synthesis of 2-hydroxy-4-(undec-10-enyloxy) benzaldehyde

The synthesis of 2-hydroxy-4-(undec-10-enyloxy) benzaldehyde was carried out in the presence of 2,4-dihydroxysalicylaldehyde (1.26 g, 9.12 mmol), 11-bromo-1-undecene (2.0 ml, 9.12 mmol), potassium bicarbonate (0.91 g, 9.12 mmol), and tetrabutylammonium bromide (0.29 g, 0.91 mmol) as depicted in Scheme 3.1.

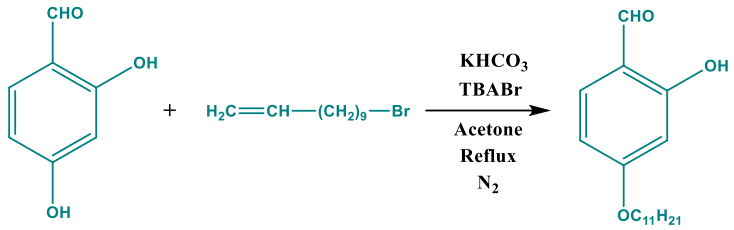

Scheme 3.1. Synthesis of 2-hydroxy-4-(undec-10-enyloxy) benzaldehyde.

All the reagents were put into a round flask (250 ml) and dissolved in acetone (45.0 ml). The reaction was carried out under reflux and nitrogen atmosphere and was monitored by TLC (SiO_2, cyclohexane/ethyl acetate = 90/10). After 7 days, the solution was cooled to room temperature, filtered and dried under vacuum. The brown oil obtained was portioned between HCl (1 M) and Et_2O. The aqueous phase was discharged, while the organic phase was extracted (two times) with a saturated solution of NaCl, dried with sodium sulphate, filtered, and evaporated to dryness. After anhydrification, the yellow oil obtained was purified by column chromatography on silica gel and eluted with a mixture of cyclohexane/ethyl acetate (98/2). The product of interest was obtained as a yellow oil (1.91 g, 6.58 mmol, 72%).

^{1}H NMR (Varian Unity S500, 500 MHz, 27 °C, $CDCl_3$): δ (ppm) = 1.30–1.55 (m, 12H; -$OCH_2CH_2CH_2(CH_2)_6CH{=}CH_2$), 1.80 (m, 2H, -$OCH_2CH_2CH_2(CH_2)_6CH{=}CH_2$), 2.14 (m, 2H, -$OCH_2CH_2CH_2(CH_2)_6CH{=}CH_2$), 4.00 (t, $^3J_{HH}$ = 12.5 Hz, 2H, -$OCH_2CH_2CH_2(CH_2)_6CH{=}CH_2$), 5.00 (m, 2H, -$CH{=}CH_2$), 5.80 (m, 1H, -$CH{=}CH_2$), 6.41 (d, $^4J_{HH}$ = 2.5 Hz, 1H, Ar-*H*), 6.52 (dd, $^3J_{HH}$ = 8.5 Hz, 1H, Ar-*H*), 7.40 (d, $^3J_{HH}$ = 8.5 Hz, 1H, Ar-*H*), 9.70 (s, 1H, C*H*O), 11.48 (s, 1H, O*H*).

3.2.2. Synthesis of Zn(salmal) Complexes *1* and *2*

The synthesis of complex **1** was achieved as previously reported.[247] In particular, the template synthesis of the Zn(salen-type) complex **1** was conducted under stirring in methanol (50 ml) in the presence of 2-hydroxy-4-(undec-10-enyloxy)benzaldehyde (1.16 g, 4.00 mmol), 2,3-diaminomaleonitrile (0.22 g, 2.00 mmol), zinc perchlorate hexahydrate (0.75 g, 2.00 mmol), and triethylamine (2 ml). The reaction was carried out under reflux and nitrogen atmosphere (Scheme 3.2). After 24 h, the solution was cooled at room temperature, filtered and washed with diethyl ether. The orange solid was dried under vacuum at 140 °C for 2h. After drying a dark red-brown powder was obtained (1.27 g, 1.77 mmol, 88.4 %).

$C_{40}H_{50}N_4O_4Zn$ (716.24): calcd. C, 67.08; H, 7.04; N, 7.82; found C, 67.50; H, 6.99; N, 7.94. MALDI-TOF: m/z = 715 ($[C_{40}H_{51}N_4O_4Zn]^+$, $(M+H)^+$, 100%). λ_{max} (THF): 337 nm, 382 nm, 447 nm, and 551 nm (ε = 45000) (Figure A1). ^{1}H NMR (500 MHz, DMSO-d_6, TMS): δ (ppm) = 1.25-1.42 (m, 24H; CH_2), 1.72 (m, 4H; CH_2), 2.01 (m, 4H; CH_2-CH), 4.00 (t, $^3J_{HH}$ = 7.0 Hz, 4H; OCH_2), 4.95 (m, 4H; CH=CH_2), 5.79 (m, 2H; CH=CH_2), 6.20 (d, $^4J_{HH}$ = 2.5 Hz, 2H; ArH), 6.23 (dd, $^3J_{HH}$ = 9.5 Hz, $^4J_{HH}$ = 2.5 Hz, 2H; ArH), 7.35 (d, $^3J_{HH}$ = 9.5 Hz, 2H; ArH), 8.38 (s, 2H; CH=N) (Figure A2). ^{13}C NMR (125 MHz, DMSO-d_6, TMS): δ = 25.93, 28.73, 28.91, 28.95, 29.19, 29.25, 29.40, 33.63, 39.49, 39.82, 39.99, 40.08, 40.15, 40.24, 40.32, 40.41, 40.49, 40.58, 68.13, 105.08, 107.85, 112.47, 114.65, 115.10, 120.94, 138.48, 139.30, 161.43, 167.00, 176.94.

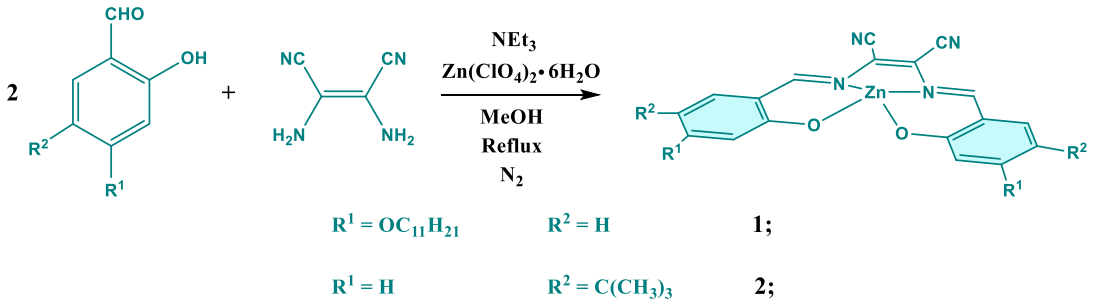

Scheme 3.2. Synthesis of complexes **1** and **2**.

Similar procedure was used for the synthesis of complex **2**,[227] using 5-*t*-butyl-2-hydroxybenzaldehyde (342 µl, 2.00 mmol), 2,3-diaminomaleonitrile (0.108 g, 1.00 mmol), zinc perchlorate hexahydrate (0.559 g, 1.50 mmol), and triethylamine (1.0 ml) as reagents and methanol as solvent (15 ml). The dark-brown solid was dried under vacuum at 100 °C before used (0.333 g, 0.677 mmol, 68.0 %).

$C_{26}H_{26}N_4O_2Zn$ (491.90): calcd C, 63.49; H, 5.33; N, 11.39; found C, 63.51; H, 5.34; N, 11.42. ESI-MS: m/z = 491 $[C_{26}H_{27}N_4O_2Zn]^+$ $(M+H)^+$. λ_{max} (THF): 313 nm, 372 nm, 500 nm, and 586 nm (ε = 23680) (Figure A3). ^{1}H NMR (500 MHz, DMSO-d_6): δ (ppm) = 1.26 (s, 18H, C(CH_3)$_3$), 6.76 (d, $^3J_{HH}$ = 9 Hz, 2H; ArH), 7.39 (d, $^3J_{HH}$ =9 Hz, 1H; ArH), 7.49 (dd, $^3J_{HH}$ = 9 Hz, $^4J_{HH}$ = 3 Hz, 2H; ArH), 8.60 (s, 2H, CH=N) (Figure A4). ^{13}C NMR (125 MHz, DMSO-d_6): δ = 31.39, 34.03, 112.26, 118.20, 121.97, 124.41, 131.82, 136.12, 136.97, 164.20, 173.55.

3.3. Preparation of Films for Exposure Experiments

3.3.1. Glass-Based Films of Complex *1*

The drop-casting technique was used for the preparation of glass-based films (GBFs) of complex **1** (**1**-GBFs), by casting a known volume of a THF solution of **1** (2.5×10^{-3} M) onto square glass substrates (2.5 cm × 2.5 cm). Before casting, four solvents such as cyclohexane, acetone, tetrahydrofuran (THF), and 2-propanol were used in this sequence for washing glass substrates. In particular, substrates were immersed into the solvent and sonicated for 5 minutes. Then, the glass squares were dried under nitrogen flux for 1 min. This process was repeated for each washing solvent used in this phase. Clean glass substrates were pre-heated into an oven at 80 °C for 10 min before casting. Then, 0.5 ml of the THF solution of **1** were drop-casted onto the clean glass substrates. After solvent evaporation, orange films were obtained. Cast films were annealed by a thermal treatment at 140 °C for 10 minutes in an oven, resulting in a color change of films, from orange to purple.

3.3.2. Paper-Based Films of Complexes *1* and *2*

The dip-coating technique was used to obtain paper-based films (PBFs) of complexes **1** (**1**-PBFs) and **2** (**2**-PBFs). Filter paper was cut in squares (2.5 cm × 2.5 cm) before preparation of PBFs.

1-PBFs were prepared by dipping Whatman-4 paper substrates into THF solutions of **1** (5.0×10^{-3} M and 1.0×10^{-3} M) for 2 s, obtaining films named **1**-PBF5 and **1**-PBF1, respectively. After dipping filter paper substrates into the THF solution of **1**, orange films were obtained by evaporation of the solvent. Analogously to GBFs, a thermal annealing was carried out to obtain annealed films, conducted in air or under inert atmosphere for **1**-PBFs used for colorimetric or fluorometric detection studies, respectively. In this latter case, the dip-coated films were placed into a three-necked flask (500 ml) and dry nitrogen was fluxed for 5 min. Then, the flask was heated to 150 °C with a heating mantle for 15 min, leading to a color change of films, from orange to purple. Finally, films were cooled in the flask under nitrogen flux to room temperature (15 min).

2-PBFs were prepared inside a round flask by dipping paper squares into THF solutions of **2** (1.0×10^{-3} M and 4.0×10^{-4} M), under nitrogen atmosphere at room temperature, obtaining films named **2**-PBF1 and **2**-PBF4, respectively. Then, dipped films were kept horizontal in the flask, thus obtaining gray colored films after complete evaporation of the solvent.

UV−vis diffuse reflectance and fluorescence measurements were performed on the top side of the dipped films.

3.3.3. *1*/$LuPc_2$ Bilayers

1/$LuPc_2$ bilayers were prepared from successive deposition of the two different materials onto indium thin oxide (ITO) interdigitated electrodes (IDEs). IDEs were patterned on glass substrates using lithographic techniques and consist of two pairs of 16 ITO digits with a width of 75 μm and the same spacing between them (75 μm). Before the deposition process, ITO-IDEs substrates were immersed in 10 ml of solvent and sonicated for 5 min. This procedure

was performed using two different solvents (CH_2Cl_2 and EtOH) and repeated three times for each solvent. Then, cleaned substrates were dried for 5 min under air and maintained into a desiccator before use.

The low conductive **1** sub-layer was obtained by casting 30 µL of a THF solution of the complex (3.0 mg/mL) onto cleaned ITO-IDEs substrates. After the complete evaporation of the solvent, a high conductive top layer of $LuPc_2$ was thermally evaporated using a UNIVEX 250 thermal evaporator. The evaporation procedure was conducted under vacuum (initial pressure: 5.0×10^{-7} mbar) by heating the metalated phthalocyanine at 350 °C in order to obtain a constant evaporation rate of *ca.* 0.2 Å/s. Annealed bilayers were obtained by thermal treatment of the as-prepared bilayers at 140 °C for 10 min.

3.3.4. *1*:$LuPc_2$ Mixed Films

1:$LuPc_2$ mixed films were prepared from solutions containing the two complexes using the drop-casting technique. THF stock solutions of complex **1** (3.0 mg/mL) were prepared by dissolving the appropriate amount of solid compound in 10 mL of solvent, while stock solutions of $LuPc_2$ (*ca.* 0.20 mg/mL) were obtained from their saturated THF solutions after filtration. From these stock solutions, mixed solutions having different mass concentration ratios (1:2, 1:1, and 2:1 of **1**:$LuPc_2$, respectively) were prepared by mixing the appropriate volume of THF stock solutions.

Mixed films were obtained by casting 100 µL of the mixed solution onto cleaned ITO-IDEs substrates at room temperature. Then, annealed mixed films were obtained by thermal treatment of as-prepared films at 140 °C for 10 min.

3.4. Measurements

3.4.1. General Measurements

^{1}H NMR and ^{13}C NMR experiments were performed using a Varian Unity S 500 (499.88MHz for ^{1}H) spectrometer at 27 °C. ESI-MS spectra of complexes **1** and **2** were recorded on acetonitrile solutions (4.0×10^{-6} M) using a Thermo Scientific LCQ-DECA ion trap mass spectrometer equipped with an ESI ion source (capillary temperature 350 °C, sheath gas 30 a.u., source voltage 5.0 kV, capillary voltage -10 V). Spectra were acquired in negative mode. Elemental analyses of complexes **1** and **2** were performed on a EuroVector EA3100 elemental analyzer.

3.4.2. XRD and Thermogravimetric Measurements

X-ray diffraction (XRD) patterns of as-prepared and annealed **1**-PBFs were achieved before and after exposure to ethylenediamine (EDA) in grazing incidence mode (0.5°) using a Rigaku diffractometer, equipped with a rotating anode of Cu Kα radiation (λ = 1.5418 Å), operating at 45 kV and 200 mA.

Thermogravimetric measurements were performed with a Mettler Toledo TGA2 by introducing complex **1** into a working chamber fed by a flow of pre-purified nitrogen (50 sccm) at a heating/cooling rate of 5 °C/min at atmospheric pressure. Before recording the

thermograms, solid **1**, after exposure to saturated BA and EDA vapors, was heated to 50 °C for 20 min under nitrogen flow.

3.4.3. Optical Measurements

Optical absorption measurements of as-prepared and annealed **1**-GBFs, and **1**/$LuPc_2$ and **1**:$LuPc_2$ films were performed in transmittance with an Agilent Cary 60 spectrophotometer. UV−vis diffuse reflectance spectra on **1**-PBFs and **2**-PBFs were recorded with a JASCO V-750 spectrophotometer before and after exposure to VOCs.

Raman spectra of **1**/$LuPc_2$ and **1**:$LuPc_2$ films were recorded using a Renishaw inVia Raman microscope equipped with a 473 nm laser (max power 12 mW), as excitation source. Spectra were collected using a variable laser power in a range of 400 – 2500 cm^{-1}.

Fluorescence measurements of as-prepared and annealed GBFs and PBFs were performed in a front-face configuration (incident angle of the excitation light 30°) with a Jasco FP-8200 spectrofluorometer equipped with a film holder, model FLH-809 (Ex/Em slits = 5/5 nm

Sensitive detection measurements were carried out at room temperature (23 ± 3 °C) and in a relative humidity (RH) range between 40% and 60%.

3.4.4. AFM Measurements

Atomic Force Microscopy (AFM) measurements of as-prepared and annealed **1**/$LuPc_2$ and **1**:$LuPc_2$ films were performed using an AFM Bruker Icon 2 under controlled atmosphere. Surface scans were performed in nanoDMA peak force tapping mode (using ScanAsyst-Air-HR Si probe of spring constant 0.4 N/m) with a scan rate of 0.5 Hz, a peak force frequency of 2 kHz and amplitude of 30 nm. All measurements were performed at room temperature, at a constant RH value of 25%.

3.4.5. Electrical Measurements

I – V characteristics of as-prepared and annealed **1**/$LuPc_2$ and **1**:$LuPc_2$ films were obtained using a Keithley 6517B electrometer in an applied bias range from -10 to +10 V. The applied bias was started and ended at 0 V to avoid any polarization effect. For each film, the I – V curve was recorded for three consecutive cycles.

Impedance spectroscopy measurements were performed on as-prepared and annealed **1**/$LuPc_2$ and **1**:$LuPc_2$ films using a Solartron SI 1260 impedance analyzer. The impedance signal was recorded in a range of frequencies between 100 Hz up to 10 MHz, and by varying the DC bias (from 0 up to 10 V) under a constant AC bias (100 mV).

All electrical measurements were performed at room temperature and in a range of RH between 30 – 60 %.

3.5. Vapor Exposure Experiments

3.5.1. Exposure to Saturated Vapors

Exposure to saturated vapors of the involved VOCs was carried out at room temperature (23 ± 3 °C) in a sealed glass chamber (500 mL). In particular, **1**-GBFs, **1**-PBFs or **2**-PBFs were placed inside the chamber in the presence of the volatile liquid (5 mL into a flat-bottom vessel). The saturated vapor concentration for each VOC was calculated with the following formula:

$$C = \left(\frac{P_{VOC}}{P_{atm}}\right) \times 10^6 \quad \textbf{(3.1)}$$

where C is the VOC concentration (ppm), P_{VOC} is its vapor pressure (mmHg), and P_{atm} is the atmospheric pressure (760 mmHg). The vapor pressure at 23 °C for each VOC was calculated from Antoine equation:[248,249]

$$log_{10}P = A - \frac{B}{T+C} \quad \textbf{(3.2)}$$

where P is the vapor pressure of the VOC (mmHg), T is the temperature (°C), and A, B and C are Antoine coefficients.

Annealed **1**-GBFs, **1**-PBFs and **2**-PBFs were exposed to BA vapors for 5 min and 15 min of all other investigated VOCs. In the case of detection of aliphatic diamine vapors, as-prepared **1**-PBFs were exposed for 10 min to EDA and 30 min for all the other amines, while annealed films were exposed 5 min for EDA and 10 min for the other volatile diamines. These exposure times allowed for maximum color change and saturation of the absorbance/fluorescence intensity for each film.

3.5.2. Static Exposure Experiments

The optical response of PBFs after exposure to known concentrations of all involved VOCs was investigated under static conditions. The experimental apparatus used for static exposure is reported in Figure 3.1. It consists of a three-necked flask of known volume (1.15 L) in which the films were suspended in the central neck inside the flask by means of a copper wire and closed with a stopper. A multiparametric instrument, equipped with a thermo-hygrometric probe for real-time monitoring of temperature and RH, is fitted in a lateral neck of the closed flask. The other neck is sealed with a suba seal cap, through which the appropriate volume of the volatile liquid is introduced into the flask, using a Hamilton microliter syringe, allowing its complete evaporation. The exposure time was set at 30 min for each VOC investigated using annealed **1**-PBFs, 60 min for as-prepared **1**-PBFs, and 90 min for **2**-PBFs, at room temperature (controlled with a heating mantle) and in a range of RH between 40% and 60%. These exposure times ensure the maximum color change and saturation of the absorbance/fluorescence intensity for each exposed film over the entire concentration range investigated.

The desired concentration of the VOCs involved was calculated by the static liquid gas distribution method with the following formula:[250]

$$C = \left(\frac{22.414 \times \rho_a \times T \times V_a}{273.15 \times MM_a \times V_{TOT}}\right) \times 10^6 \quad \textbf{(3.3)}$$

where C (ppm) is the concentration of the VOC, ρ_a (g/mL) is the density of the pure liquid VOC, T (K) is the temperature in the exposure conditions, V_a (mL) is the volume of the pure VOC, MM_a (g/mol) is the molecular mass of the VOC, and V_{TOT} (L) is the total volume of the sealed glass chamber used for the static exposure.

Figure 3.1. Experimental apparatus for static exposure of PBFs to VOC vapors.

Since to achieve concentrations of the VOCs below 500 ppm would require adding sub-microliter volumes of pure liquids into the sealed chamber, solutions of *n*-pentane (NP, *b.p.* 36.1 °C) or diethyl ether (Et_2O, *b.p.* 35.0 °C) were prepared, with a concentration of 0.473 M and 0.0473 M of the VOCs involved. These concentrations ensure that the maximum volume of solution added into the flask does not exceed 100 μL, such that 1 μL added = 1 ppm of the 0.0473 M solution (covering the range 1 to 100 ppm), and 1 μL added = 10 ppm of the 0.473 M solution (covering the range 10 to 1000 ppm). For NH_3, methylamine (MA), and ethylamine (EA), aqueous solutions standardized by titration with 0.10 M aqueous HCl solutions were used.

For vapor concentrations ≥ 1000 ppm, the appropriate volumes of the pure VOC, calculated with eq. 3.3, were injected into the sealed chamber, allowing their complete evaporation. Fluorescence measurements of **1**-PBFs after exposure to BA and EDA were performed immediately after the exposure.

3.5.3. Competitive Experiments

Competitive experiments were performed by evaluating the fluorescence response of annealed **1**-PBFs to BA vapors in the presence of potential interferents in a ratio of 1:10. Both BA and the interferent, 50:500 ppm, respectively, were introduced into the experimental apparatus described above (Figure 3.1) containing the film. Analogously to the BA detection experiments, the exposure time was set to 45 min.

3.6. RGB Color Analysis

Photographic images of PBFs of complexes **1** and **2** before and after exposure to BA and Py vapors were collected using a Samsung Galaxy S23 smartphone camera, under defined illumination conditions (1600 – 2000 lux), and at a constant distance between the camera from the films (15 cm). RGB values of each film were obtained from their digital images or directly captured using an android app (*Color Detector* developed by Galaxy studio apps). Normalized rgb values were calculated using the following formulae:[251]

$$r = \frac{R}{R+G+B} \quad \textbf{(3.4)}$$

$$g = \frac{G}{R+G+B} \quad \textbf{(3.5)}$$

$$b = \frac{B}{R+G+B} \quad \textbf{(3.6)}$$

where R, G, and B are the absolute values of red, green and blue, respectively.

The color change of PBFs upon exposure to BA and Py was estimated from the color difference equation:[252]

$$\Delta E_{RGB} = \sqrt{(R_x - R_0)^2 + (G_x - G_0)^2 + (B_x - B_0)^2} \quad \textbf{(3.7)}$$

where R_0, G_0, and B_0 represent the RGB values of pristine films, while R_x, G_x, and B_x represent the same values after exposure. The same formula was used to calculate the color difference with normalized rgb values.

Mean RGB or rgb values were calculated from at least three replicate measurements. Similar RGB values were obtained from RGB captured directly from films or from their digital images.

3.7. Calculation of the Limit of Detection

The limit of detection (*LOD*) was calculated in the dynamic linear range of the calibration curve with the following formula:[253,254]

$$LOD = K \times \frac{S_b}{S} \quad \textbf{(3.8)}$$

where K is a constant, S_b is the standard deviation of the blank, and S is the slope derived from the linear fit curve. The calibration curve was obtained from the plot of the absorbance/fluorescence intensity, fluorescence intensity ratio, or mean ΔE_{rgb} data versus the concentration of the amine added.

For vapoluminescent detection of BA vapors, the S_b was calculated from the fluorescence intensity values of annealed **1**-PBF5s.

For vapochromic detection of BA vapors, **1**-PBF1s in addition to **1**-PBF5s were used. The absorbance intensity of the longest wavelength absorption maximum and/or the mean ΔE_{rgb} data before and after exposure were monitored.

For EDA vapor detection, the calibration curve was obtained by considering the ratio I_0/I, where I_0 and I are the fluorescence intensity values of **1**-PBF5s before and after exposure, respectively. S_b was estimated from n replicate measurements of the fluorescence emission, I_{0n}, of the ratio I_0/I_{0n}, where I_0 is the mean value of the fluorescence emission calculated on all the replicates.

In the case of vapochromic Py detection, the absorbance intensity of the longest wavelength absorption maximum and/or the mean ΔE_{rgb} data from **2**-PBFs before and after exposure, were monitored, using both **2**-PBF1s and **2**-PBF4s. S_b was estimated from the absorption maximum intensity and/or from the ΔE_{rgb} values calculated for all the replicate measurements.

All data regarding the number of replicates, S_b, S and the calculated LOD values are reported in Table 3.1. Each point in the calibration curves was calculated as the mean value obtained from at least three replicate measurements.

Table 3.1. Parameters used for the calculation of LOD values for **1**-PBFs and **2**-PBFs.

Film	Detection Method	Volatile Amine	Replicates of the blank	Standard Deviation	Slope	LOD (ppm)
1-PBF5	Fluorometric	BA	100	27	28	2.0
1-PBF5	RGB color analysis	BA	20	8.01×10^{-3}	6.13×10^{-3}	3.9
1-PBF1	RGB color analysis	BA	25	3.91×10^{-3}	4.18×10^{-3}	2.8
1-PBF5	Fluorometric	EDA	120	0.031	0.014	6.6
2-PBF1	RGB color analysis	Py	20	1.13×10^{-3}	3.61×10^{-5}	94
2-PBF4	RGB color analysis	Py	30	6.75×10^{-4}	5.61×10^{-5}	36

3.8. Gas Exposure Experiments

Gas exposure experiments in the presence of specific concentrations of NH_3 (from 10 up to 90 ppm) were performed on as-prepared and annealed **1**/$LuPc_2$ bilayers and **1**:$LuPc_2$ mixed films having a specific mass ratio (1:2). Sensing experiments were conducted using a homemade workstation consisting of three interconnected fluidic lines equipped with mass flow controllers (MFCs) and electric valves (EV) that control the mass flow of NH_3, synthetic dry air, and water vapor (constant total flow rate of 550 NmL/min), and mix them appropriately to obtain the desired concentration of NH_3 and RH (Scheme 3.3).

The RH value was controlled before starting each experiment (RH calibration) by switching the flow of synthetic air derived from MFC 2 to a RH sensor by EV2.

During the exposure period, the flow of synthetic air was vented by switching EV3, while NH_3 flow from MFC 1 and humid air from MFCs 3 and 4 were mixed and conveyed

to the test cell. Conversely, during the desorption period the synthetic air flow was through the EV3 and mixed with humid air, while NH_3 was vented by EV1.

The relative response (*RR*) of the films upon exposure to NH_3 was calculated with the following formula:[255]

$$RR\ (\%) = \frac{I_f - I_0}{I_0} \times 100 \qquad \textbf{(3.9)}$$

where *RR* is the relative response, I_0 is the recorded current before exposure, while I_f is the current at the end of the exposure time.

All the experimental parameters, such as time of exposure/desorption, total flow, control of humidity value, and switching of the valves were controlled by a homemade and customized software. All NH_3 sensing studies were performed at room temperature (23 ± 3 °C) and RH of 45% using a test cell with a volume of 8 cm^3. All experiments were repeated for four exposure/desorption cycles under a constant applied bias of 5V.

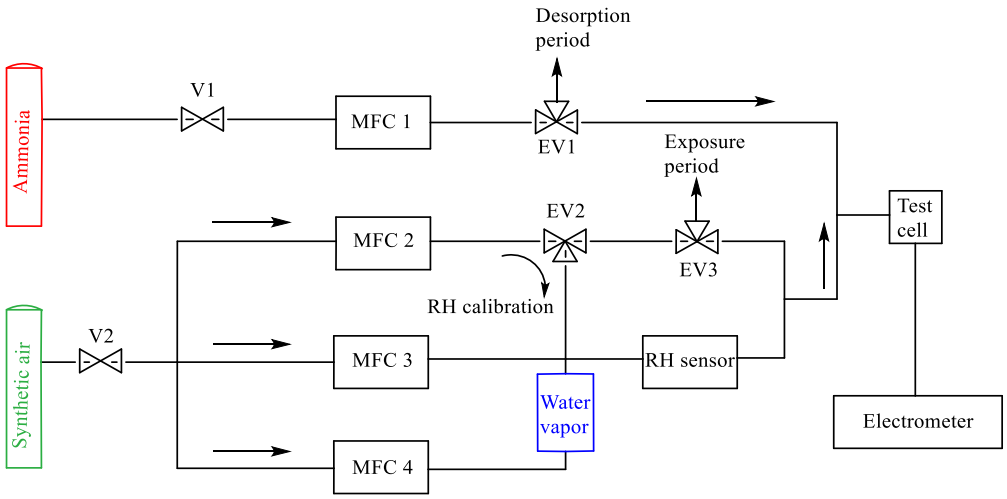

Scheme 3.3. Schematic representation of the experimental apparatus used for dynamic exposure of bilayer and mixed films to NH_3.

Chapter 4

Selective and Sensitive Detection of Primary Mono- and Diamine Vapors

Contents

4.1. Introduction

Amines are a class of organic compounds derived from ammonia, in which one, two, or all three hydrogen atoms are replaced by hydrocarbon groups. They are classified as primary, secondary, or tertiary amines on the basis of the number of carbon chains directly bounded with the nitrogen atom. Analogously to ammonia, these compounds possess basic properties due to the presence of a lone pair of electrons on the nitrogen atoms. The basicity of these compounds is higher with respect to ammonia, thanks to the greater electron density on the alkyl-amine nitrogen (inductive effect). The basicity of amines can be defined in terms of Brønsted or Lewis basicity. With the increase of the number and length of side chains, the basicity is influenced by an increasing inductive effect. In particular, considering the Brønsted basicity, tertiary amines are those with the stronger basicity. On the other hand, for Lewis basicity it is necessary to consider not only the inductive effect, but also the steric hindrance, which also depends on the reference Lewis acid.

Aliphatic monoamines are widely involved in chemical industries as intermediates for production of plasticizers, fertilizers, detergents, polymers, *etc*.[19] Also, their presence in food products is accompanied by unpleasant odors and is often related to food spoilage processes.[256] Moreover, aliphatic monoamines with short chain length (C2 – C8) possess high volatility and toxicity at low concentration (ppm). In fact, eye, skin and throat irritation, corneal edema, and formation of nitrosamines are some effects related to their exposure for prolonged time.[24,257] Among aliphatic amines, BA is used in chemical industries as reactant, or intermediate in many synthetic routes.[258,259] The release of this amine into the environment can arise from industries or from decomposition processes of food products. Because of its high volatility (93 mmHg at 25 °C) the main risk for human health is the inhalation. At low concentration (tens ppm), several disorders such as headache, throat and eye irritation can occur after a short exposure time (few minutes). Instead, prolonged exposure can cause vomiting, nausea, and, in some cases, damage to the nervous system.[260,261] Because of its toxicity, exposure to 300 ppm of BA is considered as the Immediately Dangerous for Life and Health (IDLH) value for the National Institute of Occupational Safety and Health (NIOSH).[262] On the other hand, the OSHA established a PEL ceiling value (PEL–C) for BA vapors as 5 ppm,[263] representing "the concentration that shall not be exceeded even instantaneously".

Diamines are a class of organic compounds characterized by the presence of two amine groups in their structure. They can be distinguished in aliphatic or aromatic diamines, depending on the presence of aliphatic chains (*e.g.*, 1,6-diaminohexane) or aromatic rings (*e.g.*, 1,4-phenylenediamine) between nitrogen atoms. In general, diamines are widely used in industrial production of copolymers (reaction between diamines and diacids), surfactants and many other chemicals.[259,264] They possess basic properties like monoamines, and can therefore be classified as Brønsted or Lewis bases, and a lower volatility than their counterparts containing only one amino group.

The simplest diamine is 1,2-diaminoethane or ethylenediamine (EDA), which is used as raw material for the production of some chemicals in industries as lubrication additives, composite explosives, *etc*.[265,266,267,268] A noteworthy industrial application of this diamine is the production of ethylenediaminetetraacetic acid (EDTA), through the reaction between

EDA, formaldehyde and sodium cyanide.[269] Exposure to EDA vapors (hundreds ppm) for short time can cause irritation of nasal mucosa, while prolonged exposure time can lead to several respiratory disorders.[270] In fact, the NIOSH has established a concentration of 1000 ppm as the IDLH value for this substance,[271] while, the PEL time-weighted average value (PEL–TWA), as the concentration allowed for eight hours per day out of a total of forty hours per week, reported by OSHA is 10 ppm.[272]

On the other hand, some aliphatic diamines (*e.g.*, putrescine and cadaverine), together with some polyamines (*e.g.*, spermine and spermidine), are regarded as biogenic amines (BAs).[273] BAs are a very important class of amines, deriving from the enzymatic decarboxylation of amino acids, because they take part in different metabolic pathways and several biological processes in living organisms.[274] The concentration of these substances may increase during spoilage processes in several types of food such as cheese, meat, fish, or wine.[275,276,277,278] High concentrations of BAs are toxic for human health by ingestion or inhalation of their vapors. For example, ingestion of high amount of BAs (hundreds of mg/kg) can cause vomiting, diarrhea and nausea.[279,280] Furthermore, BAs can be used as food freshness indicators.[281,282]

In summary, exposure to high concentrations of mono- and diamine vapors poses significant risks to human health, and due to the widespread use of these substances in industry and their potential release into the environment, their quantitative detection is very important for both public and individual health and environmental safety.

4.2. Optical Methods for Vapor-Phase Detection of Primary Mono- and Diamines

Classical methods for the detection of primary mono- and diamines are typically GC, GC-MS, HPLC, LC-MS, *etc.*[283,284,285,286,287] Among them, only few techniques (*e.g.*, GC-MS) can be used for the vapor-phase detection of volatile amines, and expensive instrumentations, trained operators, and sample pretreatments before analysis are often required. As previously detailed in Section 2.1, development of chemical sensors, in particular optical chemosensors (Section 2.2), can represent a good alternative for the detection of these classes of analytes with the advantage of fast detection, good sensitivity, and simple analytical instrumentation.

Several examples of optical sensors for the detection of volatile amines and BAs, using static or dynamic exposure experiments, are reported in the literature.[288,289,290,291,292,293,294,295,296,297,298,299] Table 4.1 summarizes literature data for the quantitative detection of volatile primary aliphatic amine vapors.

For example, referring to BA detection under static conditions, You *et al.* developed a tunable multicolor luminescent system by combining different fluorophores containing amino acids directly linked to 2-formylbenzenesulfonamide.[300] The combination of three appropriate amino-containing fluorophores produces a white solution which, upon addition of an amine and/or a base, exhibits a color change from white to red, blue, or yellow. Then, acetonitrile solution of the fluorescent probe was written onto Whatman filter paper. In this case, a blue emission is observed under a 365 nm light after complete evaporation of the solvent. Exposure to BA vapors in a range 0 – 100 ppm shows an initial quenching of the

blue emission (0 – 0.10 ppm) and a subsequent formation of a new emission band corresponding to yellow emission (2.5 – 100 ppm). For the former range, a limit of detection for BA is calculated as 0.026 ppm. Some cycles of exposure to BA and HCl show also an excellent recyclability and switchability.

Table 4.1. Literature data of optical chemosensors for the detection of primary aliphatic amine vapors.

Material	Volatile amine	Detection method	LOD or Lowest Detected Conc. (linear range)	Selectivity Studies	Exposure Method	Ref
Fluorescent Polymer	benzilamine	Fluorescence	30 ppm	no	static	301
Organic Compound	*tert*-butylamine	Optical absorption	1 ppb (0.14-1.4 ppm)	no	dynamic	302
Metal-doped Carbon dots	ethylamine	Colorimetric array	1.4 ppb (0.008–1600 ppm)	yes	static	303
Metal-doped Carbon dots	isopropylamine	Colorimetric array	39 ppb (0.05-828 ppm)	yes	static	303
Organic Compound	*n*-propylamine	Fluorescence	29 ppm	yes	static	304
Organic Compound	*sec*-butylamine	Optical absorption and Fluorescence	1234.12 ppm	yes	static	305
Metallo-porphyrin	BA	Optical absorption	0.1 ppm	yes	dynamic	306
Metallo-porphyrin	BA	Optical absorption	50 ppm (90-3200 ppm)	yes	dynamic	307
Conjugated Polymer	BA	Optical absorption and Fluorescence	6.3 ppm	yes	dynamic	308
Liquid Crystals	BA	Optical response	10 ppm	no	static	309
Organic Compound	BA	Fluorescence	0.026 ppm (0 - 0.10 ppm)	no	static	300

Yang *et al*. reported a liquid crystals sensor doped with lauric aldehyde as optical sensor for the detection of BA.[309] Liquid crystals doped with appropriate concentration of lauric aldehyde are dispersed on clean glass slides (0.5 cm × 0.5 cm) and then exposure to BA vapors is conducted in a sealed chamber. Optical response of liquid crystals is observed through a polarized optical microscope in transmission mode. They found that liquid crystals doped with 0.1 wt% of lauric aldehyde allow the detection of 10 ppm of BA, observed by a bright-to-dark optical transition. Also, this system shows specificity to BA compared with the response obtained by exposure to other volatile compounds and reversible dark-to-bright transition when the sample is left in air.

Despite linear aliphatic diamines possess lower volatility than linear aliphatic monoamines containing the same chain length, linear aliphatic diamines having low molecular mass (NH_2-$(CH_2)_n$-NH_2, n = 2–5) are volatile at room temperature and atmospheric pressure.

Several optical systems have been developed for the qualitative vapor-phase detection of diamine vapors, mainly EDA, as organic molecules, polymers, covalent organic structures, *etc.*[295,310,311] Some of them are also used to detect these diamines in real samples, particularly in spoiled foods. These data are collected in Table 4.2 and Table 4.3.

Table 4.2. Literature data of optical chemosensors for the qualitative detection of EDA vapors.

Material	Detection method	Substrate	Selectivity Studies	Exposure Method	Ref
Metal complex	Optical absorption		no	static	312
Inorganic metal compound	Colorimetric	Paper	no	static	313
Metal-organic compound	Optical absorption		yes	static	288
Metal-organic compound	Optical absorption		no	static	314
Polymeric compound	Optical absorption	Glass	no	static	315
Metal organogel	Fluorescence	Glass	yes	static	316
Metal-organic framework	Fluorescence	Glass	yes	static	317
Coordination polymer	Optical absorption		yes	static	318
Metal complex	Optical absorption	Paper	yes	static	319
Organic compound	Fluorescence		yes	static	320
Organic compound	Optical absorption		yes	static	321

Despite the great interest for these diamines, however, only few examples of molecular materials allowing the quantitative detection of their vapors are reported in the literature, summarized in Table 4.4.

For quantitative EDA vapors detection, Dou *et al.* developed an *o*-phthalaldehyde (OPTA)/thiol molecular system that allows the detection of EDA in both solution and solid state.[330] In particular, the reaction between OPTA and mercaptosuccinic acid (MSA) leads to the formation of a molecular intermediate that shows evident optical absorption and fluorescence changes in the presence of EDA. The OPTA-MSA solution shows a yellow color and an enhancement of the fluorescence emission after the addition of EDA in a range between 0 – 30 μM. The preparation of a hydrogel-based dual-mode sensing system for the detection of different EDA vapor concentrations (0-160 ppm) is also described. In this case,

the colorimetric and fluorescent changes are in accordance with whose observed in solution, and evaluated by RGB analysis, resulting that the hydrogel-based system is able to detect hundreds of ppb of EDA vapors in a dynamic linear range of 3.2 – 64.0 ppm.

Table 4.3. Literature data of optical chemosensors for the qualitative detection of volatile aliphatic diamines vapors.

Material	Aliphatic diamine	Detection method	Substrate	Selectivity Studies	Exposure Method	Ref
Organic compound	DAB	Colorimetric	Silica composite	no	static	322
Organic compound	DAB DAPe	Fluorescence	Silica gel	yes	static	323
Metal complex	DAB	Fluorescence	Paper and TLC plates	no	static	324
Organic compound	DAB	Optical absorption and Fluorometric	Glass	no	static	325
Metal-organic framework	EDA DAPr	Fluorescence	Paper	yes	static	326
Organic compound	EDA, DAPr, DAB, DAPe	Fluorescence	Glass	yes	static	327

Table 4.4. Literature data of optical chemosensors developed for the quantitative detection of volatile diamines vapors under static conditions.

Material	Aliphatic diamine	Detection method	Substrate	LOD or Lowest Detected Conc. (linear range)	Selectivity Studies	Ref
Organic compound	DAPe	RGB analysis (Fluorescence)	Paper	500 ppm	yes	328
Organic compound	DAPe	RGB analysis (Fluorescence)	Paper	7.16 ppm	yes	329
Organic compound	EDA	RGB analysis (color and Fluorescence)	PVA hydrogel	700 ppb (3.2 – 64.0 ppm)	yes	330
Organic compound	EDA	Fluorescence	Paper	28.5 ppm	yes	331

Koner *et al.* reported sensing studies of EDA and other diamines in solution and solid-phase, using a ratiometric perylenediimide-based fluoroprobe.[331] In this case, the sensing performance of this molecular system towards diamine vapors arises from an aggregation-induced emission mechanism that allows the formation of a new emission band at 580 nm, with the concomitant decrease of the main emission band centered at 478 nm. The application for the detection of EDA and putrescine vapors using the pristine solid perylenediimide fluorophore and after deposition onto paper substrates is also reported. The

lowest detected concentration under static exposure to EDA and putrescine vapors is 28.5 and 4.3 ppm, respectively. For both substances quenching of the fluorescence emission is observed, and it is accompanied by a color change from bright orange to red (EDA) or purple (putrescine).

4.3. Properties of the Zn(salmal) Complex *1*

Complex **1** has been previously investigated by Di Bella *et al.* in several studies for its interesting properties and wide range of applications, both in solution and in solid phase.[201,203,226,241] In particular, studies on solutions of complex **1** in non-coordinating solvents suggest the presence of aggregated species, through the formation of intermolecular axial Zn···O interactions between two or more molecules of the complex. On the other hand, in coordinating solvents, monomeric adducts are formed, by axial coordination of the Zn(II) center with the solvent.[182] Di Bella *et al.* also demonstrated the deaggregation of **1** dissolved in a non-coordinating solvent (dichloromethane, DCM) by addition of a certain amount of a coordinating solvent (*e.g.*, THF) (Figure 4.1) or a Lewis base, resulting in the formation of monomeric adducts.[247,332]

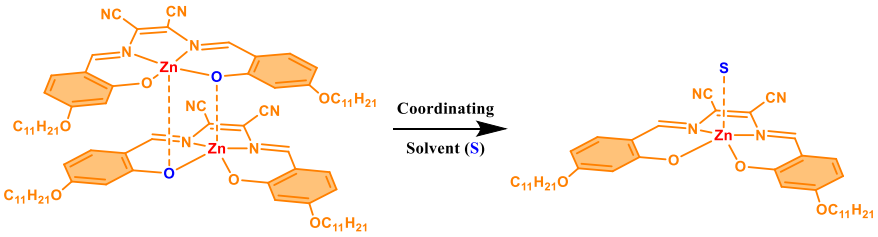

Figure 4.1. Schematic representation of deaggregation of **1** in the presence of a coordinating solvent.

More importantly, on switching from aggregate species to monomeric adducts, dramatic changes in the optical absorption and fluorescence properties of **1** are observed. In fact, optical absorption spectra of aggregate species and adducts are very different, with an enhancement of the fluorescence intensity upon deaggregation (fluorescence quantum yields, $\Phi = 0.08 – 0.16$ for aggregates, vs. $\Phi = 0.24$ for monomeric adducts).[247] Therefore, complex **1** was investigated for the colorimetric/fluorometric sensing in solution of different classes of Lewis bases.[201,226]

Di Bella *et al.* have also investigated the thermochromic and vapochromic properties of complex **1** in the solid phase.[240] Complex **1** was obtained as orange-red powder after crystallization from methanol. When this solid is heated at 140 °C for 10 min, a color change from orange-red to red-brown is observed. The comparison of the XRD patterns of these two solids shows two different phases. In particular, a lamellar structure is associated with the orange-red powder (H-aggregates), while a hexagonal columnar structure (red-brown powder, J-aggregates) is obtained by a thermally-induced phase-transition (Figure 4.2). Differential scanning calorimetry thermograms show an irreversible endothermic phase-transition at 131 °C accompanied by a naked-eye color change from the starting orange-red solid to the red-brown solid.

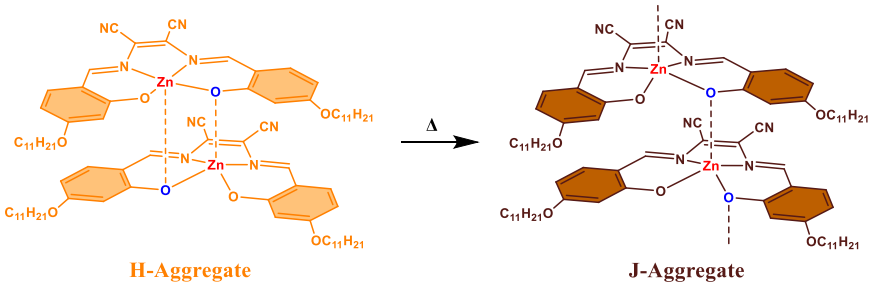

Figure 4.2. Irreversible phase-transition of **1** from H-aggregates to J-aggregates induced by thermal treatment.

Exposure of the heated solid to saturated vapors of isopropylamine (IPA), used as reference volatile Lewis base, involves a color change from red-brown to red. In this case, the XRD pattern is very different with respect to that of the starting or the heated. Thermogravimetric analysis (TGA) of the solid after exposure shows a weight loss consistent with the IPA content, thus suggesting a stoichiometric chemisorption of amine vapors. Interestingly, the complete restoration of the initial color of the powder is observed upon a thermal treatment of the exposed solid (140 °C), indicating a reversible vapochromic behavior.

Thin films of **1** were obtained by drop-casting of a DCM solution of the complex onto glass substrates. As-prepared films were obtained after the complete evaporation of the solvent, while annealed films were obtained by thermal treatment of the as-prepared films. The colors of these films are very similar to those observed for powders of **1** before and after thermal annealing. XRD patterns of films are almost similar compared with the powder samples, thus suggesting an analogous structure. Also, vapochromic properties of annealed films upon exposure to IPA vapors are comparable with those of the powder samples.

These results represent good starting points for further investigations on the vapochromic properties of **1**, and the potential application of this molecular material as a chemosensor for VOCs with Lewis basicity.

4.4. Aim of this Study

This chapter describes the development of a molecular material based on a Zn(salen)-type complex for the selective and sensitive detection of specific volatile pollutants. In particular, the Zn(salmal) complex, **1**, having alkoxy chains (-$OC_{11}H_{21}$) as lateral substituents was investigated for its known vapochromic properties. This material has also been found to possess vapoluminescent properties. Both vapochromic and vapoluminescent properties were applied for the development of simple, disposable, and low-cost paper-based films of **1** (**1**-PBFs) as chemosensors for the selective and sensitive detection of mono- and diamine vapors. To this end, the following section is divided in four parts.

The first part (Section 4.5.1) explores the vapochromic/vapoluminescent properties of aggregates of complex **1** as films deposited on glass substrates. In particular, the vapochromic and vapoluminescent properties of **1**-GBFs were initially investigated by exposure to different classes of VOCs under saturated vapor conditions.

In the second part (Section 4.5.2), the optimization of the preparation procedure of **1**-PBFs was first achieved by comparing different substrates and deposition techniques, as well

as their optimal storage conditions, in order to achieve high repeatability and optical uniformity of the chemosensor. Then, the vapoluminescent response of annealed **1**-PBFs prepared from a 5.0×10^{-3} M THF solution of **1**, named **1**-PBF5s, upon exposure to defined vapor concentrations of the involved VOCs and the sensitive detection of BA, chosen as reference volatile aliphatic monoamine, were studied.

The third part (Section 4.5.3) describes the sensitive vapochromic detection of BA vapors using as-prepared and annealed **1**-PBFs. In particular, **1**-PBFs prepared from a 1.0×10^{-3} M THF solution, named **1**-PBF1s, were used in addition to **1**-PBF5s. The color changes of these films after exposure were analyzed by UV-vis reflectance spectra and RGB color analysis. Simulated experiments of BA vapor leakage have also been reported.

The fourth part (Section 4.5.4) is focused on the vapoluminescent response of **1**-PBF5s towards volatile aliphatic diamines and the sensitive detection of EDA, chosen as reference volatile diamine.

The quantitative detection of BA and EDA was performed by static exposure to specific vapor concentrations using **1**-PBFs and color/fluorescence emission changes. Furthermore, a selective fluorescence response to these analytes compared to other classes of VOCs has been demonstrated. Finally, a sensing mechanism based on XRD and thermogravimetric analyses of films before and after exposure is proposed.

4.5. Results and Discussion

4.5.1. Optical Properties of Aggregates of Complex *1*

4.5.1.1. Optical absorption and fluorescence emission of *1*-GBFs

Films of **1** were prepared by drop-casting of a THF solution of **1** (2.5×10^{-3} M) onto glass substrates, as previously described (Section 3.3.1). After solvent evaporation, the as-prepared films show an orange color comparable to that of films previously obtained from a DCM solution of **1** (1.0×10^{-3} M),[240] but with higher optical uniformity. Annealed films were obtained by thermal treatment of as-prepared **1**-GBFs into an oven at 140 °C for 10 min. Optical properties of as-prepared and annealed films were investigated by optical absorption and fluorescence measurements (Figure 4.3).

Different optical absorption spectra for as-prepared and annealed **1**-GBFs are observed (Figure 4.3a). In particular, the optical absorption spectrum related to the as-prepared films shows a broad band at λ = 442 nm and a stronger absorption band envelope centered at *ca.* 350 nm. After thermal annealing, the formation of a new band centered at λ = 563 nm and a hypochromism in the region between 300 and 400 nm are observed, in agreement with the color variations observable to the naked eye, from yellow-orange to red-brown.

Interestingly, both the as-prepared and annealed **1**-GBFs also exhibit photoluminescence. In particular, an emission band centered at 600 nm characterizes the as-prepared **1**-GBFs, while an emission band is observed at 641 nm for the annealed **1**-GBFs (Figure 4.3b). Again, the wavelength relative to the emission maximum for the as-prepared and annealed films is consistent with the color observed with the naked eye under an UV lamp (λ_{exc} = 365 nm). Therefore, in addition to the vapochromic characteristics, the

fluorescence emission properties of **1**-GBFs suggest that this material also behaves as vapoluminescent.

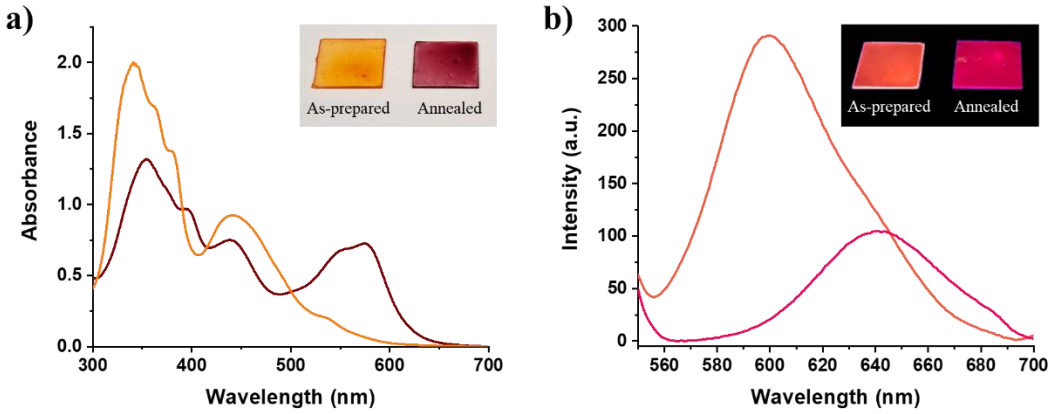

Figure 4.3. Optical absorption **(a)** and fluorescence **(b)** spectra (λ_{exc} = 500 nm, related to an isosbestic point) of as-prepared and annealed **1**-GBFs. Insets: photographic images of as-prepared and annealed films under natural light (left) and under 365 nm light (right).

*4.5.1.2. Vapochromic and vapoluminescent properties of **1**-GBFs*

In order to evaluate the vapochromic and vapoluminescent properties of **1**-GBFs, as-prepared and annealed films were exposed to BA, used as reference volatile Lewis base. Exposure to saturated vapors of BA (113088 ppm at 23 °C) was performed into a sealed glass chamber, as previously described (Section 3.5.1). The optical absorption spectra of as-prepared films after exposure to BA vapors show two new absorption bands in the region between 420 and 530 nm, with maximum of absorption centered at λ = 451 nm and λ = 501 nm, and small changes in the region between 300 and 400 nm (Figure 4.4a). These changes in optical absorption properties are accompanied by a change in color of the as-prepared **1**-GBFs from yellow-orange (before exposure) to orange (after exposure). Fluorescence emission spectra show the formation of a new, more intense band centered at λ = 613 nm after the exposure to saturated vapors of BA (Figure 4.4b).

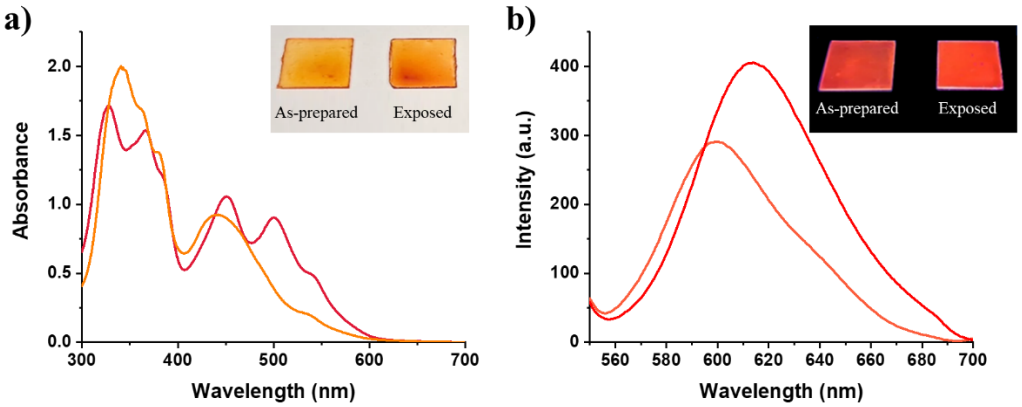

Figure 4.4. Optical absorption **(a)** and fluorescence **(b)** spectra (λ_{exc} = 473 nm, related to an isosbestic point) of as-prepared **1**-GBFs before and after exposure to saturated BA vapors. Insets: photographic images of as-prepared and exposed films under natural light (left) and under 365 nm light (right).

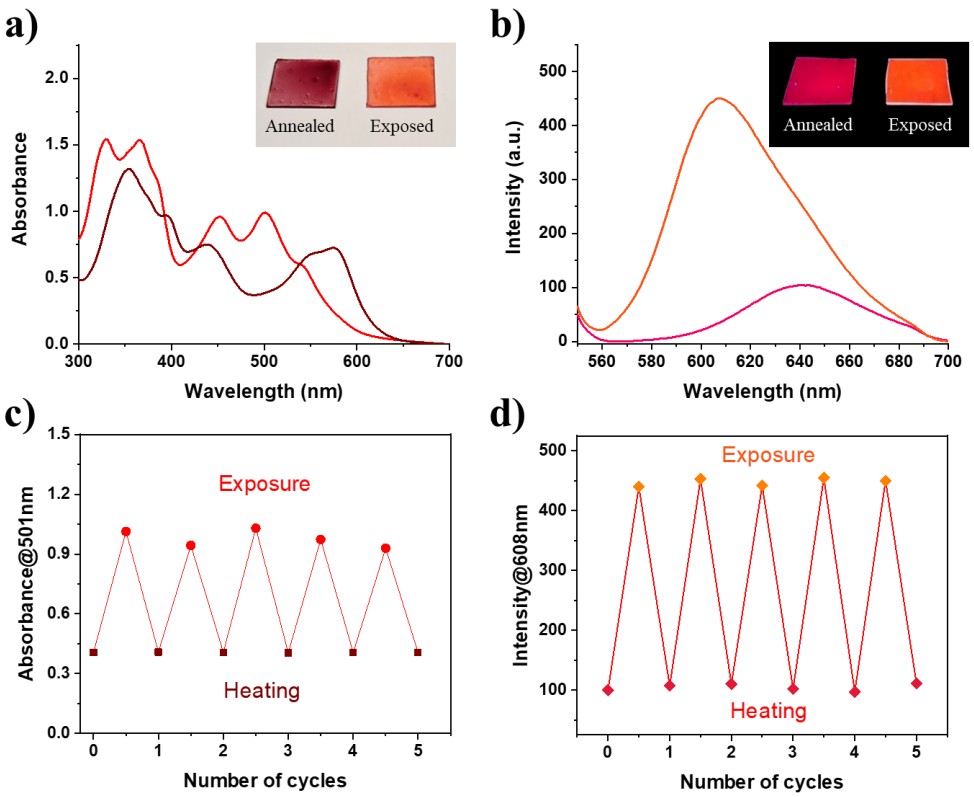

Figure 4.5. Optical absorption **(a)** and fluorescence **(b)** spectra (λ_{exc} = 538 nm, related to an isosbestic point) of annealed **1**-GBFs before and after exposure to saturated BA vapors. Insets: photographic images of annealed and exposed films under natural light (left) and under 365 nm light (right). Optical absorption **(c)** and fluorescence **(d)** intensity changes at λ_{abs} = 501 nm and λ_{em} = 608 nm, respectively, upon cycles of exposure to saturated vapors of BA and subsequent thermal heating at 120 °C.

The optical absorption spectra of annealed **1**-GBFs recorded before and after the exposure to BA are completely different (Figure 4.5). In particular, analogously to as-prepared films, two new absorption bands centered at λ = 451 nm and λ = 501 nm are observed after exposure. The region between 300 and 400 nm is also profoundly different, as shown in Figure 4.5a. The observed changes in optical absorption spectra can be related to the color change from red-brown to red observed with the naked eye. Fluorescence emission spectra show the formation of a new emission band at λ = 608 nm, about five times more intense than the emission of the annealed film (Figure 4.5b). Under the UV lamp, clear color changes from red to orange are observed. Thus, in addition to vapochromism, the annealed films exhibit marked vapoluminescence, never previously observed for this family of molecular materials. Furthermore, only few other examples of vapoluminescent Zn(II) coordination complexes are reported in literature.[333,334]

The vapochromic and vapoluminescent properties of **1**-GBFs were demonstrated by successive cycles of exposure of the annealed films to saturated vapors of BA, followed by thermal treatment at 120 °C for desorption of BA. The variation of the optical absorption and fluorescence emission intensity of annealed **1**-GBFs in the maximum of absorption and emission after exposure to BA vapors (λ_{abs} = 501 nm and λ_{em} = 608 nm, respectively), are reported in Figure 4.5c and Figure 4.5d. A complete restoration of the initial optical

absorption/fluorescence spectrum is observed for 5 cycles of exposure/heating. This demonstrates a complete sorption/desorption process involved in the detection of BA vapors. Furthermore, comparing these results, a greater variation in fluorescence intensity is observed than the variation in optical absorption. Thus, this demonstrates the vapochromic/vapoluminescent properties of complex **1** supported on glass substrates, which will be further explored in the following section by exposure to different classes of VOCs.

*4.5.1.3. Vapochromic and vapoluminescent response of **1**-GBFs to VOCs*

The comparison between the optical absorption and fluorescence emission changes after exposure to saturated vapors of BA for as-prepared and annealed **1**-GBFs, clearly indicate that the latter possesses a better response respect to the as-prepared films. Therefore, annealed films were chosen to explore their optical response to different families of VOCs having Lewis basic character.

The following volatile compounds were chosen as prototypes for the various classes of VOCs: methanol (MeOH) for alcohols; diethyl ether (Et_2O) for ethers; acetone (ACE) for chetons; acetaldehyde (AA) for aldehydes; acetonitrile (ACN) for nitrile compounds; THF for oxygenated heterocycles; *n*-butylthiol (BuSH) for mercaptans; ethyl acetate (AcOEt) for esters; acetic anhydride (Ac_2O) for anhydrides; acetic acid (AcOH) for carboxylic acids; N,N-dimethylformamide (DMF) for ammides; BA for primary amines; diethylamine (DEA) for secondary amines; triethylamine (TEA) for tertiary amines; aniline (AN) for aromatic amines; Py for heterocyclic aromatic amines; EDA for primary diamines.

In order to explore the vapochromic and vapoluminescent properties of **1**-GBFs, annealed films were initially exposed to saturated vapors of these VOCs and then optical absorption and fluorescence emission spectra were recorded (Figure 4.6). Exposure to saturated vapors of each involved VOC was carried out into a sealed glass chamber for 15 min, except for BA and EDA (5 min).

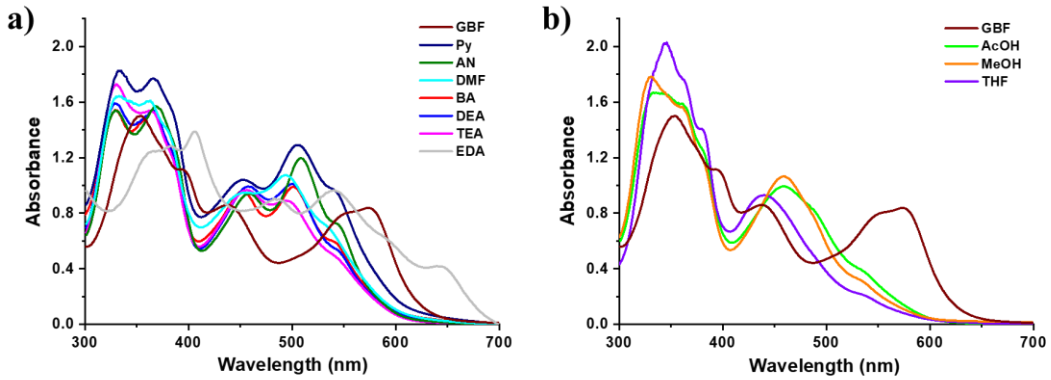

Figure 4.6. Optical absorption spectra of annealed **1**-GBFs exposed to saturated vapors of **(a)** N-VOCs and **(b)** O-VOCs.

For BuSH, Et_2O, ACE, AA, ACN and Ac_2O no relevant optical absorption changes of annealed **1**-GBFs are observed (the color of the films remained unchanged). For the other investigated VOCs, a color change of annealed films, from red-brown to red or orange, is observed by naked-eye and measured by optical absorption spectra. On the basis of their

functional group and the different response achieved, they were divided in N-VOCs and O-VOCs. In particular, for N-VOCs it is possible to observe a common absorption maximum around λ = 455 nm and at longer wavelength (between 493 and 508 nm) and the formation of two new absorption bands in the region between 300 and 400 nm (Figure 4.6a). In the case of EDA vapors, the formation of two new absorption bands centered at 406 and 643 nm is observed, in addition to the optical absorption changes observed for all other N-VOCs. A color change of the annealed films from red-brown to red is observed for all the investigated N-VOCs, with the exception of EDA, which shows a color change from red-brown to brown. On the other hand, completely different absorption spectra are observed for exposure of annealed **1**-GBFs to O-VOCs. In particular, for AcOH and MeOH a hyperchromism is observed in the region between 300 and 400 nm and a new absorption band centered at λ = 458 nm, while for THF an absorption is found at λ = 440 nm (Figure 4.6b). Furthermore, after exposure to AcOH and MeOH a color change from red-brown to orange is observed, while for THF the color change is from red-brown to yellow-orange.

Analogously, the vapoluminescent response of annealed **1**-GBFs was investigated after exposure to saturated vapors of various VOCs and then their emission was recorded by front-face fluorescence spectroscopy (incident angle of excitation light of 30°). Based on the absorption spectra (Figure 4.6), to ensure comparable absorbance, fluorescence spectra were collected with a λ_{exc} = 508 nm for N-VOCs and λ_{exc} = 459 nm for O-VOCs (Figure 4.7).

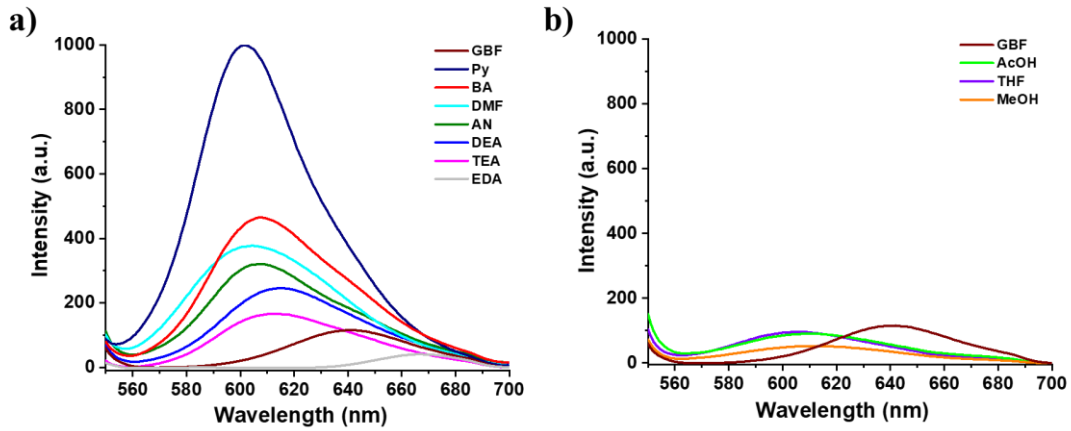

Figure 4.7. Fluorescence spectra of annealed **1**-GBFs exposed to saturated vapors of **(a)** N-VOCs (λ_{exc} = 508 nm) and **(b)** O-VOCs (λ_{exc} = 459 nm).

In agreement with the observed optical absorption spectral variations, no fluorescence spectral changes are observed after exposure to BuSH, Et_2O, ACE, AA, ACN and Ac_2O, while for the remaining analytes the formation of a new fluorescent emission band is observed. In particular, for N-VOCs the new fluorescent emission bands are between 601 and 612 nm, while for O-VOCs between 605 and 610 nm. Surprisingly, and in sharp contrast, the formation of a new, less intense emission band, centered at 670 nm, is observed after exposure to saturated vapors of EDA. Furthermore, an important difference in the response of the annealed **1**-GBFs can be observed when considering the fluorescence emission intensity. Indeed, with the exception of EDA, a higher fluorescence intensity is observed after exposure to N-VOCs than to O-VOCs.

Complete restoring of the initial optical absorption or fluorescence spectra of the annealed films is also observed by successive exposure/heating cycles towards all these investigated VOCs having Lewis basic character.

In addition to VOCs with Lewis basic character, the response of annealed GBFs was also explored by exposure to aliphatic and aromatic VOCs, such as *n*-pentane (NP), DCM, cyclohexane (Cy), and benzene (Bz). As expected, exposure to saturated vapors of these VOCs for 15 minutes shows no significant optical or color changes.

4.5.2. Vapoluminescent Detection of Primary Monoamine Vapors by *1*-PBFs

In the previous Sections (4.5.1.2 and 4.5.1.3), a larger change in fluorescence intensity than that of optical absorption upon exposure to BA vapors and a different fluorescence response towards VOCs having Lewis basicity were obtained for annealed **1**-GBFs. Therefore, in order to obtain a simple, disposable and portable system with improved optical uniformity for selective and sensitive detection of VOCs, paper substrates were investigated to support complex **1** and then the films were annealed to be used for fluorescent detection studies.

4.5.2.1. Preparation procedure and storage conditions of *1*-PBFs

Paper is a low-cost, flexible, and lightweight material. In recent years, paper used as a substrate has attracted increased interest due to its versatility in the development of sensors and devices.[335,336,337,338]

As described for GBFs, the drop-casting technique was initially used also for the preparation of films of **1** using paper substrates, but in this case a low optical uniformity was obtained (Figure A5). For this reason, the dip-coating approach was used to prepare **1**-PBFs. Dip-coating is a simple deposition technique consisting in dipping the substrate into a solution containing the sensing material. This technique was used to obtain **1**-PBFs by dipping paper squares (2.5 cm × 2.5 cm) into a THF solution of **1** (2.5×10^{-3} M). After solvent evaporation at room temperature, orange films were obtained and, analogously to GBFs, a color change from orange to red-brown was observed upon thermal annealing at 140 °C for 10 min.

In order to optimize the optical properties of **1**-PBFs, some tests were performed, such as keeping the paper immersed in the solution of **1** for different times (2 s, 30 s, 1, 2, 5 and 10 minutes) before the evaporation of the solvent. However, the time of dipping was found to be irrelevant on the properties of **1**-PBFs, thus the shortest time of 2 s was chosen for successive preparations. Also, different concentrations (2.5×10^{-3} M, 3.5×10^{-3} M, 5.0×10^{-3} M, and 6.5×10^{-3} M) of the THF solution of **1** were tested. An increase in the intensity of the reflectance spectrum of the annealed **1**-PBFs prepared with these solutions is observed, in line with the gradual increase in color tone, easily observable by the naked eye (Figure A6), together with a linear dependence ($R^2 = 0.9880$) of the absorbance intensity at 547 nm with increasing concentration of the starting THF solution of **1**. The latter results suggest an increasing amount of the complex adsorbed on paper substrates. In order to verify the effective amount of **1** deposited on paper, **1**-PBFs were washed with 7 mL of pure THF for

three times, to dissolve the complex adsorbed on paper substrates. Then, UV-vis absorption spectra of the solutions of **1** were collected and the concentrations for each solution were calculated using the Beer-Lambert equation. From the concentration, the mole amount of **1** deposited on paper substrates were calculated. The results show a good linearity between the concentration of the starting solution of **1** used for the preparation of **1**-PBFs and the effective amount of the complex deposited on the paper substrates (Figure A6). Among different concentrations tested for the preparation of **1**-PBFs, the concentration of 5.0×10^{-3} M was chosen for the successive preparations of the films (**1**-PBF5s) used for vapoluminescent investigations, because it represents the lowest concentration that avoids the interference due to the fluorescence emission of the paper substrate (Figure A7).

The repeatability and uniformity of fluorescence intensity of **1**-PBF5s is a crucial feature for their application as vapoluminescent chemosensors for VOCs. To this end, different kinds of filter paper were tested for the development of **1**-PBF5s, using the aforementioned optimized procedure. In particular, six types of filter paper with different thickness and pore size were explored: Whatman-4, Whatman-42, Scharlau T2, Scharlau T3, Scharlau T4, and Albet DP 412 110. Among these, Whatman-4 filter paper ensures better repeatability, with a fluorescence intensity comparable to that of other types of filter paper (Figure A8). However, paper films prepared with this procedure suffer from small fluctuations of the fluorescence intensity signal, that seems to be strongly related to the change in the RH during the annealing process. Therefore, to avoid this drawback, the annealing was performed under nitrogen atmosphere, as described in Section 3.3.2. Using this optimized procedure, similar optical absorption and fluorescence spectra of the as-prepared and annealed **1**-PBF5s (Figure A9) were obtained compared to the GBFs (Figure 4.3), and complete repeatability and uniformity of the fluorescence intensity of the films is ensured, as a key prerequisite for quantitative detection of VOCs.

Stable fluorescence emission of **1**-PBF5s is also essential for their use. However, it was observed that fluorescence tends to decrease over time in the case of annealed films. To explain this behavior, two possible phenomena can be hypothesized: i) degradation of the complex caused by the acidity of the paper;[339] or ii) adsorption of water vapor from the air. For this reason, before dipping, the paper squares were washed with ethanol or basic solutions of $Ca(OH)_2$. However, fluorescence spectra of annealed **1**-PBF5s with or without this pre-treatment show negligible differences. Therefore, the decrease of fluorescence intensity for the annealed **1**-PBF5s was monitored in different RH conditions. The results show first a fast and then a less pronounced decrease of the fluorescence intensity of **1**-PBF5s, monitored within 7 h, with a more pronounced decrease with increasing in the RH value (Figure 4.8).

These results suggest that **1**-PBF5s should necessarily be maintained under a nitrogen atmosphere before being used for fluorescence measurements. In fact, the fluorescence of annealed films, kept under this condition and monitored for one month, remain almost unchanged. For the same reason, the as-prepared **1**-PBF5s were also stored under nitrogen atmosphere before being used. Therefore, all following studies on the vapoluminescent properties of **1**-PBF5s were carried out on films maintained under an inert atmosphere before exposure to VOCs.

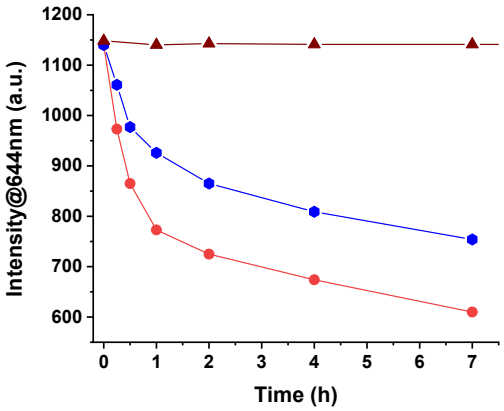

Figure 4.8. Fluorescence intensity of annealed **1**-PBF5s (λ_{exc} = 500 nm) within 7 h under inert atmosphere (red-wine), at 40 % RH (blue) and at 60 % RH (red).

*4.5.2.2. Sensing performance of **1**-PBFs*

The results reported in the previous Section (4.5.1.3) demonstrated the vapochromic and vapoluminescent properties of GBFs to various classes of VOCs, with a more favorable response in terms of fluorescence. Analogously to GBFs, the vapoluminescent response of the annealed **1**-PBF5s in the presence of BA vapors, prepared with the optimized procedure described above, was also investigated (Figure 4.9).

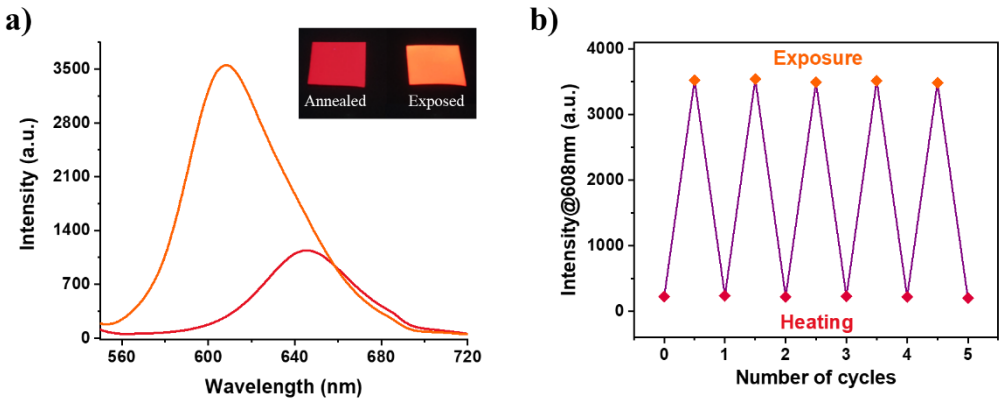

Figure 4.9. (a) Fluorescence spectra (λ_{exc} = 522 nm, related to an isosbestic point) of annealed **1**-PBF5s before and after exposure to saturated BA vapors. Inset: photographic image of annealed and exposed films under 365 nm light. **(b)** Fluorescence intensity changes at λ_{em} = 608 nm upon cycles of exposure to saturated vapors of BA and subsequent thermal heating at 120 °C.

Fluorescence emission spectra of annealed **1**-PBF5s before and after exposure to saturated vapors of BA were performed using λ_{exc} = 522 nm, as an isosbestic point determined from the UV-vis reflectance spectra (Figure A10). Annealed films are characterized by an emission band centered at 644 nm. After exposure to BA vapors, an enhancement of the fluorescence and the formation of a new emission band at λ_{em} = 608 nm is observed. Under the UV lamp, color changes similar to those observed for GBFs, from red to orange, are observed.

The vapoluminescent properties of **1**-PBF5s were also demonstrated by successive cycles of exposure/heating of annealed films to saturated vapors of BA (Figure 4.9b), using the same conditions described for GBFs. The variation of the fluorescence emission intensity of annealed **1**-PBF5s at λ_{em} = 608 nm shows a complete restoration/disappearance of the band emission at 608 nm for 5 cycles of exposure/heating. Analogously to GBFs, this result further demonstrates a complete sorption/desorption process involved in the detection of BA also for annealed **1**-PBF5s, with stronger and, hence, more favorable vapoluminescence and superior fluorescence homogeneity.

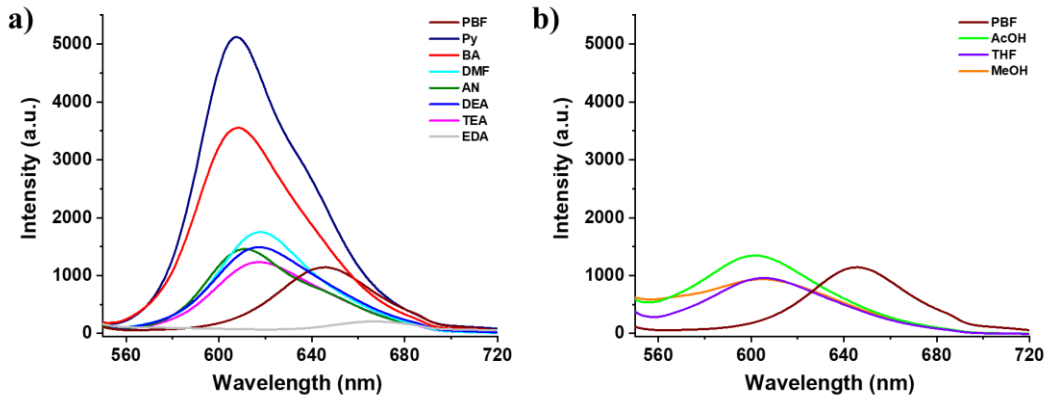

Figure 4.10. Fluorescence spectra of annealed **1**-PBF5s (λ_{exc} = 500 nm) exposed to saturated vapors of **(a)** N-VOCs and **(b)** O-VOCs.

The fluorescence response of annealed **1**-PBF5s towards different classes of VOCs was also explored. Fluorescence spectra of the annealed **1**-PBF5s after exposure to saturated vapors of involved VOCs (Figure 4.10) compare well with those previously obtained with GBFs (Figure 4.7), except for a small blue-shift of the emission maximum (less than 6 nm for all the VOCs, except for DMF, 10 nm), and a stronger fluorescence intensity. Therefore, given the advantages of increased optical uniformity and sensitivity, **1**-PBF5s have been used for further investigations on VOCs detection.

4.5.2.3. Selectivity studies towards primary monoamines

In evaluating the response of **1**-PBF5s to various VOCs it is important to note that under saturated vapors conditions the concentrations of the VOCs investigated are very different (Table B1). Therefore, an appropriate comparison of the fluorescence can be made by exposing **1**-PBF5s to the same concentration for each VOC. To this purpose, the concentration of 300 ppm was chosen because it represents the IDLH value reported by NIOSH for BA,[262] as the volatile Lewis base used as reference.

Since to achieve concentrations of the VOCs below 500 ppm it would be needed to add sub-microliter volumes of the pure liquids into a sealed chamber (1.15 L), it was therefore necessary to prepare solutions of VOCs with appropriate concentration. To choose the appropriate solvent for the preparation of these solutions, the fluorescence response of annealed **1**-PBF5s after exposure to 500 ppm of BA as pure liquid and that after exposure to 500 ppm of BA dissolved in various solvents, such as NP, DCM, and Cy, was compared.

Results show a negligible decrease in the fluorescence intensity for NP and DCM solutions, while higher decrease is observed for Cy solutions, compared to the fluorescence response after exposure to the pure liquid (Figure A11). Therefore, NP was chosen as the solvent for preparing the solutions because it is chemically inert to the VOCs involved and does not interfere with the sensing response of **1**-PBF5s. NP solutions with a concentration of 0.473 M and 0.0473 M of each analyte were prepared by diluting the appropriate volume of the pure analyte into volumetric flasks. The appropriate volume of the pure liquid was calculated using the static liquid gas distribution method (eq. 3.3).

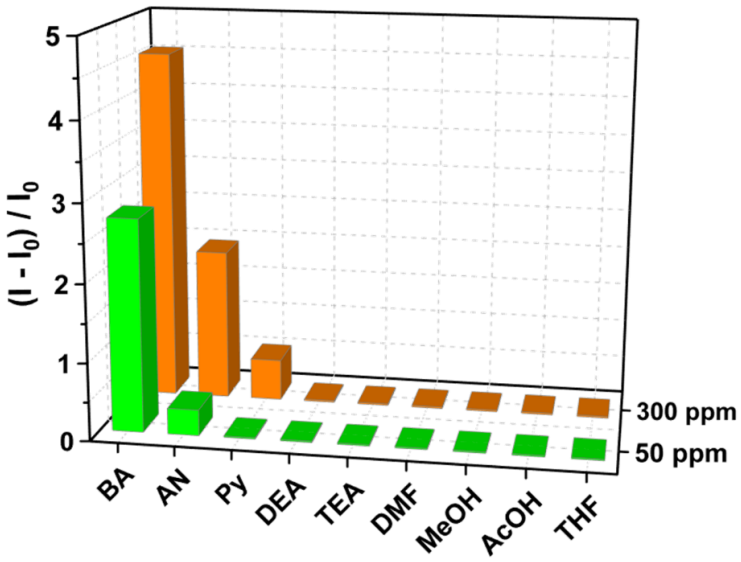

Figure 4.11. Fluorescence intensity of **1**-PBF5s after static exposure to different VOCs at 300 ppm and 50 ppm. In the diagram I is the fluorescence intensity after exposure and I_0 is the fluorescence intensity of the starting annealed films at λ_{em} = 617 nm (λ_{exc} = 500 nm).

Exposure to 300 ppm of each investigated VOC was carried out under static conditions for 30 min and the fluorescence spectra were collected immediately after exposure. Under these conditions, a fluorescence response of **1**-PBF5s occurs only for BA, AN and Py (Figure 4.11). Moreover, a further selective response of **1**-PBF5s is evident by decreasing the concentration of the involved VOCs to 50 ppm. In fact, going from 300 ppm to 50 ppm, **1**-PBF5s show a selective response to the primary amines BA and AN, with a higher response for the former. Therefore, in the following sections the quantitative detection of BA compared to all other VOCs investigated will be further explored.

4.5.2.4. Effect of relative humidity, time of exposure and temperature on sensing performance

The sensing performance of annealed **1**-PBF5s for the detection of volatile primary amines under real-world conditions was also investigated. When a chemosensor is used for the detection of vapors or gases, two parameters need to be considered: i) temperature and ii) RH. Both are two very important parameters, especially when quantitative detection is involved. Furthermore, paper substrates can easily absorb water molecules, and their presence can potentially interfere with the sensing performance of **1**-PBF5s. In the previous

Section (4.5.2.1), the stability of annealed **1**-PBF5s under different percentages of RH overtime was evaluated, showing a decrease of the initial fluorescence emission for RH of 40% and 60%, while no relevant changes are observed under nitrogen atmosphere. Analogously, the potential effect of RH on the response of annealed **1**-PBF5s after exposure is considered here.

In particular, exposure to 50 ppm of BA was conducted for 30 min in a RH range between 30% and 80%. Fluorescence spectra collected immediately after exposure show a lower fluorescence intensity (less than 10%) for an RH value of 80% and a slight increase in fluorescence emission (about 5%) for an RH value of 30% compared to the fluorescence response collected at an RH value of 50% (Figure 4.12a). On the other hand, small differences in the fluorescence after exposure to BA are observed for RH values near the reference value of 50%, such as 40% and 60% (+1.8% and -0.9% respectively). Therefore, it can be concluded that the response of **1**-PBF5s is almost independent in a RH range between 40% and 60% (Figure 4.12b).

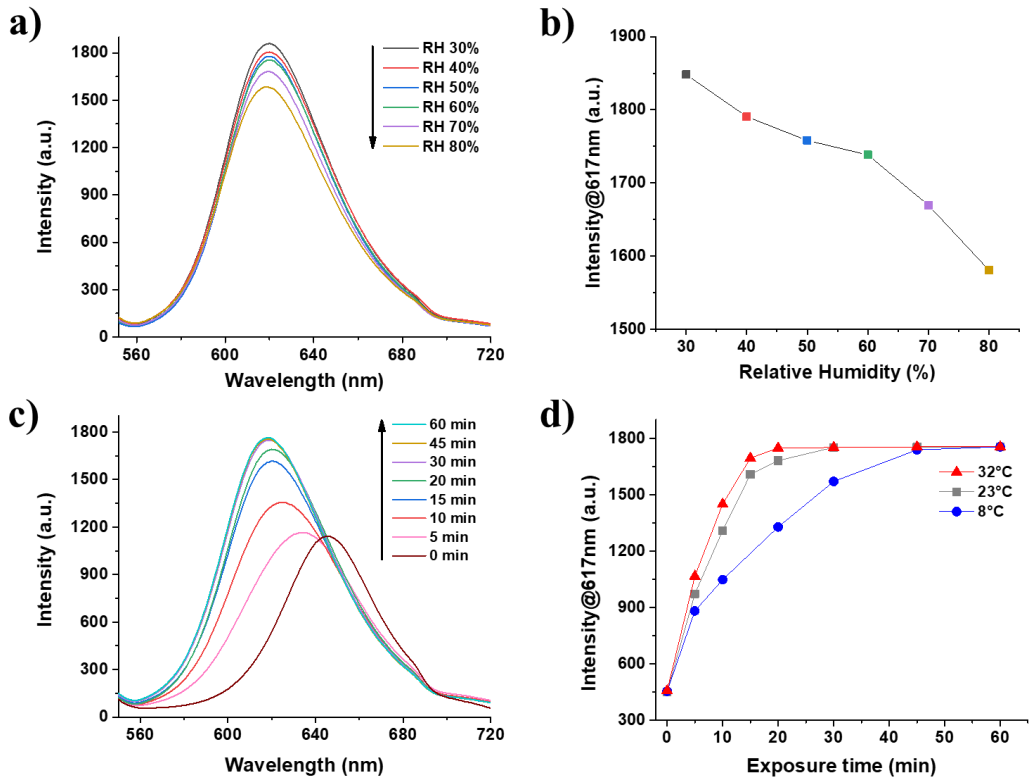

Figure 4.12. **(a)** Fluorescence spectra of **1**-PBF5s (λ_{exc} = 500 nm) after exposure to 50 ppm of BA vapors recorded in a RH range between 30 – 80%. Each spectrum was recorded in an independent experiment. **(b)** Variation of the fluorescence intensity at 617 nm of **1**-PBF5s after exposure to 50 ppm of BA vapors recorded as a function of the relative humidity. **(c)** Fluorescence spectra of **1**-PBF5s after exposure to 50 ppm of BA vapors (T = 23 °C) recorded as a function of exposure time. Each spectrum was recorded in an independent experiment. **(d)** Variation of the fluorescence intensity at 617 nm as a function of exposure time to 50 ppm of BA vapors (RH = 50%) at three different temperatures.

Considering the reference RH value of 50%, the response of annealed **1**-PBF5s to 50 ppm of BA at room temperature (23 °C) was explored overtime (Figure 4.12c). The

formation of the new emission band at 617 nm, and a gradual increase of the fluorescence emission are observed, reaching a saturation point after an exposure time of 30 min. Thus, this exposure time was considered for the successive exposure experiments involving annealed **1**-PBF5s conducted at room temperature.

Also, the potential effect of temperature on the sensing performance of **1**-PBF5s was evaluated. In this case, **1**-PBF5s were exposed to 50 ppm of BA at different temperatures, under a constant RH of 50%, and then the fluorescence emission was measured. Exposure to BA vapors at temperatures lower and higher (8 °C and 32 °C) than room temperature (23 °C) was performed after pre-cooling/heating of the glass chamber used for the static exposure experiments (Figure 3.1). Under these conditions, similar fluorescence emission of **1**-PBF5s at 617 nm is obtained for exposure at 32 and 23 °C, while lower fluorescence intensity is observed at 8 °C. As expected, monitoring the fluorescence emission at 617 nm after exposure to BA vapors for different exposure times, a faster reaching of the saturation point is observed with increasing temperature (Figure 4.12d). In particular, considering the exposure time of 30 min at 23 °C as a reference, the saturation point is reached approximately 20 min after exposure at 32 °C, while 30 min are required for exposure at 8 °C.

In summary, slight changes in the fluorescence response of **1**-PBF5s to BA vapors are observed in a RH range of 40 – 60%. Also, the interaction between the chemosensor and the volatile amine is independent from the exposure temperature. Moreover, different kinetics associated with the interaction process as a function of the exposure temperature are observed, with the reaching of a saturation point for different exposure times. All these results demonstrate the potential application of annealed **1**-PBF5s for real-world detection of primary amine vapors under average indoor or outdoor RH and temperature conditions.

4.5.2.5. Quantitative detection of primary monoamine vapors

In the previous Section 4.5.2.3, the selective response of annealed **1**-PBF5s towards primary amines was demonstrated. Therefore, quantitative detection experiments were carried out by exposure to specific concentrations of BA (0 – 1000 ppm) and AN (0 – 300 ppm). The excitation wavelength was chosen to be approximately related to the longest wavelength absorption maximum for the involved species (500 nm for BA, and 508 nm for AN).

Exposure of annealed **1**-PBF5s to BA vapors involves the formation of a new emission band centered at λ_{em} = 617 nm after the addition of 25 ppm, which progressively increases up to 375 ppm (Figure 4.13a), accompanied by a gradual color change, from red to orange, observable by naked-eye under a UV lamp (Figure 4.13b). For higher concentrations of BA, a slight shift of the emission maximum to 608 nm is also observed. An exponential increase of the fluorescence emission intensity at λ_{em} = 617 nm is achieved, with a saturation point reached for a concentration around 750 ppm (Figure 4.13c). Moreover, a dynamic linear range of response of annealed **1**-PBF5s is obtained from 0 up to 50 ppm (Figure 4.13d), with a good linearity coefficient (R^2 = 0.9965). The LOD value, calculated from the standard deviation of blank and the slope derived from the linear fit in the range 0 – 50 ppm, is 2.0 ppm.

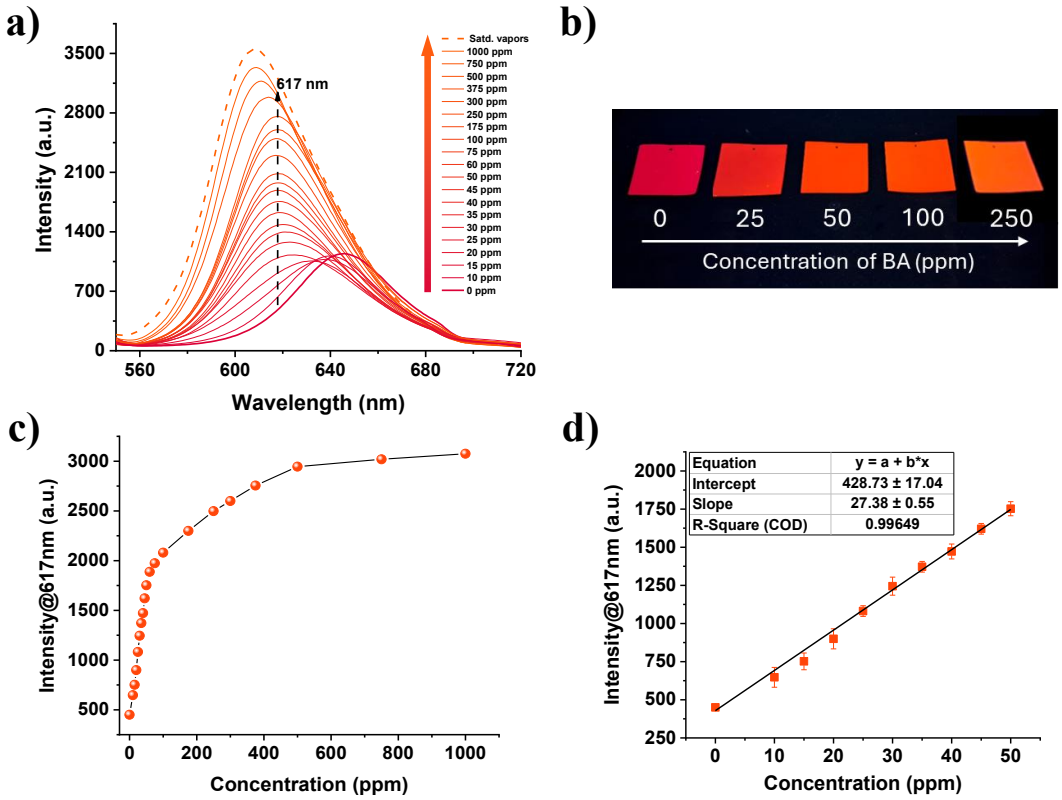

Figure 4.13. **(a)** Fluorescence spectra of **1**-PBF5s exposed to increasing concentrations of BA vapors (λ_{exc} = 500 nm). Each spectrum was recorded in an independent experiment. **(b)** Photographic images of **1**-PBF5s under 365 nm light after exposure to different concentrations of BA (range 0 – 250 ppm). **(c)** Variation of fluorescence intensity at λ_{em} = 617 nm as a function of the concentration of BA. **(d)** Linear best fit in the dynamic linear range from 0 up to 50 ppm of BA (weight given by data error bars).

This response to low ppm concentrations of BA vapors is very important for the potential application of annealed **1**-PBF5s for air quality monitoring. As abovementioned, the OSHA PEL–C and IDLH values for BA vapors are 5 and 300 ppm, respectively.[262,263] The calculated LOD for BA vapor detection (2.0 ppm) using **1**-PBF5s is below the PEL–C established by OSHA. Furthermore, for concentrations above 50 ppm the response of **1**-PBF5s is non-linear, however it is possible to distinguish 300 ppm from similar BA concentrations (*e.g.*, 150 or 500 ppm) by evaluating the emission intensity at 617 nm of **1**-PBF5s after exposure. Therefore, **1**-PBF5s are useful for detecting PEL–C and IDLH values for BA vapors.

These results compare favorably with optical sensors reported in the literature developed for the quantitative detection of BA vapors, both in static.[309,300] and dynamic conditions[306,307,308] (Table 4.1), since annealed **1**-PBF5s represent a unique example combining enough sensitivity (lower than the PEL–C), high selectivity (compared to most common N-VOCs) and an adequate dynamic linear range.

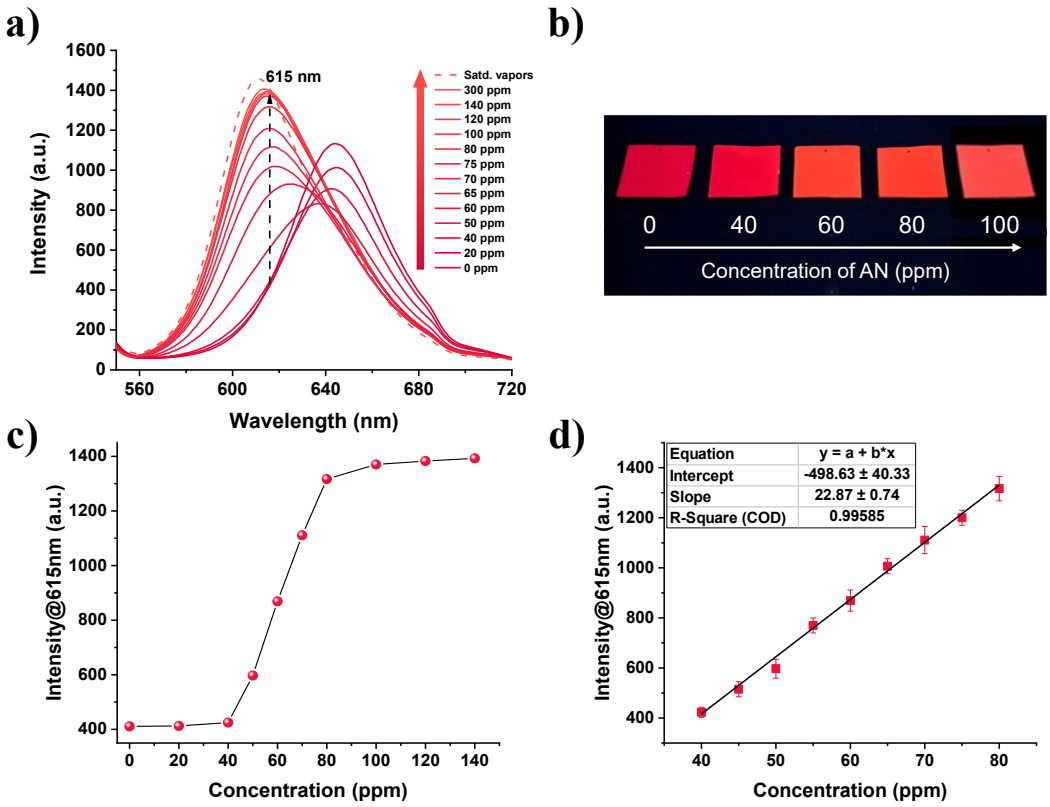

Figure 4.14. **(a)** Fluorescence spectra of **1**-PBF5s exposed to increasing concentrations of AN vapors (λ_{exc} = 508 nm). Each spectrum was recorded in an independent experiment. **(b)** Photographic images of **1**-PBF5s under 365 nm light after exposure to different concentrations of AN (range 0 – 100 ppm). **(c)** Variation of fluorescence intensity at λ_{em} = 615 nm as a function of the concentration of BA. **(d)** Linear best fit in the dynamic linear range from 40 up to 80 ppm of AN (weight given by data error bars).

Exposure of **1**-PBF5s to AN vapors shows different results than those obtained with exposure to BA. In particular, an initial decrease in fluorescence emission is observed up to 40 ppm of AN, then the formation of a new emission band centered at λ_{em} = 615 nm is obtained with exposure to 70 ppm, which progressively increases up to 140 ppm (Figure 4.14a). The increase of the fluorescence emission band is accompanied by a gradual color change from red to red-orange observable under UV light (Figure 4.14b). In this case, the saturation point is reached at 120 ppm (Figure 4.14c). A dynamic linear range from 40 up to 80 ppm is obtained (Figure 4.14d), with a good linearity coefficient (R^2=0.9959).

Although in the case of AN vapor detection, **1**-PBF5s are clearly not the most sensitive system developed for their quantitative detection, however, similarly to BA, no competitive experiments are reported for the other existing optical chemosensors (Table B2).

Therefore, although it is not possible to calculate an LOD, it is possible to distinguish AN vapor concentrations lower than those reported as the IDLH value by NIOSH (100 ppm)[340] in the linear dynamic range obtained, with the advantage of a selective response in the absence of other volatile monoamines.

4.5.2.6. Competitive experiments

The selective detection of toxic and/or dangerous compounds for human health is an important feature of sensors, in order to discriminate them and estimate the risk of exposure in their presence. Many chemical sensors reported in literature possess interesting sensing performances but suffer of low selectivity to specific analytes.

The selectivity of annealed **1**-PBF5s was further evaluated by competitive experiments performed at room temperature (23 °C) and at constant RH value (50%), considering BA as reference primary monoamine in the presence of other potential interferents (Py, DEA, TEA, DMF, MeOH, DMF, ACE, AA, Et_2O, Ac_2O, ACN, AcOEt) in a ratio of 1:10. The mixture, BA/interferent (50:500 ppm respectively) was introduced by a Hamilton microliter syringe into the same apparatus used for quantitative detection experiments, and the time of exposure was established as 30 min. Then, fluorescence spectra were collected, and the fluorescence response was compared with the response obtained for the exposure of **1**-PBF5s to 50 ppm of BA and 500 ppm of the interferent.

Competitive experiments were carried out in two different static exposure conditions: i) both BA and the interferent were introduced together into the sealed chamber containing the **1**-PBF5; and ii) BA and the interferent were first introduced into the sealed chamber and then, after 10 min, the **1**-PBF5 was introduced into the chamber. Considering Py as interferent, the results showed negligible differences in the fluorescence intensity using the two different methods, thus the following competitive experiments were carried out considering the first exposure method.

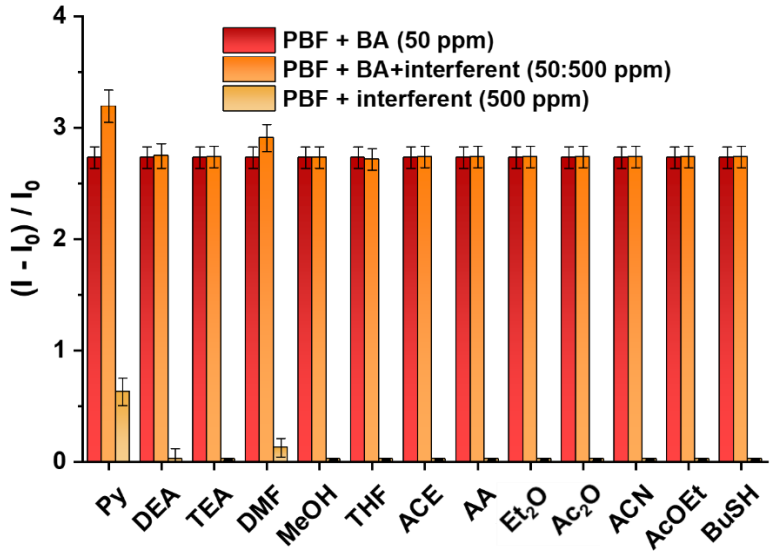

Figure 4.15. Comparison of the fluorescence response of **1**-PBF5s upon exposure to 50 ppm of BA (red bars), exposure to BA:interferent in a ratio 1:10 (orange bars), and exposure to 500 ppm of the interferent (yellow bars).

Figure 4.15 shows an increase in fluorescence intensity in the presence of Py (<16%) and DMF (<6%), a slight increase in the presence of DEA (<0.5%), while no relevant differences are observed for all other analytes, compared to the fluorescence intensity obtained in the presence of 50 ppm of BA. The response of annealed **1**-PBF5s upon exposure to 500 ppm of each interferent was also considered. In particular, exposure to 500 ppm of Py

shows the formation of a new emission band centered at λ_{em} = 633 nm, with an emission of fluorescence intensity almost similar to that before exposure, while negligible changes are observed for all other interferents, compared to the fluorescence intensity of the starting annealed **1**-PBF5s (Figure A12).

In summary, competitive experiments further demonstrate the very high selectivity of the annealed **1**-PBF5s for BA vapors compared to the other investigated VOCs.

4.5.2.7. Vapoluminescent response to other primary monoamines and ammonia

Since the high selectivity to BA vapors over other classes of VOCs was demonstrated, further investigations on the vapoluminescent response of annealed **1**-PBF5s toward other relevant aliphatic primary amines were performed. In particular, the fluorescence response to *sec*-butylamine (*s*-BA), *tert*-butylamine (*t*-BA), propylamine (PA), isopropylamine (IPA), ethylamine (EA), and methylamine (MA) was investigated and compared to that of BA. Furthermore, ammonia was also considered.

Exposure of PBFs to 300 ppm of these volatile amines shows a color change from red-brown to red (with different color tone) easily observable by naked-eye for all the amine involved, while no significant color changes are observed for NH_3. The fluorescence spectra recorded after exposure of **1**-PBF5s to these amines show the formation of a new emission band centered at *ca.* 617 nm for all the aliphatic amines involved, with the exception of *t*-BA and NH_3 (Figure A13). Considering the fluorescence intensity of the starting annealed **1**-PBF5s as reference, higher fluorescence emission is observed for *s*-BA, PA, and IPA, while less intense emission is obtained for EA and MA. Interestingly, for lower vapor concentration (50 ppm), a relevant change of the fluorescence emission intensity is achieved only for PA (Figure A13).

A further comparison of the fluorescence response obtained after exposure to BA versus all other volatile aliphatic amines involved is reported in Figure 4.16. Although the fluorescence response upon exposure to 300 ppm of all the other amines is lower than that of BA, it is interesting to note that *s*-BA shows a fluorescence response comparable to PA, while *t*-BA and IPA show a similar response to EA. Furthermore, going from 300 ppm to 50 ppm, an appreciable and similar fluorescence response is observed in the case of *s*-BA and PA. Although a fluorescence response is observed for *s*-BA and PA at these concentrations, their presence in the atmosphere is still limited compared to BA vapors.[341] Thus, these results also demonstrate a selective response of the annealed **1**-PBF5s towards low vapor concentrations ($\leq$ 50 ppm) of BA along the volatile aliphatic primary amine series.

The response obtained for NH_3 and the other primary amines could be related to their different Lewis basicity in gas/vapor-phase,[342,343] but this property alone cannot completely explain the results obtained. On the other hand, the parent chain length seems to play a relevant role in the observed vapoluminescent response. Indeed, a clear increase in the fluorescence response is observed with increasing length of the parent chain (comparison of the fluorescence response of BA with PA, EA or MA), while similar responses are obtained for amines having the same parent chain (*s*-BA and PA, or *t*-BA, IPA and EA). Furthermore, a parent chain length $\geq$ 3 seems to be critical to obtain a relevant fluorescence response of **1**-PBF5s at low vapor concentration (50 ppm).

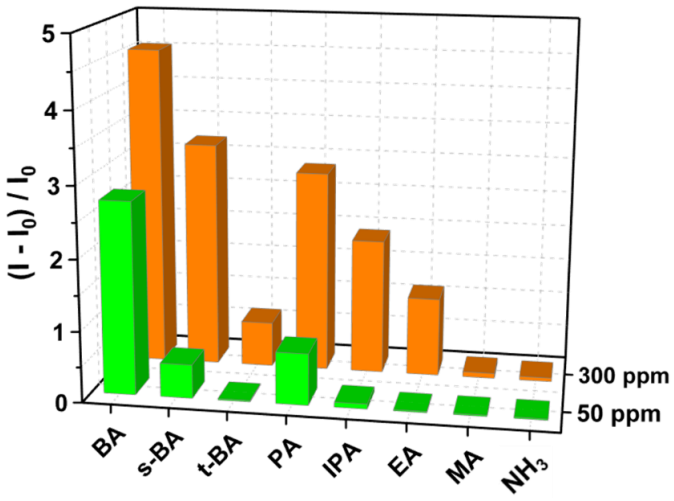

Figure 4.16. Fluorescence intensity of **1**-PBF5s after static exposure to different primary aliphatic amines at 300 ppm and 50 ppm. In the diagram I is the fluorescence intensity after exposure and I_0 is the fluorescence intensity of the starting annealed PBFs at λ_{em} = 617 nm (λ_{exc} = 500 nm).

*4.5.3. Vapochromic Detection of BA Vapors by **1**-PBFs*

The fluorescence response of annealed **1**-PBF5s towards BA vapors (Section 4.5.2.5) allowed the detection of very low concentrations (LOD = 2.0 ppm), but is limited for on-site detection. On the other hand, in addition to the fluorescence changes, significant optical absorption (Section 4.5.1.3) and color changes, from red-brown to red, are also observed after exposure of **1**-PBF5s to vapors of this volatile monoamine (Figure A10). Therefore, based on the vapochromic properties of annealed **1**-PBF5s, the quantitative detection of BA vapors was also explored by analyzing the RGB color changes of the films before and after exposure.

*4.5.3.1. Preparation procedure and storage conditions of vapochromic **1**-PBFs*

As-prepared and annealed films of **1** used for vapochromic investigations were prepared using the optimized procedure described in Section 4.5.2.1, with small modifications. After evaporation of the solvent at room temperature, an orange color is obtained for the as-prepared **1**-PBF5s and **1**-PBF1s, while red-brown films are achieved after thermal annealing in air at 140 °C of the as-prepared films. Thus, nearly identical colors and comparable UV-vis reflectance spectra of **1**-PBF5 and **1**-PBF1 are obtained for annealed films prepared by heating at 140 °C for 10 min in air or nitrogen atmosphere. Therefore, the heat treatment of the as-prepared **1**-PBFs to obtain the annealed **1**-PBFs used for subsequent colorimetric investigations was performed in air, without the need to operate under nitrogen atmosphere.

The color stability of **1**-PBFs was monitored by UV-vis reflectance spectra. First, the effect of different illumination conditions (50, 200, 1500 lux) was evaluated on as-prepared and annealed **1**-PBFs stored into round flasks under nitrogen atmosphere and at room temperature (22 ± 3 °C). No relevant changes in reflectance spectra are observed for as-prepared **1**-PBF5s and **1**-PBF1s at low lighting levels (≤ 200 lux) monitored for two weeks, while very small changes are observed only at higher illumination levels (≥ 1500 lux) (Figure 4.17a and Figure 4.17b).

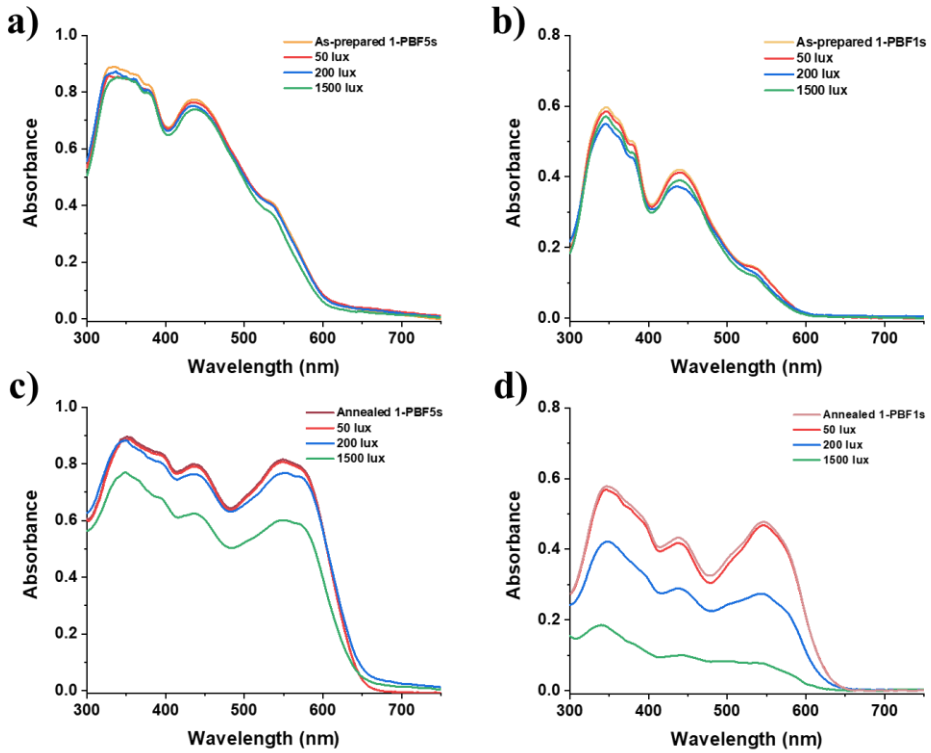

Figure 4.17. UV-vis reflectance spectra of as-prepared **(a,b)** and annealed **(c,d)** **1**-PBFs stored under nitrogen atmosphere after two weeks of exposure to different illumination conditions. UV-vis reflectance spectra of freshly-prepared films are reported as reference.

Conversely, while no significant color changes are observed for annealed **1**-PBF5s and **1**-PBF1s kept in the dark (≤ 50 lux), as monitored by UV-vis reflectance spectra (measurements up to two weeks), a significant reduction in the intensity of the reflectance spectra is observed for films exposed to light, with a more marked effect in the case of the highest illumination level (Figure 4.17c and Figure 4.17d).

The effect of RH on the color stability of both as-prepared and annealed **1**-PBFs was also considered. **1**-PBFs were stored in the dark in a RH range from 30 to 70%. The effect of the RH was found to be irrelevant on the reflectance spectra and, hence, on the color stability of all **1**-PBFs involved (measurements up to two weeks). Indeed, identical reflectance spectra were obtained by comparing the reflectance spectra of films stored under different RH conditions with those of **1**-PBF stored under nitrogen.

Overall, as-prepared and annealed **1**-PBFs, even when obtained in air and stored at room temperature under nitrogen atmosphere or at average RH conditions in the dark, are quite stable over time and hence suitable for on-site sensing applications.

4.5.3.2. Selectivity of 1-PBFs towards primary amine vapors

Analogously to the investigations on the vapoluminescent response of **1**-PBFs towards various N-VOCs and O-VOCs (Section 4.5.2.3), the vapochromic response of as-prepared and annealed **1**-PBFs was also evaluated considering the same VOCs. Again, the concentration of 300 ppm was considered first because it represents the IDLH value for BA,[262] as the reference volatile Lewis base.

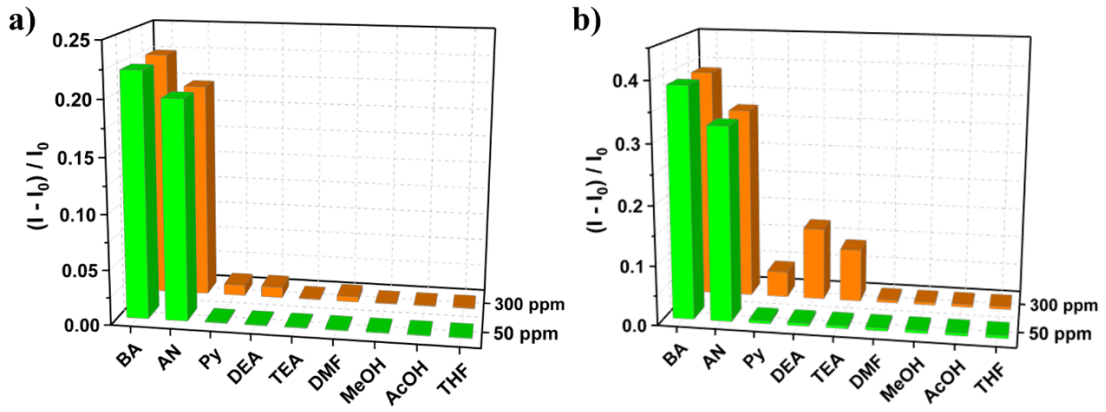

Figure 4.18. Absorbance intensity of **(a)** annealed **1**-PBF5s and **(b)** annealed **1**-PBF1s after static exposure to different VOCs at 300 ppm and 50 ppm. In the diagram I is the absorbance intensity after exposure and I_0 is the absorbance intensity of the starting annealed **1**-PBF5s and **1**-PBF1s at λ_{abs} = 500 nm and λ_{abs} = 503 nm, respectively.

Starting from annealed **1**-PBF5s, exposure to 300 ppm of each investigated VOC under static conditions for 30 min, results in a relevant response in the presence of BA and AN, and in a very weak response for Py, DEA, and DMF (Figure 4.18a). Compared to **1**-PBF5s, a similar trend in the vapochromic response to BA and AN, characterized by a greater variation of the $(I - I_0)/I_0$ ratio, is obtained using annealed **1**-PBF1s (Figure 4.18b), with a more marked response also in the case of Py, DEA, and TEA. Moving to lower vapor concentrations, from 300 ppm to 50 ppm, a selective vapochromic response towards BA and AN is obtained using both annealed **1**-PBF5s and **1**-PBF1s. These results further confirm the high selectivity of annealed **1**-PBFs towards volatile primary amines, as previously observed in the case of vapoluminescent detection studies using annealed **1**-PBF5s (Section 4.5.2.3).

Analogously, as-prepared **1**-PBF5s and **1**-PBF1s show a significant vapochromic response for BA and AN (Figure A14), and a weaker response mainly toward Py and DEA upon exposure to 300 ppm of the involved VOCs (exposure time 1 hour). Again, a higher variation in the response is obtained for **1**-PBF1s than for **1**-PBF5s.

Thus, as previously demonstrated by vapoluminescent studies, a selective vapochromic response to primary amines compared to all other VOC classes studied is obtained also for both as-prepared and annealed **1**-PBFs. Therefore, further investigations regarding the quantitative vapochromic detection of BA vapors will be explored in the following sections.

*4.5.3.3. Vapochromic response of annealed **1**-PBFs towards BA vapors*

Annealed **1**-PBF5s were exposed to different concentrations of BA, and the UV-vis reflectance spectra before and after exposure were collected (Figure 4.19a). Reflectance spectra of the annealed **1**-PBF5s show an envelope in the range 300 – 400 nm, and two absorption bands centered at *ca.* 436 and 547 nm. After exposure to increasing concentrations of BA, small changes are observed in the region between 300 – 400 nm and a small shift of the band at 436 nm (from 436 to 445 nm), while the region between 480 – 550 nm is characterized by the disappearance of the band at 547 nm and the appearance of a new characteristic band centered at 500 nm.

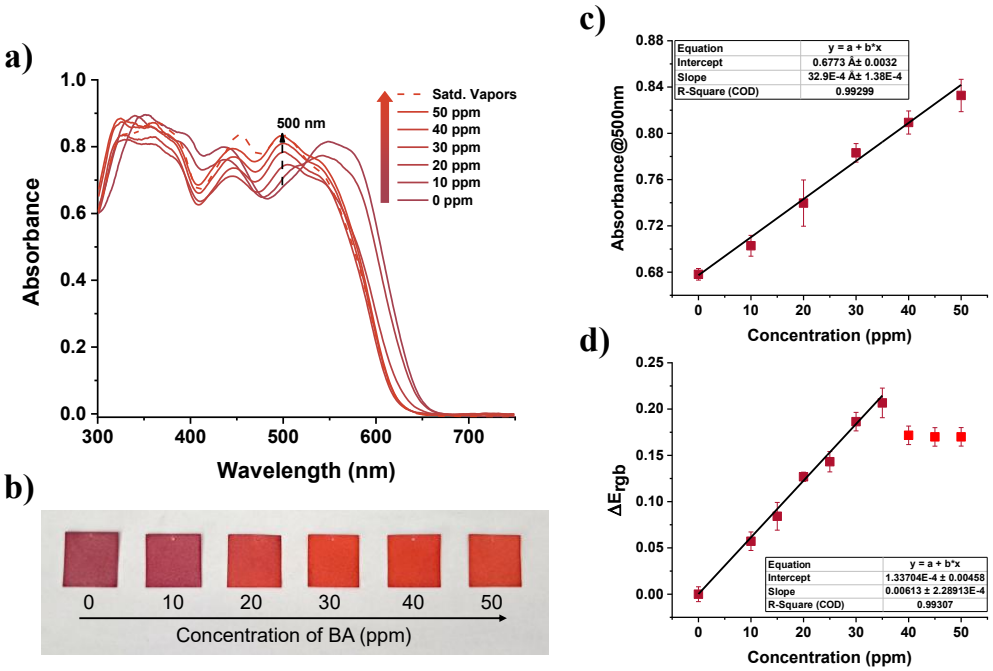

Figure 4.19. **(a)** UV-vis reflectance spectra of annealed **1**-PBF5s exposed to increasing concentrations of BA. Each spectrum was recorded in an independent experiment. **(b)** Photographic images of **1**-PBF5s under natural light after exposure to different concentrations of BA (range 0 – 50 ppm). Variation of **(c)** the absorbance at 500 nm and **(d)** mean ΔE_{rgb} values as a function of the concentration of BA vapors, and linear best fit in the dynamic range (weight given by data error bars). The data points marked in red are not included in the linear fit.

In particular, the formation of the new absorption band at 500 nm is observed upon exposure to 20 ppm of BA, according to a visible color change from red-brown to red (Figure 4.19b), which progressively increases up to 50 ppm. Considering the absorbance intensity at 500 nm, a linear response is obtained in the range 0 – 50 ppm (Figure 4.19c), showing a good linearity coefficient (R^2 = 0.9930). A LOD of 4.6 ppm is calculated in this dynamic linear range. Therefore, comparing these results with previous investigations on the fluorescence response of annealed **1**-PBF5s (Section 4.5.2.5), the same dynamic linear range of response after exposure to BA vapors is obtained, with a comparable LOD.

Then, color changes were also evaluated by acquiring the RGB values of each film using an Android smartphone app (*Color Detector* developed by Galaxy studio apps). RGB values were captured directly on the films under constant illumination (*ca.* 200 lux) using a Samsung Galaxy S23 smartphone camera, then normalized rgb values were obtained from equations 3.4 – 3.6 (Section 3.6), and finally the color difference (ΔE_{rgb}) was calculated for each exposed film (eq. 3.7). In this case, a smaller linear range of response is obtained from the ΔE_{rgb} plot versus BA concentration (0 – 35 ppm, R^2 = 0.9931), than that obtained from the related UV-vis reflectance spectra, but with a comparable calculated LOD (3.9 ppm) (Figure 4.19d). These results demonstrate the potential application of the RGB color analysis approach for quantitative detection of BA vapors using annealed **1**-PBF5s.

Interestingly, improvements in the sensitivity of annealed **1**-PBFs to BA vapors were achieved by using a more dilute THF solution of **1** (1.0×10^{-3} M) for their preparation. In this case, annealed **1**-PBF1 films are characterized by UV-vis reflectance spectra of very

similar shape (Figure 4.20a), compared to those of the films prepared from more concentrated THF solution (Figure 4.19a), but less intense and with a lighter color visible to the naked eye (Figure 4.20b). After exposure to BA vapors, the appearance of a new absorption band at 503 nm is observed, with a linear response in the range from 0 to 30 ppm (R^2 = 0.9872) (Figure 4.20c). Furthermore, a lower LOD is obtained in this case with respect to annealed **1**-PBF5s (3.7 *vs* 4.6 ppm). Considering the RGB color analysis (Figure 4.20d), a smaller dynamic linear range (0 – 20 ppm) and, again, a lower LOD (2.8 ppm) are obtained compared to those observed for annealed **1**-PBF5s (0 – 35 ppm and 3.9 ppm). Note that, the calculated LOD from RGB color analysis (2.8 ppm) is very similar to that obtained using annealed **1**-PBF5s for the fluorometric detection of BA vapors (2.0 ppm, Section 4.5.2.5).

Also, the sensing performance of annealed **1**-PBFs stored for two weeks in round flasks at RH = 50% was also evaluated. In particular, annealed **1**-PBF5s and **1**-PBF1s were exposed to 25 and 15 ppm of BA vapors, respectively, and UV-vis reflectance spectra were collected after exposure. Very interestingly, an almost similar response of these films stored in the dark for two weeks is achieved compared to freshly prepared films (Figure A15).

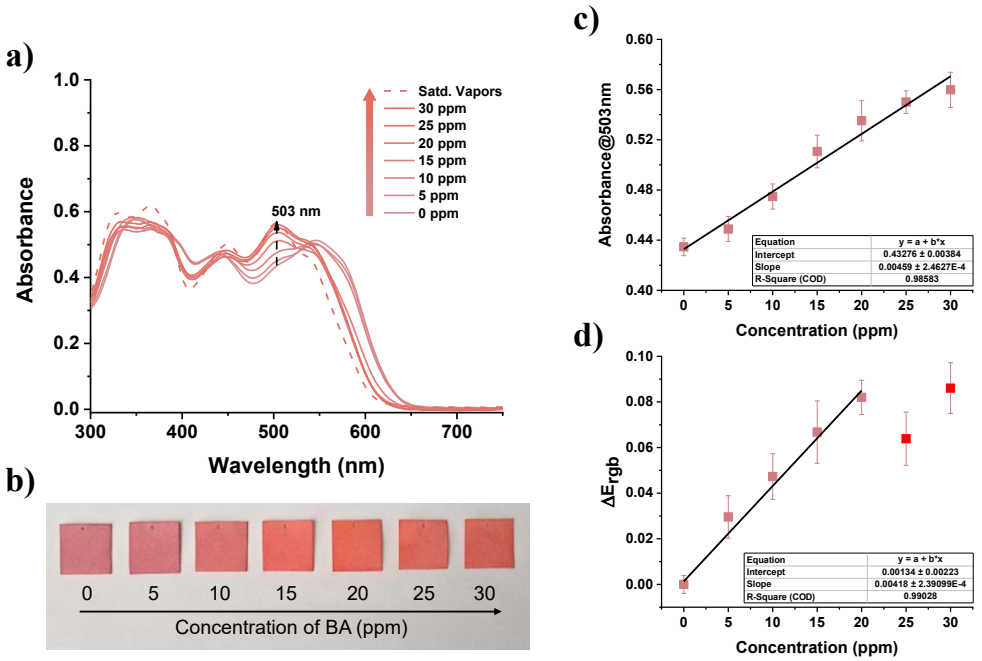

Figure 4.20. **(a)** UV-vis reflectance spectra of annealed **1**-PBF1s exposed to increasing concentrations of BA. Each spectrum was recorded in an independent experiment. **(b)** Photographic images of **1**-PBF1s under natural light after exposure to different concentrations of BA (range 0 – 30 ppm). Variation of **(c)** the absorbance at 503 nm and of **(d)** mean ΔE_{rgb} values as a function of the concentration of BA vapors, and linear best fit in the dynamic range (weight given by data error bars). The data points marked in red are not included in the linear fit.

In summary, the potential colorimetric detection of BA vapors using the vapochromic properties of annealed **1**-PBFs was first investigated by reflectance spectral analysis. The decrease in the concentration of the THF solution of **1** (from 5.0×10^{-3} M to 1.0×10^{-3} M) leads to an increase in the sensitivity of **1**-PBFs towards BA vapors (from 4.6 ppm for **1**-PBF5s to 3.7 ppm for **1**-PBF1s). Interestingly, comparable results, with improved sensitivity (3.9 and 2.8 ppm), are also obtained from a simple RGB color analysis of vapochromic films

before and after exposure, which in turn is almost similar to that obtained from fluorescence measurements, although with a reduced linear dynamic range. In all cases, LOD values lower than the PEL–C established by OSHA for BA vapors (5 ppm)[263] are obtained.

4.5.3.4. *Vapochromic response of as-prepared **1**-PBFs towards BA vapors*

Based on the results reported in the previous section for the sensitive vapochromic detection of BA vapors, further investigations on the colorimetric response of **1**-PBFs were performed using as-prepared films. Again, to obtain as-prepared **1**-PBFs, THF solutions of **1** having concentrations of 5.0×10^{-3} M and 1.0×10^{-3} M were used and then exposure to specific concentrations of BA vapors was carried out.

Starting from the as-prepared **1**-PBF5 films, exposure to increasing concentrations of BA vapors in a range from 100 up to 4000 ppm leads to relevant changes in the reflectance spectra (Figure 4.21a). In particular, the formation of a new absorption band centered at 497 nm is observed upon exposure to 1000 ppm, which gradually increases up to 3000 ppm. By monitoring the absorbance intensity at 497 nm, a progressive increase is obtained with the saturation point reached around 4000 ppm BA (Figure 4.21b). A dynamic linear range of the response of as-prepared films towards BA vapors, characterized by a good linear coefficient (R^2 = 0.9879) is obtained from 100 up to 500 ppm (Figure 4.21c). Analogous results are obtained for as-prepared **1**-PBF1 films, but with a saturation point observed at *ca.* 2000 ppm of BA (Figure 4.22).

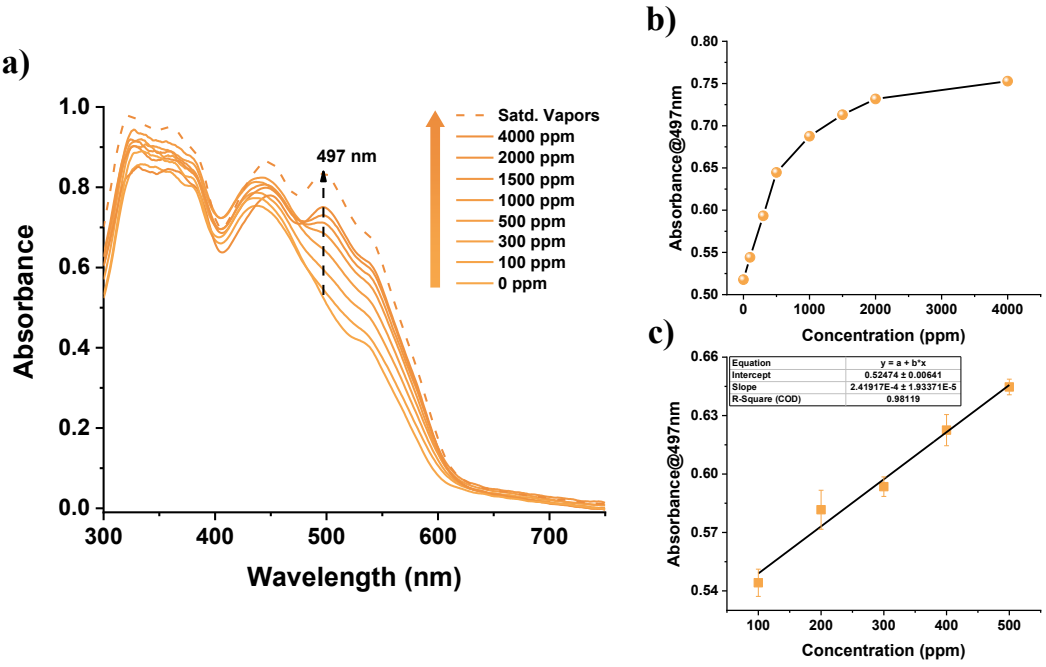

Figure 4.21. **(a)** UV-vis reflectance spectra of as-prepared **1**-PBF5s exposed to increasing concentrations of BA. Each spectrum was recorded in an independent experiment. **(b)** Variation of the absorbance intensity at 497 nm as a function of the concentration of BA. **(c)** Linear best fit in the dynamic linear range from 100 up to 500 ppm of BA (weight given by data error bars).

RGB color analysis of as-prepared films before and after exposure to BA vapors was also performed. Again, RGB values were captured directly on the films under constant illumination (*ca.* 200 lux), using a smartphone camera of Samsung Galaxy S23 and then used for the calculation of ΔE_{rgb}. For the as-prepared **1**-PBF5s a gradual color change, from yellow-orange orange, easily observable by naked-eye, is detected in the range 100 – 500 ppm of BA (Figure 4.23a). A good linear relationship ($R^2 = 0.9563$) is obtained from the color difference plot versus the BA concentration in this range (Figure 4.23c), analogously to the results of the reflectance spectral changes (Figure 4.21c). Similar results are also obtained for as-prepared **1**-PBF1s, but with a more marked color change in the BA vapor concentration range 100 – 500 ppm, and a higher linear coefficient ($R^2 = 0.9639$, Figure 4.23b and Figure 4.23d).

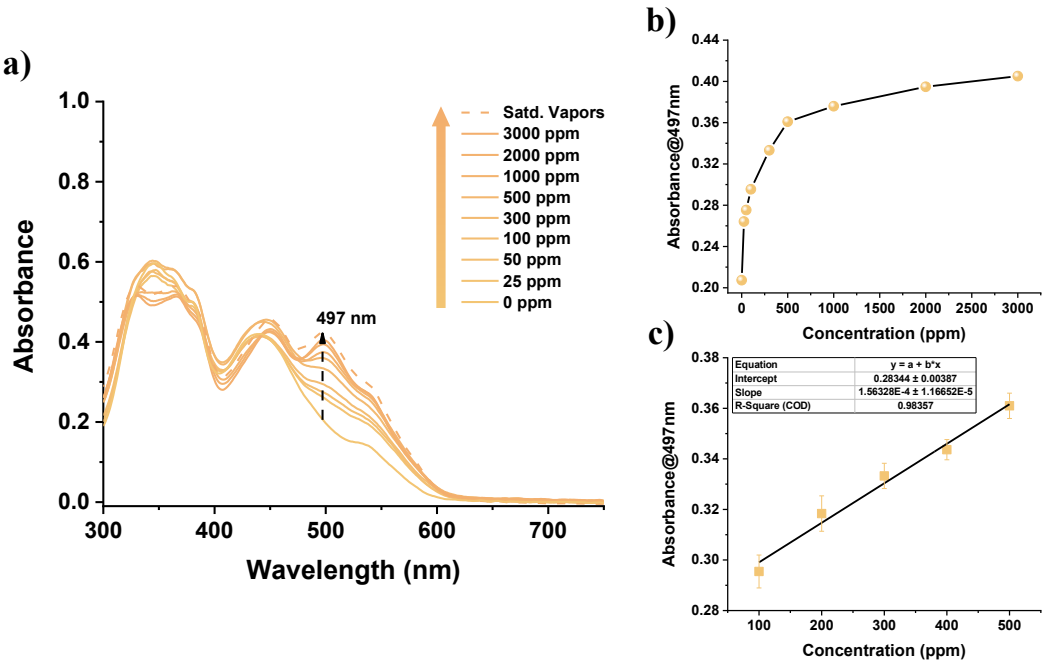

Figure 4.22. **(a)** UV-vis reflectance spectra of as-prepared **1**-PBF1s exposed to increasing concentrations of BA. Each spectrum was recorded in an independent experiment. **(b)** Variation of the absorbance intensity at 497 nm as a function of the concentration of BA. **(c)** Linear best fit in the dynamic linear range from 100 up to 500 ppm of BA (weight given by data error bars).

The overall results show a visible color change, accompanied by changes in the UV-vis reflectance spectra, for both as-prepared **1**-PBFs after exposure to higher concentrations of BA (from hundreds to thousands of ppm) compared to the corresponding annealed **1**-PBFs. Moreover, as-prepared **1**-PBFs allow to estimate the 300 ppm vapor concentration of BA, representing the IDLH value established by NIOSH,[262] both by evaluating the absorbance intensity at 497 nm and by the color difference of **1**-PBFs after exposure. Therefore, even if as-prepared films have a lower sensitivity to BA vapors than the corresponding annealed films, unlike the latter they allow the detection of the IDLH value (300 ppm) established for this substance.

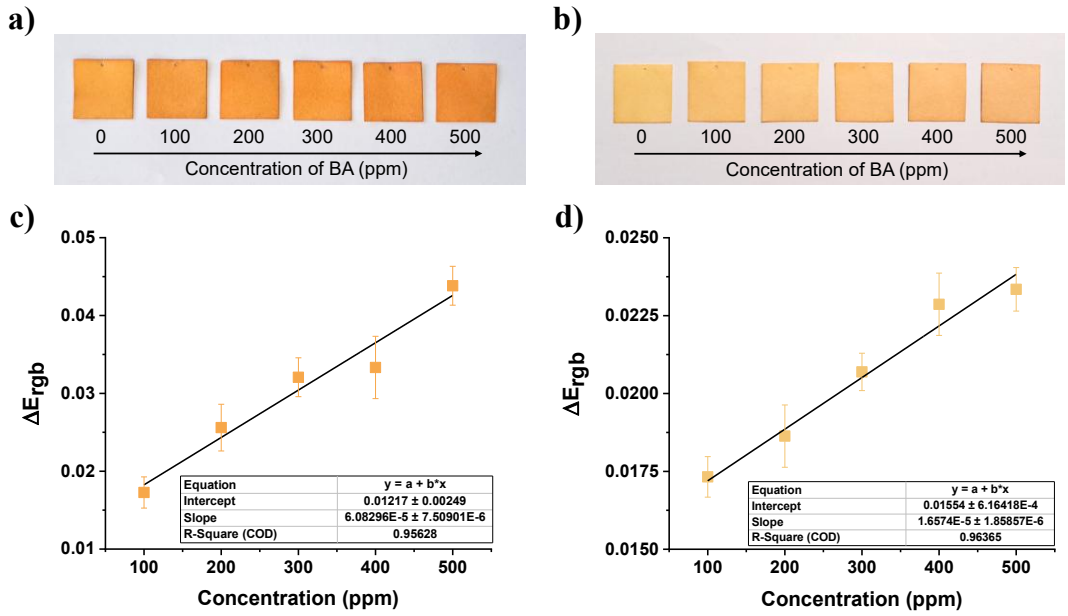

Figure 4.23. Photographic images of **1**-PBF5s **(a)** and **1**-PBF1s **(b)** under natural light after exposure to different concentrations of BA (range 0 – 500 ppm). Variation of mean ΔE_{rgb} values as a function of the concentration of BA vapors of **1**-PBF5s **(c)** and **1**-PBF1s **(d)**, and linear best fit in the dynamic range (weight given by data error bars).

4.5.3.5 Detection of BA vapors in semi-confined spaces from simulated leakage experiments

In order to assess the reliability of the vapochromic response of **1**-PBFs under conditions closer to practical use, a series of tests were carried out for simulating the accidental release of BA vapors in poorly ventilated or semi-confined spaces. For this purpose, the narrow glass tail of a sealed conical flask, containing 10 mL pure BA, was used as a model for simulating an accidental release of BA vapors within semi-confined spaces (Figure 4.24). Such experimental configuration can be regarded as a potential simulated leakage model of indoor pollution caused by the accidental release of volatile amines. In fact, the progressive diffusion of BA from a localized leakage point, and its detection over time, closely resembles the behavior of indoor contaminants in semi-confined spaces.

A **1**-PBF1 was placed at a certain distance (l = 60 cm) from the tail of the flask and its vapochromic response was monitored over time, while the release of BA vapors occurred through the tail of the glass, via a nitrogen stream (P = 0.5 bar) that forced the evaporation of pure BA (Figure 4.24). A naked-eye color change of **1**-PBF1 is observed after 30 s of exposure inside the semi-confined environment (Figure 4.24). A plausible quantitative estimation of the detected BA vapor concentration was further investigated by RGB color analysis of the films before and after the accidental BA release. RGB values, captured directly on the films using a Samsung Galaxy S23 smartphone camera under indoor illumination (*ca.* 200 lux), were normalized to the corresponding rgb values (Figure 4.24, eqs. 3.4 – 3.6), and, consequently, the ΔE_{rgb} was calculated for the exposed film, according to eq. 3.7. Interestingly, by means of the linear fit reported in Figure 4.20d, the ΔE_{rgb} calculated is

consistent with a BA concentration of about 4 ppm, close to the PEL–C established by OSHA for BA vapors (5 ppm).[263]

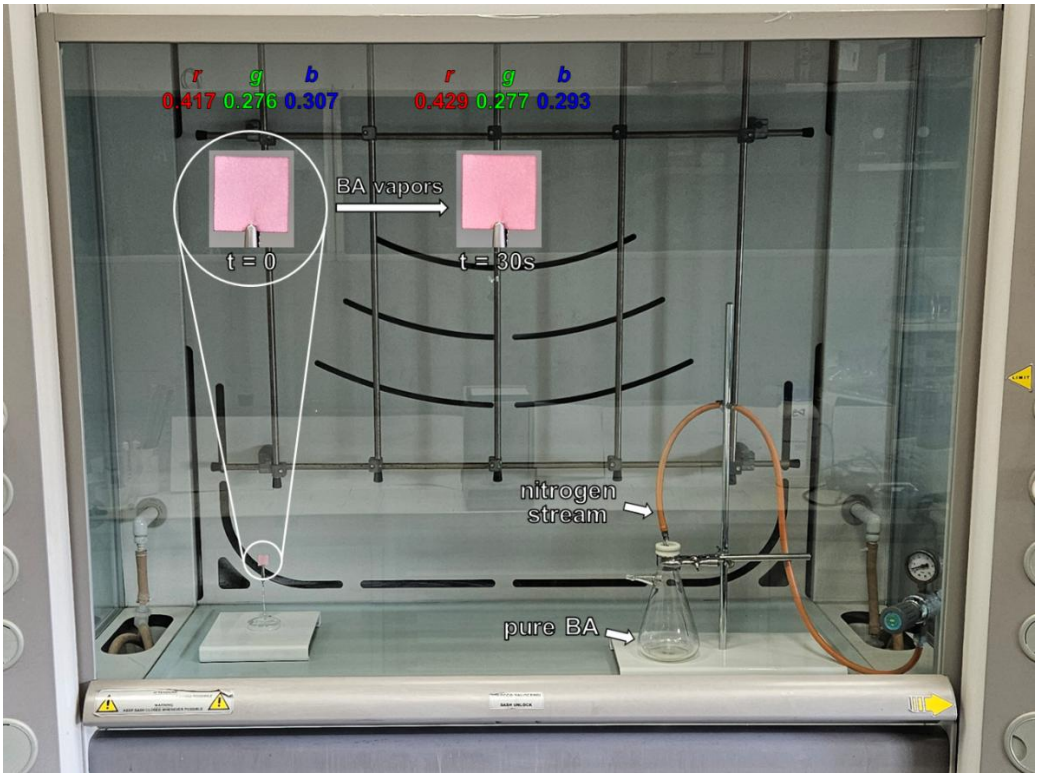

Figure 4.24. Experimental setup for simulating an accidental release of BA vapors within a semi-confined space in the presence of annealed **1**-PBF1s. Pure BA (10 mL) is contained in a sealed conical flask (volume = 500 mL). The conical flask is connected to a continuous nitrogen stream operating at 0.5 bar in order to force the evaporation of BA. The glass tail (diameter = 5 mm) of the conical flask acts out the escape of BA vapors. The annealed **1**-PBF1 is placed 60 cm from the BA steam outlet and monitored over time.

Similar simulated leakage experiments were carried out by using the as-prepared **1**-PBF1s. Changes in its rgb values of the film were monitored over time, with a progressive color change visible by naked-eye (Figure 4.25). The RGB color analysis of the as-prepared **1**-PBF1 before and after exposure, and using the linear fit reported in Figure 4.23d, allowed to estimate the BA vapor concentration. After 360 s of exposure inside the semi-confined environment, a value of approximately 250 ppm is reached, very close to the IDLH value established by NIOSH for BA vapors (300 ppm).[262]

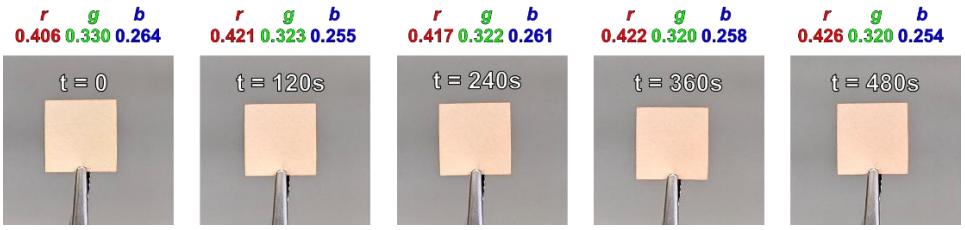

Figure 4.25. Photographic images of **1**-PBF1s and related rgb color changes after exposure to BA vapors over time inside a semi-confined space in a simulated leakage experiment (see Figure 4.24).

The results obtained from simulated leakage experiments indicate that both as-prepared and annealed **1**-PBF1s are suitable not only for detecting BA vapors under static exposure conditions, but also for detecting BA vapors in semi-confined environments, mimicking the accidental release and diffusion of a volatile amine, enabling the detection of the PEL-C and the IDLH value. Thus, these experiments demonstrate that **1**-PBF1s are suitable for the real-time detection of indoor amine contamination, with potential implications for safety monitoring in laboratories, industrial facilities, and other semi-confined work environments where primary amines are handled.

*4.5.4. Vapoluminescent Detection of Primary Diamine Vapors by **1**-PBFs*

In the previous sections, the optical response of annealed **1**-GBFs and **1**-PBFs (Sections 4.5.1.3 and 4.5.2.2, respectively) towards saturated vapors of EDA (13824 ppm at 23 °C), chosen as reference volatile diamine, has been reported in comparison to monotopic VOCs. In particular, the optical absorption and fluorescence spectra are completely different from those of all other N-VOCs studied. Therefore, from this starting point, further investigations on the vapochromic/vapoluminescent response of as-prepared and annealed **1**-PBF5s, prepared using the optimized procedure described in Section 4.5.2.1, after exposure to volatile aliphatic diamine vapors were considered.

*4.5.4.1. Discriminative vapochromic and vapoluminescent properties of **1**-PBFs towards mono- and diamine vapors*

The different optical properties (optical absorption and fluorescence emission) of as-prepared and annealed **1**-PBF5s before and after exposure to saturated EDA vapors were studied and compared with those after exposure to BA, as a reference volatile primary aliphatic monoamine. As shown in Figure 4.26a, the optical absorption spectrum of the as-prepared films is characterized by a broad absorption band centered at *ca.* 440 nm and an envelope between 300 and 400 nm. After exposure to saturated EDA vapors for 10 minutes, batochromism of the 440 nm band is observed and, even more interestingly, a new characteristic band appears at longer wavelength (λ = 638 nm). In contrast, exposure to saturated vapors of BA for 10 min involves an hyperchromism in the region between 300 – 400 nm, and the formation of two new absorption bands centered at 446 and 501 nm, respectively. Therefore, exposure to these volatile amines, namely EDA and BA, results in very different color changes, from yellow-orange to dark brown for EDA and red-orange for BA, respectively. Interestingly, the fluorescence emission of as-prepared **1**-PBF5s before and after exposure is also very different (Figure 4.26b). In particular, after exposure to EDA vapors a complete quenching of the initial fluorescence emission band at 600 nm of as-prepared **1**-PBF5s is observed, accompanied by the appearance of a new, very weak emission band at 665 nm. Instead, a new more intense band centered at 608 nm is observed after exposure to saturated vapors of BA. These fluorescence changes are reflected in the color changes observed with the naked eye under UV light (365 nm) after exposure to EDA and BA, like those observed under natural light.

In the case of annealed **1**-PBF5s (Figure 4.27a), an envelope between 300 and 420 nm and a broad feature absorption band at 560 nm are observed. After exposure to saturated vapors of EDA (5 min), the resulting absorption spectrum is quite similar to that obtained in the case of as-prepared **1**-PBF5s, with the formation of a new band at 638 nm, while exposure to BA vapors for the same exposure time leads to the formation of two new absorption bands centered at 452 and 501 nm, respectively.

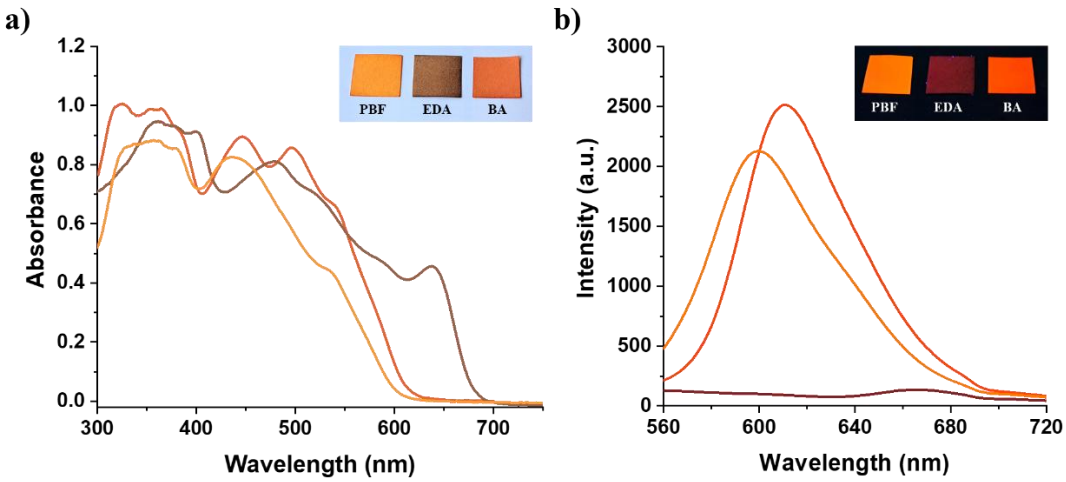

Figure 4.26. UV-vis reflectance **(a)** and fluorescence **(b)** spectra (λ_{exc} = 460 nm) of as-prepared **1**-PBF5s before and after exposure to saturated vapors of EDA and BA. Insets: photographic images of as-prepared **1**-PBF5s and exposed films under natural light (left) and under 365 nm light (right).

Moreover, annealed **1**-PBF5s are characterized by a color change from red-brown to dark brown (EDA) or red (BA) after exposure. Furthermore, the fluorescence spectra of the annealed **1**-PBF5s appear very different after exposure to EDA and BA vapors (Figure 4.27b). In particular, the emission band of the annealed **1**-PBF5s (λ_{em} = 644 nm) disappears completely in both cases but while exposure to EDA leads to the complete quenching of the fluorescence emission and the appearance of a very weak emission band at 665 nm, in the case of BA the formation of a new, more intense band centered at 608 nm is observed.

These results clearly show that as-prepared and annealed **1**-PBF5s are characterized by different optical behavior upon exposure to volatile primary aliphatic mono- or diamines. Furthermore, the same color change from yellow-orange (as-prepared films) or red-brown (annealed films) to dark brown is observed after exposure to saturated EDA vapors, which is consistent with the appearance of the new longer-wavelength (λ = 638 nm) absorption band after exposure. Finally, a significant quenching of fluorescence emission is obtained for both as-prepared and annealed **1**-PBF5s after exposure to EDA vapors, as never previously observed for all other classes of VOCs investigated.

The vapoluminescent properties of annealed **1**-PBF5s toward EDA vapors were also investigated using the same approach described previously (Sections 4.5.1.2 and 4.5.2.2). In particular, successive cycles of exposure to saturated EDA vapors were performed (Figure 4.28), followed by heating the film at 220 °C for 10 min. This temperature is necessary for complete desorption of EDA from the film, according to the TGA (vide infra, Section 4.5.5). After the first exposure/heating cycle, the fluorescence emission intensity of annealed **1**-

PBF5s is only partially restored. Furthermore, subsequent exposure of this film to EDA vapors allows to reach the same final state observed at the first exposure, but, again, a lower fluorescence emission intensity is obtained after heating.

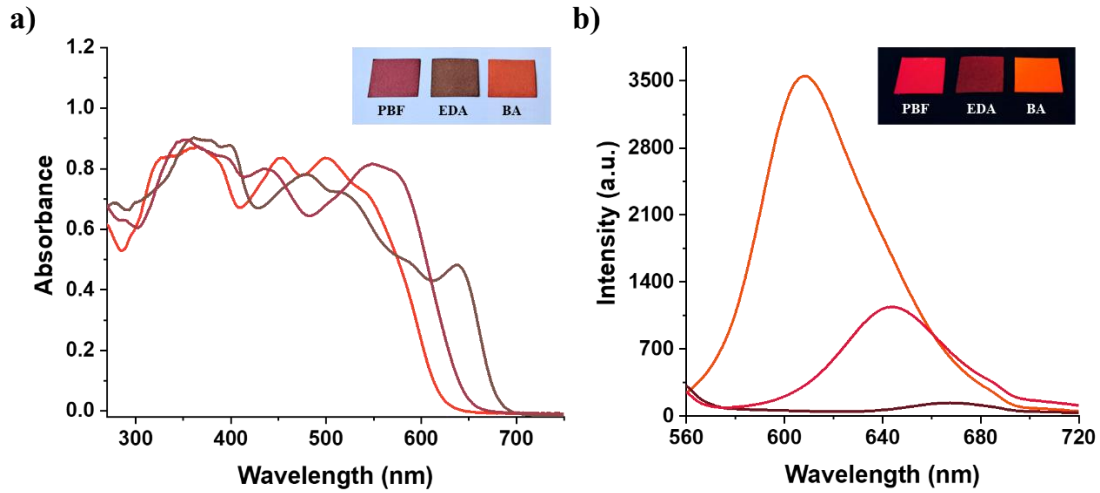

Figure 4.27. UV-vis reflectance **(a)** and fluorescence **(b)** spectra (λ_{exc} = 460 nm) of annealed **1**-PBF5s before and after exposure to saturated vapors of EDA and BA. Insets: photographic images of annealed **1**-PBF5s and exposed films under natural light (left) and under 365 nm light (right).

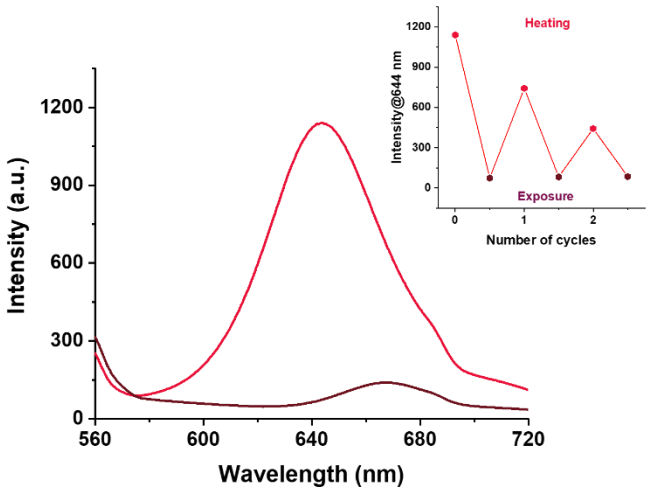

Figure 4.28. Fluorescence spectra (λ_{exc} = 460 nm) of annealed (red curve) and exposed (brown curve) **1**-PBF5s. Inset: fluorescence intensity changes at λ_{em} = 644 nm upon cycles of exposure to saturated vapors of EDA and subsequent thermal heating at 220 °C.

These experiments show only a partial restoration of the initial emission properties of annealed **1**-PBF5s after desorption of EDA vapors, in contrast to what was previously observed in the case of the monotopic BA (Section 4.5.2.2). Therefore, these results suggest that annealed **1**-PBFs can be used as chemodosimeter for the detection of EDA vapors.

4.5.4.2. Vapochromic and vapoluminescent properties to other volatile diamines

Based on the optical properties of **1**-PBFs observed in the presence of EDA vapors, further studies were conducted on the vapochromic/vapoluminescent response of as-prepared and annealed **1**-PBF5s by exposure to other volatile linear aliphatic diamines. In particular, optical absorption and fluorescence properties of both as-prepared and annealed films were explored by exposure to saturated vapors of 1,3-diaminopropane (DAPr), 1,4-diaminobutane (DAB), 1,5-diaminopentane (DAPe), which represent the most relevant volatile diamines, and then compared with the results obtained for EDA. The exposure time was set as 60 min for as-prepared films and 30 min for annealed films.

The reflectance spectra of as-prepared **1**-PBF5s after exposure to saturated diamine vapors show two new absorption bands centered at 458 and 503 nm for DAPr, the formation of a new band at 579 nm and a broader absorption band centered at *ca.* 458 nm after exposure to DAB, while in the case of DAPe negligible absorption changes are observed (Figure 4.29a). These results parallel the colors changes observed in films after exposure, from orange-yellow to brown (DAB) or red (DAPr and DAPe). On the other hand, fluorescence spectra show a quenching of the fluorescence emission of as-prepared **1**-PBF5s (λ_{em} = 600 nm) in the case of DAPr and DAB, accompanied by the formation of a new weaker emission band (617 and 624 nm, respectively) (Figure 4.29b). This behavior is similar to that observed upon exposure to EDA vapors, but with a less pronounced quenching of the fluorescence emission. Interestingly, for DAPe a more intense emission band is observed at 619 nm, which is very similar to the behavior observed in the case of BA.

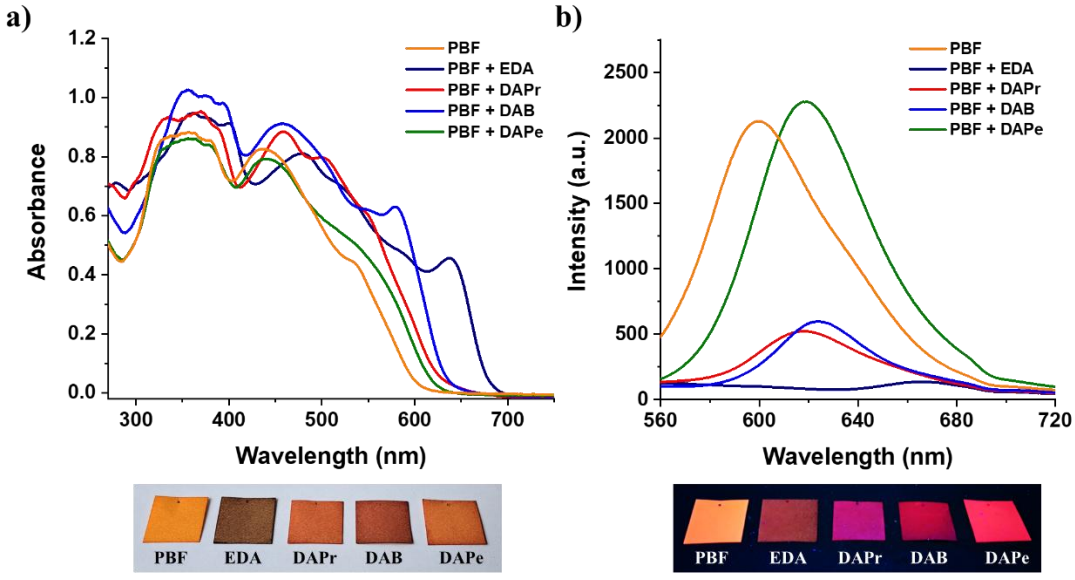

Figure 4.29. UV-vis reflectance **(a)** and fluorescence **(b)** spectra (λ_{exc} = 520 nm) of as-prepared **1**-PBF5s before and after exposure to saturated vapors of volatile linear aliphatic diamines. Bottom: photographic images of films under natural light (left) and UV light (right).

Analogous color changes are observed for annealed films after exposure to saturated vapors of these diamines compared with as-prepared films. Furthermore, similar reflectance spectra are obtained for DAPr and DAB, while a more intense red color (compared to the analogous as-prepared **1**-PBF5s after exposure) and the appearance of two new absorption

bands centered at 453 and 505 nm characterize the annealed **1**-PBF5s after exposure to DAPe (Figure 4.30a). In the latter case, both the color and the reflectance spectrum are very similar to those observed after exposure to BA vapors. Also in this case, for DAPr and DAB the quenching of the initial fluorescence emission of annealed films (λ_{em} = 644 nm) is observed, with the formation of a weaker emission band centered at 620 and 634 nm, respectively, while the formation of a new emission band at λ = 623 nm, characterized by an higher fluorescence intensity, is observed for DAPe (Figure 4.30b).

Thus, a similar optical behavior characterizes **1**-PBF5s after exposure to saturated vapors of EDA, DAPr, and DAB, with a relevant quenching of the fluorescence emission. On the other hand, different UV-vis reflectance spectra are found for as-prepared and annealed films upon exposure to DAPe, but with an enhancement of the emission intensity in both cases. Furthermore, among the series of diamines studied, very characteristic optical absorption and fluorescence properties are observed in the case of EDA, which allow it to be easily distinguished from other diamines under these conditions. It is important to emphasize that higher changes in fluorescence emission are observed for both as-prepared and annealed **1**-PBF5 films after exposure than for optical absorption. Therefore, the vapoluminescent properties of these films appear more favorable for subsequent comparisons of mono- and diamine vapor response and for quantitative detection of EDA vapors.

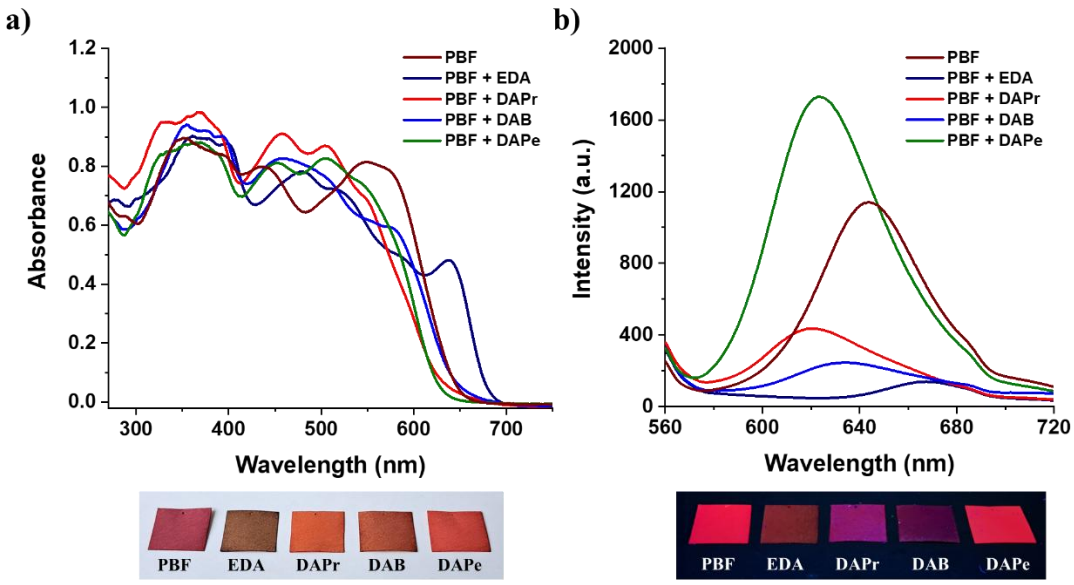

Figure 4.30. UV-vis reflectance **(a)** and fluorescence **(b)** spectra (λ_{exc} = 520 nm) of annealed **1**-PBF5s before and after exposure to saturated vapors of volatile linear aliphatic diamines. Bottom: photographic images of films under natural light (left) and UV light (right).

4.5.4.3. Vapoluminescent response towards volatile diamine vapors

Based on the results of the previous section, further investigations on the vapoluminescent response of as-prepared and annealed **1**-PBFs towards volatile aliphatic diamines were performed by exposure to specific vapor concentrations (100, 500, and 1000 ppm). For both as-prepared and annealed films, the obtained fluorescence emission strongly depends on the vapor concentration of the different diamines involved (Figure A16 and

Figure A17). Thus, for better comparison of the fluorescence response upon exposure, it is useful to consider the quenching efficiency (QE), calculated using the following formula:

$$QE = \left(1 - \frac{I}{I_0}\right) \times 100 \quad \textbf{(4.1)}$$

where I is the fluorescence intensity obtained after exposure, while I_0 is the initial fluorescence intensity for as-prepared or annealed **1**-PBFs, whose intensity values are considered in their maximum of emission.

Considering the as-prepared **1**-PBF5s, a very high QE is observed in the case of saturated vapors of EDA (QE = 96%) and progressively lower QEs are achieved for DAPr and DAB in the same conditions (75% and 71%, respectively), while an enhancement of the fluorescence emission is obtained for DAPe (Figure 4.31a). By decreasing the vapor concentration, a significant QE is observed at 1000 ppm for EDA and DAPr (44% and 27% respectively), while by decreasing to 500 ppm the fluorescence quenching becomes evident only in the case of EDA (QE = 20%). On the other hand, high QEs are observed for annealed films after exposure to saturated vapors of EDA and DAB, (approximately 75%), a QE value around 50% is observed for DAPr, while again an increase in fluorescence emission is obtained for DAPe. (Figure 4.31b). It is very interesting to note that high QEs are observed by decreasing the concentration of EDA, DAPr and DAB, however, at 100 ppm, the fluorescence emission quenching is relevant only in the case of EDA (QE = 57%), while negligible changes are obtained for all other diamines (QE < 10%).

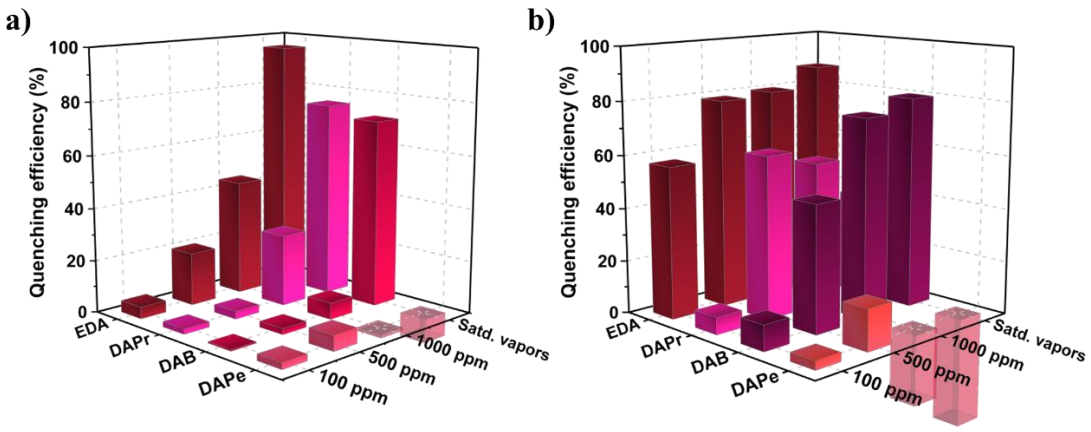

Figure 4.31. Fluorescence quenching efficiency of as-prepared **(a)** and annealed **(b)** **1**-PBF5s after exposure to different vapor concentrations of the involved aliphatic diamines. Negative values of QE correspond to an enhancement of the fluorescence emission.

These results demonstrate a relevant fluorescence quenching for as-prepared **1**-PBF5s at high EDA vapor concentrations (≤ 500 ppm), and a selective response of annealed **1**-PBF5s at low EDA vapor concentrations (≤ 100 ppm) among all other volatile aliphatic diamines. Thus, the sensing performances of as-prepared and annealed **1**-PBFs were explored in the presence of specific vapor concentrations of EDA.

4.5.4.4. Quantitative detection of EDA vapors

As discussed in the previous sections, very distinct optical absorption and fluorescence responses are observed for all diamines, and more pronounced changes are observed in the latter case. For this reason, the sensitive detection of EDA vapors was performed by fluorescence measurements using as-prepared and annealed **1**-PBF5s in the presence of specific concentrations of EDA.

From static exposure experiments of the as-prepared **1**-PBF5s to EDA vapors (from 100 up to 5000 ppm) a gradual batochromic shift and quenching of the emission band centered at 600 nm is observed, until the formation of a less intense emission band centered at 665 nm for saturated EDA vapors (Figure 4.32a). The quenching of the fluorescence intensity is almost linear up to 1000 ppm (Figure 4.32b), until reaching a saturation point around 5000 ppm. Furthermore, under UV light, a gradual color change from orange to dark brown is observed with the naked eye (Figure 4.32c). It is very interesting to note that 1000 ppm corresponds to the IDLH value established by NIOSH for EDA,[271] therefore it can be easily detected by a simple evaluation of the emission intensity by exposure of the as-prepared films.

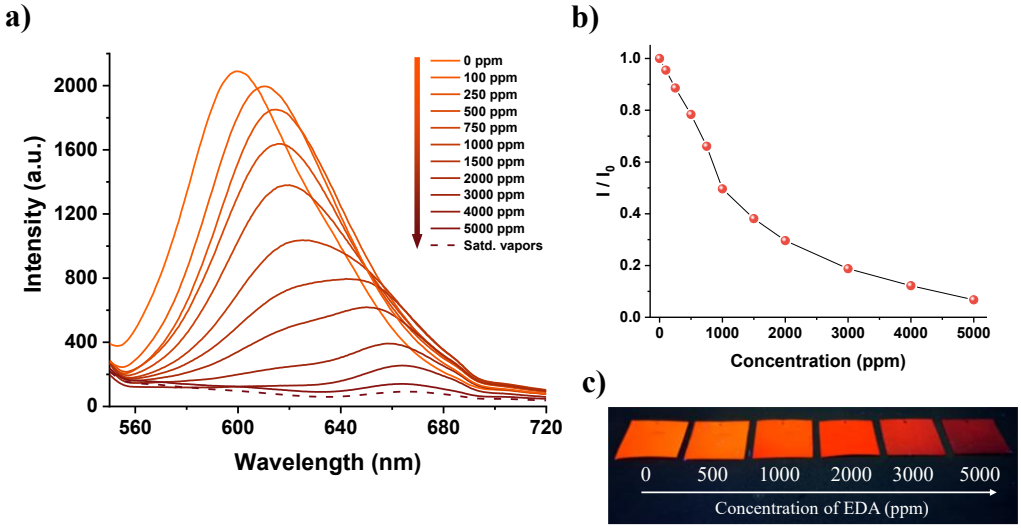

Figure 4.32. **(a)** Fluorescence spectra of as-prepared **1**-PBF5s exposed to EDA vapors (λ_{exc} = 520 nm). Each spectrum was recorded in an independent experiment. **(b)** Fluorescence intensity ratio of the maximum of emission after (I) and before (I_0) exposure as a function of the concentration of EDA. **(c)** Photographic images of as-prepared **1**-PBF5s under 365 nm light upon exposure to different concentrations of EDA (range 0 – 5000 ppm).

On the other hand, performing quantitative detection of EDA vapors using annealed **1**-PBF5s yields very different results compared to as-prepared films (Figure 4.33a). From 10 to 100 ppm the fluorescence emission band remains centered at 644 nm, while a bathochromic shift of the band is achieved after 150 ppm, until 1000 ppm, with the appearance of a new less intense emission band centered at 665 nm. The reaching of the saturation point is observed around 250 ppm of EDA (Figure 4.33b). The gradual quenching of the fluorescence emission is accompanied by a color change from red to dark-brown, observable under UV light (Figure 4.33d). More interestingly, a linear response upon exposure to EDA vapors is observed in the range 0 – 100 ppm (Figure 4.33c), with a very good linearity coefficient (R^2 = 0.9967). Consequently, an estimated LOD of 6.6 ppm was calculated in this dynamic linear

range, which is lower than the PEL–TWA of 10 ppm established by OSHA for EDA vapors.[272]

Comparing these results with the two reported quantitative data on optical chemosensors for the sensitive detection of EDA vapors (Table 4.4),[330,331] the annealed **1**-PBF5s show good detection performance. Although these literature data[330,331] also report selective detection of EDA over other amines, the currently **1**-PBFs are obtained using a simpler and less time-consuming procedure. Furthermore, the combination of as-prepared and annealed **1**-PBFs can lead to the detection of EDA vapors in a wide range of concentrations (from tens to thousands ppm), that also include the IDLH value reported by NIOSH,[271] allowing the estimation of the human health risk in case of long/short exposure times to this substance. From these features, it is evident that as-prepared and annealed **1**-PBFs represent a very unique example of sensor for the selective and sensitive detection of EDA vapors.

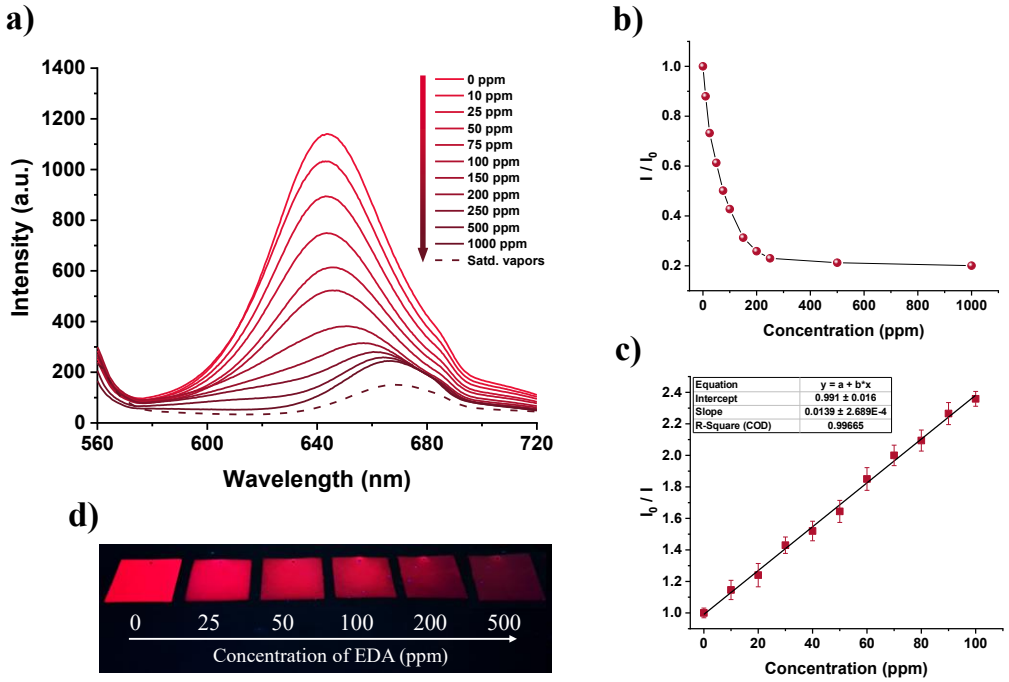

Figure 4.33. **(a)** Fluorescence spectra of annealed **1**-PBF5s exposed to EDA vapors (λ_{exc} = 520 nm). Each spectrum was recorded in an independent experiment. **(b)** Fluorescence intensity ratio of the maximum of emission after (I) and before (I_0) exposure as a function of the concentration of EDA. **(c)** Linear best fit in the dynamic linear range from 0 up to 100 ppm of EDA (weight given by data error bars). **(d)** Photographic images of annealed **1**-PBF5s under 365 nm light upon exposure to different concentrations of EDA (range 0 – 500 ppm).

*4.5.5. Sensing Mechanism of **1**-PBFs for the Detection of Primary Mono- and Diamine Vapors*

The very interesting optical properties observed for the **1**-PBFs give the possibility to distinguish primary aliphatic mono- and diamines, especially in the cases of BA and EDA, therefore further investigations were conducted to clarify and propose a sensing mechanism. In particular, solid-state investigations, such as XRD measurements, were performed on both

as-prepared and annealed PBFs, while TGA was conducted on dried solid **1**, before and after exposure to BA and EDA vapors (Figure 4.34).

The XRD patterns recorded for as-prepared films show a sharp peak at 2θ = 3.20° and a broad peak at 2θ = 6.60°, while two diffraction peaks at 2θ = 3.60° and 6.25°, respectively, are observed for the annealed films (Figure 4.34a). In comparison, the diffraction peaks associated with the annealed PBFs are shifted by approximately 0.40° compared to those observed for the as-prepared films. This difference in XRD patterns is related to the different crystallographic structure of the as-prepared and annealed PBFs. In particular, the XRD pattern of as-prepared films is consistent with a highly organized lamellar structure (H-aggregates), while after thermal treatment, an irreversible phase transition lead to the formation of a hexagonal columnar structure (J-aggregates).[240]

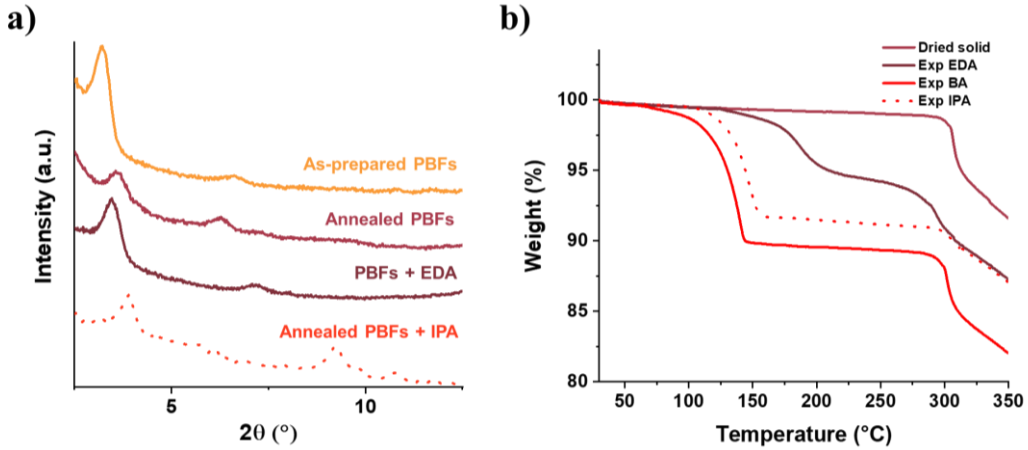

Figure 4.34. **(a)** Low-angle XRD patterns of as-prepared and annealed **1**-PBF5s before and after exposure to saturated vapors of EDA. Identical XRD patterns are observed for both types of films after exposure to EDA vapors. **(b)** TGA of dried solid **1** before and after exposure to saturated vapors of BA and EDA. XRD and TGA after exposure to saturated IPA vapors (dotted line) is reported for comparison.

After exposure to saturated vapors of EDA (5 min), both as-prepared and annealed films reach almost the same final state, that is characterized by a sharp peak centered at 2θ = 3.45° and a broad peak at 2θ = 7.15°. On the other hand, comparing these results with XRD pattern of annealed PBFs exposed to saturated IPA vapors, as previously reported,[240] yields a very different XRD pattern. In particular, three main peaks at *ca.* 2θ = 3.90°, 9.24°, and 10.76° are observed in the latter case.

These results suggest the formation of two different crystallographic structures upon chemisorption of mono- and diamine vapors using as-prepared or annealed **1**-PBFs. Furthermore, from XRD patterns it can be hypothesized the existence of a self-assembled structure with higher symmetry after the chemisorption of EDA vapors, compared to that formed after exposure to IPA. A possible explanation could be the formation of intermolecular adducts in a molar ratio of 2:1, where two molecules of **1** interact with one molecule of the diamine, instead of the formation of monomeric adducts in a molar ratio of 1:1 in the case of monoamines.

To demonstrate this hypothesis, TGA of the dried solid **1** was performed before and after exposure to BA and EDA, under the same conditions used for the paper films (Figure

4.34b). No relevant weight loss is observed until 300 °C for dried solid **1**, while different TGA curves characterize the solid after exposure to saturated vapors of the two volatile amines. In particular, for BA vapors a weight loss of 9.5% is obtained at about 140 °C, while for EDA a weight loss of 4.5% is obtained at about 220 °C. For comparison, the thermogram of the dried solid **1** exposed to IPA vapors shows a weight loss of 7.5% at about 140 °C.[240]

The weight loss observed after exposure to BA vapors (9.5%) is consistent with the formation of monomeric adducts, *i.e.*, **1**·BA adducts (calculated 9.3%), analogously to what was previously reported in the case of IPA vapors (calculated 7.62% *vs.* observed 7.5% for **1**·IPA adducts),[240] while the formation of intramolecular (**1**)$_2$·EDA di-adducts (calculated 4.0%) likely occurs in the case of exposure to EDA vapors.

The overall results not only demonstrate the formation of stoichiometric monomeric adducts or di-adducts, after chemisorption of mono- or diamines respectively, but can also explain the different optical behavior leading to their discrimination, related to their different crystallographic structure. It is therefore possible to schematically represent the formation of the two different adducts formed in the presence vapors of a monotopic or ditopic amine, as shown in Scheme 4.1.

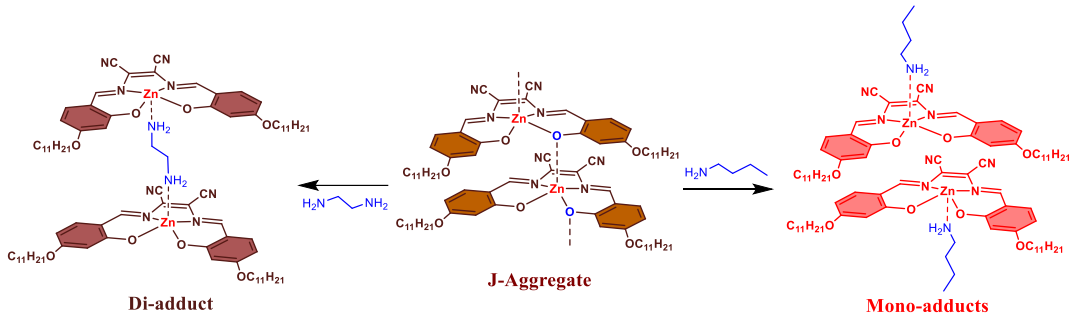

Scheme 4.1. Proposed sensing mechanism for the formation of mono- and di-adducts upon chemisorption of volatile aliphatic mono- or diamine vapors to aggregates of complex **1**, respectively.

4.6. Conclusion

In this chapter, the development of a novel molecular chemosensor on paper films based on a Zn(salmal) complex, **1**, which exhibits vapochromic and vapoluminescent properties is reported. First, the appropriate choice of the substrate and the optimization of the deposition conditions for the preparation of films were studied. For glass substrates, the drop-casting technique was used to obtain GBFs with good optical uniformity. Then, the vapochromic and vapoluminescent properties of the as-prepared and annealed GBFs were achieved by exposure to saturated vapors of BA, as a reference volatile Lewis base. Also, exposure of annealed GBFs to saturated vapors of different classes of VOCs showed high variations in both optical absorption and fluorescence spectra, especially for N-VOCs and O-VOCs. Subsequently, films of **1** were obtained and optimized on paper substrates. **1**-PBFs prepared by the dip-coating approach, according to an optimized procedure and kept under appropriate storage conditions before their use, are characterized by superior fluorescence repeatability and uniformity compared to **1**-GBFs, as a key prerequisite for the quantitative detection of VOCs. Thus, exposure of annealed **1**-PBFs to specific concentrations of VOCs show a selective fluorescence response toward low vapor concentrations (50 ppm) of volatile

primary amines, such as BA and AN. Only slight changes in the fluorescence response of annealed **1**-PBFs to defined BA vapor concentrations are observed in the relative humidity range of 40 – 60% and as a function of temperature and exposure time.

Quantitative detection of BA vapors from fluorescence measurements using annealed **1**-PBFs results in a linear dynamic range of 0 – 50 ppm and in a calculated LOD of 2.0 ppm, below the 5 ppm PEL–C established by OSHA for BA vapors. Furthermore, fluorescence measurements of annealed **1**-PBF allow estimating the exposure limit for BA (IDLH value of 300 ppm defined by NIOSH). A very high selectivity of annealed **1**-PBFs to BA vapors is obtained by competitive experiments based on the comparison of the fluorescence response after exposure to other volatile aliphatic monoamines.

Optical absorption changes of **1**-PBFs also allowed the colorimetric selective detection of BA vapors. In particular, the color changes after exposure of annealed **1**-PBFs, estimated both by reflectance changes or appropriate RGB color analysis of films after vapor exposure, also enable quantitative detection of BA vapors below their PEL-C value. On the other hand, as-prepared **1**-PBFs allow to detect the IDLH vapor concentration of 300 ppm BA by evaluating the absorbance changes or color difference. Therefore, the combination of as-prepared and annealed PBFs allows for accurate detection of PEL-C and IDLH values for BA vapors, and this, combined with RGB color analysis, could represent a simple and efficient detection method for on-site detection of BA vapors.

Simulated leakage experiments of BA vapors indicate that both as-prepared and annealed **1**-PBF1s are useful in systems that mimic the accidental release and diffusion of volatile amines in semi-confined environments, enabling the detection of the PEL-C and the IDLH value, thus demonstrating their suitability for the real-time detection of indoor amine contamination, with potential implications for safety monitoring in laboratories, industrial facilities, and other semi-confined work environments where primary amines are handled.

A very distinct optical behavior is observed after exposure of as-prepared and annealed **1**-PBFs to saturated vapors of mono- and diamines, BA (fluorescence enhancement) and EDA (fluorescence quenching), a necessary condition for their discriminative detection. Therefore, exposure of **1**-PBFs to saturated vapors of volatile aliphatic diamines (NH_2-$(CH_2)_n$-NH_2; n = 2–5) shows dramatic changes in the optical properties of both as-prepared and annealed films, and a quenching of the fluorescence emission for each diamine involved, except DAPe. However, exposure of annealed **1**-PBFs to low vapor concentrations (≤ 100 ppm) shows a selective fluorescent response for EDA vapors. Sensitive detection of EDA vapors using as-prepared films allows their detection over a wide concentration range (100 – 5000 ppm), including even the IDLH value (1000 ppm), while a LOD value (6.6 ppm), lower than the PEL (10 ppm), is obtained for annealed films in a range up to 100 ppm. A sensing mechanism for the detection of mono- and diamine vapors by films of **1** is also proposed based on XRD measurements of **1**-PBFs and TGA of powders of **1** before and after exposure.

Overall, PBFs of complex **1** represent the first example of a Zn(salen)-type, molecular-based sensor for the discriminative and sensitive detection of volatile primary mono- and diamine vapors, both by evaluating their optical absorption (color) or fluorescence changes, with great advantages of simple preparation and high temporal stability in the perspective of practical application for real-time monitoring of dangerous amine vapors in relevant working environments.

Chapter 5

Vapochromic Detection of Pyridine Vapors

Contents

5.1. Introduction

Heterocyclic amines are a class of compounds characterized by at least one carbon ring where one or more carbon atoms are replaced by nitrogen atoms. They can be classified on the basis of their chemical structure in aliphatic (*e.g.,* pyrrolidine) and aromatic (*e.g.,* pyridine) heterocycles. The main source of exposure to heterocyclic aromatic amines is the consumption of well-cooked food,[344,345,346] in particular meat.[347,348,349,350] In fact, more than 30 different heterocyclic aromatic amines have been identified in protein-rich cooked food.[344,351] They are also produced in meat cooked at low temperatures for long periods of time.[351,352] They can also derive from the burning of tobacco, together with polycyclic aromatic hydrocarbons.[351] Ingestion or exposure to high concentration of these substances can lead to adverse effects on human health, such as cancer, and several types of tumors (*e.g.,* colon, liver, prostate, breast, skin, *etc*.).[349,353,354,355,356]

Among them, pyridine (Py) is a volatile heterocyclic aromatic amine widely involved in industrial processes as a reactant, solvent or intermediate in several synthetic routes.[357,358,359] In particular, it is used for the synthesis of insecticides, herbicides, fragrances, pharmaceuticals, dyes, rubber, *etc*. The worldwide production of Py exceeds 20,000 tons per year, and environmental analyses of emissions from some manufacturing industries have revealed high concentrations of Py vapors (hundreds to thousands of ppm).[360] In this context, some industrial processes, including coal gasification, steel manufacture, processing of oil shale, *etc*. are responsible for the release of Py vapors into the environment.

Py is toxic by ingestion, inhalation and skin absorption. Short-term exposure to Py vapors (tens ppm) depresses the nervous system and can cause headache, dizziness, loss of appetite, salivation, nausea and lack of coordination.[361,362] Furthermore, prolonged exposure to Py vapors may result in damage of heart, kidney, and liver. Py is also considered as a carcinogenic and teratogenic compound.[363,364] Because of its toxicity, the NIOSH established a concentration of 1000 ppm as the IDLH value for this substance,[365] while the PEL–TWA value established by OSHA corresponds to 5 ppm.[366]

Therefore, the release of Py vapors into the environment poses significant risks to environmental safety and human health.[367] Therefore, selective and sensitive detection of Py vapors over a wide concentration range is not only desirable, but essential to mitigate exposure risks.[368]

5.2. Vapor-Phase Detection Methods for Pyridine vapors

In recent years, different types of chemosensors have been developed for the detection of Py vapors. These systems are based on small molecules,[369,370,371] perovskite functional dyes,[372] metal-organic frameworks,[373,374] supramolecular organic frameworks,[375] fullerenes,[376] nanoparticles,[377] hybrid polymeric materials,[378,379] polyazobenzenes,[380] and cationic conjugated polymers.[381] Among these various classes of chemosensors, vapochromic/vapoluminescent materials represent a highly desirable alternative for the rapid, on-site detection of Py vapors.[128,382,383,384,385,386,387,388] The main advantage of their use is clearly the ability to undergo color changes, visible even to the naked eye, without the need for complex instrumentation. However, most of reported optical and

vapochromic/vapoluminescent chemosensors do not allow quantitative detection of this substance. Literature data of optical chemosensors involving the qualitative detection of Py vapors are collected in Table 5.1, while those involving various detection methods for sensitive detection of Py vapors are reported in Table 5.2.

Table 5.1. Literature data of optical chemosensors for the qualitative detection of Py vapors.

Material	Substrate	Detection method	Selectivity Studies	Exposure Method	Ref
Organic compound	Glass	Optical absorption	not available	Dynamic	371
Perovskite dye	Glass	Colorimetric and fluorescence	not available	Dynamic	372
Fullerene	Au-electroded quartz	Piezoelectric	no	Static	376
Au nanoparticles	Glass capillary	Surface enhanced Raman scattering	not assessed	Static	377
Polyazobenzene		Colorimetric	no	Static	380
Porphyrins	PVC and mica	Optical absorption and fluorescence	yes	Static	383
Metal complex	Glass	Fluorescence	not assessed	Static	128
Metal complex		Optical absorption	yes	Static	384
Metal complex		Color change	yes	Static	385

Referring to colorimetric quantitative detection methods of Py vapors under static conditions, Wang *et al*. reported a zinc porphyrin-containing polyimide (ZPCPI) nanofibrous membrane characterized by vapochromic properties.[387] ZPCPI nanofibers were prepared by imidization of the as-spun copoly(amic acid) nanofibers, as appropriate precursors of ZPCPI nanofibers, by heating step by step to increasing temperatures (80 °C (0.5 h), 160 °C (1 h), and 250 °C (4 h)) under nitrogen atmosphere. Then, the ZPCPI nanofibrous membrane was deposited on a clean glass cover slide and placed in a sealed testing chamber. The sensing performance of the ZPCPI membrane was first evaluated in the presence of 30 ppm of Py vapors. Under these conditions, a color change from reddish brown to olivine is observed, and a bathochromic shift of the Soret band and a red-shift of the Q-bands are also achieved in the corresponding solid state absorbance spectra, with a calculated LOD of 0.041 ppm. Furthermore, significant changes in fluorescence emission are observed upon exposure to different concentrations of Py vapor.

Elosua *et al.* developed an optical fiber sensor based on a vapochromic 1D β-$Co(py)_2Cl_2$ complex.[388] This complex shows a blue-violet color as powder, and its color changes to pink-white in the presence of Py vapors. In order to fix this material on the cleaved end fiber of the sensor, sensor head was immersed in a THF solution containing the vapochromic complex, poly vinyl chloride (PVC), and tributylphosphate. Then, a thermal curing process

was performed by placing the sensor head into an oven at 80 °C for 15 min. Fabrication factors such as the number of layers and the dipping speed were optimized on the basis of the optical absorption spectra and reflected optical signal of sensor heads exposed to 66 ppm of Py. A linear dynamic range of response between 18 and 66 ppm was achieved, with a calculated LOD of 1 ppm.

Table 5.2. Literature data of chemosensors for the quantitative detection of Py vapors.

Material	Detection method	Linear Range (ppm)	LOD (ppm)	Selectivity Studies	Exposure Method	Ref
Metalated phthalocyanine	Chemiresistive	1 – 3	0.0079	no	Dynamic	369
Organic compound	Chemiresistive	0.375 – 7500	0.375	no	Dynamic	370
Hybrid polymeric material	Chemiresistive	28 – 138	not available	yes	Dynamic	379
Metal-organic framework	Piezoelectric	5 – 50	1.603	yes	Static	373
Metal-organic framework	Piezoelectric	0.3 – 25	0.04	yes	Static	374
Hybrid polymeric material	MZI waveguide	0 – 400	0.476	yes	Static	378
Supramolecular organic framework	Fluorescence	not available	5	yes	Static	375
Conjugated polymer	Fluorescence	not available	33	yes	Dynamic	381
Copper(I)-cluster	Fluorescence	2000 – 12000	344	yes	Static	382
Metal complex	Fluorescence	1000 – 10000	722	yes	Static	386
Metallo-porphyrin	Colorimetric and fluorescence	0 – 50	0.041	yes	Static	387
Metal complex	Optical fiber	18 – 66	1	not available	Static	388

5.3. Properties of the Zn(salmal) Complex **2**

Recently, a Zn(salmal) complex, **2**, has been reported by Di Bella *et al.* for its deaggregation and transmetalation properties in solution,[227,228] and, more interestingly, for its peculiar thermochromic and vapochromic properties in solid state.[243]

The presence of aggregates/adducts of **2** was demonstrated by NMR measurements using coordinative and non-coordinative solvents, namely DMSO-d_6 and $CDCl_3$, respectively.[227] The significant shift of proton signals observed on passing from DMSO-d_6 to $CDCl_3$ are consistent with the existence of 1:1 adducts, **2**·DMSO-d_6, in the coordinating solvent, while formation of dimeric aggregates in a solution of the non-coordinating $CDCl_3$ are observed, as previously found for analogous Zn(salmal) derivatives. Also, the

deaggregation properties of **2** were investigated by monitoring the UV-vis optical absorption spectrum of a $CHCl_3$ solution of **2** after the addition of Py or IPA (Figure 5.1). A color change of the solution from red-wine to indigo is observed in both cases.

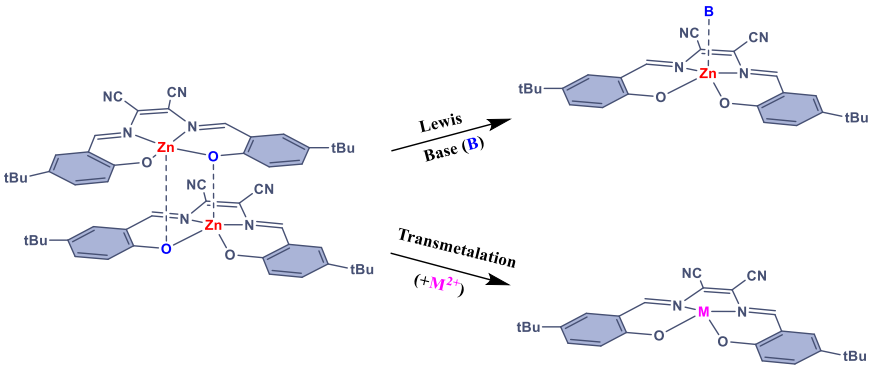

Figure 5.1. Schematic representation of deaggregation of **2** in the presence of a Lewis base and transmetalation with M^{2+} ions.

Then, the transmetalation ability of **2** towards the most common divalent and some trivalent cations in relation to the stability of the starting adduct was considered. Initially, the occurrence of transmetalation was achieved immediately after the addition of stoichiometric amounts of aqueous solutions of nitrate salts to ACN solutions of **2**. Peculiar changes in the optical absorption spectrum of **2**, consistent with transmetalation, are observed only in the case of the addition of $Cu(NO_3)_2$ (Figure 5.1). The transmetalation properties of complex **2** have been usefully exploited for the selective detection of Cu^{2+} ions in aqueous solution.[228]

The unique thermochromic and vapochromic behavior of complex **2** has also been recently reported.[243] The pristine solid of **2** shows a dark brown color after drying and becomes red brown when left in air. The red brown solid heated in an oven for at 150 °C shows a thermochromism (color change from red-brown to gray) associated with a phase transition. The XRD diffractograms of the red-brown and gray solids are in accordance with a tetragonal *P4/mmm* and orthorhombic *Pmmm* space groups, respectively, as results from the Rietveld refinement analysis of experimental XRD patterns. However, the gray solid returns red- brown by cooling in air. This behavior is related to the presence of water molecules as it was demonstrated by TGA (3.6% loss *vs.* calcd. 3.5%) and attenuated total reflection−Fourier transform infrared (ATR− FTIR) measurements. However, the gray solid obtained from red-brown solid heated at 150 °C and then cooled under a nitrogen atmosphere, or by solvent evaporation from a THF solution of **2** under anhydrous conditions remains unchanged. In fact, a flat thermogram is obtained for the DSC of the gray solid in an investigated temperature range from 40 to 200 °C, and no significant weight loss until the decomposition temperature (onset, 250 °C) is observed from TGA of the solid. Therefore, the gray solid obtained under anhydrous conditions does not show any thermochromism and/or absorption of water molecules. Again, an orthorhombic *Pmmm* space group, consistent with a dimeric structure, results from the Rietveld refinement analysis of the gray solid prepared by solvent evaporation under anhydrous conditions.

Cast films were prepared by drop-casting of a THF solution of **2** onto glass substrates.[243] A red brown color of the films is observed after the complete evaporation of the solvent in air, while blue gray films are obtained after the evaporation of the solvent under anhydrous conditions. Furthermore, blue gray films show a distinctive optical response upon exposure to saturated vapors of some volatile N–VOCs and O–VOCs. In particular, an irreversible color change from gray to yellow is observed upon exposure to saturated vapors of primary aliphatic amines, a red brown color is obtained upon exposure to secondary and tertiary aliphatic amines, while a vapochromic behavior with a significant color change from gray to purple, associated with the formation of stoichiometric 1:1 adducts, is achieved after exposure to saturated vapors of Py (Figure 5.2).

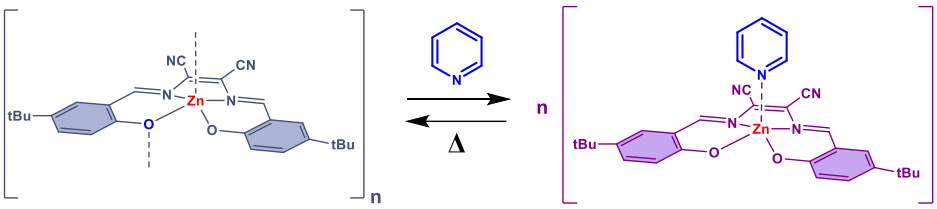

Figure 5.2. Vapochromic behavior of complex **2** upon exposure to saturated Py vapors.

The interesting vapochromic properties of cast films of **2** towards some saturated VOC vapors represent good starting points for further investigations on the potential application of this molecular material as a chemosensor for the sensitive and selective detection of VOCs having Lewis basicity.

5.4. Aim of the Study

This chapter describes the development of a molecular material based on a Zn(salen)-type complex for the selective and sensitive detection of Py vapors. In particular, the Zn(salmal) complex, **2**, having *t*-but groups (-C_4H_9) as lateral substituents was further investigated for its known vapochromic properties.

Based on the optimized procedure described in Section 3.3.2, the preparation of paper-based films of **2** (**2**-PBFs) under anhydrous conditions was first achieved and the appropriate storage conditions for the successive studies were investigated.

The vapochromic properties of **2**-PBFs were initially investigated by exposure to saturated vapors of different VOCs. Exposure to defined vapor concentration (1000 ppm) was also considered for studies on the sensitive detection of Py, as reference volatile heterocyclic aromatic amine, among the other investigated VOCs. Then, their quantitative detection was performed by static exposure of **2**-PBFs to specific Py vapor concentrations.

The corresponding color changes after exposure were analyzed by UV-vis reflectance spectra and RGB color analysis. Furthermore, the selective response of **2**-PBFs to Py compared to other VOCs involved was demonstrated, also considering analogous heterocyclic amines.

5.5. Results and Discussion

5.5.1. Preparation Procedure and Storage Conditions of **2**-PBFs

2-PBFs were prepared using the optimized procedure described in Section 4.5.2.1, with minor modifications. In particular, complex **2** was deposited by dipping paper substrates for few seconds into THF solutions of **2**, having two different concentrations, 1.0×10^{-3} M and 4.0×10^{-4} M, under anhydrous conditions, to prepare films named **2**-PBF1 and **2**-PBF4, respectively. The dipping procedure and the successive evaporation of the solvent were conducted at room temperature (22 ± 3 °C) into a round flask under nitrogen atmosphere. During the evaporation of the solvent the films were kept horizontal. Gray films having different color tone (lighter color in the case of diluted THF solution) were obtained after the complete evaporation of the solvent. This procedure ensures optical homogeneity and repeatability of the films, as a fundamental prerequisite for the subsequent quantitative studies.

First, the color stability of films under different lighting and relative humidity conditions was investigated. Initially, the effect of different illumination levels (50, 200, 1500 lux) was explored on **2**-PB1 films, stored in round flasks at room temperature (22 ± 3 °C) in a nitrogen atmosphere.

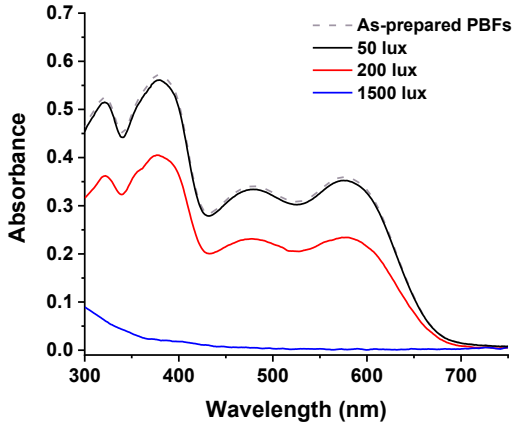

Figure 5.3. UV-vis reflectance spectra of as-prepared **2**-PBF1s stored under nitrogen atmosphere after three weeks of exposure to different illumination conditions. The UV-vis reflectance spectrum of freshly-prepared **2**-PB1 films (dotted line) is reported as reference.

UV-vis reflectance measurements of **2**-PBF1s stored in the dark (50 lux) show no significant changes up to one month. On the other hand, a significant reduction in the intensity of the reflectance spectra is observed for films exposed to light (200 lux), with a more marked effect in the case of the highest illumination level (1500 lux), also accompanied by a complete discoloration of films after three weeks in the latter case (Figure 5.3). These results suggest that **2**-PBF1s should remain stable for several months if stored in the dark, at room temperature and under inert atmosphere.

Based on these results, the effect of different RH values on **2**-PBF1s stored in the dark was then evaluated (Figure A18). For films stored at RH ≤ 50 %, small changes are observed in the region between 300 – 400 nm (measurements up to one month), while a significant

reduction in the absorbance intensity of the films stored at higher RH (> 70 %) is observed only after a few days. Similar results were also obtained in the case of **2**-PBF4s.

In summary, **2**-PBFs show sufficient stability under inert atmosphere and can be stored even under average indoor conditions, *i.e.,* room temperature (22 ± 3 °C), RH (50 ± 10 %), and low lighting levels (< 500 lux), allowing their use in real-world applications.

5.5.2. Vapochromic Response of **2**-PBFs to VOCs

Given the interesting vapochromic properties of the solid complex **2** and/or its cast films in the presence of VOCs,[243] they were further explored using PBFs prepared by the procedure described above (Section 5.5.1).

The optical response of **2**-PBF1, towards several volatile compounds, representative of the principal classes of N–VOCs and O–VOCs, was initially evaluated under saturated vapors condition. In particular, the following volatile compounds were chosen as prototypes of N–VOCs and O–VOCs: BA (primary amines); DEA (secondary amines); TEA (tertiary amines); Py (heterocyclic aromatic amines); DMF (ammides); ACN (nitrile compounds); MeOH (alcohols); Et_2O (ethers); ACE (ketones); THF (oxygenated heterocycles); AcOEt (esters).

The UV-vis reflectance spectrum of as-prepared **2**-PBF1s shows two absorption bands in the region between 300 and 400 nm (322 and 383 nm, respectively), and two defined bands in the visible region, centered at 480 and 575 nm, respectively, responsible of its gray color (Figure 5.4). Distinctive color and reflectance spectral changes are observed after exposure to saturated vapors of the involved N–VOCs and O–VOCs for 15 min.

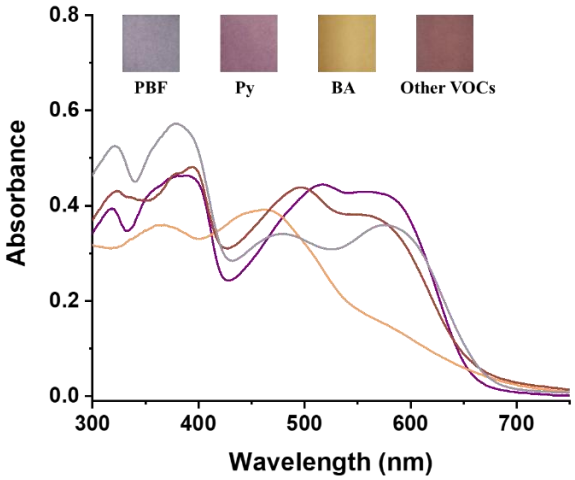

Figure 5.4. UV-vis reflectance spectra of **2**-PBF1s exposed to saturated vapors of N-VOCs and O-VOCs. Inset: photographic images of pristine **2**-PBF1s and after exposure to VOCs under natural light.

In particular, for BA vapors a change from gray to yellow is observed, accompanied by the appearance of two broad bands centered at 363 and 454 nm respectively, while for Py vapors a purple color is observed accompanied by hypochromism in the region between 300 – 400 nm, with the formation of a new, more intense band at 516 nm and an increase in the intensity of the band at 575 nm. For all the other VOCs studied, a color change from gray to red-brown is observed, characterized by hypochromism in the region between 300 and 400

nm and the formation of two bands at 460 and 560 nm respectively. Thus, **2**-PBF1s exhibit distinct color changes, easily observed by the naked-eye, and peculiar optical absorption bands after exposure to different classes of VOCs, which, in turn, allow distinguishing primary aliphatic and heterocyclic aromatic amines from all other N–VOCs and O–VOCs involved.

The vapochromic properties of **2**-PBF1s towards Py were demonstrated by successive cycles of exposure to saturated vapors of Py, followed by thermal heating at 150 °C. Figure 5.5 shows the variation of the optical absorption intensity of films in the maximum of absorption (λ_{abs} = 575 nm) before and after exposure to Py vapors. A complete restoration of the initial optical absorption spectrum is observed for 4 cycles of exposure/heating.

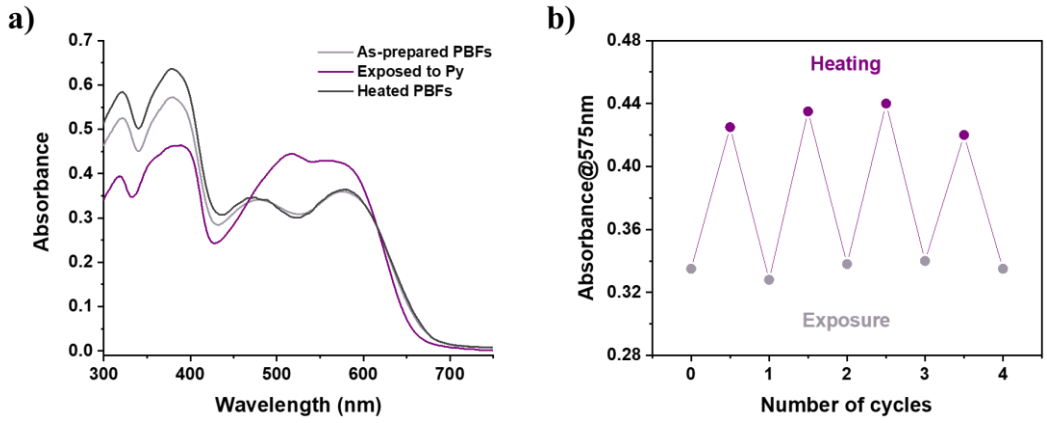

Figure 5.5. (a) UV-vis reflectance spectra of **2**-PB1 films. (**b**) Optical absorption intensity changes at λ_{abs} = 575 nm upon cycles of exposure to saturated vapors of Py and subsequent thermal heating at 150 °C.

These results demonstrate a complete chemisorption/desorption process involved in the presence of Py vapors. On the other hand, the yellow color observed after exposure to BA vapors remains unchanged after heating and/or exposure to other volatile Lewis bases, indicating a presumable demetalation of the complex,[243] while for all the other VOCs investigated only a partial restoration of initial reflectance spectrum of **2**-PBF1s is obtained (the red brown color turns light red brown upon heating at 120 °C for 15 min).

Comparing the optical response of PBFs of complexes **1** and **2** after exposure to saturated BA vapors, the formation of stable adducts is demonstrated for the former in Section 4.5.5, while a demetalation is suggested in the latter case. This indicates a greater stability of complex **1** compared to that of complex **2** supported on paper substrates. This plausible lower stability is relevant to discriminate primary amines from all the other N–VOCs and O–VOCs in the latter case.

*5.5.3. Sensing Performance of **2**-PBFs to VOCs*

As anticipated in Section 4.5.2.3, exposure to saturated vapors of different VOCs corresponds to different concentrations depending on the vapor pressure of each VOCs involved (Table B1). Therefore, an appropriate assessment of the detection performance of **2**-PBF1s should be made by exposing them to the same concentration for each VOC. To this

end, the concentration of 1000 ppm was chosen because it represents the IDLH value reported by NIOSH for Py vapors,[365] chosen as reference volatile Lewis base.

Exposure to this vapor concentration was performed for each VOC studied under static conditions for 90 min by injecting appropriate volumes of pure VOCs into a sealed chamber (1.15 L, Figure 3.1), allowing complete evaporation. Then UV-vis reflectance spectra of **2**-PBF1s after exposure were collected.

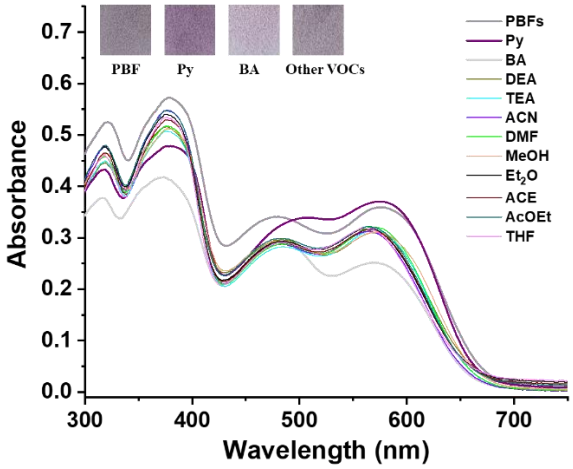

Figure 5.6. UV-vis reflectance spectra of **2**-PBF1s exposed to 1000 ppm of the involved N-VOCs and O-VOCs. Inset: photographic images of pristine **2**-PBF1s and after exposure to 1000 ppm of each VOC.

Under these conditions, the optical response of **2**-PBF1s is quite different for the VOCs involved (Figure 5.6). Films turn grape in color after static exposure to 1000 ppm of Py vapors, with the consequent formation of a new band at *ca.* 505 nm, and a slight increase of the absorption band at 575 nm. In contrast, an overall decrease of the absorption intensity of the reflectance spectrum of **2**-PBF1s is observed after exposure to 1000 ppm of BA, particularly pronounced that at 575 nm. This change in the absorption intensity is consistent with the observed color change (discolor) of the exposed films compared to pristine films. On the other hand, no color changes are observed after exposure to 1000 ppm of all other VOCs involved, resulting in reflectance spectra very similar to those of the pristine films.

Therefore, exposure of **2**-PBF1s to 1000 ppm of various VOCs results in a selective optical response towards Py vapors and, in the case of BA, a small color change of the films (discoloration). Based on these results, further investigations on the sensitive detection of Py and BA among all other investigated VOCs are reported in the following section.

*5.5.4. Quantitative Detection of Py and BA vapors by **2**-PBFs*

Further studies on the optical response of **2**-PBF1s towards different vapor concentrations (500 – 5000 ppm) of Py and BA were performed (Figure 5.7). In the former case, relevant changes in reflectance spectra are observed in the visible region (Figure 5.7a). In particular, a small and gradual increase of the band at 575 nm is observed, accompanied also by an initial red-shift of the band centered at 480 nm (from 480 to 505 nm up to 1000 ppm of Py), and then followed by the formation of a new absorption band centered at 513 nm upon exposure to 5000 ppm of Py vapors. These spectral changes are also associated to

a gradual color change visible by naked-eye (Figure 5.7b). While no significant color changes are observed upon exposure to a Py vapor concentration of 500 ppm, a gradual visual color change from gray to purple is observed for vapor concentrations ≥ 750 ppm.

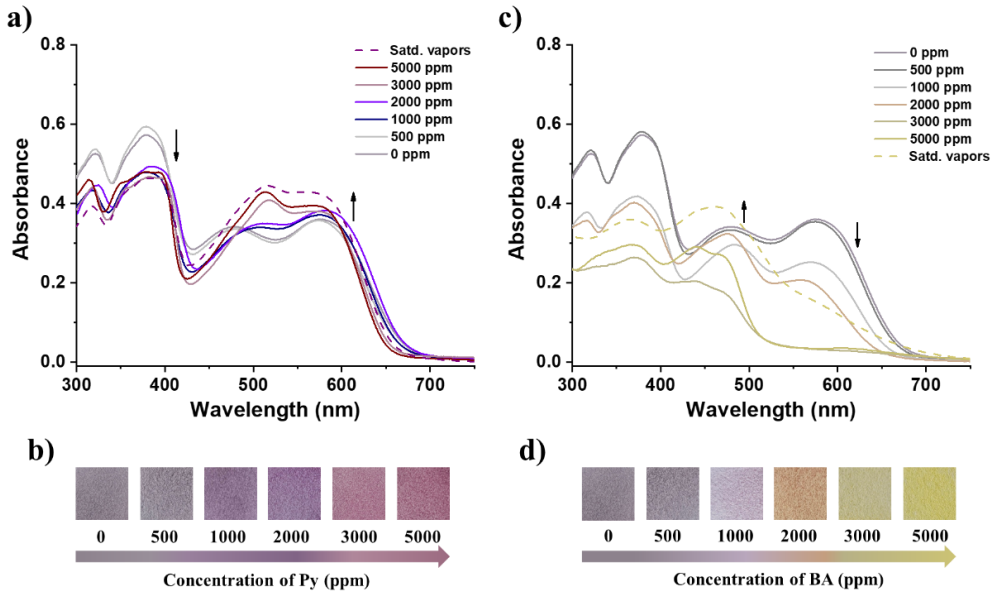

Figure 5.7. UV-vis reflectance spectra of **2**-PBF1s exposed to increasing vapor concentrations of Py **(a)** and BA **(c)**. Each spectrum was recorded in an independent experiment. Photographic images of **2**-PBF1s upon exposure to increasing vapor concentrations of Py **(b)** and BA **(d)**.

On the other hand, completely different reflectance spectra are obtained with exposure to increasing concentrations of BA (Figure 5.7c). In this case, the disappearance of the band centered at 575 nm and the appearance of a new, less pronounced, broad band at *ca.* 460 nm are observed after exposure to 3000 ppm of BA. Therefore, exposure of **2**-PBF1s to BA vapors results in a relevant color change from gray to yellow-brown at vapor concentrations ≥ 2000 ppm (Figure 5.7d). Conversely, exposure to higher BA vapor concentrations (3000 ppm) leads to a yellow color, associated with almost complete demetallation of the complex.

Therefore, the naked-eye color changes of **2**-PBF1s upon exposure to Py and BA are useful for detecting the presence of Py vapors in a concentration range between 500 – 5000 ppm, including the IDLH value for this substance, and for discriminatively detecting BA at vapor concentrations ≥ 2000 ppm.

5.5.5. Detection of Py Vapors by RGB Color Analysis of **2**-PBFs

The rich visual color changes observed after exposure of **2**-PBF1s to increasing vapor concentrations of Py provide a broad space for the quantitative recognition of this substance and the design and development of simple detection tools for on-site detection.[101] In particular, the chromic response of films can be detected using portable electronic devices, such as a smartphone, and represented in the RGB color space (more details are reported in Section 2.2.1).[389] Therefore, a smartphone-assisted RGB color analysis of **2**-PBF1s before and after exposure to Py vapors was performed, and the RGB color was captured using an Android color recognition app (*Color Detector* developed by Galaxy studio apps). However,

RGB values are very sensitive to illumination changes, such as shadows or shines, and device-dependent, making color analysis difficult.[389,390] To overcome these problems, the absolute R, G, and B values obtained from the color recognition app can be conveniently converted into normalized values, denoted as r, g, and b, using eqs. 3.4 – 3.6 (Section 3.6).[251,390]

The normalized rgb color space is effective in color analysis of **2**-PBF1s under different lighting conditions and even using different smartphones. In fact, comparable rgb values are obtained by performing an independent set of experiments in which the RBG values were captured from digital images of films before and after exposure to 1000, 3000 and 5000 ppm of Py vapors using three different smartphones (Samsung Galaxy S23, Xiaomi MI A3, and iPhone 12 Pro Max), and under two lighting conditions, 1800 lux and 30 lux, respectively (Figure 5.8). Absolute RGB values are very different from each other, both between the two lighting conditions and between the different smartphones. On the other hand, RGB normalization returns comparable rgb values, both in the two lighting conditions and between the different smartphones. Therefore, using normalized RGB values should lead to similar results across different devices, such as smartphones, while also minimizing the effect of different lighting conditions on the acquisition of RGB values.

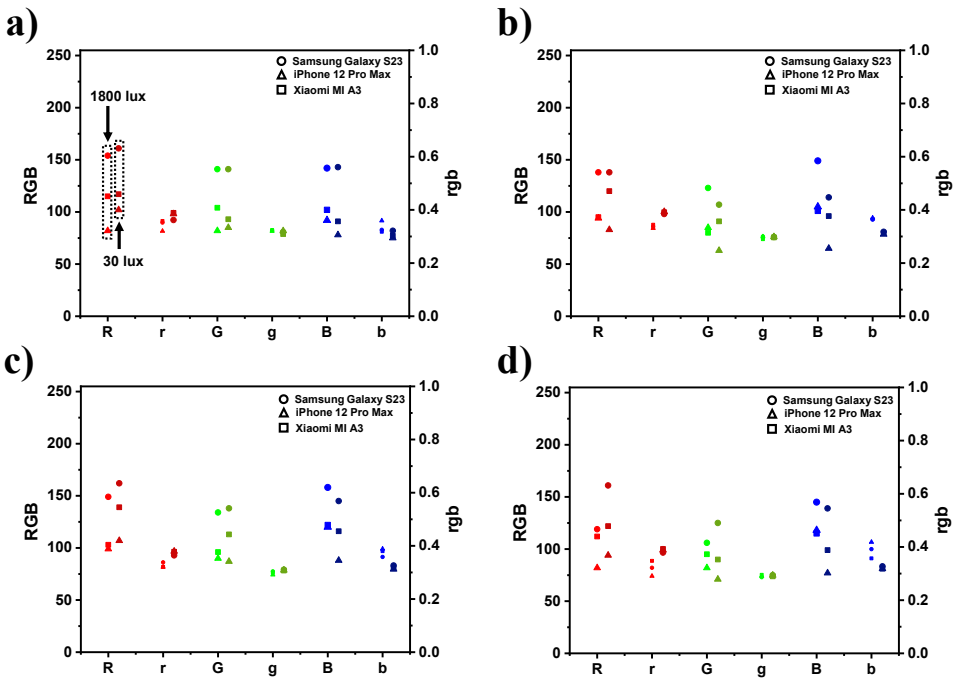

Figure 5.8. Absolute RGB and normalized rgb values of **2**-PBF1s before **(a)** and after exposure to 1000 **(b)**, 3000 **(c)**, and 5000 **(d)** ppm of Py vapors captured with three different smartphones and under two different lighting conditions (as indicated in **(a)**).

Given the significant color change of **2**-PBF1s after exposure to Py vapors (from 500 to 5000 ppm, Figure 5.9a), the color analysis of as-prepared and exposed films was further performed using a Samsung Galaxy S23 smartphone under an almost constant lighting condition (1600 – 2000 lux) by the calculation of ΔE_{rgb} (eq. 3.7) before and after exposure. Indeed, comparing the various possible relationships between the rgb values and Py vapor

concentration, the ΔE_{rgb} before and after exposure best describes the observed color changes, while all other relationships are weaker or not significant (Figure A19 and Figure A20). Therefore, the mean RGB values obtained from at least three replicates were normalized to rgb values (Figure 5.9b) and then used for the calculation of ΔE_{rgb}. The plot of calculated ΔE_{rgb} as a function of Py vapor concentration (Figure 5.9c) shows a linear dynamic range up to 5000 ppm characterized by a good linearity coefficient (R^2 = 0.992), with an estimated LOD of 578 ppm.

Furthermore, using mean rgb values derived from different smartphones (Figure 5.8), the ΔE_{rgb} as a function of the concentration of Py vapors show a linear relationship, with the slope of the linear best fit nearly identical to that obtained from the set of replicate measurements using a same smartphone (Samsung Galaxy S23) under nearly constant illumination conditions (1600 – 2000 lux) (Figure A21).

These results are truly impressive because they demonstrate that an accurate detection of Py vapors in the concentration range of 750 – 5000 ppm can be made using a simple detection approach, *i.e.* smartphone-assisted RGB color analysis of **2**-PBF1s before and after exposure, and a proper analysis such as normalization of RGB values to their rgb values and, finally, calculation of the ΔE_{rgb}.

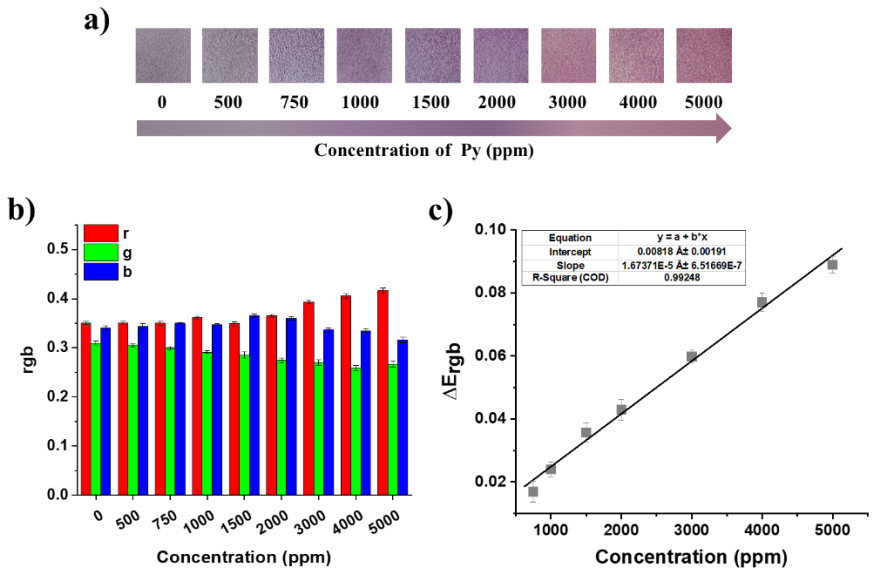

Figure 5.9. (a) Photographic images of **2**-PBF1s before and after exposure to increasing concentrations of Py. **(b)** Mean rgb values of **2**-PBF1s before and after exposure to Py vapors. **(c)** Mean ΔE_{rgb} values as a function of the concentration of Py vapors and the related linear best fit in the range 750 – 5000 ppm (weight given by data error bars).

In this context, it is also instructive to consider the absolute RGB values to check whether their RGB analysis is suitable to adequately quantify different Py vapor concentrations. Considering the mean RGB values of the set of data used for the rgb analysis in Figure 5.9, a good linearity coefficient (R^2 = 0.997) is obtained from the plot of the ΔE_{RGB} as a function of Py vapor concentration, over a vapor concentration range between 750 – 5000 ppm (Figure A22), with an increased standard deviation of the mean values and an estimated LOD of 425 ppm. This estimated LOD represents an unreliable value since

2-PBF1s are not responsive at this Py vapor concentration (Figure 5.9 and Figure 5.7). Therefore, the RGB color analysis of absolute RGB values captured using a smartphone under nearly constant lighting, apparently leads to similar results than those using RGB color analysis performed by normalized values. However, care must be taken when analyzing RGB data for sensing applications, otherwise unreliable results may be obtained. Therefore, smartphone-assisted RGB color analysis using absolute RGB values is device-dependent even when performed under standardized conditions (especially lighting conditions), so its repeatability remains rather limited.

In summary, the results of this study indicate that the presence of Py vapors in the range of 500 to 5000 ppm can be easily identified by the color change of the films, by the naked-eye, and quantitatively detected by a smartphone-assisted color recognition app and a proper RGB color analysis, without the need for difficult measurements or complex instrumentation. Therefore, **2**-PBF1s are suitable chemosensors for the sensitive and selective detection of Py vapors. In fact, they selectively detect Py from those of most common VOCs at the IDLH concentration (1000 ppm),[365] and up to concentrations of 5000 ppm. On the other hand, for higher vapor concentrations (≥ 2000 ppm) **2**-PBF1s discriminately detect also primary amine vapors in addition to Py vapors. These vapor concentrations are useful in industrial and environmental settings for workplace safety and environmental monitoring.[361,391]

5.5.6. *Improved Sensitivity of **2**-PBFs for the Detection of Py Vapors*

In the previous Sections (5.5.4 and 5.5.5) the selective and sensitive detection of Py vapors using **2**-PBF1s was demonstrated by both UV-vis reflectance spectra and RGB color analysis. Based on these results, **2**-PBF4s were also prepared from dilute THF solutions of **2** (4.0×10^{-4} M), using the same procedure previously described (Section 5.5.1), trying to improve their sensitivity to Py vapors.

In this case, paler gray **2**-PBF4s are obtained after the evaporation of the solvent under nitrogen atmosphere. The UV-vis reflectance spectrum (Figure 5.10) of these films is very similar to that of **2**-PBF1s (Figure 5.6). In particular, two defined bands are observed in the region between 300 and 400 nm, and two absorption bands, slightly shifted compared to **2**-PBF1s, centered at 484 nm and 568 nm characterize the visible region of their reflectance spectrum.

Spectral changes of **2**-PBF4s after static exposure to 300 ppm of Py and BA vapors (Figure 5.10) are very similar to those of **2**-PBF1s exposed to 1000 ppm (Figure 5.6). In particular, an increase in the intensity of the absorption bands at 484 nm and at 568 nm, the latter blue-shifted at 560 nm, is observed after exposure to Py vapors, while an overall decrease in the absorbance intensity of the reflectance spectrum is observed in the case of BA, with a more pronounced decrease of the in band at 568 nm with respect to **2**-PBF1s. These spectral changes are accompanied by an evident color change from pale-gray to violet and lilac after exposure of **2**-PBF4s to Py and BA vapors, respectively. On the other hand, only a small color change and a slight overall decrease of the reflectance spectrum is obtained for all the other VOCs involved. Therefore, significant changes in color and absorbance are observed only for Py and BA among all other VOCs involved. Therefore, **2**-PBF4s behave as

2-PBF1s in terms of selective detection of Py and BA vapors, but with significantly improved sensitivity as they are responsive to lower vapor concentrations (300 ppm).

Furthermore, exposure of **2**-PBF4s to BA vapors in a concentration range from 100 up to 1000 ppm, reveals that they are responsive to concentrations ≥ 300 ppm (lilac colored), becoming completely demetalated (yellow films) at 1000 ppm (Figure A23). Therefore, **2**-PBF4s are also useful for discriminatively detect BA vapors versus other VOCs at concentrations ≥ 300 ppm.

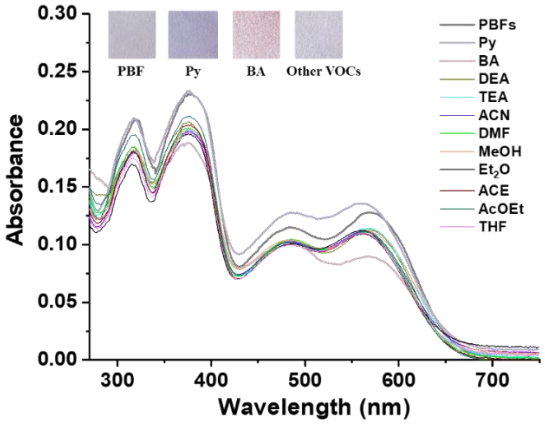

Figure 5.10. UV-vis reflectance spectra of **2**-PBF4s exposed to 300 ppm of the involved N-VOCs and O-VOCs. Inset: photographic images of pristine **2**-PBF4s and after exposure to 300 ppm of VOCs.

UV–vis reflectance spectra recorded after static exposure to increasing concentrations of Py vapors using **2**-PBF4s indicate a gradual increase of the optical absorption bands centered at 484 nm and 560 nm. The saturation point is reached after exposure to a concentration of approximately 1000 ppm. Considering the increase of the absorbance at 560 nm as a function of Py vapors concentration, a linear dynamic range from 0 up to 1000 ppm is obtained (Figure 5.11), with a very good linearity coefficient (R^2 = 0.9977), with an estimated LOD of 94 ppm.

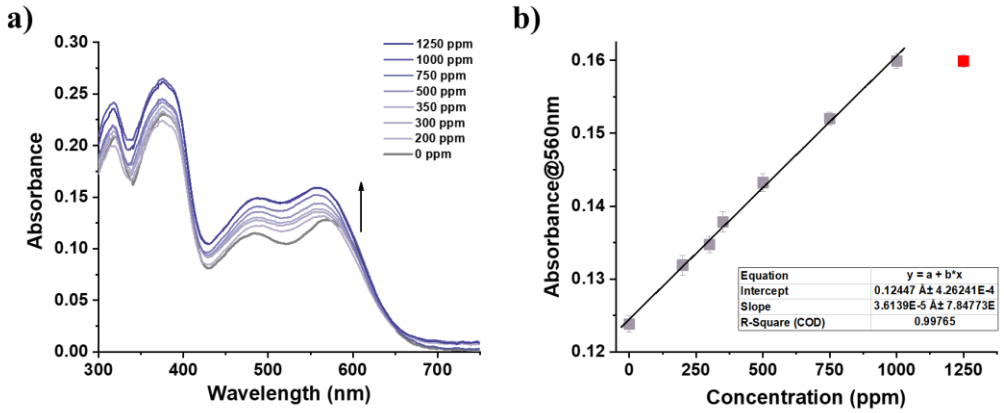

Figure 5.11. **(a)** UV-vis reflectance spectra of **2**-PBF4s exposed to increasing concentrations of Py. Each spectrum was recorded in an independent experiment. **(b)** Mean ΔE_{rgb} values as a function of the concentration of Py vapors and related linear best fit in the range 100 – 1000 ppm (weight given by data error bars). The data points marked in red are not included in the linear fit.

These variations in the optical spectra are also associated with a progressive change in the color of the **2**-PBF4s, visible to the naked eye, from pale-grey to violet (Figure 5.12a). The RGB color analysis of films before and after exposure to Py vapors in this concentration range (100–1000 ppm) was also performed using normalized rgb values (Figure 5.12b). The plot of ΔE_{rgb} as a function of Py vapor concentration shows a linear dynamic range up to 750 ppm (Figure 5.12c), characterized by a very good linearity coefficient (R^2 =0.9904), with an estimated LOD of 36 ppm.

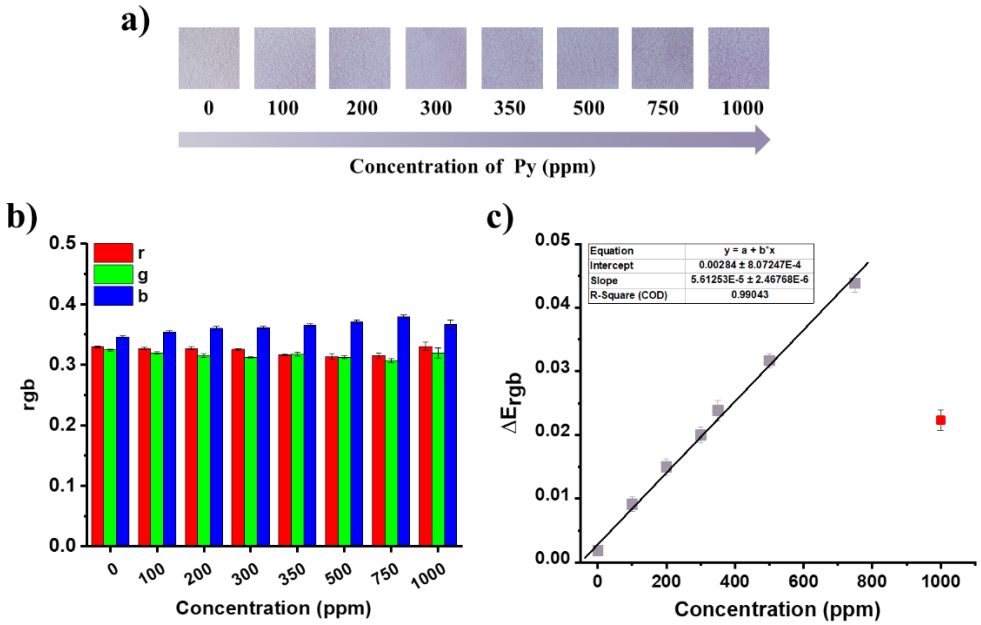

Figure 5.12. **(a)** Photographic images of **2**-PBF4s before and after exposure to increasing concentrations of Py. **(b)** Mean rgb values of **2**-PBF4s before and after exposure to Py vapors. **(c)** Mean ΔE_{rgb} values as a function of the concentration of Py vapors and the related linear best fit in the range 0 – 750 ppm (weight given by data error bars). The data point marked in red is not included in the linear fit.

Interestingly, the results obtained from UV–vis reflectance spectra and RGB color analysis of **2**-PBF4s exposed to Py vapors are consistent with each other, thus validating the RGB method. Furthermore, it turns out that RGB color analysis from **2**-PBF4s is more sensitive in detecting Py vapors than from optical absorption changes, since RGB color analysis involves the overall spectral changes of films and not just the spectral changes at a specific wavelength. This further demonstrates the efficiency of the present RGB color analysis approach for sensing studies involving vapochromic materials.

Furthermore, the improved sensitivity of **2**-PBF4s towards Py vapors demonstrates that it is possible to modulate the sensitivity of the chemosensor and its linear response range by varying the amount of material deposited on the substrate. Thus, the combination of both **2**-PBF4s (linear dynamic range up to 750 ppm) and **2**-PBF1s (linear dynamic range 750–5000 ppm) allows the sensitive and selective detection of Py over a very broad vapor concentration range (from tens to thousands of ppm).

Comparing these results with other optical chemosensors reported in the literature for the sensitive detection of Py vapors involving colorimetric responses,[387,388] it emerges that, although **2**-PBFs are not the most sensitive chemosensors developed for the quantitative

detection of Py, they possess key advantages such as: i) selective detection of Py vapors in a very wide concentration range; ii) very simple preparation procedure, especially compared with the optical fiber sensor developed by Elosua *et al.*[388]; iii) high portability combined with smartphone-assisted RGB color analysis, allowing on-site detection of Py vapors.

These features constitute a unique example among the chemosensors reported in the literature for the detection of this substance. In fact, literature data on chemosensors based on optical,[375,381,382,386,387,388] chemiresistive,[369,370,379] or piezoelectric[373,374] response for the quantitative detection of Py vapors (Table 5.3), require expensive and benchtop instrumentation, which affects their portability in real-world applications for on-site monitoring. Moreover, most of them possess a limited linear dynamic range[369,373,374,387,388] or are not selective (Table 5.3).[369,370,388]

Table 5.3. Comparison of the sensing performance and portability of various chemosensors for the quantitative detection of Py vapors.

Type of sensor	Detection method	LOD (linear range)	Selectivity Studies	Portability	Ref
Metalated Phthalocyanine	Chemiresistive	0.0079 ppm (1 – 3 ppm)	no	Moderate	369
Organic Compound	Chemiresistive	0.375 ppm (0.375 – 7500 ppm)	no	Moderate	370
Hybrid polymeric material	Chemiresistive	not available (28 – 138 ppm)	yes	Moderate	379
Metal-organic framework	Piezoelectric	1.603 ppm (5 – 50 ppm)	yes	Low	373
Metal-organic framework	Piezoelectric	0.04 ppm (0.3 – 25 ppm)	yes	Low	374
Hybrid polymeric material	MZI waveguide	0.476 ppm (0 – 400 ppm)	yes	Moderate	378
Supramolecular organic framework	Fluorescence	5 ppm (not available)	yes	Moderate	375
Conjugated Polymer	Fluorescence	33 ppm (not available)	yes	Moderate	381
Copper(I)-cluster	Fluorescence	344 ppm (2000 – 12000 ppm)	yes	Moderate	382
Metal Complex	Fluorescence	722 ppm (1000 – 10000 ppm)	yes	Moderate	386
Metallo-porphyrin	Colorimetric and fluorescence	0.041 ppm (0 – 50 ppm)	yes	Moderate	387
Metal Complex	Optical fiber	1 ppm (18 – 66 ppm)	not available	Moderate	388
Complex 2	RGB color analysis	578 ppm (750 – 5000 ppm)	yes	High	*This work*
Complex 2	RGB color analysis	36 ppm (0 – 750 ppm)	yes	High	*This work*

5.5.7. Vapochromic Response of 2-PBFs to Other Volatile Heterocyclic Amines

Further investigations on the optical response of **2**-PBFs towards other volatile heterocyclic amines were also performed. In particular, the following compounds were chosen as representative compounds of three different classes of heterocyclic amines (reported in parentheses): i) piperidine and pyrrolidine (alicyclic amines); ii) pyrrole (heterocyclic aromatic amines); 2-methylpyridine or α-picoline, 4-methylpyridine or γ-picoline, and 2,6-dimethylpyridine or α,α′-lutidine (pyridine derivatives).

A different optical response of **2**-PBF1s is obtained after exposure to 1000 ppm of each of these heterocyclic amines (Figure 5.13). In particular, no significant changes in the color of the films, and consequently in reflectance spectra, are observed after exposure to alicyclic amines and pyrrole (Figure 5.13a), thus they behave like the above involved VOCs, except Py and BA. On the other hand, for 4-methylpyridine, color and spectral changes similar to those of Py are observed, while some spectral reflectance changes are obtained in the cases of 2-methylpyridine and 2,6-dimethylpyridine, but they do not give rise to significant color changes (Figure 5.13b).

Considering **2**-PBF4s exposed to 300 ppm of the various heterocyclic amines, a similar optical response to that observed for **2**-PBF1s after exposure to 1000 ppm of these substances is obtained (Figure A24). Therefore, **2**-PBFs allow the selective detection of Py vapors, from the most common VOCs and other volatile heterocyclic amines, with the exception of 4-methylpyridine.

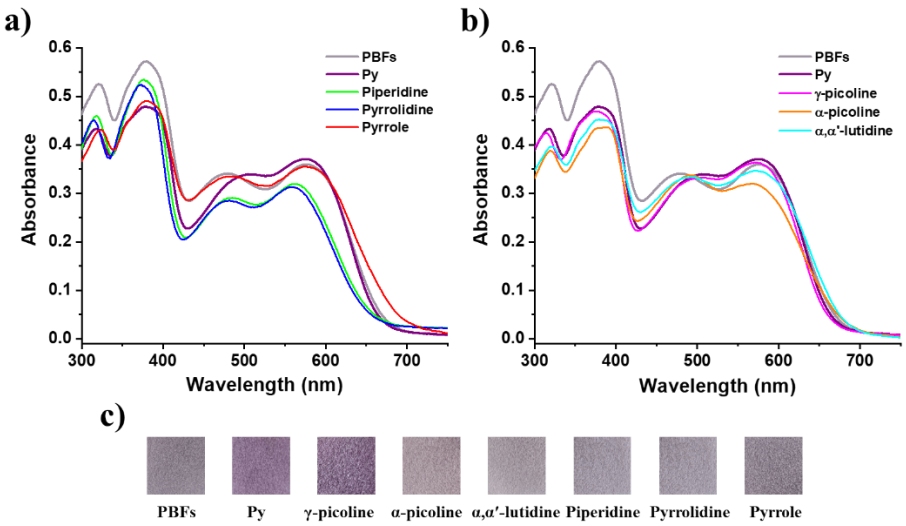

Figure 5.13. UV-vis reflectance spectra of **2**-PBF1s before and after static exposure to a vapor concentration of 1000 ppm of **(a)** alicyclic amines (piperidine, pyrrolidine) and heterocyclic aromatic amines (pyrrole), and **(b)** pyridine derivatives (α-picoline, γ-picoline, α,α′-lutidine). **(c)** Photographic images of **2**-PBF1s before and after exposure to a vapor concentration of 1000 ppm of the heterocyclic amines involved.

The selectivity of **2**-PBFs towards Py vapors with respect to the principal classes of N–VOCs, with the exception of primary amines where a demetalation occurs,[243] may be related to the Lewis basicity and the steric hindrance on the donor atom, as also illustrated for

complex **1** in Section 4.5.5. In fact, the sensing mechanism for the detection of Py vapors using **2**-PBFs films can be related to the formation of stable **2**·Py adducts, as previously demonstrated.[243] Thus, the selective response of **2**-PBFs can be explained on the basis of the less steric hindrance and the strong Lewis basicity of Py compared to that of sterically encumbered secondary and tertiary amines, including alicyclic amines.[392] Furthermore, the steric hindrance on the donor atom caused by the presence of α-methyl(s) substituent(s) is responsible for the observed behavior towards the vapors of the pyridine derivatives involved in this study. On the other hand, O–VOCs exhibit a lower propensity to form stable adducts with films of **2** because of their lower Lewis basicity compared to N–VOCs.[392]

5.6. Conclusion

This chapter reports the development of a simple and effective approach for the sensitive and selective detection of Py vapors using a vapochromic Zn(salmal) complex, **2**, deposited on paper substrates. The dip-coating technique was used for the fabrication of **2**-PBFs, ensuring high optical homogeneity, as a key prerequisite for quantitative investigations. The modulation of the linear range of response and the sensitivity of **2**-PBFs was achieved by acting on the concentration of THF solutions of **2**, resulting in a different amount of material deposited on paper substrates. Also, the effect of RH and lighting exposure on the storage conditions of **2**-PBFs were evaluated.

The vapochromic properties of as-prepared **2**-PBFs were investigated by exposure to saturated vapors of various N–VOCs and O–VOCs, resulting in a discriminative response towards Py and BA compared to all other VOCs involved in the study. Moreover, exposure of **2**-PBFs to defined concentrations of Py and BA vapors results in peculiar naked-eye color changes, that allow the detection of Py vapors in a concentration range between 500 – 5000 ppm, including the IDLH value for this substance established by the NIOSH, and the discriminative detection of BA at vapor concentrations ≥ 2000 ppm.

Quantitative detection of Py vapors was achieved by smartphone-assisted RGB color analysis of **2**-PBF1s before and after exposure. In particular, the normalization of the absolute RGB values into the corresponding rgb values, and finally the calculation of the ΔE_{rgb} allows an accurate quantitative detection of Py vapors. Instead, **2**-PBF4s show an improved sensitivity towards Py vapors (linear range of response 0 – 750 ppm). Thus, the use of **2**-PBFs prepared using concentrated and diluted solutions of **2** allows the sensitive and selective detection of Py over a very wide vapor concentration range (from tens to thousands of ppm). The vapochromic response of **2**-PBFs in the presence of other volatile heterocyclic amines (1000 and 300 ppm) shows that they are still selective for Py vapors, with the exception of 4-methylpyridine.

The results obtained from the RGB analysis are assessed in comparison with those obtained from the UV–vis reflectance spectra, being consistent with each other. Therefore, a proper smartphone-assisted RGB color analysis could represent a general approach for the detection of VOCs, using vapochromic materials deposited on films, without the need of sophisticated measurements or any complex instrumentation. These results also demonstrate that smartphone-assisted RGB color analysis using absolute RGB values can lead to unreliable and hardly repeatable results for sensing applications.

Overall, PBFs obtained from the vapochromic complex **2** represent a simple, reliable, portable, disposable, and cost-effective chemosensor that, combined with proper RGB color analysis readout, is useful for on-site detection of pyridine vapors in various industrial and environmental settings.

Chapter 6

Conductometric Gas Sensors based on Organic Heterojunctions

Contents

6.1. Introduction

Organic semiconductors Organic semiconductors have been extensively exploited in last decades, resulting in significant advances in material design and device engineering in diverse fields, such as energy conversion, electronic applications, *etc.*[393,394,395,396] They have some advantages over their inorganic counterparts, such as easy tuning of their frontier energy levels, structural properties, and low-cost fabrication processes (*e.g.,* solution processing), *etc.* However, for some specific applications, such as photovoltaics, the charge separation/storage process induced by external stimuli (*e.g.*, light) is less efficient in organic semiconductors than in inorganic semiconductors, due to their lower dielectric constant. This results in coulombically bound electron–hole pairs, as opposite to the formation of free charges observed in inorganic semiconductors. In general, the electrical properties and charge separation performance of semiconductor heterostructures are better than those of single semiconductor materials, due to a synergistic effect. Therefore, the fabrication of heterojunctions based on organic semiconductors has attracted great attention, especially for gas sensing devices (Section 2.3), thanks to the advantages over their inorganic counterparts, such as simpler preparation methods, integration on flexible materials, and low operating temperature.[393,397]

Heterostructures consist of two or more types of materials which are physically or chemically bonded together, exhibiting a distinct junction interface. The electrical properties of the heterojunction depend on several factors. First, the effective separation of charges and the formation of a built-in electric field at the interface depend on the contact and the nature (conductor or semiconductor) of the materials involved in the heterojunction.[132] Then, the energy levels of the involved materials play a relevant role in the effective charge transport of the electrons and holes,[398,399] and the supramolecular organization at the interface, especially the molecular orientation, can significantly influence the light absorption and charge transport in the device.[400] Other factors such as semiconductivity (*n*- or *p*-type), Fermi level, and work function can affect the in-built electric field and potential barriers at the heterojunction interface.

The formation of organic-organic heterostructures poses additional challenges compared to their inorganic counterparts, related to compositional homogeneity and the architecture of the heterostructure.[401] These problems are associated with the additional degrees of freedom of organic molecules, related to their molecular structure and spatial orientation. Furthermore, the architecture of the heterojunction has an impact on the optical and electronic properties. In fact, in organic heterojunction devices, the combination of two or more organic materials can lead to the formation of different heterojunction architectures, *e.g.,* planar heterojunctions (PHJs) or bulk heterojunctions (BHJs).[401,402] In these systems the charge transport and related conductivity are highly dependent on the interface architecture.[403,404] Therefore, the modulation of these properties makes them suitable systems for many applications, such as photovoltaics,[405] organic transistors,[406] lasers,[407] light emitting diodes,[408] gas sensors,[409] optoelectronic devices,[410] photocatalysis,[411] energy storage systems,[412] *etc*. The most common organic semiconductor materials used for the preparation of heterojunction devices are MOFs,[413] π-conjugated polymers,[414] BODIPY,[415] porphyrins,[416] metalated phthalocyanines,[417] fullerene,[418] small molecules,[419] *etc.* Among these, metalated

phthalocyanines have recently been investigated as suitable organic layers for the preparation of bilayer heterojunction devices with interesting electrical properties useful for gas sensing.[144]

6.2. Phthalocyanines

Phthalocyanines are a class of organic compounds characterized by the combination of four isoindole units to form a planar macrocycle. According to Huckel's aromaticity theory, these compounds possess aromatic behavior due to their 18 delocalized π electrons throughout the planar structure. Phthalocyanines are closely related to porphyrins considering their chemical and electronic structures (Figure 6.1), and possess high thermal and chemical stability.

The synthesis for the simplest phthalocyanine (H_2Pc) consists in the cyclotetramerization reaction of phthalodinitrile in the presence of lithium, using pentanol as solvent.[420,421] Also, starting from phthalodinitriles with side groups, substituted phthalocyanines can be easily obtained with the same procedure. This class of compounds is characterized by interesting optical properties. Optical absorption spectra of phthalocyanines in neutral or basic solutions show two characteristic bands, Soret (or B-band) and Q-bands, centered at *ca.* 300 and 650 nm, respectively. The presence of these bands is related to π – π* transitions between HOMO and LUMO levels.

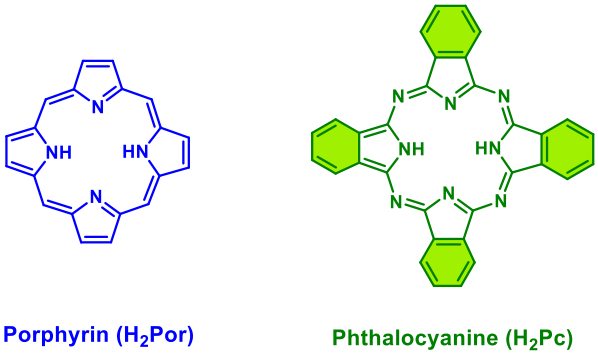

Figure 6.1. Chemical structures of simplest metal free porphyrin and phthalocyanine.

The chemical properties of phthalocyanines are easily tunable by introduction of different substituents in 4 and 5 positions of the external aromatic rings.[422,423] For example, long carbon chains lead to the formation of liquid crystals and increased solubility in organic solvents (*e.g.*, dichloromethane), while the introduction of sulfonic groups can increase their solubility in water. In addition, many other functional groups and specific synthetic strategies are used for the functionalization of peripheral benzene rings. On the other hand, the electrical properties of these compounds are modulated by the degree of oxidation or the formation of metal complexes.[424]

Phthalocyanines find applications in dye-sensitized solar cells,[425] light emitting diodes,[426] non-linear optics,[427] organic thin-film transistors,[428] batteries and supercapacitors,[429] heterojunction devices,[144] *etc.* Thanks to the presence of several nitrogen atoms in the central cavity of the molecule, phthalocyanines can act as chelating agents and lead to the formation

of metalated compounds.[430] In particular, four coordinative bonds are formed with trivalent or tetravalent metal ions. Depending on the ionic radius of the metal ion, metalated *mono*-($MPcL_n$, n = 1 or 2) or *bis*-phthalocyanine (MPc_2) can be synthesized (Figure 6.2). In particular, for transition metals, square planar metal complexes are obtained, with the presence of axial ligands in the case of tri- and tetravalent cations, while for lanthanides and actinides the formation of *bis*-phthalocyanine is preferential.

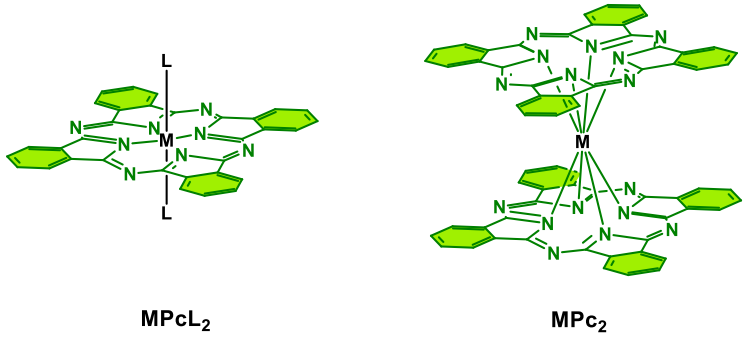

Figure 6.2. Chemical structures of mono- and bis-phthalocyanines.

For example, in the case of lutetium, the Lu^{3+} cation is larger than the cavity of a Pc macrocycle, thus a square-base antiprism *bis*-phthalocyanine is obtained, in which the trivalent cation is at the center of the antiprism and forms four bonds with four nitrogen atoms for each macrocycle. Although the formation of *bis*-phthalocyanines is preferential for lanthanide ions, it is also possible to obtain *mono*-phthalocyanines by reducing the reaction time or increasing the amount of metal salt in the reaction mixture. Among the wide range of phthalocyanine derivatives, metalated radical phthalocyanines (*e.g.*, $LuPc_2$) are widely studied thanks to their very interesting electrical properties.

6.3. Properties of Lutetium bis-phthalocyanine

Lutetium *bis*-phthalocyanine ($LuPc_2$) (Figure 6.3) is known as the first intrinsic semiconductor,[431,432] and it is characterized by interesting optical and electrical properties, both in solution and in solid state.[433]

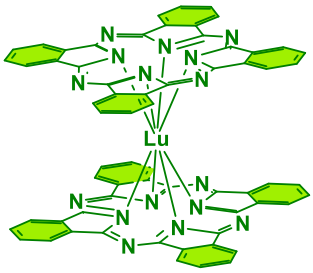

Figure 6.3. Chemical structure of lutetium *bis*-phthalocyanine.

Both the UV-vis absorption spectra of $LuPc_2$ solutions and the evaporated films show the presence of the typical Soret and Q-bands of phthalocyanines, with the addition of other bands centered at 460, 910, and 1380 nm. Even more interestingly, a broad band around

2050 nm is observed, related to an intermolecular charge transfer process, corresponding to the initial creation of charge carriers in $LuPc_2$ thin films (eq. 6.1). An evident shift of this band to *ca.* 2450 nm is observed by thermal treatment at 250 °C, with a significant increase in the extinction coefficient, also accompanied by an increase in the conductivity of the material.[433] This behavior derives from the formation of charged molecules under external stimulus and can be also observed under an applied bias. In the latter case, the migration of the charge carriers in the material is responsible for the high conductivity of $LuPc_2$ thin films.

$$2\ LuPc_2 \xrightarrow{h\nu \text{ or } \Delta} LuPc_2^{+} + LuPc_2^{-} \qquad \Delta E = 0.5\ eV\ (at\ 2450\ nm) \qquad \textbf{(6.1)}$$

Comparing the electrical properties of metal free and metalated phthalocyanines with that of $LuPc_2$, a completely different conductivity is observed. In particular, metal free and some metalated phthalocyanines (MPc, M = Zn, Cu, *etc.*) possess a very low concentration of charge carriers (1×10^4 carriers/cm^3) due by their high redox potential (around 2.0 eV) and they are therefore mainly classified as insulators. On the other hand, $LuPc_2$ and other radical phthalocyanines possess high current densities (5×10^{16} carriers/cm^3) thanks to their low redox potential (*ca.* 0.5 eV). In the latter case, the low redox potential is due by an electronic charge transfer between a Semi-Occupied Molecular Orbital (SOMO) of one molecule to the same level of another molecule.[434] Clearly, the energy needed for this process is lower than in the case of charge transfer between the HOMO and LUMO levels for metal free and metalated phthalocyanines. Obviously, doping processes or the presence of structural defects in the molecular structure can lead to dramatic changes in the conductivity of these materials.

In solid state, $LuPc_2$ molecules are characterized by the presence of weak intermolecular interactions, such as van der Waals forces. From XRD measurements of single crystals of $LuPc_2$ emerges that different crystalline structures can be observed.[434] Among them, the γ-form is the more stable and is characterized by an orthorhombic phase where the planes corresponding to the two macrocycles are parallel and rotated of 41°. Also, each molecule interacts with other four molecules by π – π interactions (intermolecular distances of 3.2 – 3.4 Å).

$LuPc_2$ has been widely investigated by Bouvet *et al.* as top layer in PHJs, as an emerging type of architecture for the development of gas sensors.[435,436] Very interesting results have recently be obtained for the sensitive detection of NH_3,[437,438,439,440,441,442,443,444] and some of these heterostructures have also shown an ambipolar behavior in the presence of external stimuli, such as visible and UV light illumination.[445,446,447,448,449,450]

6.4. Aim of the Study

This chapter describes the development of molecular material-based conductometric sensors for the sensitive detection of NH_3. To this end, the low-conductive complex **1** was used for the preparation of films on indium thin oxide interdigitated electrodes (ITO-IDE) in combination with a highly conductive material, such as $LuPc_2$. In particular, successive depositions and a solution processing approach were used to prepare **1**/$LuPc_2$ bilayer films and **1**:$LuPc_2$ mixed films, respectively.

Morphological, optical and electrical properties of these films were studied before and after thermal annealing. Bilayer and mixed films, characterized by a different architecture of the heterojunction, exhibit distinct optical and electrical properties, which in turn are very different from those of the individual materials. The effect of the different mass ratio of the two complexes in **1**:$LuPc_2$ mixed films on their properties was also considered.

The potential application of these heterojunctions as gas sensors was investigated by dynamic exposure to different NH_3 concentrations in the range of 10 to 90 ppm. Higher detection performance is observed for mixed films compared to bilayers.

This research activity, within the PhD program, was carried out at the "Institut de Chimie Moléculaire de l'Université de Bourgogne" (Dijon, France).

6.5. Results

6.5.1. **1**/$LuPc_2$ Bilayers

Bilayers composed of complex **1** and $LuPc_2$ (**1**/$LuPc_2$) were obtained in two different steps: i) deposition of the sub-layer of **1** by drop-casting a THF solution of the complex (3.0 mg/mL) onto ITO-IDEs substrates; ii) deposition of the high-conductive $LuPc_2$ top layer by thermal evaporation of solid $LuPc_2$ under secondary vacuum (Section 3.3.3). As mentioned in previous chapters (Section 4.3), complex **1** possesses an interesting thermochromic behavior.[240] In particular, it consists of a thermal-induced phase transition, from a lamellar (H-aggregates) to a hexagonal columnar structure (J-aggregates), which occurs at *ca*. 140 °C. A different arrangement of each molecular unit within the assembled structure, from H- to J-type aggregates, leads to the formation of a new absorption band at longer wavelengths (565 nm).[240] Therefore, annealed **1**/$LuPc_2$ bilayers were obtained by thermal treatment of as-prepared bilayers at 140 °C. Morphological, optical, and electrical properties of both as-prepared and annealed bilayers are reported in the following sections.

6.5.1.1. Morphological investigation

Morphological characterization of the top layer of the as-prepared and annealed **1**/$LuPc_2$ bilayers was performed by AFM measurements. 3D and 2D AFM images of as-prepared bilayers show a uniformly rough surface (Figure 6.4a and Figure 6.4b) with an estimated root mean square (RMS) roughness of *ca.* 30 nm. The height profile, measured across the blue line marked on the corresponding 2D AFM image, shows an average height of ~60 nm (Figure 6.4c). Slight morphological changes are observed in the 3D and 2D AFM images of annealed bilayers (Figure 6.4d and Figure 6.4e).

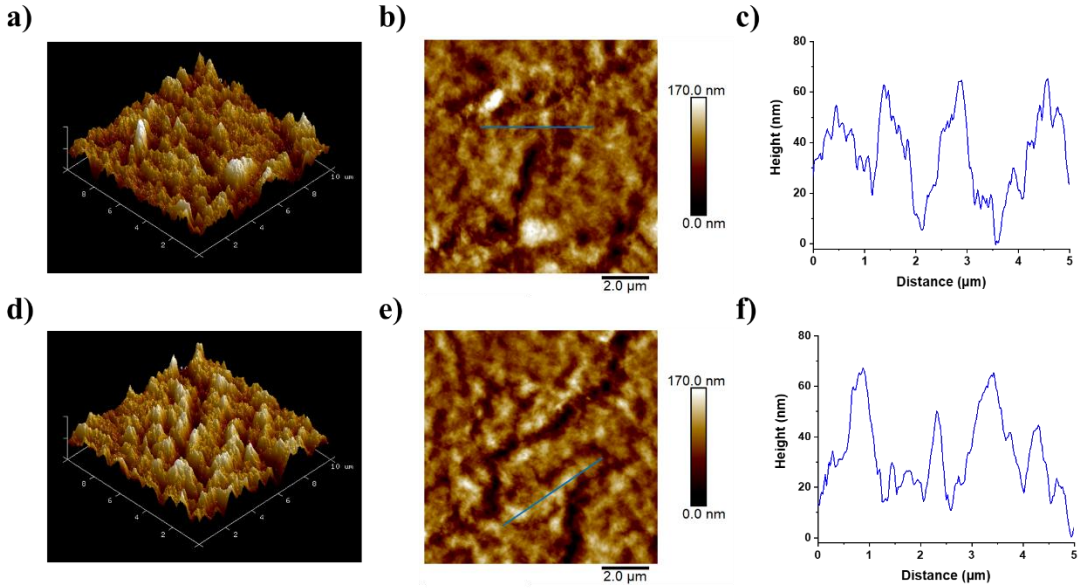

Figure 6.4. 3D **(a, d)** and 2D **(b, e)** AFM images of as-prepared (top) and annealed (bottom) **1**/$LuPc_2$ bilayers on ITO-IDEs. Height profiles of the as-prepared **(c)** and annealed **(f)** bilayers measured across the blue line marked on the corresponding 2D AFM images. The scan area in all images is 100 μm^2.

6.5.1.2. Optical characterization

The optical properties of as-prepared and annealed **1**/$LuPc_2$ bilayers were investigated by UV-vis absorption and Raman spectra. Starting from as-prepared bilayers, its optical spectrum shows a strong absorption band centered at 342 nm, two broad bands centered about 440 nm and 570 nm, and a sharp absorption band centered at 670 nm (Figure 6.5a). A small red shift of the band at 342 nm and higher absorption intensity of the bands centered at 440 nm and 575 nm are observed after annealing (Figure 6.5b). Comparing these results with the optical absorption spectra recorded from films of the two starting materials, the absorption bands observed in the region 400 – 600 nm are mainly related to complex **1**,[240] while the absorption band at longer wavelength corresponds to the Q-band of $LuPc_2$.[246] Therefore, the recorded optical spectra of the as-prepared and annealed bilayers are found to be the convolution of the spectra of the starting materials of complex **1** and $LuPc_2$.

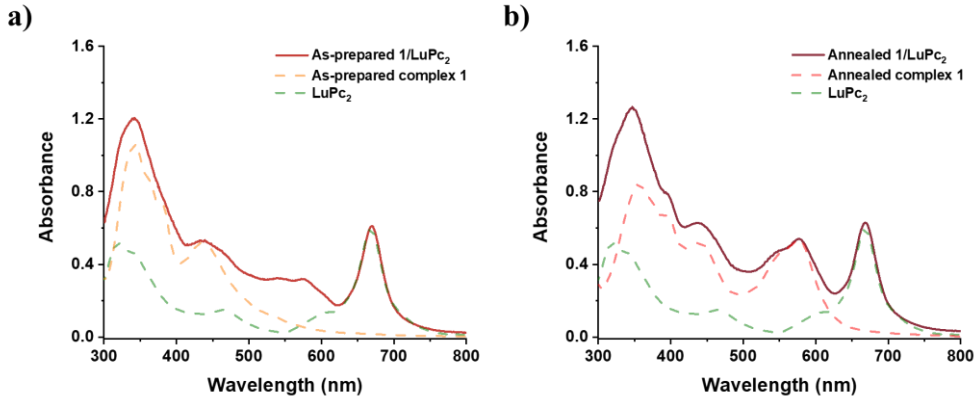

Figure 6.5. UV-vis absorption spectra of as-prepared **(a)** and annealed **(b)** **1**/$LuPc_2$ bilayers. The optical absorption spectra of the films of complex **1** and $LuPc_2$ are reported for comparison.

Raman spectroscopy measurements of **1**/$LuPc_2$ bilayers, at variable laser power, were also performed. The Raman spectrum of the as-prepared bilayers, recorded using a laser power of 0.12 mW, shows several peaks in the range between 500 and 1750 cm^{-1} (Figure 6.6a), mainly related with that of the $LuPc_2$ complex. In fact, the Raman spectrum of $LuPc_2$ films is mainly composed of peaks associated with the Pc ring breathing (673 cm^{-1}), C–H bending (1175 cm^{-1}), iso-indole stretching (1408 cm^{-1}), C=C pyrrole stretching (1511 cm^{-1}), and aromatic C=C stretching (1600 cm^{-1}).[451] On the other hand, the appearance of new peaks in a wider wavenumber range (500 – 2250 cm^{-1}) is observed using higher laser power (6.0 mW) (Figure 6.6b). These peaks are mostly related with those of complex **1**, reflecting the composition of the lower layer. Thus, several peaks associated with aromatic C–O stretching (1181 cm^{-1}), C–N stretching (1374 cm^{-1}), aromatic C=C stretching (1516 and 1553 cm^{-1}), C=N stretching (1618 cm^{-1}) and C≡N stretching (2217 cm^{-1}) can be assigned.[452]

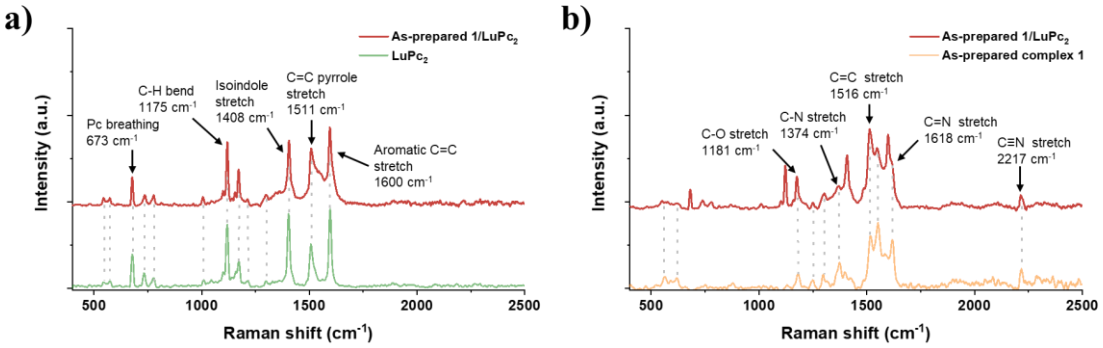

Figure 6.6. Raman spectra of the as-prepared **1**/$LuPc_2$ bilayers recorded using a laser power of 0.12 mW **(a)** and 6.0 mW **(b)**. The Raman spectra of the films of complex **1** and $LuPc_2$ are reported for comparison.

In the case of annealed **1**/$LuPc_2$ bilayers, the recorded Raman spectra are quite similar to those observed before annealing (Figure A25).

6.5.1.3. Electrical properties

I – V characteristics of **1**/$LuPc_2$ bilayers before and after annealing were collected in a range of applied voltage from -10 to +10 V (Figure 6.7a). A symmetric non-linear curve is observed for as-prepared bilayer films. The estimated apparent energy barrier (U_{th}), derived from the tangent to the I – V curve at the higher applied bias and its successive extrapolation on the x-axis, returns a value of 2.91 V. After annealing, an increase of the conductivity of **1**/$LuPc_2$ bilayers is obtained and the non-linear curve that characterized as-prepared films becomes almost linear. Very interestingly, the extrapolated U_{th} of the annealed bilayers (1.45 V) results lower compared to that of as-prepared bilayers.

Impedance spectroscopy measurements were performed on both as-prepared and annealed **1**/$LuPc_2$ bilayers in a wide range of frequencies (100 Hz – 10 MHz) under a constant AC bias (100 mV). For as-prepared bilayer films, two distinct semicircles having different amplitudes are observed in the corresponding Nyquist plots (Figure 6.7b). In particular, the high frequency semicircle is very small compared to that at low frequency. A decrease in the amplitude of the low frequency semicircle is observed by increasing the DC voltage up to 10 V, while the amplitude of the high frequency semicircle remains unchanged

(inset Figure 6.7b). In the case of annealed bilayers, similar results are observed in Nyquist plots (Figure 6.7c), but the low frequency semicircles result smaller compared to those of the as-prepared bilayers. A very good fitting of the experimental data in both Nyquist plots is obtained by considering an equivalent circuit containing two-component Ri-CPEi elements connected in series (Figure 6.7d).

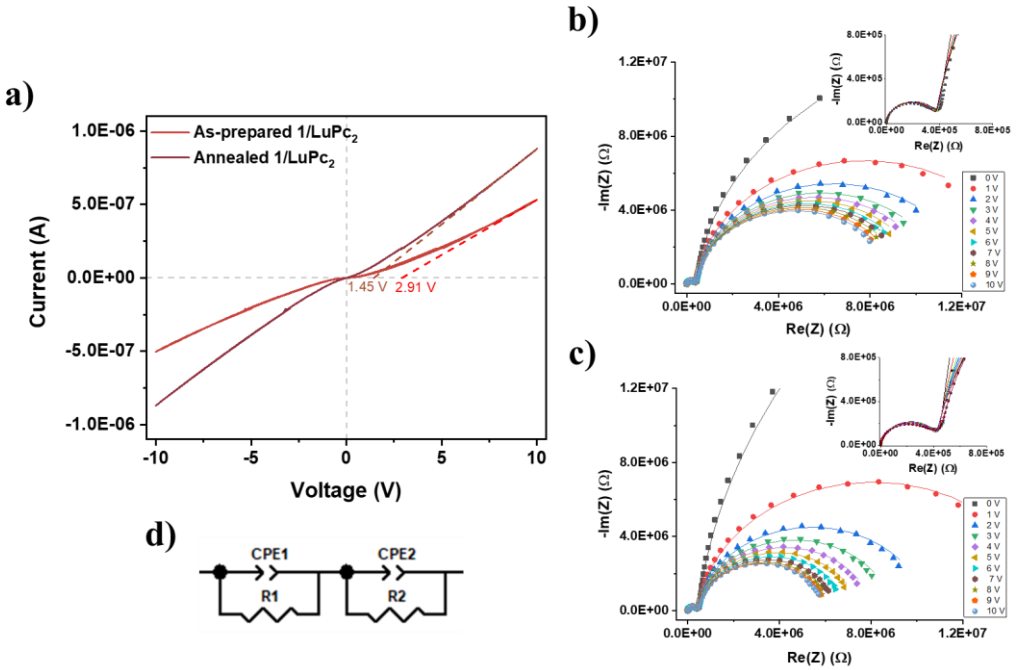

Figure 6.7. **(a)** I – V characteristics of as-prepared and annealed **1**/$LuPc_2$ bilayers. Nyquist plots of as-prepared **(b)** and annealed **(c)** bilayer films. Insets: zoom at the high frequency semicircles. The impedance response for each film recorded at different DC voltage and fitted using the reported equivalent circuit **(d)**.

6.5.1.4. Ammonia exposure experiments

Exposure experiments to 90 ppm of ammonia (NH_3) at a constant RH value (45%) were performed on **1**/$LuPc_2$ bilayer films. For the prepared bilayers, a continuous decrease in current intensity is observed under exposure to NH_3 (10 min) and a partial recovery of the initial current intensity under synthetic air (30 min) (Figure 6.8a). The mean difference in current intensity after and before exposure to NH_3 is of *ca.* -7.67×10^{-9} A with a relative response (RR, see eq. 3.9) of -4.12%.

An analogous response (decrease in current intensity) is observed for the annealed **1**/$LuPc_2$ bilayers after exposure to NH_3 (Figure 6.8b). In this case, a larger variation of the current intensity (-2.33×10^{-8} A) and a higher RR value (-8.01%) are obtained compared to as-prepared bilayers. In both as-prepared and annealed **1**/$LuPc_2$ films, a gradual baseline drift is observed during each desorption cycle, probably due by the incomplete desorption of NH_3.

Exposure to different NH_3 concentrations (10 – 90 ppm, steps of 20 ppm) were also performed on as-prepared and annealed **1**/$LuPc_2$ bilayers (Figure A26). For these measurements, an exposure time of 1 min and a desorption time of 4 min were considered. Under these conditions, a continuous decrease in current is observed for all the investigated concentrations, with a larger current variation in the case of annealed bilayers. Again, a gradual shift of the baseline is observed.

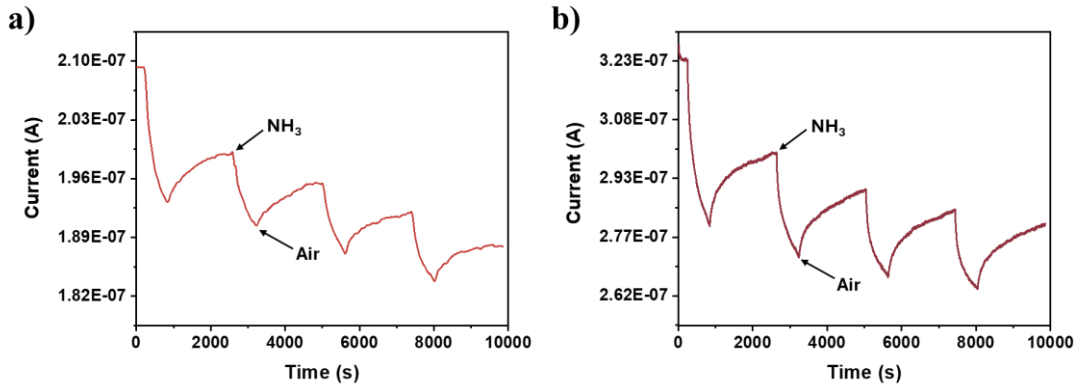

Figure 6.8. Current response to subsequent NH_3 exposure (90 ppm, 4 cycles) of as-prepared **(a)** and annealed **(b)** **1**/$LuPc_2$ bilayers. Exposure experiments were performed with exposure and recovery times of 10 and 30 min, respectively.

6.5.2. *1*:$LuPc_2$ Mixed Films

The solution-processing approach was used for the preparation of mixed films (Section 3.3.4). In particular, mixed THF solutions with different mass concentration ratios (1:2, 1:1, and 2:1 of **1**:$LuPc_2$, respectively) were used for their preparation. As-prepared films were obtained after complete evaporation of the solvent from the mixed solutions (100 µL) cast onto ITO-IDEs substrates. Again, a thermal treatment at 140 °C was performed on as-prepared films, obtaining annealed films. Morphological, optical, and electrical characterizations, like those performed on bilayers, were also performed for mixed films.

6.5.2.1. Morphological investigation

Surface morphological investigations on as-prepared and annealed **1**:$LuPc_2$ mixed films were performed by AFM measurements. A uniform surface with the presence of pillar-like structures can be observed in 3D and 2D AFM images of as-prepared 1:2 mixed films (Figure 6.9a and Figure 6.9b). For these films, an RMS roughness value of ~35 nm was obtained. The height profile, measured across the blue line marked on the corresponding 2D AFM images, indicates an average height of ~120 nm (Figure 6.9c). On the other hand, an increase in the width and height of the pillars is observed in the 3D and 2D AFM images of mixed films after annealing (Figure 6.9d and Figure 6.9e). Indeed, an RMS roughness of ~60 nm is obtained, and an increased average height (~190 nm) is evident from the height profile of the annealed mixed films (Figure 6.9f) compared to the as-prepared films.

An alveolar uniform morphology is observed for the as-prepared 1:1 mixed films (Figure A27). A rough surface with numerous holes can be observed from its 3D image, and an average hole diameter of approximately 1.0 µm is estimated from the 2D image, with an RMS roughness of ~30 nm. An increase in the diameter of holes (1.5 µm) is observed in both 3D and 2D images of annealed 1:1 mixed films, and an estimated RMS roughness of *ca.* 35 nm is obtained. The as-prepared and annealed 2:1 mixed films are characterized by a similar surface morphology to that of the 1:1 mixed films (Figure A28), with similar hole sizes and a higher RMS roughness (~60 nm).

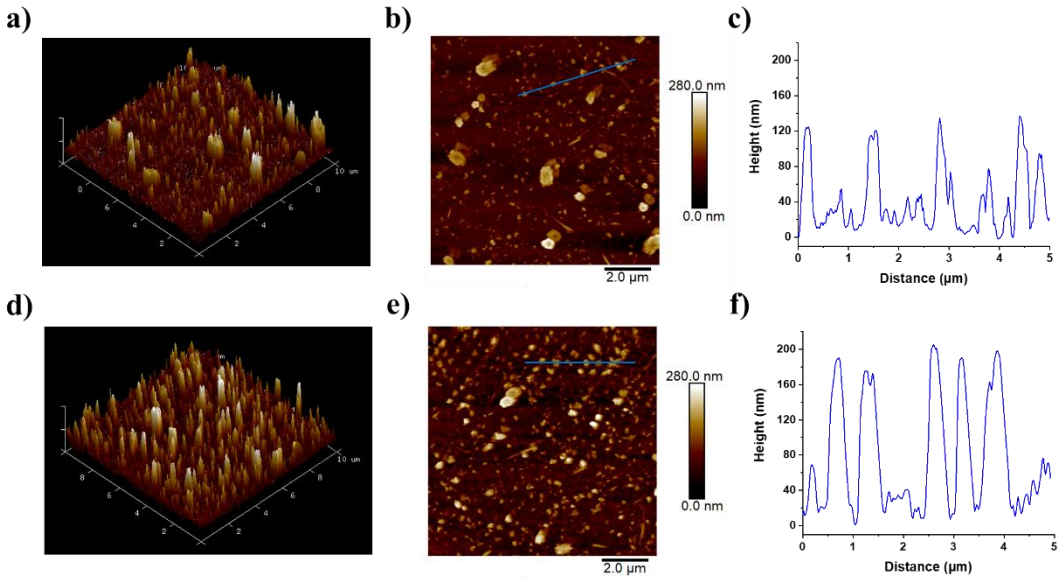

Figure 6.9. 3D **(a, d)** and 2D **(b, e)** AFM images of as-prepared (top) and annealed (bottom) 1:2 mixed films on ITO-IDEs. Height profiles of the as-prepared **(c)** and annealed **(f)** 1:2 mixed films measured across the blue lines marked on the corresponding 2D AFM images. The scan area in all images is 100 μm^2.

6.5.2.2. Optical characterization

The UV-vis optical absorption spectrum of the as-prepared 1:2 mixed films is characterized by a band envelope in the region between 300 – 400 nm, a broad band centered at 442 nm, and a sharp absorption band at longer wavelength, centered at 670 nm (Figure 6.10a). After annealing, a hypochromism between 300 and 400 nm, with the appearance of a broad band centered at *ca.* 575 nm, and a red shift of the band at longer wavelengths (*ca.* 13 nm) are observed (Figure 6.10b). Analogous results are obtained for 1:1 and 2:1 mixed films before and after annealing (Figure A29).

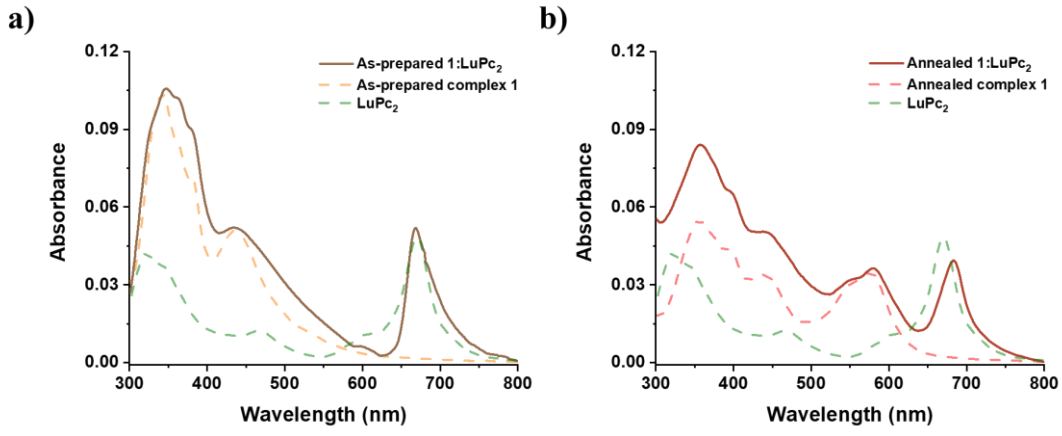

Figure 6.10. UV-vis absorption spectra of as-prepared **(a)** and annealed **(b)** 1:2 mixed films. The optical absorption spectra of complex **1** and $LuPc_2$ films are reported for comparison.

The optical microscope image of the as-prepared 1:2 mixed films (Figure 6.11a), acquired at 50× magnification, shows a uniform surface morphology with the presence of

small round dark spots. Raman spectra of these films were recorded on two different points on the surface, using a laser power of 0.12mW. In particular, spectra recorded on the round dark spots show several peaks in the range between 500 and 1750 cm^{-1}, almost entirely associated with those of the Raman spectrum of the $LuPc_2$ films (Figure 6.11b). Instead, Raman spectra recorded in the other areas, different than the round dark spots, are mostly related to the Raman spectrum of films of **1** (Figure 6.11c). Very similar Raman spectra are observed for 1:2 mixed films after thermal annealing (Figure A30).

Comparable Raman spectra were also achieved for 1:1 and 2:1 mixed films.

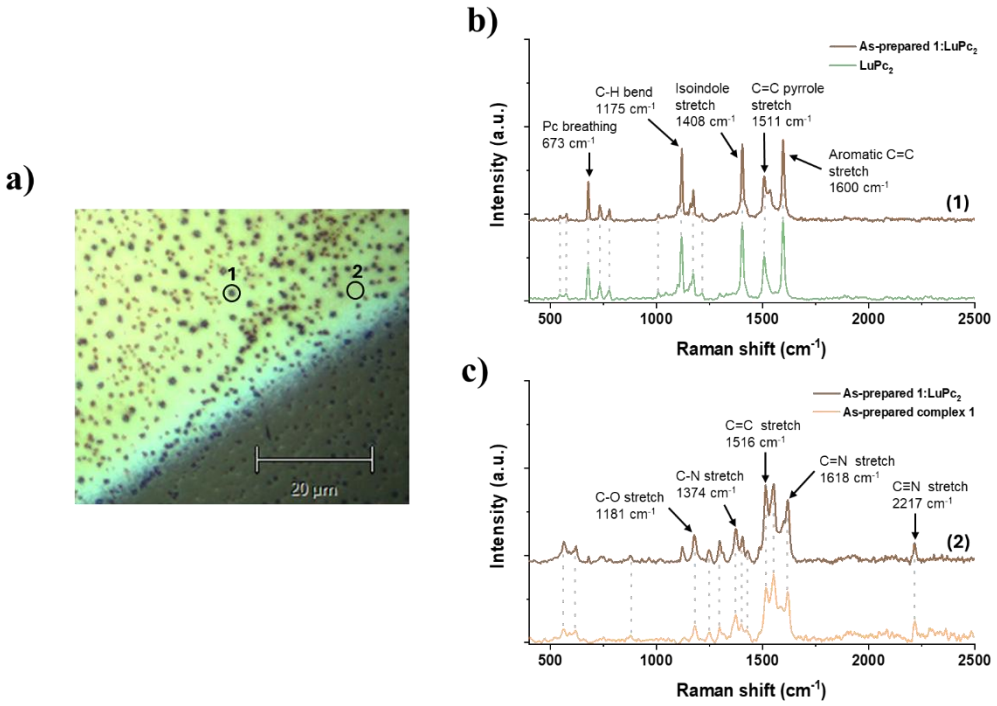

Figure 6.11. **(a)** Optical microscope image of the surface of as-prepared 1:2 mixed film. **(b**, **c)** Raman spectra (laser power of 0.12 mW) from two different spots of the as-prepared 1:2 mixed film (spectra (1) and (2) are from circles 1 and 2 in Figure 6.11a). The Raman spectra of complex **1** and $LuPc_2$ films are reported for comparison.

6.5.2.3. Electrical properties

The I – V characteristic of the as-prepared 1:2 mixed films shows a symmetric non-linear behavior of the current upon the applied voltage in a range between -10 to +10 V (Figure 6.12a), with an extrapolated U_{th} value of 6.32 V. The current intensity at 10 V is *ca*. ten times higher than that of the as-prepared **1**/$LuPc_2$ bilayers. After annealing, a higher conductivity and a similar trend of the I – V curve are observed. In this case, a lower U_{th} value than that of the as-prepared films is extrapolated (6.12 V). Symmetric non-linear curves are also obtained for the as-prepared and annealed 1:1 and 2:1 mixed films (Figure A31). Again, a higher conductivity is observed for the annealed films in all cases.

Impedance spectroscopy measurements of as-prepared 1:2 mixed films were performed under the same experimental conditions described for bilayers. The presence of one full semicircle is observed for the as-prepared films (Figure 6.12b). In the Nyquist plots, a high decrease in the amplitude of the semicircle is observed by increasing the DC bias up to 10 V.

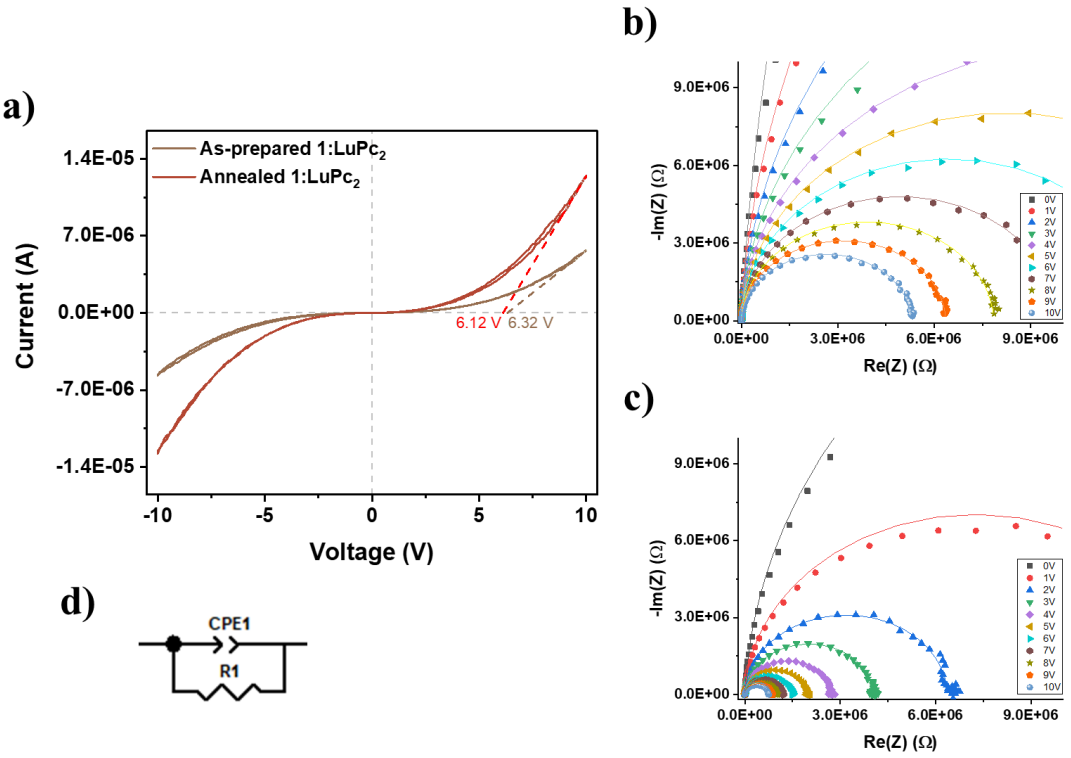

Figure 6.12. **(a)** I – V characteristics of as-prepared and annealed 1:2 mixed films. Nyquist plots of as-prepared **(b)** and annealed **(c)** 1:2 mixed films. The impedance response for each film was recorded at different DC voltage and fitted using the reported equivalent circuit **(d)**.

Even for the 1:2 annealed mixed films only a semicircle is observed (Figure 6.12c). According to the higher conductivity of the annealed films, a lower amplitude of the semicircle under the same applied DC bias is obtained for mixed films after annealing. Similar results are obtained for 1:1 mixed films (Figure A32), while the very low conductivity of 2:1 mixed films prevents the formation of any semicircle (Figure A33). For all the mixed films involved, the resulting impedance signal is adequately described by an equivalent circuit composed of one-component R-CPE element (Figure 6.12d).

6.5.2.4. Ammonia exposure experiments

Exposure experiments to gaseous NH_3 were performed only on 1:2 mixed films because of their higher conductivity compared to that of 1:1 and 2:1 films.

Upon exposure to 90 ppm of NH_3, a significant decrease in the current is observed for the as-prepared mixed films, with a rapid and almost complete restoration of the initial current under synthetic air (Figure 6.13a). A mean difference in current intensity after and before NH_3 exposure of *ca.* -6.81×10^{-7} A, and also a RR value of -39.9% are calculated. On the other hand, an increase in the recorded current is observed for the annealed 1:2 mixed films after exposure to NH_3 (Figure 6.13b), characterized by an almost complete restoration of the initial current under synthetic air, at least starting from the third exposure/desorption cycle. In this case, a mean current variation of $+13.3 \times 10^{-7}$ A and a RR value of +133.9% are obtained.

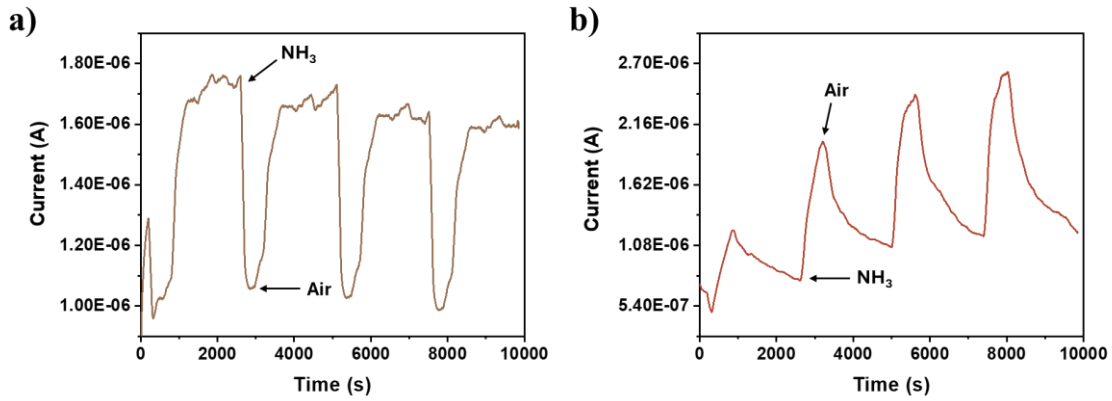

Figure 6.13. Current response to subsequent NH_3 exposure (90 ppm, 4 cycles) of as-prepared **(a)** and annealed **(b)** 1:2 mixed films. Exposure experiments were conducted considering an exposure and recovery time of 10 and 30 min, respectively.

Exposure to different NH_3 concentrations were also performed for 1:2 mixed films (Figure A34). Considering the same exposure conditions used for bilayers, relevant changes in the current intensity are observed both in as-prepared and annealed **1**:$LuPc_2$ mixed films for all the investigated concentrations (10 – 90 ppm, steps of 20 ppm). Analogously to the exposure to 90 ppm NH_3, a significant decrease in current is observed for the as-prepared films, while an increase in current is obtained for the annealed films. A slight increase of the baseline is observed for both as-prepared and annealed mixed films.

6.6. Discussion

The morphological, optical and electrical properties of as-prepared and annealed **1**/$LuPc_2$ bilayer and **1**:$LuPc_2$ mixed films were investigated and compared, with the aim of probing the architecture of the related heterojunctions and developing simple and low-cost conductometric gas sensors. For the preparation of bilayers, drop-casting of **1** was used, followed by thermal evaporation of $LuPc_2$ under secondary vacuum, while for the mixed 1:$LuPc_2$ films, the solution processing approach was used, using mixed THF solutions. In both cases, a very good surface coverage of the ITO-IDEs substrates was observed, resulting in the formation of films with high uniformity.

Starting from morphological investigations, a completely different surface topography is observed from the comparison of bilayers with mixed films, as expected. In particular, a uniform rough surface of the $LuPc_2$ top layer is observed from 3D and 2D AFM images of as-prepared and annealed **1**/$LuPc_2$ bilayers. On the other hand, as-prepared and annealed 1:2 mixed films are characterized by the growth of pillar-like structures, with higher height and width of the pillars in the latter case. Comparing 1:1 and 2:1 mixed films with 1:2 mixed films, increasing the **1**:$LuPc_2$ mass ratio in the films leads to the formation of an alveolar network.

Raman spectroscopy measurements of the as-prepared bilayers, recorded using a laser power of 0.12 mW, show several peaks in the range between 500 and 1750 cm^{-1}, all of which can be associated with those of $LuPc_2$ films, consistent with the composition of the top layer

in the bilayers. Instead, Raman spectra recorded using a higher laser power (6.0 mW) can be mainly associated with those of films of **1**, thus reflecting the composition of the lower layer. In the case of 1:2 mixed films, surface optical microscope images and Raman spectra, the latter compared with those of the pure complex **1** and $LuPc_2$ films, provided information on their composition. The optical microscope images of as-prepared and annealed 1:2 mixed films show a uniform surface morphology with the presence of small round dark spots. The Raman spectra recorded in these spots can be almost entirely associated with those of the Raman spectrum of $LuPc_2$ films, while those recorded in the other areas, different than the round dark spots, are mostly related to the Raman spectrum of films of **1**. Therefore, optical microscope images and Raman spectra of as-prepared and annealed 1:2 mixed films suggest the segregation of $LuPc_2$ in small domains (*ca.* 0.5 μm) dispersed into a matrix of **1**, also related with the pillar-like structures observed in the corresponding AFM morphological images (Scheme 6.1b). Consequently, the Raman spectra of annealed 1:2 mixed films appears very similar to those of the as-prepared mixed films, since annealing only leads to an increase in the height and width of the pillars, *i.e.*, of $LuPc_2$ domains. Bilayer and 1:2 mixed films are sketched in Scheme 6.1.

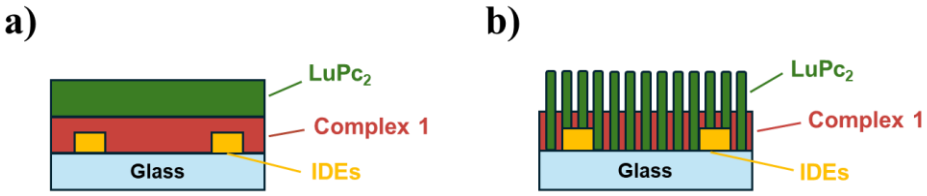

Scheme 6.1. Schematic view of the structure of bilayer **(a)** and 1:2 mixed films **(b)**.

From optical absorption measurements, some interesting differences can be observed between as-prepared and annealed bilayers and mixed films. UV-vis absorption spectra of bilayer films appear quite similar before and after annealing, except for the different absorbance of the band centered at 575 nm, associated with J-type aggregates in complex **1** after the phase-transition.[240] However, it seems that in the case of the as-prepared **1**/$LuPc_2$ bilayers the presence of the broad band at *ca.* 570 nm could be due to a partial phase-transition occurred under vacuum during the evaporation of $LuPc_2$. In fact, from a comparison between absorption spectra of bilayers with those of the starting materials, all the observed bands in the region between 300 – 600 nm can be mainly related to complex **1**, except for the longer wavelength peak related to the Q-band of $LuPc_2$. Analogously to bilayers, all the bands observed in UV-vis absorption spectra of as-prepared and annealed mixed films can be associated with the two starting materials. More interestingly, in addition to the appearance of band centered at 575 nm associated with the J-type aggregates in **1**, a red shift of the Q-band of $LuPc_2$ (from 670 to 683 nm) is observed after annealing for all the mixed films, independently of the amount of the two materials in the film. These two main features indicate a significant reorganization of the molecular materials in mixed films during the annealing process. Therefore, it can be hypothesized that the phase transition of **1** induces an increase of intermolecular π-π interactions in $LuPc_2$ domains, with a consequent red-shift of the Q-band.

The investigation on the electrical properties of bilayers and mixed films were initially performed by I – V measurements. A symmetric non-linear I – V curve in a range of applied bias from -10 V to +10 V is observed for all as-prepared **1**/$LuPc_2$ bilayer and **1**:$LuPc_2$ mixed films. The same I – V curve shape characterizes all the investigated bilayer and mixed films after thermal annealing, but a decrease in the extrapolated U_{th} values is observed with a consequent increase in their conductivity. Note that, the non-linear behavior of the I – V curves can be related to the different work functions of the starting materials involved, although the I – V curves of both pure materials are characterized by a linear trend. In particular, I – V curves of complex **1** and $LuPc_2$ pure materials are characterized by completely different conductivity compared to bilayers, complex **1** is highly resistive in both as-prepared and annealed films (Figure A35), while $LuPc_2$ films possess higher conductivity (Figure A36). This difference in their electrical conductivity can be related to a different energy gap. In fact, higher energy gap values are obtained from Tauc plots for as-prepared and annealed films of complex **1** (2.55 eV and 2.04 eV, respectively) (Figure A37) compared to that of $LuPc_2$ (0.5 eV), as previously determined by photoemission spectroscopy and electrochemistry.[453] The decrease in the energy gap of **1** on passing from as-prepared to annealed films can also explain the increased conductivity of bilayer and mixed films after thermal annealing. Another interesting point is that from the I – V characteristics it is evident that the conductivity of the mixed films can be easily tuned by changing the **1**:$LuPc_2$ mass ratio in the film (Figure A38), and a change in the U_{th} values is observed by varying the $LuPc_2$ content in the films, from 4.11 V to 6.32 V when switching from 2:1 to 1:2 as-prepared films, and the same trend is observed for the annealed films, with smaller values (from 3.60 V to 6.12 V, respectively). The higher U_{th} values for mixed films compared to bilayers can be attributed to the different morphology of the films. In fact, on the basis of AFM and Raman measurements, **1**:$LuPc_2$ mixed films can be considered as a series of conductometric $LuPc_2$ domains dispersed into the low conducting matrix of **1** (see, morphological and optical analysis), resulting in a series of interfaces from one electrode to the other. However, this low conducting matrix is more conductive than a layer of pure complex **1** because it may contain small amounts of $LuPc_2$.

Further studies on the electrical properties of bilayer and mixed films were performed by impedance spectroscopy measurements in a range of frequencies from 100 Hz to 10 MHz, and at a constant AC bias (100 mV). As expected, two semicircles having different amplitudes are observed in Nyquist plots of as-prepared bilayers. The high and low frequency semicircles can be attributed to bulk and interfaces, respectively.[445] A decrease of the amplitude of the low frequency semicircle is observed by increasing the DC voltage from 0 up to 10 V, consistent with an increase of the interfacial charge transport, suggesting the presence of a sharp interface, as in PHJs. On the other hand, the Nyquist plots of the as-prepared 1:2 mixed film show the presence of only one full semicircle, suggesting a microscopic structure formed by a series of interfaces between **1** and $LuPc_2$ aggregates, consistent with the above description, as in BHJs.[454,455] A decrease in the amplitude of the low frequency semicircle for bilayers and for the full semicircle in the case of 1:2 and 1:1 mixed films is observed on passing from as-prepared to annealed films, in agreement with the increase in the conductivity shown in the corresponding I – V characteristics. The impedance signals obtained for bilayer and mixed films were fitted using the ZView software

(Scribner Associates Inc.),[456] considering equivalent circuits composed of resistances (R) and constant phase elements (CPEs) connected in parallel. The simplest circuit formed by a one-component R-CPE element (Figure 6.12d) is known as the Randles circuit. The total impedance *Z(ω)* of this circuit is calculated using the following formula:[457,458,459]

$$Z(\omega) = \frac{R}{1+(j\omega)^{\alpha}RQ} \quad \textbf{(6.2)}$$

where R is the charge-transfer resistance, j is the imaginary unit, ω is the frequency, Q and α are CPE parameters.

The simple Randles circuit can be extended to describe multiple semicircles observed in Nyquist plots by combining multiple Randles circuits in series. For example, in the case of a circuit composed by two-component Ri-CPEi elements (Figure 6.7d), the previous equation (eq. 6.2) for the calculation of *Z(ω)* becomes:

$$Z(\omega) = \frac{R_1}{1+(j\omega)^{\alpha_1}R_1Q_1} + \frac{R_2}{1+(j\omega)^{\alpha_2}R_2Q_2} \quad \textbf{(6.3)}$$

where R_1 and R_2 are the charge-transfer resistances related to the bulk and interfaces, respectively, j is the imaginary unit, ω is the frequency, and Q_1, Q_2, α_1, and α_2 are CPE parameters related to the bulk and interfaces, respectively.

Therefore, charge transport parameters such as R, α, and Q of as-prepared and annealed 1:2 mixed films and bilayers were determined using the ZView software from eq. 6.2 and eq. 6.3, respectively (Figure A39 and Figure A40). A constant value of R_1 and an exponential decay of R_2 are shown under an increasing DC bias for the as-prepared and annealed bilayers. A similar trend, but with a ten times lower resistance values, are obtained for the as-prepared and annealed 1:2 mixed films compared to bilayer films. Furthermore, very similar values of α (between 0.92 and 0.98) are obtained for the as-prepared and annealed bilayer and mixed films, and comparable Q values are observed for mixed films with Q_1 values in bilayers.

The sensing performance of bilayers and 1:2 mixed films, before and after annealing, in the presence of pollutant gases was explored to evaluate their potential application as conductometric gas sensors. In particular, it was tested at specific concentrations of NH_3 (in the range 10 – 90 ppm), chosen as reference substance, and at a constant RH value (45%), and then compared with the sensing performances of the starting materials.

Comparing the electrical response of as-prepared bilayer and 1:2 mixed films after exposure to 90 ppm of NH_3 for 10 min, a decrease in current is observed in both cases. For as-prepared bilayer films, an RR almost identical to that of the pure $LuPc_2$ films is obtained (-4.12% *vs.* -4.74%), while a tenfold higher RR characterizes the 1:2 mixed films (-39.9%). On the other hand, a similar response is observed for the annealed bilayers after exposure to NH_3 (decrease in current intensity), while an increase in current intensity involves the annealed 1:2 mixed films. In both cases the calculated RR is higher than before annealing (-8.01% and +134%, respectively). Therefore, the bilayers behave essentially as pure $LuPc_2$ films, with a decrease in current intensity after exposure to NH_3 (Figure A36). It is also important to highlight that the electrical response of $LuPc_2$ films remains unchanged even after heat treatment, while no relevant current response is observed for the as-prepared and annealed films of **1**.

To further evaluate the NH_3 sensing performance of bilayer and mixed films, exposure to different concentrations of NH_3 (from 10 to 90 ppm) were performed. According to exposure experiments to 90 ppm of NH_3, a decrease in current is observed for all the concentrations investigated in bilayers and as-prepared 1:2 mixed films, while a relevant increase of the current intensity involves annealed 1:2 mixed films. Comparing the RR response of bilayers to that obtained for $LuPc_2$ films (Figure A41), a lower calculated RR is obtained for as-prepared bilayer films for each NH_3 concentration (from -0.55% to -1.3%), while a comparable response is achieved in the case of annealed bilayers (from -0.78% to -2.1%). It is very interesting to note that in the case of as-prepared 1:2 mixed films a five-fold higher RR (from -9.5% to -13%) and an almost ten-fold higher RR for annealed 1:2 mixed films (from +8.5% to +24%) is obtained compared to bilayer and $LuPc_2$ films. Therefore, these comparisons show that both bilayers and 1:2 mixed films can discriminate different NH_3 concentrations in a range of 10 – 90 ppm, with larger variations for the latter.

On the basis of the electrical response achieved for bilayer and 1:2 mixed films after exposure to NH_3, two different mechanisms can be considered. In the case of bilayers, physisorption of NH_3 molecules occurs on the surface of the $LuPc_2$ top layer. This phenomenon causes a decrease in current intensity due to the interaction between NH_3 with $LuPc_2^+$, as the majority charge carriers, to give the neutral $LuPc_2$ form and induce a decrease in the density of positive charge carriers at the interface.[460] Because of the similar behavior observed for as-prepared 1:2 mixed films in the presence of NH_3, a similar physisorption mechanism can be proposed, but the conductive pathway followed by the charge carriers should be from one conductometric $LuPc_2$ domain to another. In this case, the pillar structures of the $LuPc_2$ domains allow for a larger number of adsorption sites for NH_3, resulting in a larger surface area exposed to the gas compared to the top layer of $LuPc_2$ in the bilayer heterojunctions. Therefore, the larger decrease in positive charge carriers and the higher RR can be explained on the basis of the different architecture of the heterojunction. After annealing, the observed current increase is likely due to a decrease of the energy barrier at the interface between $LuPc_2$ crystals and complex **1** under NH_3, leading to a current increase.

6.7. Conclusion

This chapter reports on the preparation and characterization of organic heterojunctions containing two metal complexes characterized by different conductivity, namely complex **1** (low conductivity) and $LuPc_2$ (conductive). **1**/$LuPc_2$ bilayers and **1**:$LuPc_2$ mixed films on ITO-IDEs were prepared through drop-casting/thermal evaporation and solution-processing approach, respectively. Since complex **1** is characterized by a thermally-induced phase transition, annealed films were obtained from the as-prepared films. The morphological, optical and electrical properties of both as-prepared and annealed films were studied.

Morphological characterization of films performed by AFM measurements shows a uniform rough surface in the case of bilayers, while a pillar-like or alveolar structure characterizes mixed films, depending on the mass ratio of the two materials in the films.

The composition of as-prepared and annealed films was determined by Raman spectroscopy, showing characteristic peaks of the two starting materials for both **1**/$LuPc_2$

bilayers and **1**:$LuPc_2$ mixed films, also suggesting the absence of degradation processes after thermal treatment. Optical microscope images of 1:2 mixed films show a uniform surface morphology with the presence of small round dark spots, which can be related to the pillars observed in the corresponding AFM images, and can be attributed to segregated $LuPc_2$ domains as suggested by related Raman spectra.

Further investigations on the optical properties of as-prepared and annealed bilayer and mixed films were performed by UV-vis absorption spectroscopy. All the absorption bands observed in UV-vis absorption spectra of as-prepared and annealed bilayer and mixed films can be associated with the two starting materials, and a significant change in absorption spectra is observed upon thermal annealing of both types of films, in accordance with the changes induced by the irreversible phase transition of complex **1**. In the case of mixed films, the relevant red shift of the Q-band associated with $LuPc_2$ observed after thermal treatment suggest a reorganization of the molecular materials during the annealing process, associated with an increase in intermolecular π-π interactions in $LuPc_2$ domains induced by the phase transition of **1**.

The electrical properties of bilayer and mixed films were evaluated by I – V and impedance spectroscopy measurements. Higher conductivity and U_{th} value are obtained from I – V characteristics of as-prepared 1:2 mixed films compared to as-prepared bilayers, and can be attributed to the different morphology of the films, as demonstrated from morphological and Raman characterizations. A decrease in the U_{th} value, followed by a consequent increase in the conductivity, is observed for both bilayer and mixed films upon thermal treatment. More interestingly, impedance spectroscopy measurements indicate the presence of a sharp interface between the two materials in bilayer films, according to the formation of PHJs, while in the case of 1:2 mixed films a series of small interfaces between aggregates **1** and $LuPc_2$ as in BHJs is suggested, consistent with morphological and Raman investigations.

The potential application of both bilayer and mixed films as conductometric gas chemosensors was also investigated. Exposure experiments to NH_3 result in a significant decrease in current for both as-prepared bilayer and 1:2 mixed films, with a tenfold higher RR in the second case. An increase of the RR is obtained for both bilayer and mixed films after thermal annealing, with an inversion of the response to NH_3 in the latter case.

Overall, the different electrical properties of **1**/$LuPc_2$ bilayers and **1**:$LuPc_2$ mixed films are mainly related to the different architecture of the heterojunction. An improved NH_3 sensing performance is obtained for as-prepared and annealed 1:2 mixed films compared to bilayers, with the advantage of a simpler preparation method, highlighting the unique behavior of these heterojunction devices.

Chapter 7

Conclusions

Air pollution is one of the major problems of recent years, caused by the spread of industries and the increase in human population. Much of the current research activity is focused on the development of new chemosensors with optical and electrical properties that have several advantages, such as simple, rapid, and on-site detection of these pollutants compared to classical detection methods.

This PhD thesis covers several aspects concerning the development of novel chemosensors based on Zn(salen)-type vapochromic complexes for the selective and sensitive detection of air pollutants, such as N-VOCs and ammonia. In particular, the synthesis of chemosensors, their characterization, optimization of their deposition on suitable substrates, appropriate storage conditions, setup for exposure experiments, and selective and sensitive detection studies of specific analytes are reported. The main features obtained by exploring the optical properties of the PBFs of complexes **1** and **2** are summarized as follows.

First, the dip-coating approach was involved and optimized in the preparation of PBFs, allowing to obtain films with high optical uniformity, stability and repeatability, whose sensitivity towards the vapors of specific volatile analytes can be easily tuned by changing the amount of sensing material deposited on the paper substrates, simply by changing the concentration of the initial THF solution of complexes **1** and **2** used for film preparation.

1-PBFs and **2**-PBFs are characterized by a peculiar optical response and a very high sensitivity towards N-VOCs, such as BA, EDA and Py vapors, respectively. In particular, the annealed vapoluminescent **1**-PBFs enable the sensitive detection of BA vapors (by fluorescence enhancement) within a linear dynamic range from 0 to 50 ppm and with a LOD down to 2.0 ppm, lower than the PEL-C value (5.0 ppm) for BA vapors, and allow to discriminate the vapors of this volatile amine from those of volatile aliphatic diamines, in particular EDA. In the latter case, the vapoluminescent annealed **1**-PBFs show a very peculiar optical behavior (fluorescence quenching) after exposure to EDA vapors, which also allows their quantitative detection with high sensitivity (LOD = 6.6 ppm), lower than the PEL value of 10 ppm. The same optical behavior (fluorescence quenching) in the presence of EDA vapors characterizes the vapoluminescent as-prepared **1**-PBFs, also allowing the quantification of the IDLH value of 1000 ppm for this volatile diamine. BA vapor leakage simulation experiments enabled the quantification of PEL-C and IDLH values for BA using annealed and as-prepared **1**-PBF, respectively, demonstrating their practical use for real-time detection of indoor amine contamination in semi-confined environments. In the case of **2**-PBFs, the vapochromic response towards Py vapors allowed their selective detection over a very wide vapor concentration range, from 500 to 5000 ppm, including the IDLH value for this substance.

The high selectivity of **1**-PBF and **2**-PBF towards BA, EDA and Py, respectively, was demonstrated against different classes of VOCs and further confirmed by competitive

experiments. In the case of **1**-PBFs, they are also selective to BA with respect to other primary monoamines, with the exception of propylamine and *sec*-butylamine, especially at low concentrations (tens of ppm). **1**-PBFs also show a selective vapoluminescent response for EDA at low vapor concentrations (≤ 100 ppm) compared to other volatile aliphatic diamines. On the other hand, **2**-PBFs are characterized by a selective vapochromic response to Py vapors even in the presence of other volatile heterocyclic amines, with the exception of 4-methylpyridine.

On the other hand, the color changes of vapochromic **1**-PBFs and **2**-PBFs towards BA and Py, respectively, were detected using a very simple and effective quantification method involving the RGB color analysis. Since RGB values are very sensitive to changes in illumination, RGB values of the films before and after exposure to vapors from these volatile species were collected using a smartphone color recognition app, and then the normalized RGB values were used to calculate the color difference, ΔE_{rgb}. Therefore, this developed method has the main advantage of making color analysis independent of illumination and device, as a fundamental prerequisite for accurate quantitative detection of VOCs. The reliability of this approach was assessed by comparing the results of UV-vis reflectance spectra, obtaining comparable linear dynamic ranges and LOD values, results which are also comparable to those of vapoluminescence studies in the case of **1**-PBFs. Therefore, this RGB approach can represent a general method for VOCs detection using vapochromic materials on films.

Complex **1** (insulating material) in combination with $LuPc_2$ (conductive material) was further explored in the preparation and characterization of organic heterojunctions-based conductometric sensors. **1**/$LuPc_2$ bilayers and **1**:$LuPc_2$ mixed films on ITO-IDEs were prepared through drop-casting/thermal evaporation and solution-processing approach, respectively, resulting in completely different architectures, as planar heterojunctions and bulk heterojunctions, respectively, as deduced from their morphological, optical and electrical characterization. The potential application of both **1**/$LuPc_2$ bilayers and **1**:$LuPc_2$ mixed films as conductometric gas chemosensors was also investigated, resulting in relevant current intensity changes after exposure to NH_3 in a range from 10 up to 90 ppm. From the comparison of their sensing performance, **1**:$LuPc_2$ mixed films result more sensitive (higher variation in the current) than **1**/$LuPc_2$ bilayers, and very interestingly, an inversion of the response to NH_3 characterizes annealed **1**:$LuPc_2$ mixed films.

Overall, Zn(salen)-type complexes **1** and **2** are suitable molecular materials for the development of efficient electrical and optical sensors, as heterojunctions and vapochromic/vapoluminescence materials, respectively, characterized by very high selectivity and sensitivity towards air pollutants having Lewis basicity. Furthermore, these Lewis acid Zn(salen)-type complexes are environmentally "green", sustainable and low-cost materials compared to other molecular materials based on metal complexes. Vapochromic paper-based films of these complexes represent simple, cost-effective, reliable, highly stable, portable, and disposable/reusable chemosensors for the vapor-phase detection of specific N-VOCs. The combination of these film-based vapochromic chemosensors with a proper RGB color analysis also holds the potential for practical application of on-site, real-time monitoring of hazardous volatile amine vapors in occupational and environmental settings.

Appendix A

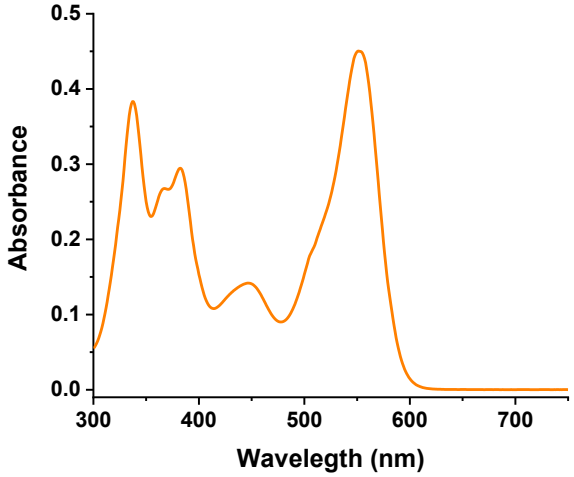

Figure A1. UV-vis spectrum of complex **1** (1.0×10^{-5} M solution in THF).

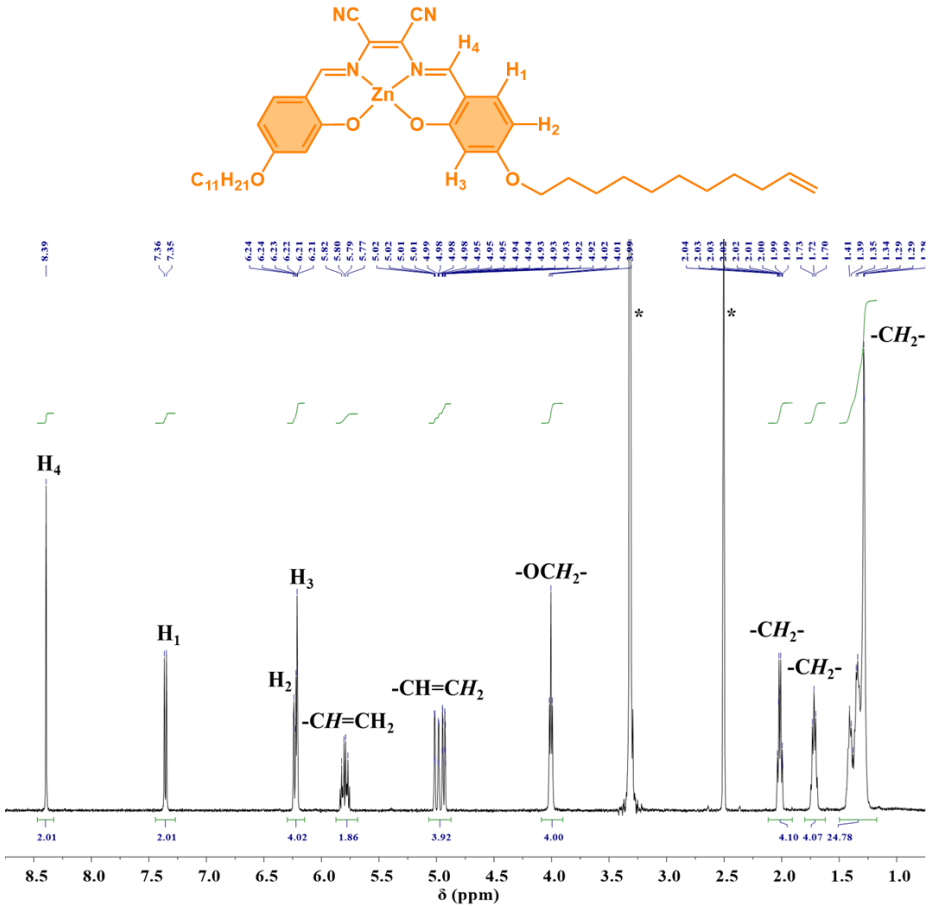

Figure A2. ^{1}H NMR spectrum of complex **1** in DMSO-d_6. Asterisked peaks refer to water and residual DMSO solvent signals.

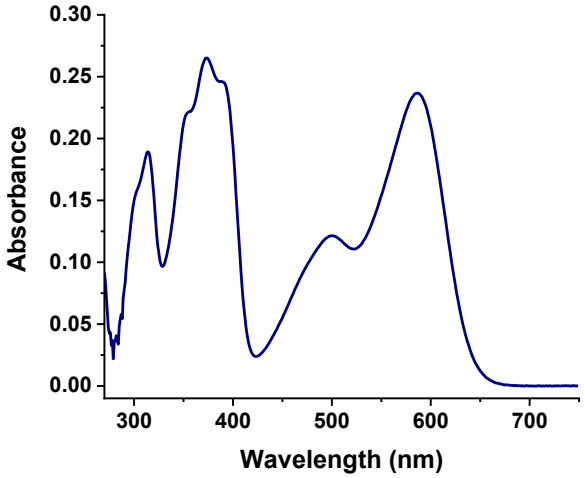

Figure A3. UV-vis spectrum of complex **2** (1.0×10^{-5} M solution in THF).

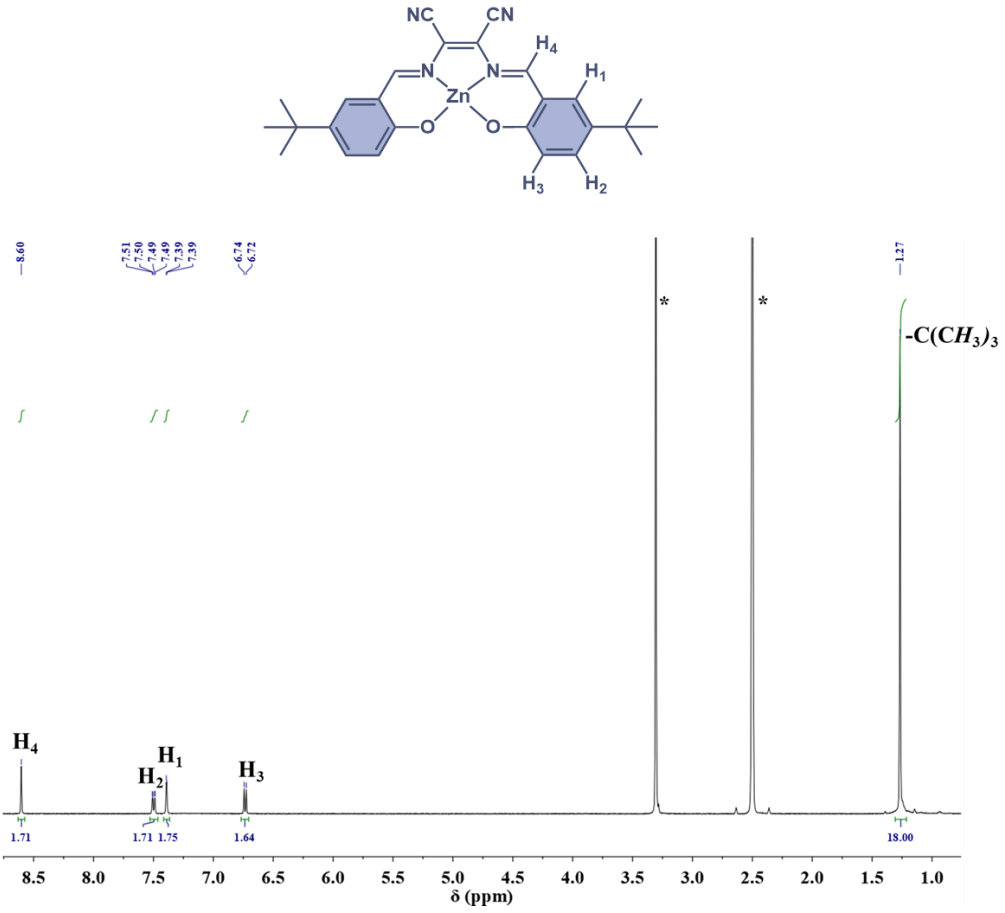

Figure A4. ^{1}H NMR spectrum of complex **2** in DMSO-d_6. Asterisked peaks refer to water and residual DMSO solvent signals.

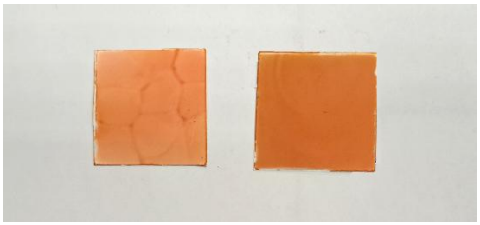

Figure A5. Complex **1** deposited on paper substrates by drop-casting (left) and dip-coating (right), from a THF solution of **1** (2.5×10^{-3} M).

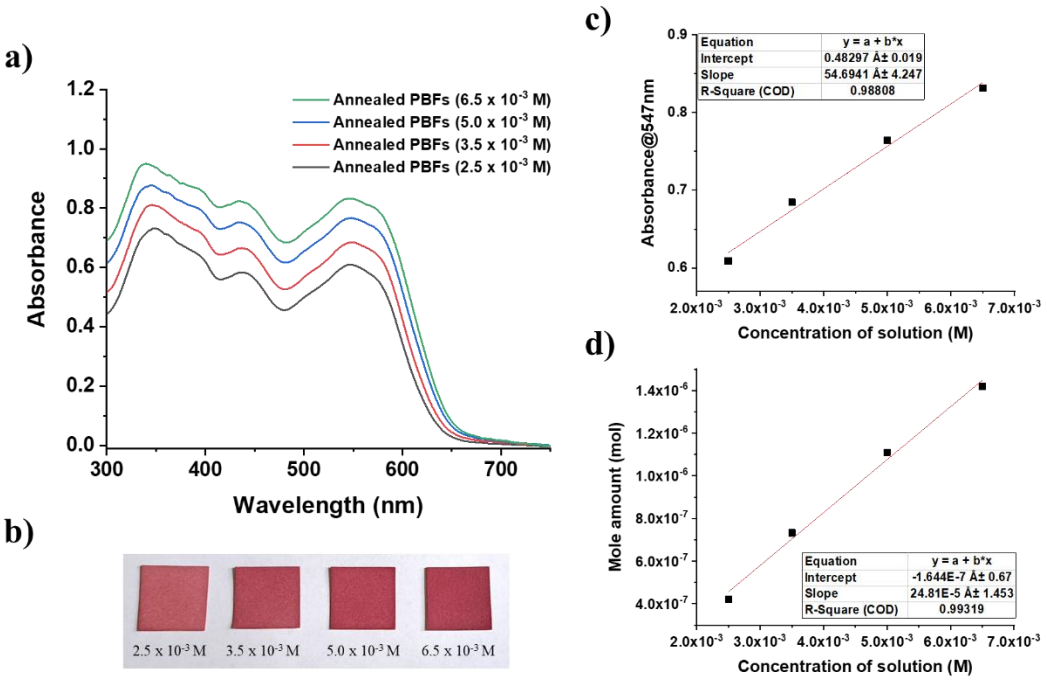

Figure A6. **(a)** UV-vis reflectance spectra and **(b)** photographic image of annealed **1**-PBFs prepared from THF solutions of **1** having different concentrations. **(c)** Variation of the absorbance at 547 nm as a function of the concentration of THF solutions used for the preparation of **1**-PBFs. **(d)** Linear fit of the mole amount of **1** absorbed on paper substrates as a function of the concentration of the solution used for the preparation of **1**-PBFs.

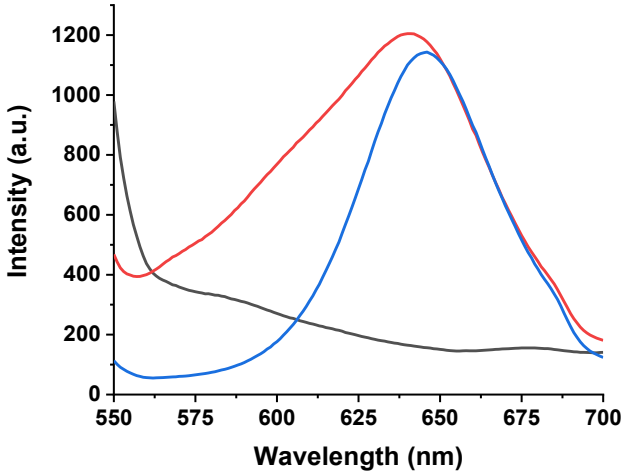

Figure A7. Comparison between fluorescence spectra of Whatman-4 filter paper (grey line) and **1**-PBFs obtained from a THF solution of **1** having a concentration of 2.5 × 10^{-3} M (red line) and 5.0 x 10^{-3} M (blue line).

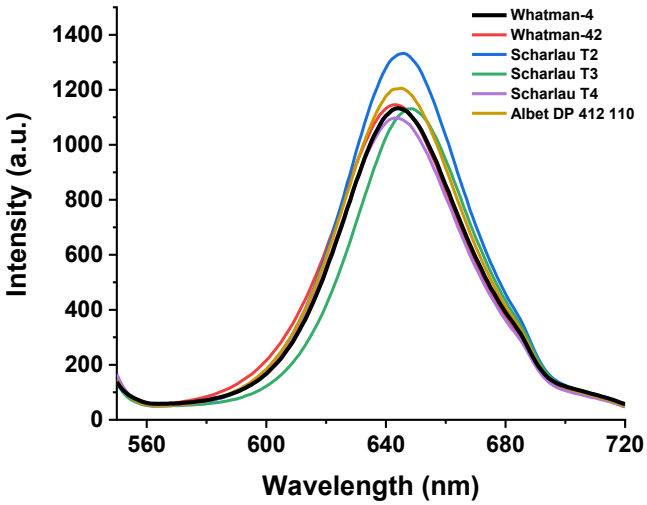

Figure A8. Fluorescence spectra of **1**-PBF5s prepared using different types of filter paper (λ_{exc} = 500 nm).

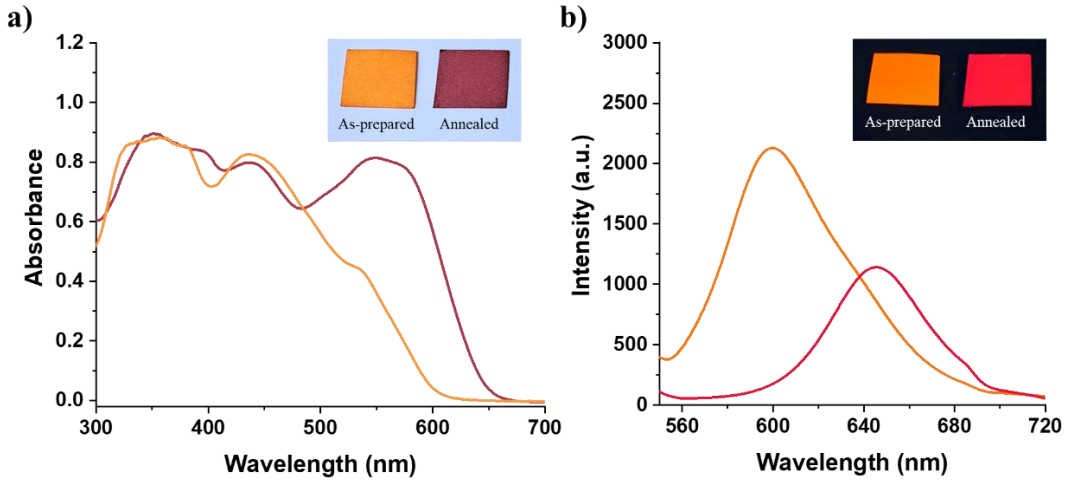

Figure A9. UV-vis reflectance **(a)** and fluorescence **(b)** spectra (λ_{exc} = 484 nm, related to an isosbestic point) of as-prepared and annealed **1**-PBF5s. Insets: photographic images of as-prepared and annealed films under natural light (left) and under 365 nm light (right).

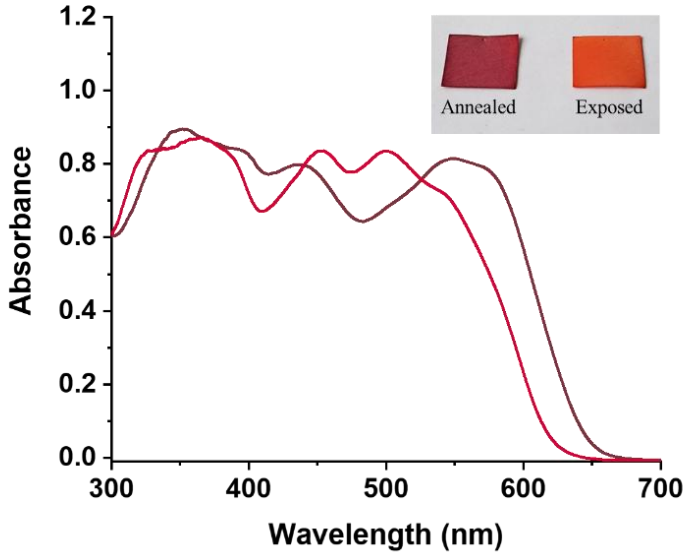

Figure A10. UV-vis reflectance spectra of annealed and exposed **1**-PBF5s. Insets: photographic image of annealed and exposed films under natural light.

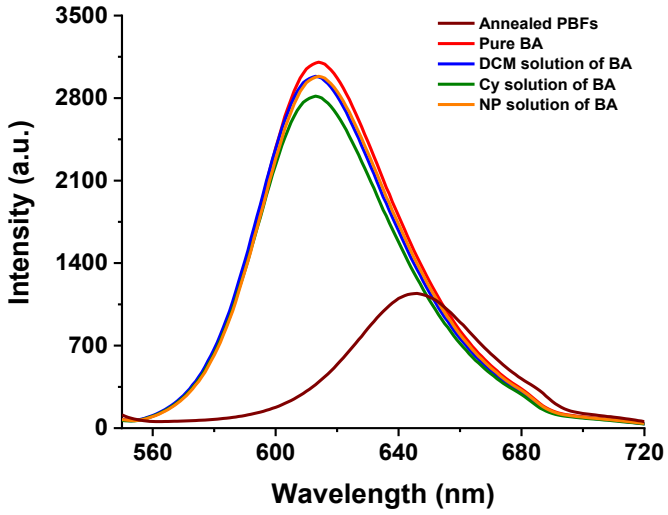

Figure A11. Fluorescence spectra of **1**-PBF5s (λ_{exc} = 500 nm) exposed to 500 ppm of BA vapors obtained by complete evaporation of pure liquid, a solution of DCM, a solution of Cy and a solution of NP.

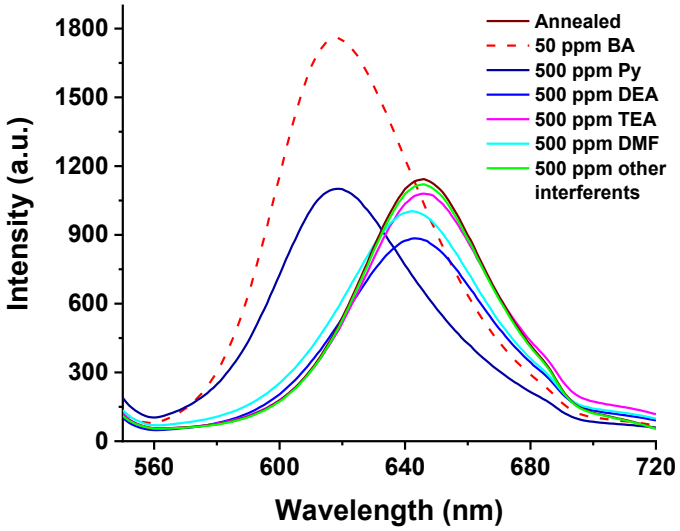

Figure A12. Fluorescence spectra of **1**-PBF5s (λ_{exc} = 500 nm) exposed to 500 ppm of interferent. The spectrum after exposure to 50 ppm of BA vapors (dotted line) is reported for comparison.

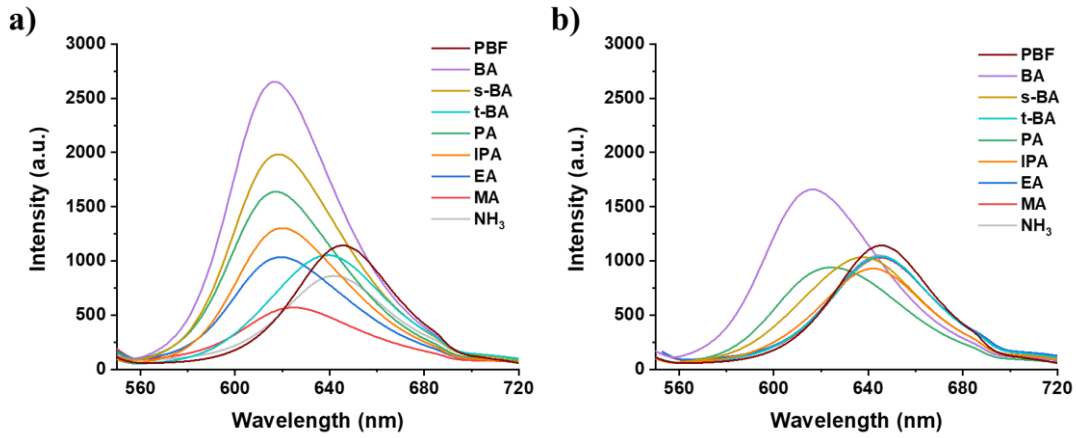

Figure A13. Fluorescence spectra of **1**-PBF5s (λ_{exc} = 500 nm) exposed to **(a)** 300 ppm and **(b)** 50 ppm of different linear aliphatic monoamine vapors.

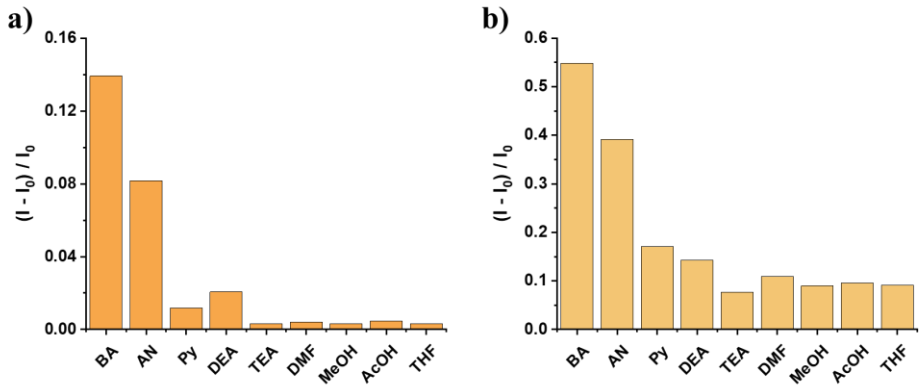

Figure A14. Absorbance intensity of as-prepared **(a)** **1**-PBF5s and **(b)** **1**-PBF1s after static exposure to different VOCs at 300 ppm. In the diagram I is the absorbance intensity after exposure and I_0 is the absorbance intensity of the starting as-prepared **1**-PBF5s and **1**-PBF1s at λ_{abs} = 497 nm.

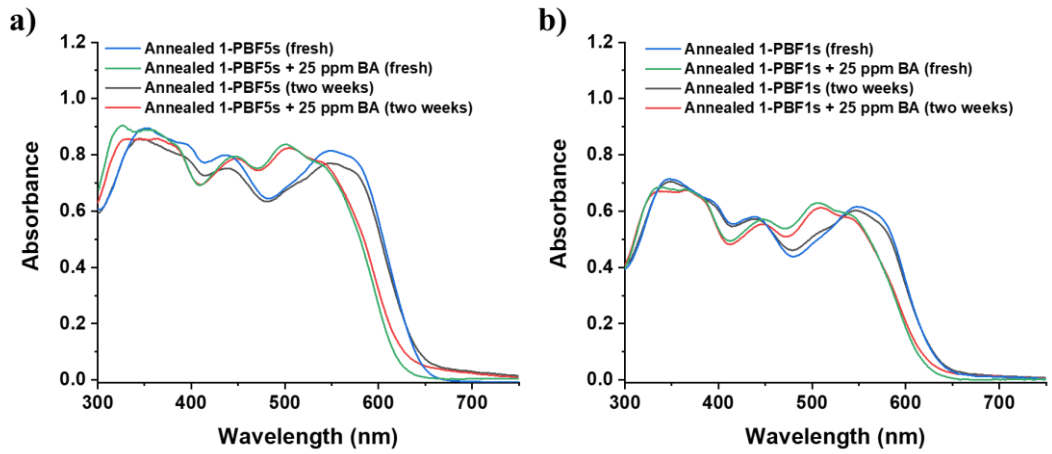

Figure A15. UV-vis reflectance spectra of annealed **(a)** **1**-PBF5s and **(b)** **1**-PBF1s freshly prepared and stored in the dark for two weeks, exposed to 25 and 15 ppm of BA, respectively.

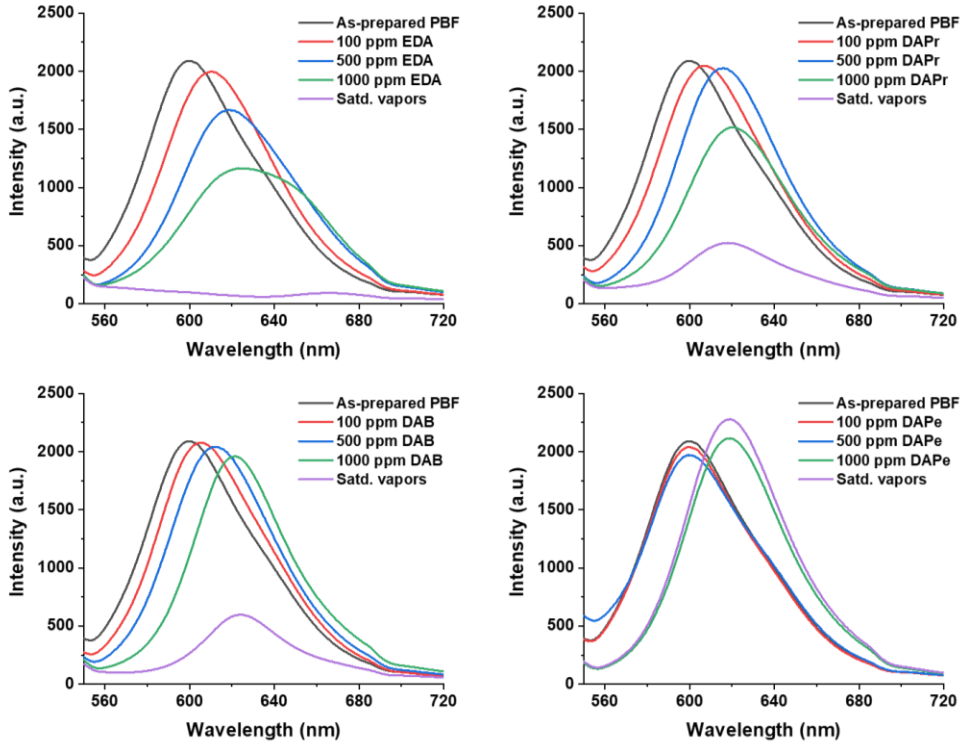

Figure A16. Fluorescence spectra of as-prepared **1**-PBF5s (λ_{exc} = 520 nm) before and after exposure to different vapor concentrations of studied volatile aliphatic diamines.

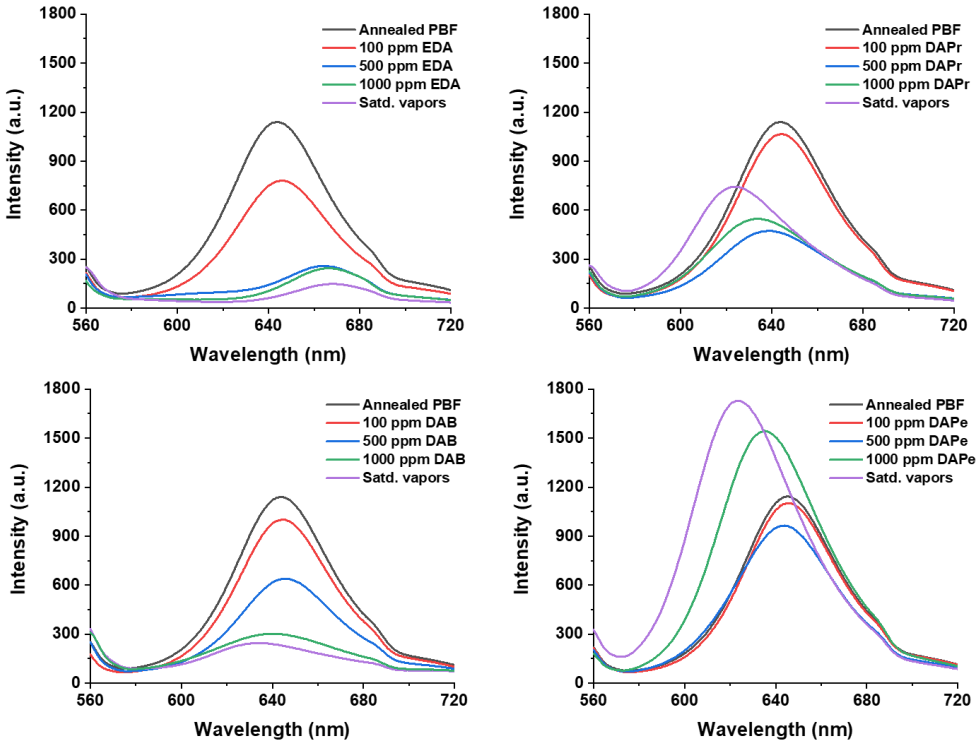

Figure A17. Fluorescence spectra of annealed **1**-PBF5s (λ_{exc} = 520 nm) before and after exposure to different vapor concentrations of studied volatile aliphatic diamines.

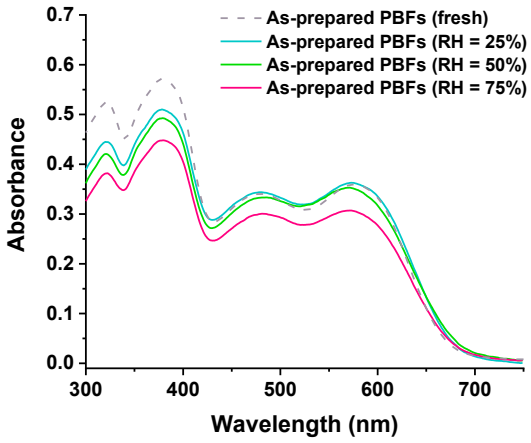

Figure A18. UV-vis reflectance spectra of as-prepared **2**-PBF1s stored in the dark (50 lux) at different RH conditions after five days. UV-vis reflectance spectra of freshly-prepared **2**-PBF1s (dotted line) is reported as reference.

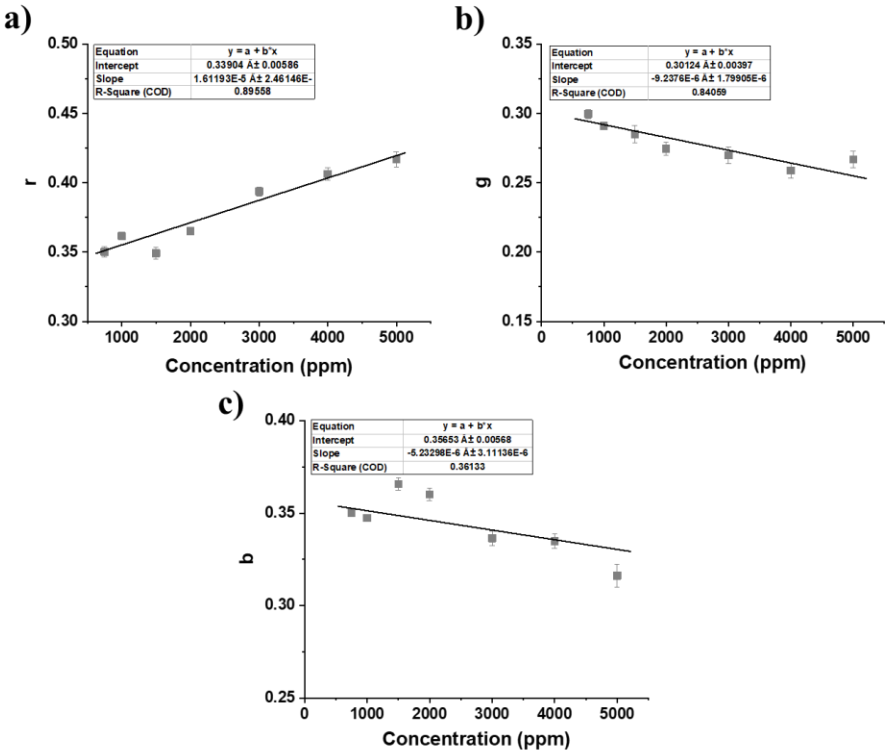

Figure A19. Mean r **(a)**, g **(b)**, and b **(c)** values of **2**-PBF1s as a function of the concentration Py vapors and the related linear best fit in the range 750 – 5000 ppm (weight given by data error bars).

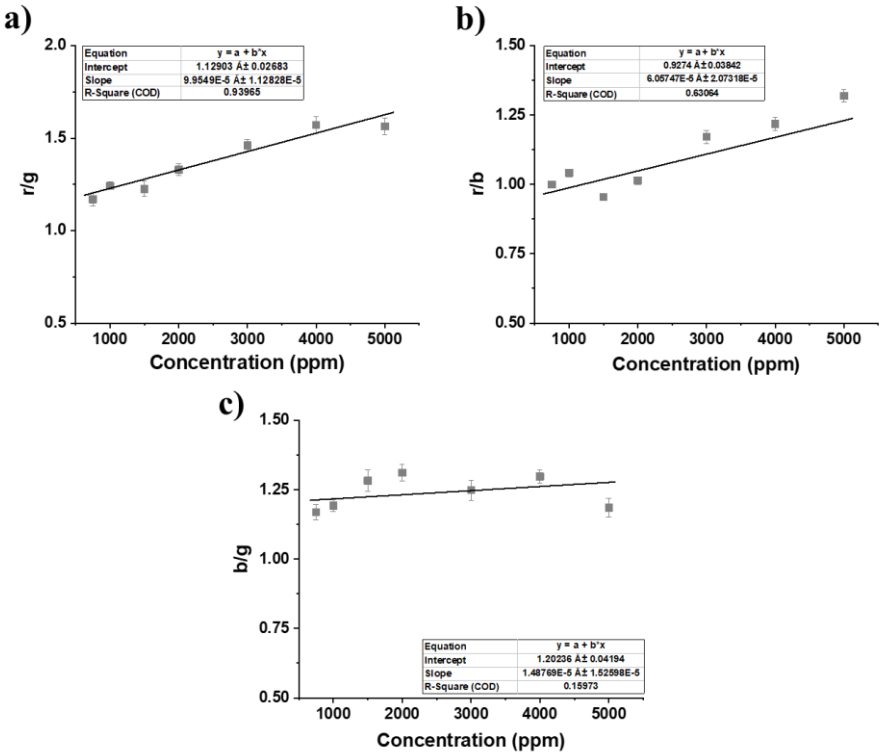

Figure A20. Mean r/g **(a)**, r/b **(b)** and b/g **(c)** ratios of **2**-PBF1s as a function of the concentration of Py vapors and the related linear best fit in the range 750 – 5000 ppm (weight given by data error bars).

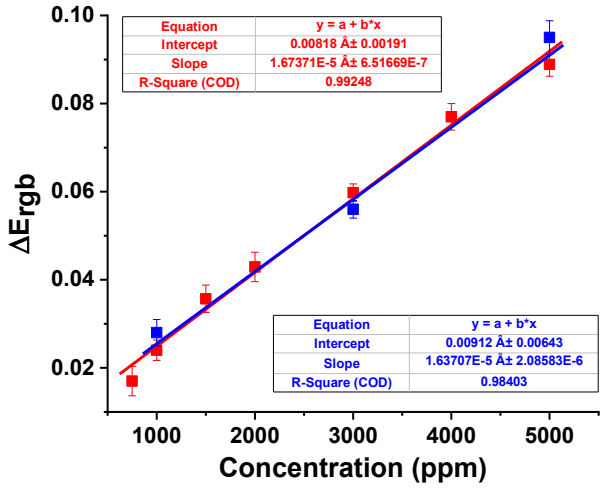

Figure A21. Mean ΔE_{rgb} values of **2**-PBF1s as a function of the concentration of Py vapors and the related linear best fits: from the set of replicate measurements (at 1600-2000 lux) using the Samsung Galaxy S23 smartphone (means and fit in red); from the independent set of experiments using three different smartphones (Samsung Galaxy S23, Xiaomi MI A3, and iPhone 12 Pro Max) under different lighting conditions (1800 lux and 30 lux) (means and fit in blue). Error bars indicate standard deviation of the means.

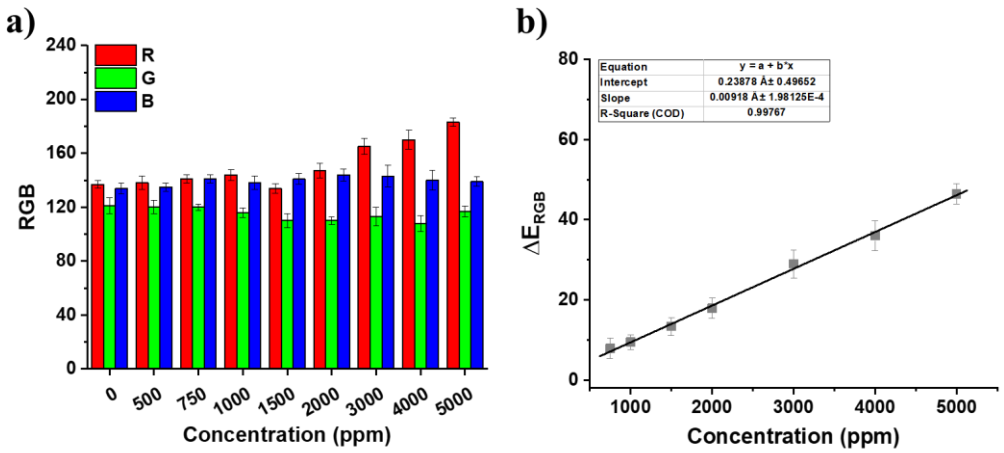

Figure A22. **(a)** Mean rgb values of **2**-PBF1s before and after exposure to Py vapors. **(b)** Mean ΔE_{rgb} values as a function of the concentration of Py vapors and the related linear best fit in the range 750 – 5000 ppm (weight given by data error bars).

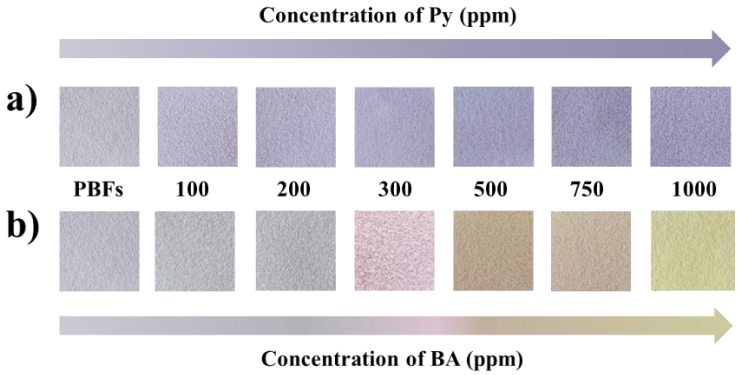

Figure A23. Photographic images of **2**-PBF4s before and after static exposure to an increasing concentration of Py **(a)** and BA **(b)** vapors.

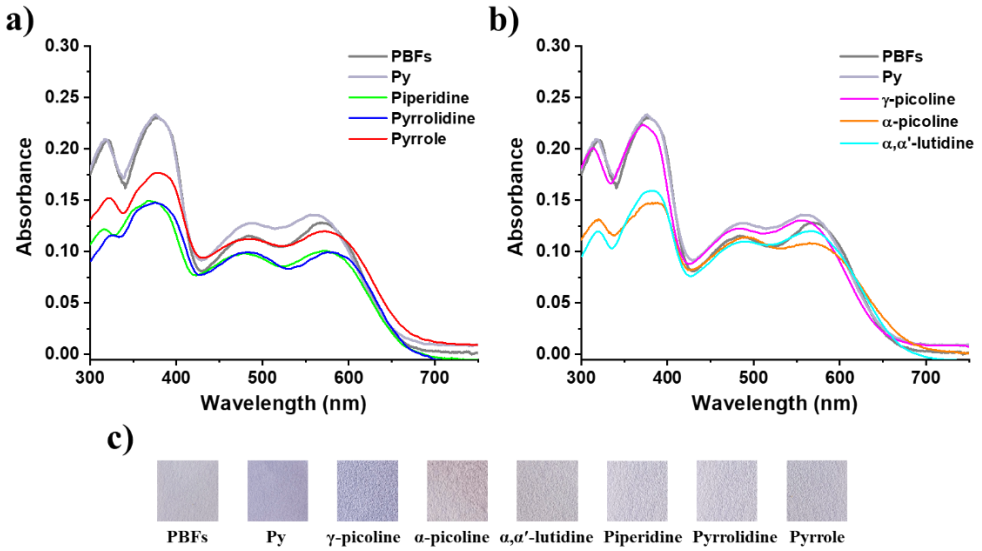

Figure A24. UV-vis reflectance spectra of **2**-PBF4s before and after static exposure to a vapor concentration of 300 ppm of **(a)** alicyclic amines (piperidine, pyrrolidine) and heterocyclic aromatic amines (pyrrole), and **(b)** pyridine derivatives (α-picoline, γ-picoline, α,α′-lutidine). **(c)** Photographic images of **2**-PBF4ms before and after exposure to a vapor concentration of 300 ppm of the heterocyclic amines involved.

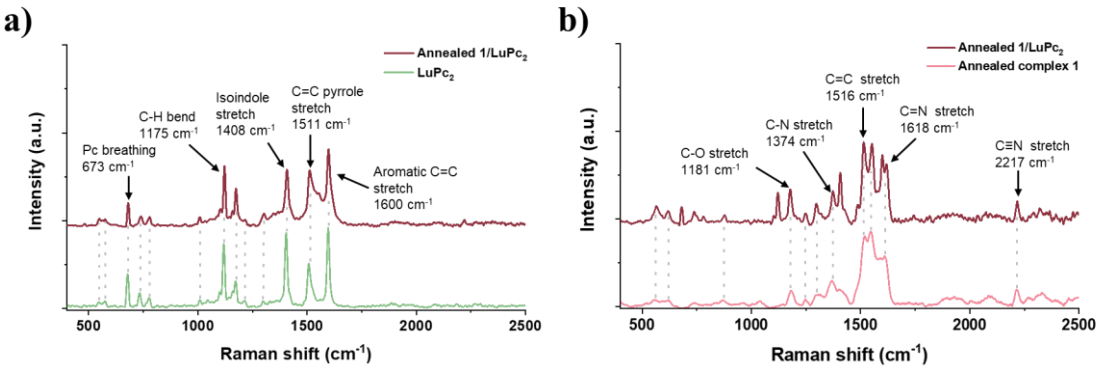

Figure A25. Raman spectra of the as-prepared bilayers recorded using a laser power of 0.12 mW **(a)** and 6.0 mW **(b)**. The Raman spectra of complex **1** and $LuPc_2$ films are reported for comparison.

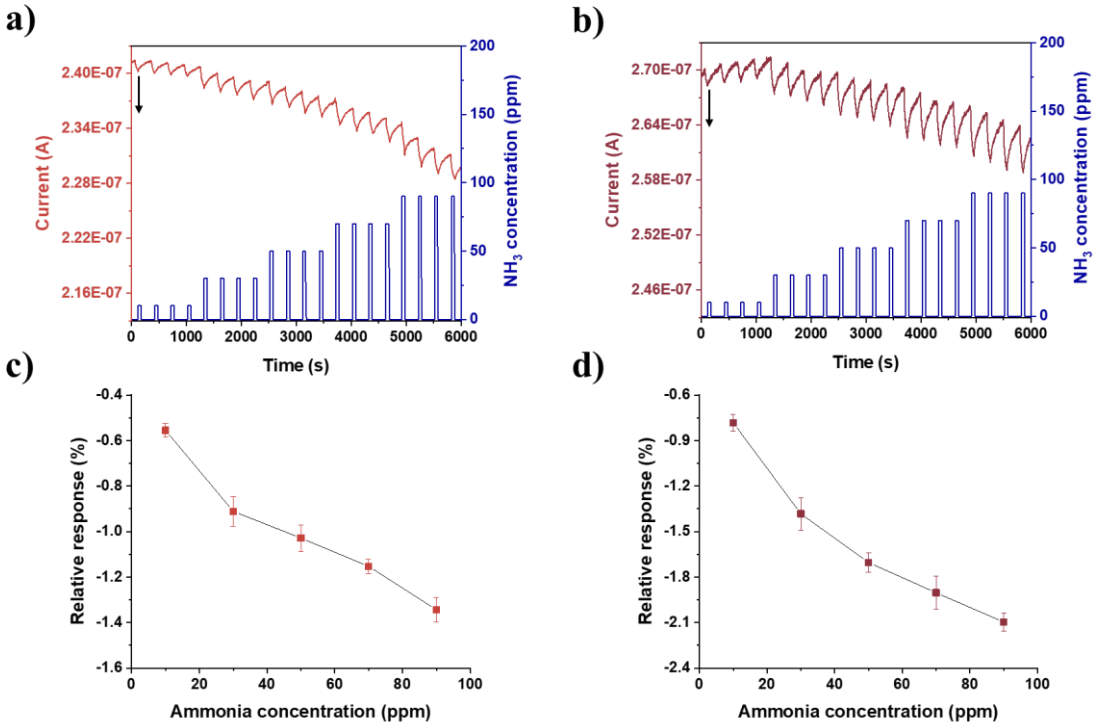

Figure A26. Current response to subsequent NH_3 exposure (4 cycles) in a range 10 – 90 ppm of as-prepared **(a)** and annealed **(b)** bilayers, and corresponding variations of RR as a function of NH_3 concentration **(c, d)**. Exposure experiments were conducted considering an exposure and recovery time of 1 and 4 min, respectively.

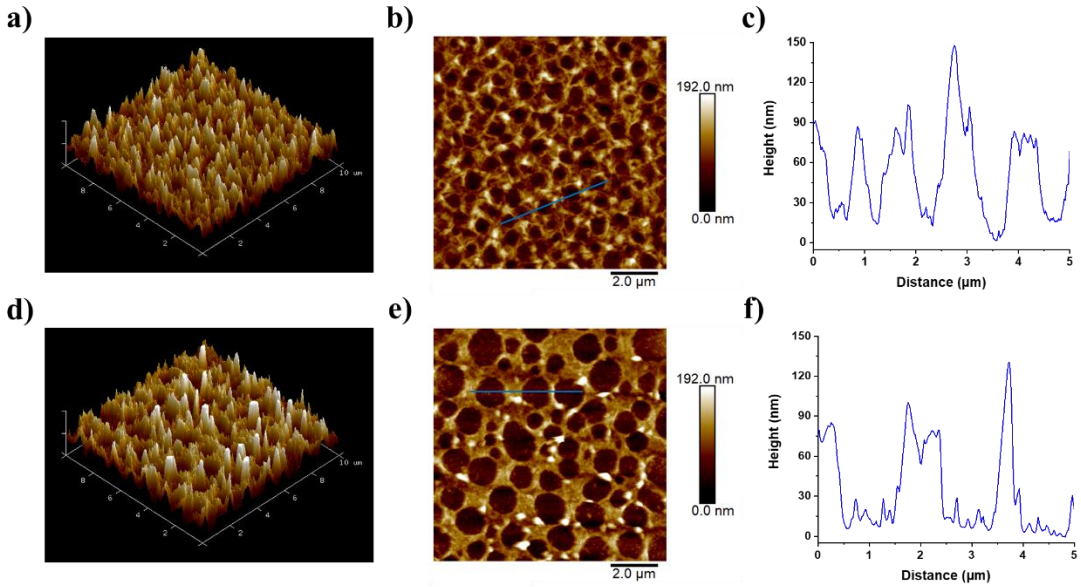

Figure A27. 3D **(a, d)** and 2D **(b, e)** AFM images of as-prepared (top) and annealed (bottom) 1:1 mixed films on ITO-IDEs. Height profiles of the as-prepared **(c)** and annealed **(f)** 1:1 mixed films measured across the blue lines marked on the corresponding 2D AFM images. The scan area in all images is 100 μm^2.

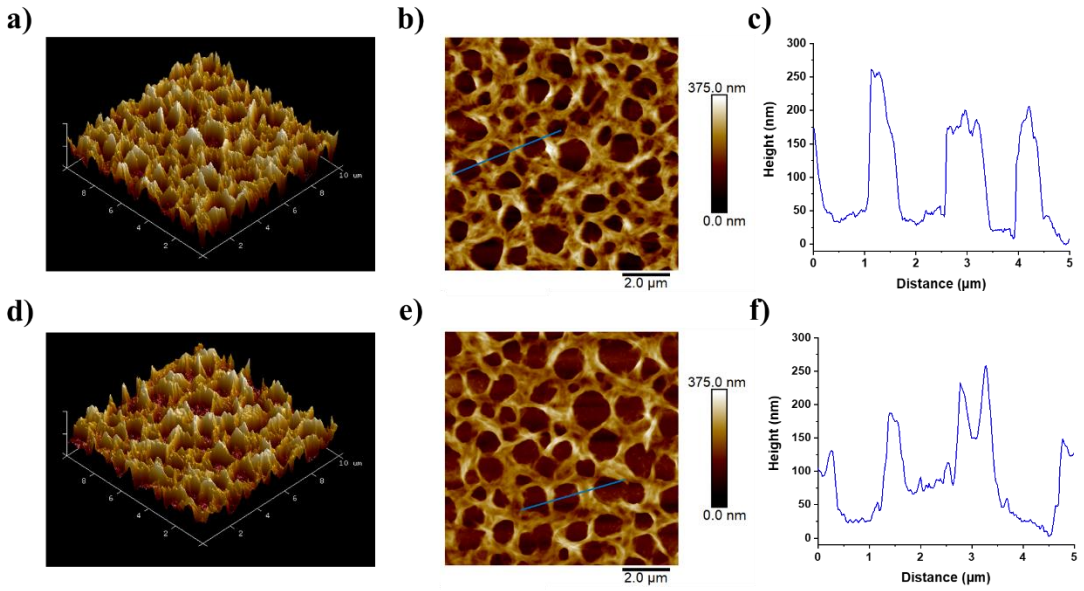

Figure A28. 3D **(a, d)** and 2D **(b, e)** AFM images of as-prepared (top) and annealed (bottom) 2:1 mixed films on ITO-IDEs. Height profiles of the as-prepared **(c)** and annealed **(f)** 2:1 mixed films measured across the blue lines marked on the corresponding 2D AFM images. The scan area in all images is 100 μm^2.

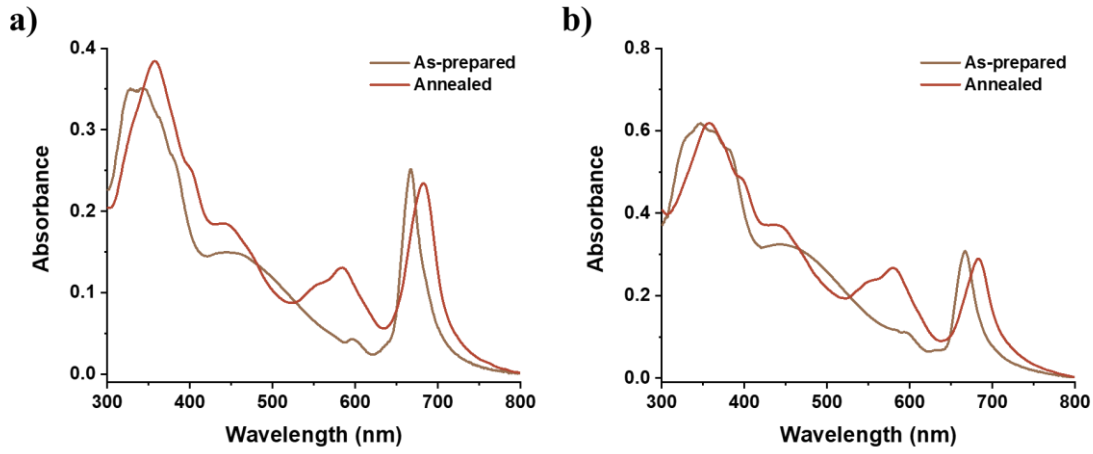

Figure A29. UV-vis absorption spectra of 1:1 **(a)** and 2:1 **(b)** mixed films before and after annealing.

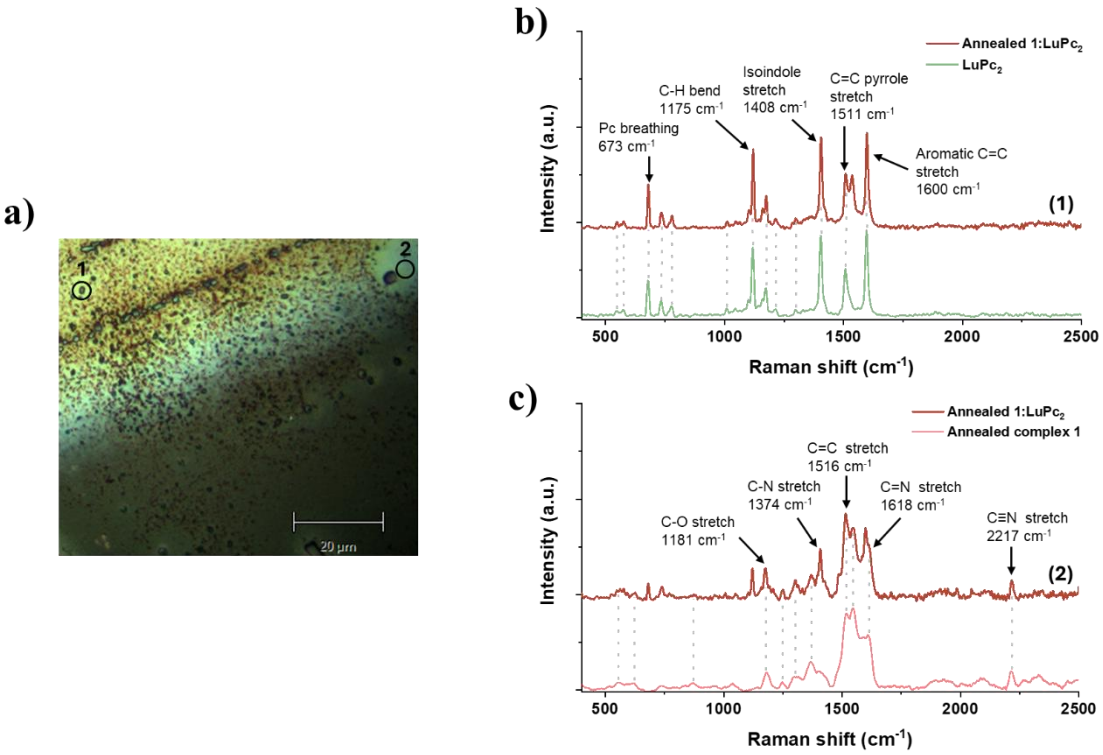

Figure A30. **(a)** Optical microscope image of the surface of annealed 1:2 mixed film. **(b**, **c)** The Raman spectra, laser power of 0.12 mW, from two different spots of the annealed 1:2 mixed film (spectra (1) and (2) are from circles 1 and 2 in Figure A6a). The Raman spectra of complex **1** and $LuPc_2$ films are reported for comparison.

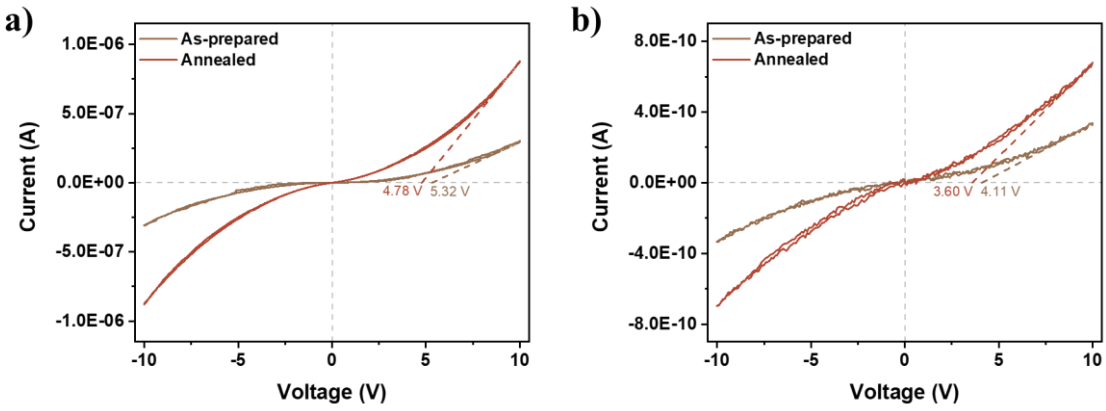

Figure A31. I – V characteristics of 1:1 **(a)** and 2:1 **(b)** mixed films before and after annealing.

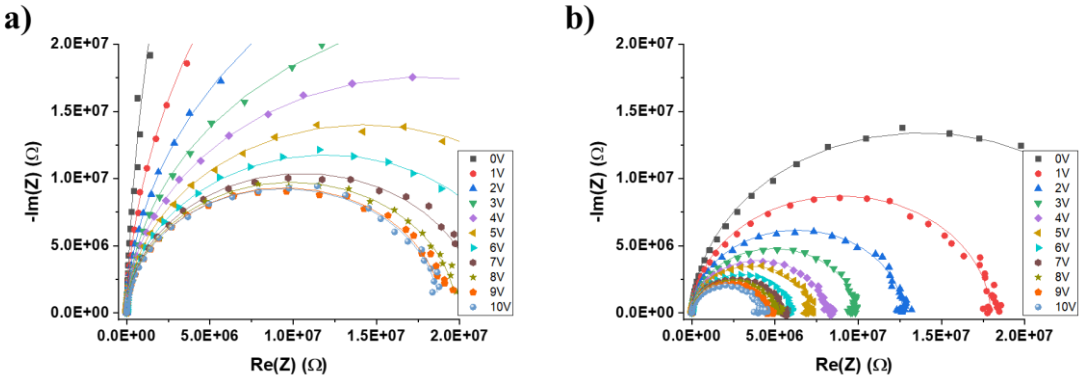

Figure A32. Nyquist plots of as-prepared **(a)** and annealed **(b)** 1:1 mixed films. The impedance response for each film was recorded at different DC voltage.

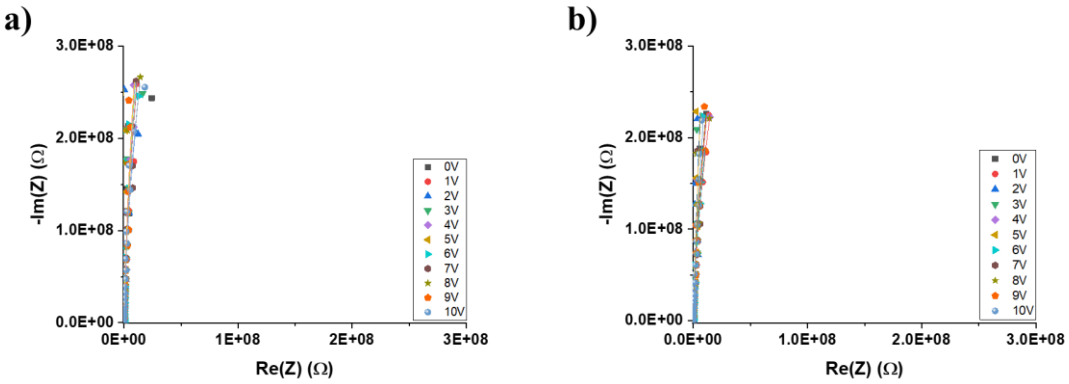

Figure A33. Nyquist plots of as-prepared **(a)** and annealed **(b)** 1:1 mixed films. The impedance response for each film was recorded at different DC voltage.

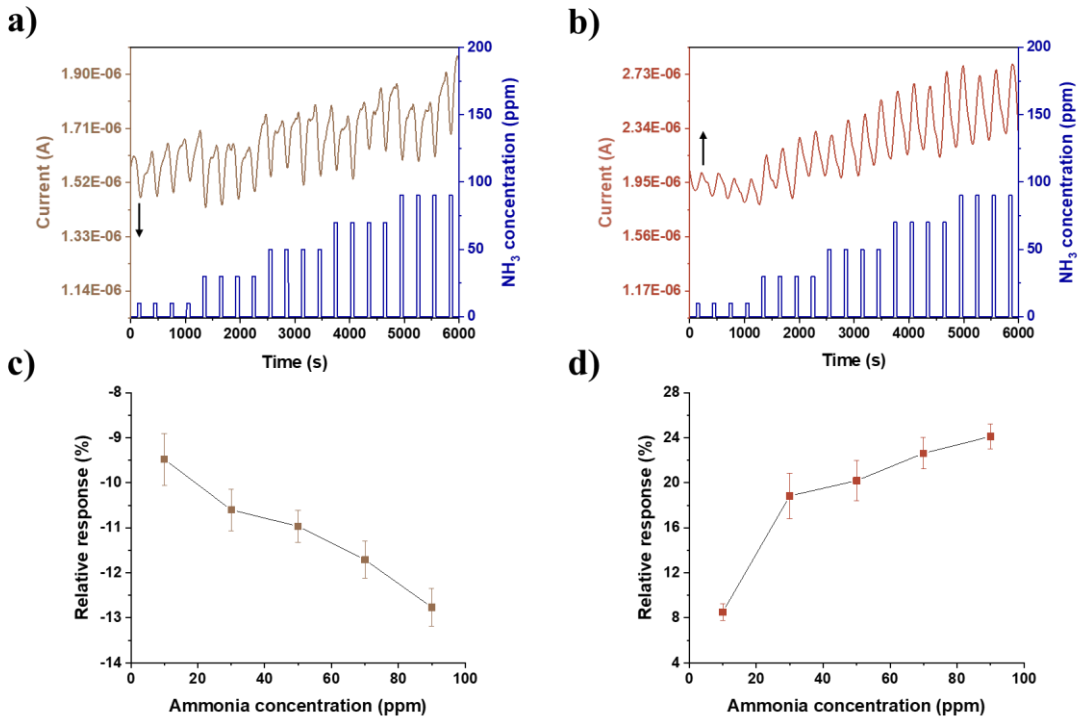

Figure A34. Current response to subsequent NH_3 exposure (4 cycles) in a range 10 – 90 ppm of as-prepared **(a)** and annealed **(b)** 1:2 mixed films, and corresponding variations of RR as a function of NH_3 concentration **(c, d)**. Exposure experiments were conducted considering an exposure and recovery time of 1 and 4 min, respectively.

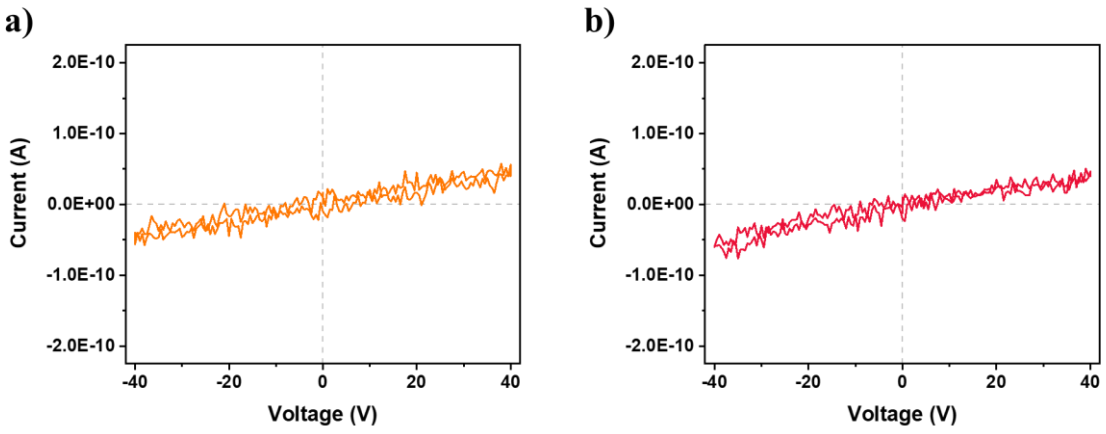

Figure A35. I – V characteristics of as-prepared **(a)** and annealed **(b)** films of complex **1**.

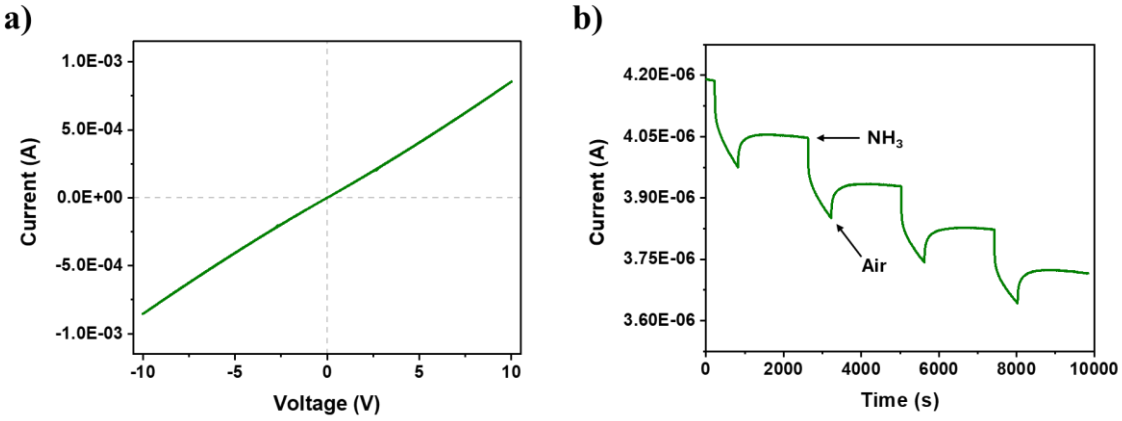

Figure A36. **(a)** I – V characteristic of thermally evaporated $LuPc_2$ films. **(b)** Current response to subsequent NH_3 exposure (90 ppm, 4 cycles) for $LuPc_2$ films. Exposure experiments were conducted considering an exposure and recovery time of 10 and 30 min, respectively.

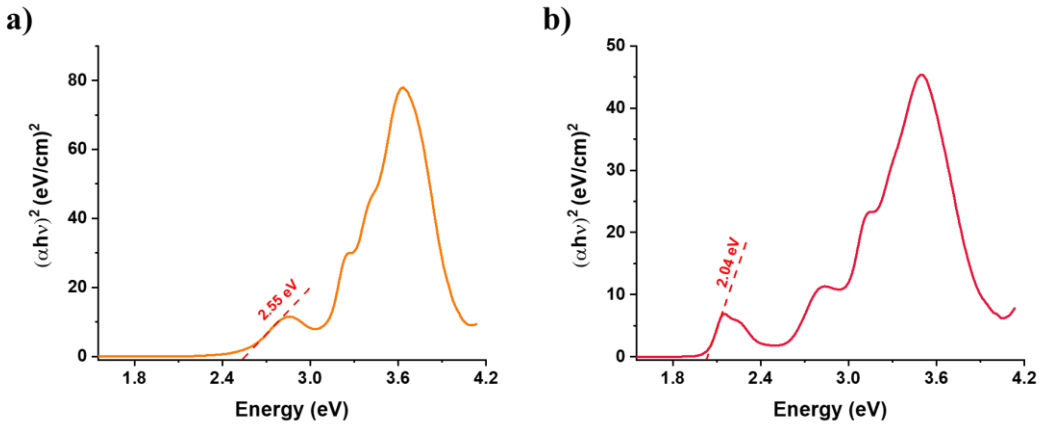

Figure A37. Tauc plots of as-prepared **(a)** and annealed **(b)** films of complex **1**.

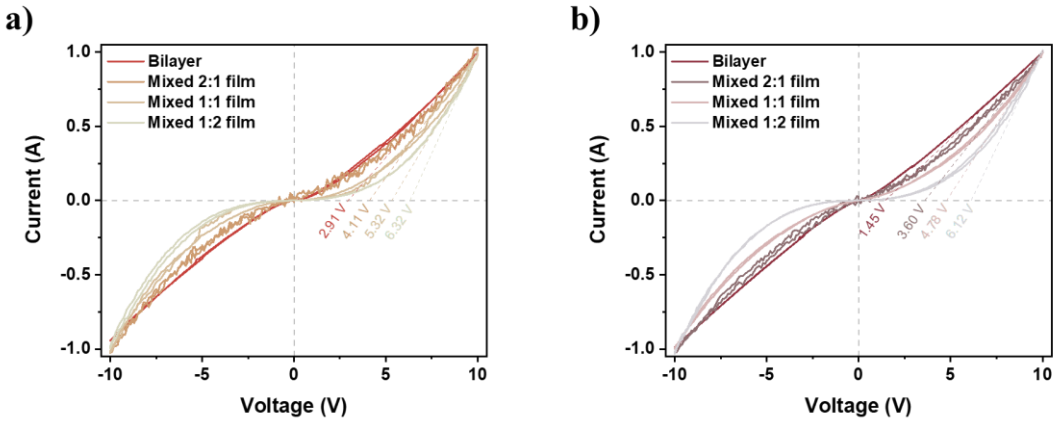

Figure A38. Normalized I – V characteristics of as-prepared **(a)** and annealed **(b)** bilayers and mixed films.

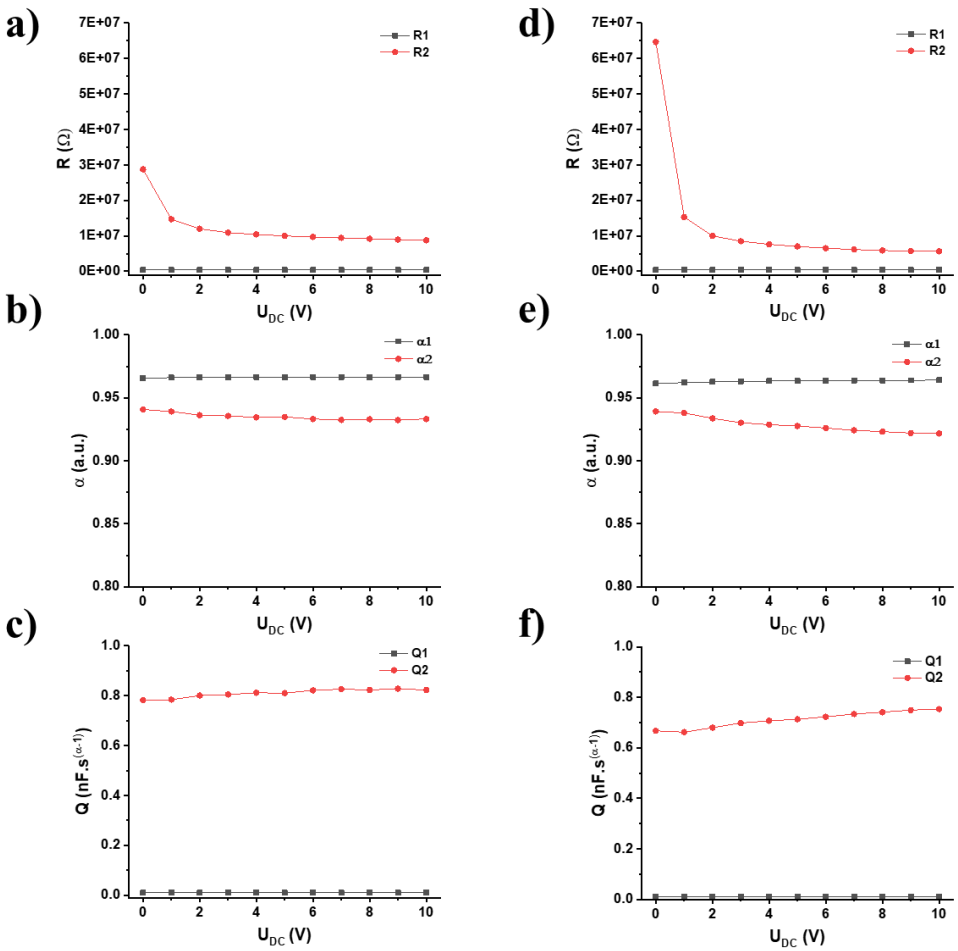

Figure A39. Variation of different charge transport parameters as a function of the applied DC bias for as-prepared **(a-c)** and annealed **(d-f)** bilayers; **(a,d)** bulk and interfacial resistances, **(b,e)** alpha parameters, and **(c,f)** bulk and interfacial effective capacitances.

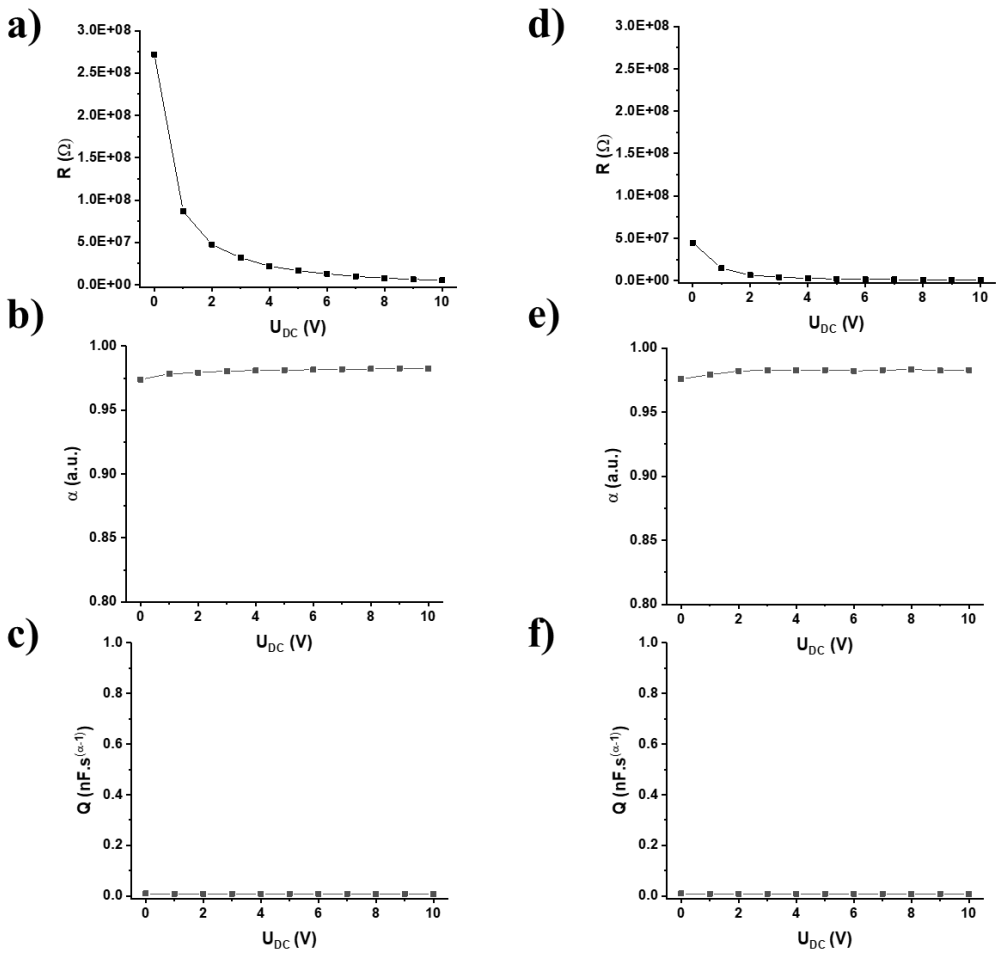

Figure A40. Variation of different charge transport parameters as a function of the applied DC bias for as-prepared **(a-c)** and annealed **(d-f)** 1:2 mixed films; **(a,d)** interfacial resistances, **(b,e)** alpha parameters, and **(c,f)** interfacial effective capacitances.

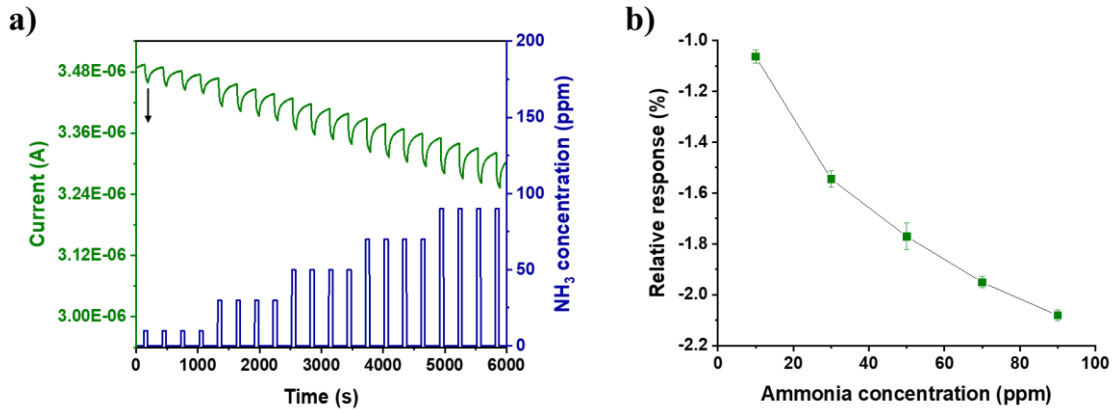

Figure A41. **(a)** Current response to subsequent NH_3 exposure in a range 10 – 90 ppm for $LuPc_2$ films, and related variation of RR as a function of the concentration. Exposure experiments were conducted considering an exposure and recovery time of 1 and 4 min, respectively.

Appendix B

Table B1. Saturated vapor concentration (Satd. Vapors) of main VOCs involved in the present optical absorption and fluorescence studies calculated by eq. 3.1. The vapor pressure of each VOC was calculated at room temperature (23 °C) using Antoine equation (eq. 3.2).

Substance	CAS No	A	B	C	Vapor Pressure (mmHg)	Satd. Vapors (ppm)
Acetaldehyde	75-07-0	7,319	1176	244,3	828,3	1089875
Acetic acid	64-19-7	7,276	1327	183,9	7,3	9572
Acetic anhydride	108-24-7	8,809	2397	265,0	3,0	4011
Acetone	67-64-1	7,317	1316	240,5	210,8	277422
Acetonitrile	75-05-8	7,544	1583	257,9	80,7	106236
Aniline	62-53-3	7,304	1670	193,6	0,4	520
Benzene	71-43-2	6,814	1090	197,1	72,6	95563
Cyclohexane	110-82-7	6,889	1201	218,8	83,8	110327
Dichloromethane	75-09-2	7,110	1151	232,4	399,8	526082
Diethyl ether	60-29-7	7,040	1111	232,7	493,1	648754
Diethylamine	109-89-7	6,552	828	170,1	182,8	240478
Ethyl acetate	141-78-6	7,260	1339	228,6	87,1	114616
Ethylenediamine	107-15-3	7,617	1593	218,6	10,5	13824
Methanol	67-56-1	8,084	1580	239,1	113,2	148988
Dimethylformamide	68-12-2	7,241	1598	213,5	3,0	4006
n-Butylamine	109-73-9	7,189	1312	226,7	85,9	113088
n-Butylthiol	109-79-5	7,582	1535	228,7	30,4	39991
n-Pentane	109-66-0	7,009	1134	238,7	472,9	622254
Pyridine	110-86-1	7,184	1463	224,6	18,9	24838
Tetrahydrofuran	109-99-9	7,060	1247	232,6	151,5	199289
Triethylamine	121-44-8	6,503	919	164,7	40,2	52876

Table B2. Literature data of optical chemosensors for the detection of AN vapors.

Material	Detection method	Substrate	LOD or Lowest Detected Conc. (Linear range)	Selectivity Studies	Exposure Method	Ref
Organic Compound	Optical absorption	Glass	200 ppm	no	dynamic	302
Conjugated Polymer	Optical absorption and fluorescence	Glass capillary	1.4 ppm	yes	dynamic	308
Organic Compound	Fluorescence	Glass	13.2 ppb (0-120 ppm)	yes	static	461
Organic Compound	Fluorescence	Indium thin oxide	6.04 ppb (0-0.26ppm)	yes	static	462
Organic Copolymer	Fluorescence	Silica gel plate	45 ppb (176-2750 ppb)	yes	dynamic	463
Organic Compound	Fluorescence	Quartz	3 ppb (0.21-860 ppm)	yes	static	464
Organic Compound	Photoluminescence	Glass	796 ppt	yes	static	465
Organic Compound	Fluorescence	Glass	100 ppb (0-90 ppm)	yes	static	466
Organic Compound	Optical absorption and fluorescence	Quartz	1 ppm, 100 ppb and 1 ppb	yes	static	467
Organic Compound	Fluorescence	Glass	8.6 ppm (10-88 ppm)	yes	static	468

Bibliography

[1] Zandalinas, S.I.; Fritschi, F.B.; Mittler, R. Global Warming, Climate Change, and Environmental Pollution: Recipe for a Multifactorial Stress Combination Disaster. *Trends Plant. Sci*. **2021**, *26*, 588–599. https://doi.org/10.1016/j.tplants.2021.02.011

[2] Okereafor, U.; Makhatha, M.; Mekuto, L.; Uche-Okereafor, N.; Sebola, T.; Mavumengwana, V. Toxic Metal Implications on Agricultural Soils, Plants, Animals, Aquatic life and Human Health. *Int. J. Environ. Res. Public Health* **2020**, *17*, 2204–2227. https://doi.org/10.3390/ijerph17072204

[3] Wasi, S.; Tabrez, S.; Ahmad, M. Toxicological effects of major environmental pollutants: an overview. *Environ. Monit. Assess.* **2013**, *185*, 2585–2593. https://doi.org/10.1007/s10661-012-2732-8

[4] Edwards, C.A. Assessing the effects of environmental pollutants on soil organisms, communities, processes and ecosystems. *Eur. J. Soil Biol*. **2002**, *38*, 225–231. https://doi.org/10.1016/S1164-5563(02)01150-0

[5] Nazari-Sharabian, M.; Ahmad, S.; Karakouzian, M. Climate Change and Eutrophication: A Short Review. *Eng. Technol. Appl. Sci. Res.* **2018**, *8*, 3668–3672. https://digitalscholarship.unlv.edu/fac_articles/562

[6] Kallenborn, R.; Halsall, C.; Dellongc, M.; Carlsson, P. The influence of climate change on the global distribution and fate processes of anthropogenic persistent organic pollutants. *J. Environ. Monit*. **2012**, *14*, 2854–2869. https://doi.org/10.1039/C2EM30519D

[7] Zwolak, A.; Sarzyńska, M.; Szpyrka, E.; Stawarczyk, K. Sources of Soil Pollution by Heavy Metals and Their Accumulation in Vegetables: a Review. *Water Air Soil Pollut*. **2019**, *230*, 164–173. https://doi.org/10.1007/s11270-019-4221-y

[8] De Silva, S.; Carson, P.; Indrapala, D. V.; Warwick, B.; Reichman, S. M. Land Application of Industrial Wastes: Impacts on Soil Quality, Biota, and Human Health. *Environ Sci Pollut Res* **2023**, *30* (26), 67974–67996. https://doi.org/10.1007/s11356-023-26893-7

[9] Kumar, M.; Gogoi, A.; Kumari, D.; Borah, R.; Das, P.; Mazumder, P.; Tyagi, V. K. Review of Perspective, Problems, Challenges, and Future Scenario of Metal Contamination in the Urban Environment. *Journal of Hazardous, Toxic, and Radioactive Waste* **2017**, *21* (4), 04017007. https://doi.org/10.1061/(ASCE)HZ.2153-5515.0000351

[10] Chaudhry, F.N.; Malik, M.F. Factors Affecting Water Pollution: A Review. *J. ecosystem ecography* **2017**, *7*, 225–227. https://doi.org/10.4172/2157-7625.1000225

[11] Babuji, P.; Thirumalaisamy, S.; Duraisamy, K.; Periyasamy, G. Human Health Risks Due to Exposure to Water Pollution: A Review. *Water* **2023**, *15* (14), 2532. https://doi.org/10.3390/w15142532

[12] Lin, L.; Yang, H.; Xu, X. Effects of Water Pollution on Human Health and Disease Heterogeneity: A Review. *Front. Environ. Sci.* **2022**, *10*. https://doi.org/10.3389/fenvs.2022.880246

[13] Dominski, F. H.; Lorenzetti Branco, J. H.; Buonanno, G.; Stabile, L.; Gameiro da Silva, M.; Andrade, A. Effects of Air Pollution on Health: A Mapping Review of Systematic Reviews and Meta-Analyses. *Environmental Research* **2021**, *201*, 111487. https://doi.org/10.1016/j.envres.2021.111487

[14] Chauhan, S.K.; Saini, N.; Yadav, V.B. RECENT TRENDS OF VOLATILE ORGANIC COMPOUNDS IN AMBIENT AIR & ITS HEALTH IMPACTS: A REVIEW. *Int. j. technol. res. eng.* **2014**, *8*, 667–678.

[15] Li, A.J.; Pal, V.K.; Kannan, K. A review of environmental occurrence, toxicity, biotransformation and biomonitoring of volatile organic compounds. *Environ. Chem. Ecotoxicol*. **2021**, *3*, 91–116. https://doi.org/10.1016/j.enceco.2021.01.001

[16] Gałezowska, G.; Chraniuk, M.; Wolska, L. In vitro assays as a tool for determination of VOCs toxic effect on respiratory system: A critical review. *Trends Analyt. Chem*. **2016**, *77*, 14–22. https://doi.org/10.1016/j.trac.2015.10.012

[17] Rumchev, K.; Brown, H.; Spickett, J. Volatile Organic Compounds: Do they present a risk to our health? *Rev. Environ. Health* **2007**, *22*, 39–57. https://doi.org/10.1515/REVEH.2007.22.1.39

[18] David, E.; Niculescu, V.-C. Volatile Organic Compounds (VOCs) as Environmental Pollutants: Occurrence and Mitigation Using Nanomaterials. *Int. J. Environ. Res. Public Health* **2021**, *18*, 13147–13162. https://doi.org/10.3390/ijerph182413147

[19] Lawrence, S. A. *Amines: Synthesis, Properties and Applications*; Cambridge University Press, **2004**.

[20] Fishbein, L. Aromatic Amines. In *Anthropogenic Compounds*; Atlas, E., Fishbein, L., Giam, C. S., Leonard, J. E., Muir, D. C. G., Powers, M. A., Schoer, J., Eds.; Springer: Berlin, Heidelberg, 1984; pp 1–40. https://doi.org/10.1007/978-3-540-38819-7_1

[21] Miller, K.; Reichert, C. L.; Schmid, M. Biogenic Amine Detection Systems for Intelligent Packaging Concepts: Meat and Meat Products. *Food Reviews International* **2023**, *39* (5), 2543–2567. https://doi.org/10.1080/87559129.2021.1961270

[22] Andre, R. S.; Mercante, L. A.; Facure, M. H. M.; Sanfelice, R. C.; Fugikawa-Santos, L.; Swager, T. M.; Correa, D. S. Recent Progress in Amine Gas Sensors for Food Quality Monitoring: Novel Architectures for Sensing Materials and Systems. *ACS Sens.* **2022**, *7* (8), 2104–2131. https://doi.org/10.1021/acssensors.2c00639

[23] Luo, X.; Zaitoon, A.; Lim, L.-T. A Review on Colorimetric Indicators for Monitoring Product Freshness in Intelligent Food Packaging: Indicator Dyes, Preparation Methods, and Applications. *Comprehensive Reviews in Food Science and Food Safety* **2022**, *21* (3), 2489–2519. https://doi.org/10.1111/1541-4337.12942

[24] Myers, R.C.; Ballantyne, B. Comparative Acute Toxicity and Primary Irritancy of Various Classes of Amines *Toxic Subst. Mech.* **1997**, *16*, 151–194. https://doi.org/10.1080/107691897229702

[25] Andrés, E.-R.; Ignacio, M.-B. K.; Maribel, M.-T. Aromatic Amines in the Environment: Ecotoxicological Effects in Vertebrates and Invertebrates: A Review. *Chemistry and Ecology* **2025**, *41* (8), 1115–1149. https://doi.org/10.1080/02757540.2025.2518271

[26] Poste, A. E.; Grung, M.; Wright, R. F. Amines and Amine-Related Compounds in Surface Waters: A Review of Sources, Concentrations and Aquatic Toxicity. *Science of The Total Environment* **2014**, *481*, 274–279. https://doi.org/10.1016/j.scitotenv.2014.02.066

[27] Pereira, L.; Mondal, P. K.; Alves, M. Aromatic Amines Sources, Environmental Impact and Remediation. In *Pollutants in Buildings, Water and Living Organisms*; Lichtfouse, E., Schwarzbauer, J., Robert, D., Eds.; Springer International Publishing: Cham, 2015; pp 297–346. https://doi.org/10.1007/978-3-319-19276-5_7

[28] Fekete, A.; Malik, A. K.; Kumar, A.; Schmitt-Kopplin, P. Amines in the Environment. *Critical Reviews in Analytical Chemistry* **2010**, *40* (2), 102–121. https://doi.org/10.1080/10408340903517495

[29] Chai, Y.; Chen, Y.; Jiang, Z.; He, Y.; Qiu, Z. Exhaled Breath Volatile Organic Compounds (VOCs) Detection Methods: GC-MS versus eNose in COPD Diagnosis-a Systematic Review and Meta-Analysis. *BMC Pulm Med* **2025**. https://doi.org/10.1186/s12890-025-04040-x

[30] Longo, V.; Forleo, A.; Giampetruzzi, L.; Siciliano, P.; Capone, S. Human Biomonitoring of Environmental and Occupational Exposures by GC-MS and Gas Sensor Systems: A Systematic Review. *International Journal of Environmental Research and Public Health* **2021**, *18* (19), 10236. https://doi.org/10.3390/ijerph181910236

[31] Khatib, M.; Haick, H. Sensors for Volatile Organic Compounds. *ACS Nano* **2022**, *16* (5), 7080–7115. https://doi.org/10.1021/acsnano.1c10827

[32] Yaqoob, U.; Younis, M. I. Chemical Gas Sensors: Recent Developments, Challenges, and the Potential of Machine Learning—A Review. *Sensors* **2021**, *21* (8), 2877. https://doi.org/10.3390/s21082877

[33] Wu, D.; C. Sedgwick, A.; Gunnlaugsson, T.; U. Akkaya, E.; Yoon, J.; D. James, T. Fluorescent Chemosensors: The Past, Present and Future. *Chemical Society Reviews* **2017**, *46* (23), 7105–7123. https://doi.org/10.1039/C7CS00240H

[34] Zhou, X.; Lee, S.; Xu, Z.; Yoon, J. Recent Progress on the Development of Chemosensors for Gases. *Chem. Rev.* **2015**, *115* (15), 7944–8000. https://doi.org/10.1021/cr500567r

[35] Baranwal, J.; Barse, B.; Gatto, G.; Broncova, G.; Kumar, A. Electrochemical Sensors and Their Applications: A Review. *Chemosensors* **2022**, *10* (9), 363. https://doi.org/10.3390/chemosensors10090363

[36] Liao, C.; Shi, J.; Zhang, M.; Dalapati, R.; Tian, Q.; Chen, S.; Wang, C.; Ling Zang, L. Optical chemosensors for the gas phase detection of aldehydes: mechanism, material design, and application. *Mater. Adv*. **2021**, *2*, 6213–6245. https://doi.org/10.1039/D1MA00341K

[37] Kuchmenko, T.A.; Lvova L.B. A Perspective on Recent Advances in Piezoelectric Chemical Sensors for Environmental Monitoring and Foodstuffs Analysis. *Chemosensors* **2019**, *7*, 39–59. https://doi.org/10.3390/chemosensors7030039

[38] Khan, S.; Chen, X.; Almahri, A.; Allehyani, E.S.; Alhumaydhi, F.A.; Ibrahim, M.M.; Ali, S. Recent developments in fluorescent and colorimetric chemosensors based on schiff bases for metallic cations detection: A review. *J. Environ. Chem.* Eng. **2021**, *9*, 106381–106402. https://doi.org/10.1016/j.jece.2021.106381

[39] Strianese, M.; Pellecchia, C. Metal Complexes as Fluorescent Probes for Sensing Biologically Relevant Gas Molecules. *Coordination Chemistry Reviews* **2016**, *318*, 16–28. https://doi.org/10.1016/j.ccr.2016.04.006

[40] Wang, T.; Zhang, N.; Bai, W.; Bao, Y. Fluorescent Chemosensors Based on Conjugated Polymers with N-Heterocyclic Moieties: Two Decades of Progress. *Polymer Chemistry* **2020**, *11* (18), 3095–3114. https://doi.org/10.1039/D0PY00336K

[41] Li, H.-Y.; Zhao, S.-N.; Zang, S.-Q.; Li, J. Functional Metal–Organic Frameworks as Effective Sensors of Gases and Volatile Compounds. *Chemical Society Reviews* **2020**, *49* (17), 6364–6401. https://doi.org/10.1039/C9CS00778D

[42] Tomić, M.; Šetka, M.; Vojkůvka, L.; Vallejos, S. VOCs Sensing by Metal Oxides, Conductive Polymers, and Carbon-Based Materials. *Nanomaterials* **2021**, *11* (2), 552. https://doi.org/10.3390/nano11020552

[43] Oliveri, I. P.; Di Bella, S. Lewis Acidic Zinc(II) Complexes of Tetradentate Ligands as Building Blocks for Responsive Assembled Supramolecular Structures. *Chemistry* **2023**, *5* (1), 119–137. https://doi.org/10.3390/chemistry5010010

[44] Di Bella, S. Lewis Acidic Zinc(ii) Salen-Type Schiff-Base Complexes: Sensing Properties and Responsive Nanostructures. *Dalton Trans.* **2021**, *50* (18), 6050–6063. https://doi.org/10.1039/D1DT00949D

[45] Achaw, O.-W.; Danso-Boateng, E. Industrial Gases. In *Chemical and Process Industries: With Examples of Industries in Ghana*; Achaw, O.-W., Danso-Boateng, E., Eds.; Springer International Publishing: Cham, 2021; pp 213–233. https://doi.org/10.1007/978-3-030-79139-1_8

[46] Kreider, P.; Lipiński, W. High-Temperature Gas–Solid Reactions in Industrial Processes. *Reviews in Mineralogy and Geochemistry* **2018**, *84* (1), 499–514. https://doi.org/10.2138/rmg.2018.84.13

[47] Zhou, X.; Zhou, X.; Wang, C.; Zhou, H. Environmental and Human Health Impacts of Volatile Organic Compounds: A Perspective Review. *Chemosphere* **2023**, *313*, 137489. https://doi.org/10.1016/j.chemosphere.2022.137489

[48] Kaikiti, C.; Stylianou, M.; Agapiou, A. TD-GC/MS Analysis of Indoor Air Pollutants (VOCs, PM) in Hair Salons. *Chemosphere* **2022**, *294*, 133691. https://doi.org/10.1016/j.chemosphere.2022.133691

[49] Poster, D.L.; Schantz M.M.; Sander L.C.; Wise S.A. Analysis of polycyclic aromatic hydrocarbons (PAHs) in environmental samples: a critical review of gas chromatographic (GC) methods. *Anal. Bioanal. Chem*. **2006**, *386*, 859–881. https://doi.org/10.1007/s00216-006-0771-0

[50] Epping, R.; Koch, M. On-Site Detection of Volatile Organic Compounds (VOCs). *Molecules* **2023**, *28* (4), 1598. https://doi.org/10.3390/molecules28041598

[51] Hulanicki, A.; Glab, S.; Ingman, F. Chemical Sensors: Definitions and Classification. *Pure and Applied Chemistry* **1991**, *63* (9), 1247–1250. https://doi.org/10.1351/pac199163091247

[52] Banica, F.-G. *Chemical Sensors and Biosensors: Fundamentals and Applications*; John Wiley & Sons: Chichester, West Sussex, UK, **2012**.

[53] Wang, B.; Anslyn, E. V. *Chemosensors: Principles, Strategies, and Applications*; John Wiley & Sons: Hoboken, New Jersey, USA, **2011**.

[54] Khanna, C.; Silakari, P. A Comprehensive Review on Chemosensor Design: Strategies, Sensing Mechanisms, and Functional Applications. *Phosphorus, Sulfur, and Silicon and the Related Elements* **2025**, *0* (0), 1–18. https://doi.org/10.1080/10426507.2025.2590007

[55] Mohan, B. Understanding the Role of Noncovalent Interactions in Gas Sensing with Metal-Coordinated Complexes (MCCs). *Top Curr Chem (Z)* **2025**, *383* (4), 44. https://doi.org/10.1007/s41061-025-00530-y

[56] Kaur, K.; Saini, R.; Kumar, A.; Luxami, V.; Kaur, N.; Singh, P.; Kumar, S. Chemodosimeters: An Approach for Detection and Estimation of Biologically and Medically Relevant Metal Ions, Anions and Thiols. *Coordination Chemistry Reviews* **2012**, *256* (17), 1992–2028. https://doi.org/10.1016/j.ccr.2012.04.013

[57] Nanto, H.; Stetter, J. R. Introduction to Chemosensors. In *Handbook of Machine Olfaction*; Pearce, T. C., Schiffman, S. S., Nagle, H. T., Gardner, J. W., Eds.; Wiley, 2002; pp 79–104. https://doi.org/10.1002/3527601597.ch4

[58] Hernik, A.; Smets, J.; Wang, Z.; Semenova, Y.; Tan, J.; Ameloot, R.; Naydenova, I. Optical Detection of Volatile Organic Compounds: A Review of Methods and Functionalized Sensing Materials. *Advanced Optical Materials* **2025**, *13* (27), e00369. https://doi.org/10.1002/adom.202500369

[59] McGinn, C. K.; Lamport, Z. A.; Kymissis, I. Review of Gravimetric Sensing of Volatile Organic Compounds. *ACS Sens.* **2020**, *5* (6), 1514–1534. https://doi.org/10.1021/acssensors.0c00333

[60] Neri, G. First Fifty Years of Chemoresistive Gas Sensors. *Chemosensors* **2015**, *3* (1), 1–20. https://doi.org/10.3390/chemosensors3010001

[61] Savin, M.; Mihailescu, C.-M.; Moldovan, C.; Grigoroiu, A.; Ion, I.; Ion, A. C. Resistive Chemosensors for the Detection of CO Based on Conducting Polymers and Carbon Nanocomposites: A Review. *Molecules* **2022**, *27* (3), 821. https://doi.org/10.3390/molecules27030821

[62] John, A. T.; Murugappan, K.; Nisbet, D. R.; Tricoli, A. An Outlook of Recent Advances in Chemiresistive Sensor-Based Electronic Nose Systems for Food Quality and Environmental Monitoring. *Sensors* **2021**, *21* (7), 2271. https://doi.org/10.3390/s21072271

[63] Srinivasan, P.; Samanta, S.; Krishnakumar, A.; Rayappan, J. B. B.; Kailasam, K. Insights into G-C_3 N_4 as a Chemi-Resistive Gas Sensor for VOCs and Humidity – a Review of the State of the Art and Recent Advancements. *J. Mater. Chem. A* **2021**, *9* (17), 10612–10651. https://doi.org/10.1039/D0TA12500H

[64] Lin, Z.; Abbott, J.; Karuso, P.; Wong, D. K. Y. Advances in Electroanalytical Sensing of Volatile Organic Compounds towards Field-Deployable Detection. *TrAC Trends in Analytical Chemistry* **2025**, *183*, 118101. https://doi.org/10.1016/j.trac.2024.118101

[65] Cho, G.; Azzouzi, S.; Zucchi, G.; Lebental, B. Electrical and Electrochemical Sensors Based on Carbon Nanotubes for the Monitoring of Chemicals in Water—A Review. *Sensors* **2021**, *22* (1), 218. https://doi.org/10.3390/s22010218

[66] Spinelle, L.; Gerboles, M.; Kok, G.; Persijn, S.; Sauerwald, T. Review of Portable and Low-Cost Sensors for the Ambient Air Monitoring of Benzene and Other Volatile Organic Compounds. *Sensors* **2017**, *17* (7), 1520. https://doi.org/10.3390/s17071520

[67] Alenezy, E. K.; Kandjani, A. E.; Shaibani, M.; Trinchi, A.; Bhargava, S. K.; Ippolito, S. J.; Sabri, Y. Human Breath Analysis; Clinical Application and Measurement: An Overview. *Biosensors and Bioelectronics* **2025**, *278*, 117094. https://doi.org/10.1016/j.bios.2024.117094

[68] Pathak, A. K.; Swargiary, K.; Kongsawang, N.; Jitpratak, P.; Ajchareeyasoontorn, N.; Udomkittivorakul, J.; Viphavakit, C. Recent Advances in Sensing Materials Targeting Clinical Volatile Organic Compound (VOC) Biomarkers: A Review. *Biosensors* **2023**, *13* (1), 114. https://doi.org/10.3390/bios13010114

[69] Yadav, N.; Garg, V. K.; Chhillar, A. K.; Rana, J. S. Detection and Remediation of Pollutants to Maintain Ecosustainability Employing Nanotechnology: A Review. *Chemosphere* **2021**, *280*, 130792. https://doi.org/10.1016/j.chemosphere.2021.130792

[70] Wang, L.; Cheng, Y.; Gopalan, S.; Luo, F.; Amreen, K.; Singh, R. K.; Goel, S.; Lin, Z.; Naidu, R. Review and Perspective: Gas Separation and Discrimination Technologies for Current Gas Sensors in Environmental Applications. *ACS Sens.* **2023**, *8* (4), 1373–1390. https://doi.org/10.1021/acssensors.2c02810

[71] Li, Z.; Hou, S.; Zhang, H.; Song, Q.; Wang, S.; Guo, H. Recent Advances in Fluorescent and Colorimetric Sensing for Volatile Organic Amines and Biogenic Amines in Food. *Advanced Agrochem* **2023**, *2* (1), 79–87. https://doi.org/10.1016/j.aac.2023.02.001

[72] Zhang, Z.; Lou, Y.; Guo, C.; Jia, Q.; Song, Y.; Tian, J.-Y.; Zhang, S.; Wang, M.; He, L.; Du, M. Metal–Organic Frameworks (MOFs) Based Chemosensors/Biosensors for Analysis of Food Contaminants. *Trends in Food Science & Technology* **2021**, *118*, 569–588. https://doi.org/10.1016/j.tifs.2021.10.024

[73] Yahya, M.; Yaman, M.; Seferoğlu, Z.; Yahya, M.; Yaman, M.; Seferoğlu, Z. Optical Chemosensors: Principles, Chemistry, Strategies, and Applications. In *Fluorescence Imaging - Recent Advances and Applications*; IntechOpen, 2022. https://doi.org/10.5772/intechopen.105968

[74] Li, T.; Liu, G.; Kong, H.; Yang, G.; Wei, G.; Zhou, X. Recent Advances in Photonic Crystal-Based Sensors. *Coordination Chemistry Reviews* **2023**, *475*, 214909. https://doi.org/10.1016/j.ccr.2022.214909

[75] Khan, S.; Le Calvé, S.; Newport, D. A Review of Optical Interferometry Techniques for VOC Detection. *Sensors and Actuators A: Physical* **2020**, *302*, 111782. https://doi.org/10.1016/j.sna.2019.111782

[76] Esteves, C.; Ramou, E.; Porteira, A. R. P.; Moura Barbosa, A. J.; Roque, A. C. A. Seeing the Unseen: The Role of Liquid Crystals in Gas-Sensing Technologies. *Advanced Optical Materials* **2020**, *8* (11), 1902117. https://doi.org/10.1002/adom.201902117

[77] Butt, M. A.; Voronkov, G. S.; Grakhova, E. P.; Kutluyarov, R. V.; Kazanskiy, N. L.; Khonina, S. N. Environmental Monitoring: A Comprehensive Review on Optical Waveguide and Fiber-Based Sensors. *Biosensors* **2022**, *12* (11), 1038. https://doi.org/10.3390/bios12111038

[78] El Kazzy, M.; Weerakkody, J. S.; Hurot, C.; Mathey, R.; Buhot, A.; Scaramozzino, N.; Hou, Y. An Overview of Artificial Olfaction Systems with a Focus on Surface Plasmon Resonance for the Analysis of Volatile Organic Compounds. *Biosensors* **2021**, *11* (8), 244. https://doi.org/10.3390/bios11080244

[79] Lopez-Torres, D.; Elosua, C.; Arregui, F. J. Optical Fiber Sensors Based on Microstructured Optical Fibers to Detect Gases and Volatile Organic Compounds—A Review. *Sensors* **2020**, *20* (9), 2555. https://doi.org/10.3390/s20092555

[80] Meher, N.; Barman, D.; Parui, R.; Iyer, P. K. Recent Development of the Fluorescence-Based Detection of Volatile Organic Compounds: A Mechanistic Overview. *J. Mater. Chem. C* **2022**, *10* (28), 10224–10254. https://doi.org/10.1039/D2TC00265E

[81] Cho, S. H.; Suh, J. M.; Eom, T. H.; Kim, T.; Jang, H. W. Colorimetric Sensors for Toxic and Hazardous Gas Detection: A Review. *Electron. Mater. Lett.* **2021**, *17* (1), 1–17. https://doi.org/10.1007/s13391-020-00254-9

[82] Szulczyński, B.; Gębicki, J. Currently Commercially Available Chemical Sensors Employed for Detection of Volatile Organic Compounds in Outdoor and Indoor Air. *Environments* **2017**, *4* (1), 21. https://doi.org/10.3390/environments4010021

[83] Ermakova, E. V.; Bessmertnykh-Lemeune, A. The Optical Sensing of Volatile Organic Compounds Using Porphyrins. *Chemosensors* **2024**, *12* (12), 253. https://doi.org/10.3390/chemosensors12120253

[84] Andre, R. S.; Sanfelice, R. C.; Pavinatto, A.; Mattoso, L. H. C.; Correa, D. S. Hybrid Nanomaterials Designed for Volatile Organic Compounds Sensors: A Review. *Materials & Design* **2018**, *156*, 154–166. https://doi.org/10.1016/j.matdes.2018.06.041

[85] Min, Y.; Yuan, C.; Fu, D.; Liu, J. Formaldehyde Gas Sensors Fabricated with Polymer-Based Materials: A Review. *Chemosensors* **2023**, *11* (2), 134. https://doi.org/10.3390/chemosensors11020134

[86] Hua, Y.; Ahmadi, Y.; Kim, K.-H. Molecularly Imprinted Polymers for Sensing Gaseous Volatile Organic Compounds: Opportunities and Challenges. *Environmental Pollution* **2022**, *311*, 119931. https://doi.org/10.1016/j.envpol.2022.119931

[87] Shen, Y.; Tissot, A.; Serre, C. Recent Progress on MOF-Based Optical Sensors for VOC Sensing. *Chem. Sci.* **2022**, *13* (47), 13978–14007. https://doi.org/10.1039/D2SC04314A

[88] Chi, Z.; Chu, S.; Wang, B.; Zhang, Z.; Liu, G.; Wang, X. Advances in Metal Complex-Based Colorimetric Sensors. *Talanta* **2026**, *297*, 128591. https://doi.org/10.1016/j.talanta.2025.128591

[89] Singh, P.; Bansal, N. K.; Dey, S.; Singh, R.; Singh, T. Recent Progress on Perovskite Materials for VOC Gas Sensing. Langmuir 2024, 40 (42), 21931–21956. https://doi.org/10.1021/acs.langmuir.4c02089

[90] Lopez-Torres, D.; Elosua, C. Humidity, Gas, and Volatile Organic Compound Sensors. In *Optical Fibre Sensors*; Villar, I., Matias, I. R., Eds.; Wiley, 2020; pp 367–398. https://doi.org/10.1002/9781119534730.ch11

[91] Han, B.; Rupam, T. H.; Chakraborty, A.; Saha, B. B. A Comprehensive Review on VOCs Sensing Using Different Functional Materials: Mechanisms, Modifications, Challenges and Opportunities. *Renewable and Sustainable Energy Reviews* **2024**, *196*, 114365. https://doi.org/10.1016/j.rser.2024.114365

[92] Kant, T.; Shrivas, K.; Tejwani, A.; Tandey, K.; Sharma, A.; Gupta, S. Progress in the Design of Portable Colorimetric Chemical Sensing Devices. *Nanoscale* **2023**, *15* (47), 19016–19038. https://doi.org/10.1039/D3NR03803C

[93] Banik, D.; Manna, S.K.; Mahapatra, A.K. Recent development of chromogenic and fluorogenic chemosensors for the detection of arsenic species: Environmental and biological applications. *Spectrochim. Acta A Mol. Biomol. Spectrosc*. **2021**, *246*, 119047–119065. https://doi.org/10.1016/j.saa.2020.119047

[94] Azzouz, A.; Vikrant, K.; Kim, K.-H.; Ballesteros, E.; Rhadfi, T.; Malik, A. K. Advances in Colorimetric and Optical Sensing for Gaseous Volatile Organic Compounds. *TrAC Trends in Analytical Chemistry* **2019**, *118*, 502–516. https://doi.org/10.1016/j.trac.2019.06.017

[95] Xu, N.; Jin, S.; Wang, L. Metal Nanoparticles-Based Nanoplatforms for Colorimetric Sensing: A Review. *Reviews in Analytical Chemistry* **2020**, *40* (1), 1–11. https://doi.org/10.1515/revac-2021-0122

[96] Na Kim, H.; Guo, Z.; Zhu, W.; Yoon, J.; Tian, H. Recent Progress on Polymer -Based Fluorescent and Colorimetric Chemosensors. *Chemical Society Reviews* **2011**, *40* (1), 79–93. https://doi.org/10.1039/C0CS00058B

[97] Calloway, D. Beer-Lambert Law. *J. Chem. Educ.* **1997**, *74* (7), 744. https://doi.org/10.1021/ed074p744.3

[98] Hemmateenejad, B.; Bordbar, M. M.; Shojaeifard, Z. Data Acquisition and Data Analysis in Colorimetric Sensor Arrays. *Chemometrics and Intelligent Laboratory Systems* **2023**, *241*, 104975. https://doi.org/10.1016/j.chemolab.2023.104975

[99] de Carvalho Oliveira, G.; Machado, C. C. S.; Inácio, D. K.; Silveira Petruci, J. F. da; Silva, S. G. RGB Color Sensor for Colorimetric Determinations: Evaluation and Quantitative Analysis of Colored Liquid Samples. *Talanta* **2022**, *241*, 123244. https://doi.org/10.1016/j.talanta.2022.123244

[100] Fan, Y.; Li, J.; Guo, Y.; Xie, L.; Zhang, G. Digital Image Colorimetry on Smartphone for Chemical Analysis: A Review. *Measurement* **2021**, *171*, 108829. https://doi.org/10.1016/j.measurement.2020.108829

[101] Bao, Y.; Wan, P.; Zhang, C.; Feng, Z.; Luo, J.; Li, K. Advances in Smartphone-Based Colorimetry and Fluorimetry. *ChemPlusChem* **2025**, *90* (8), e202500135. https://doi.org/10.1002/cplu.202500135.

[102] Mazur, F.; Han, Z.; Tjandra, A. D.; Chandrawati, R. Digitalization of Colorimetric Sensor Technologies for Food Safety. *Advanced Materials* **2024**, *36* (42), 2404274. https://doi.org/10.1002/adma.202404274

[103] Sun, L.; Rotaru, A.; Robeyns, K.; Garcia, Y. A Colorimetric Sensor for the Highly Selective, Ultra-Sensitive, and Rapid Detection of Volatile Organic Compounds and Hazardous Gases. *Ind. Eng. Chem. Res.* **2021**, *60* (24), 8788–8798. https://doi.org/10.1021/acs.iecr.1c01389

[104] Lihua, Y.; Qin, Y.; Zhao, X.; Liao, D.; Li, F.; Jiang, L.; Wen, B.; Lei, Y.; Pang, A.; Liao, L.; Aimiao, Q. Portable Intelligent Sensor Based on Chemically Induced Silver Nanoparticles Colorimetric Response for Visual Monitoring Nitride/Sulfide Gases. SSRN 2025. https://doi.org/10.2139/ssrn.5127142

[105] You, Z.; Zhao, M.; Lu, H.; Chen, H.; Wang, Y. Eye-Readable and Wearable Colorimetric Sensor Arrays for *In Situ* Monitoring of Volatile Organic Compounds. *ACS Appl. Mater. Interfaces* **2024**, *16* (15), 19359–19368. https://doi.org/10.1021/acsami.4c00312

[106] Huang, G.; Liu, Z.; Maaten, L. van der; Weinberger, K. Q. Densely Connected Convolutional Networks. arXiv January 28, 2018. https://doi.org/10.48550/arXiv.1608.06993

[107] Zhao, Q.; Li, F.; Huang, C. Phosphorescent Chemosensors Based on Heavy-Metal Complexes. *Chemical Society Reviews* **2010**, *39* (8), 3007–3030. https://doi.org/10.1039/B915340C

[108] Khan, J. Synthesis and Applications of Fluorescent Chemosensors: A Review. *J Fluoresc* **2024**, *34* (6), 2485–2494. https://doi.org/10.1007/s10895-023-03455-1

[109] Wu J.; Liu W.; Ge J.; Zhang H.; Wang P. New sensing mechanisms for design of fluorescent chemosensors emerging in recent years. *Chem. Soc. Rev*. **2011**, *40*, 3483–3495. https://doi.org/10.1039/C0CS00224K

[110] Dong, R.; Shen, Z.; Li, H.; Cheng, J.; Fu, Y. Research Progress in Fluorescent Gas Sensors Based on MOFs. *J. Mater. Chem. C* **2024**, *12* (33), 12692–12707. https://doi.org/10.1039/D4TC02491E

[111] Yang, G.; Jiang, X.; Xu, H.; Zhao, B. Applications of MOFs as Luminescent Sensors for Environmental Pollutants. *Small* **2021**, *17* (22), 2005327. https://doi.org/10.1002/smll.202005327

[112] Lázaro, A.; Pinto, A.; Rodríguez, L. Supramolecular Sensing with Luminescent Gold(I) and Platinum(II) Organometallics. *Coordination Chemistry Reviews* **2026**, *550*, 217411. https://doi.org/10.1016/j.ccr.2025.217411

[113] Peng, H.; Ding, L.; Fang, Y. Recent Advances in Construction Strategies for Fluorescence Sensing Films. *J. Phys. Chem. Lett.* **2024**, *15* (4), 849–862. https://doi.org/10.1021/acs.jpclett.3c03130

[114] Zhang, P.; Wu, T.; Cao, H.; Zhang, J.; James, T. D.; Sun, X. Fluorometric Detection of Volatile Amines Using an Indanonalkene Platform. *Org. Chem. Front.* **2023**, *10* (6), 1393–1398. https://doi.org/10.1039/D2QO02023H

[115] Li, M.; Liu, K.; Wang, L.; Liu, J.; Miao, R.; Fang, Y. Development of a Column-Shaped Fluorometric Sensor Array and Its Application in Visual Discrimination of Alcohols from Vapor Phase. *Anal. Chem.* **2020**, *92* (1), 1068–1073. https://doi.org/10.1021/acs.analchem.9b04080

[116] Exstrom, C.L.; Sowa, J.R.Jr.; Daws, C.A.; Janzen, D.; Mann, K.R. Inclusion of Organic Vapors by Crystalline, Solvatochromic [Pt(aryl isonitrile)$_4$][Pd(CN)$_4$] Compounds. "Vapochromic" Environmental Sensors. *Chem. Mater*. **1995**, *7*, 15–17. https://doi.org/10.1021/cm00049a005

[117] Drew, S. M.; Janzen, D. E.; Buss, C. E.; MacEwan, D. I.; Dublin, K. M.; Mann, K. R. An Electronic Nose Transducer Array of Vapoluminescent Platinum(II) Double Salts. *J. Am. Chem. Soc.* **2001**, *123* (34), 8414–8415. https://doi.org/10.1021/ja016010x

[118] Wenger, O. S. Vapochromism in Organometallic and Coordination Complexes: Chemical Sensors for Volatile Organic Compounds. *Chem. Rev*. **2013**, *113*, 3686–3733. https://doi.org/10.1021/cr300396p

[119] Jin, M.; Ito, H. Solid-State Luminescence of Au(I) Complexes with External Stimuli-Responsive Properties. *Journal of Photochemistry and Photobiology C: Photochemistry Reviews* **2022**, *51*, 100478. https://doi.org/10.1016/j.jphotochemrev.2021.100478

[120] Mirzadeh, N.; Privér, S. H.; Blake, A. J.; Schmidbaur, H.; Bhargava, S. K. Innovative Molecular Design Strategies in Materials Science Following the Aurophilicity Concept. *Chem. Rev.* **2020**, *120* (15), 7551–7591. https://doi.org/10.1021/acs.chemrev.9b00816

[121] Berenguer, J. R.; Lalinde, E.; Moreno, M. T. Luminescent Cyclometalated-Pentafluorophenyl Pt II , Pt IV and Heteropolynuclear Complexes. *Coordination Chemistry Reviews* **2018**, *366*, 69–90. https://doi.org/10.1016/j.ccr.2018.04.002

[122] Resines-Urien, E.; Fernandez-Bartolome, E.; Martinez-Martinez, A.; Gamonal, A.; Piñeiro-López, L.; Sanchez Costa, J. Vapochromic Effect in Switchable Molecular-Based Spin Crossover Compounds. *Chemical Society Reviews* **2023**, *52* (2), 705–727. https://doi.org/10.1039/D2CS00790H

[123] Zhang, X.; Li, B.; Chen, Z.-H.; Chen, Z.-N. Luminescence Vapochromism in Solid Materials Based on Metal Complexes for Detection of Volatile Organic Compounds (VOCs). *J. Mater. Chem.* **2012**, *22* (23), 11427. https://doi.org/10.1039/c2jm30394a

[124] Higuchi, M. Stimuli-Responsive Metallo-Supramolecular Polymer Films: Design, Synthesis and Device Fabrication. *J. Mater. Chem. C* **2014**, *2* (44), 9331–9341. https://doi.org/10.1039/C4TC00689E

[125] Li, E.; Jie, K.; Liu, M.; Sheng, X.; Zhua, W.; Huang, F. Vapochromic crystals: understanding vapochromism from the perspective of crystal engineering. *Chem. Soc. Rev*. **2020**, *49*, 1517–1544. https://doi.org/10.1039/C9CS00098D

[126] Yoshida, M.; Kato, M. Regulation of Metal–Metal Interactions and Chromic Phenomena of Multi-Decker Platinum Complexes Having π-Systems. *Coordination Chemistry Reviews* **2018**, *355*, 101–115. https://doi.org/10.1016/j.ccr.2017.07.016

[127] Jin, K.; Moon, D.; Chen, Y.; Park, J. Comprehensive Qualitative and Quantitative Colorimetric Sensing of Volatile Organic Compounds Using Monolayered Metal–Organic Framework Films. *Advanced Materials* **2024**, *36* (8), 2309570. https://doi.org/10.1002/adma.202309570

[128] Kondo, S.; Yoshimura, N.; Kobayashi, A.; Kuruppu, K. D. C.; Sameera, W. M. C.; Fujii, S.; Yoshida, M.; Kato, M. Vapoluminescent Thin-Film with Unsaturated Copper(i) Complex for Rapid Light-on Sensing of N-Heteroaromatic Vapour. *J. Mater. Chem. C* **2024**, *12* (5), 1799–1808. https://doi.org/10.1039/D3TC03571A

[129] Meng, Z.; Stolz, R. M.; Mendecki, L.; Mirica, K. A. Electrically-Transduced Chemical Sensors Based on Two-Dimensional Nanomaterials. *Chem. Rev.* **2019**, *119* (1), 478–598. https://doi.org/10.1021/acs.chemrev.8b00311

[130] Chandran, G. T.; Li, X.; Ogata, A.; Penner, R. M. Electrically Transduced Sensors Based on Nanomaterials (2012–2016). *Anal. Chem.* **2017**, *89* (1), 249–275. https://doi.org/10.1021/acs.analchem.6b04687

[131] Marco, S.; Gutierrez-Galvez, A. Signal and Data Processing for Machine Olfaction and Chemical Sensing: A Review. *IEEE Sensors Journal* **2012**, *12* (11), 3189–3214. https://doi.org/10.1109/JSEN.2012.2192920

[132] Xu, Y.; Cheng, C.; Du, S.; Yang, J.; Yu, B.; Luo, J.; Yin, W.; Li, E.; Dong, S.; Ye, P.; Duan, X. Contacts between Two- and Three-Dimensional Materials: Ohmic, Schottky, and p–n Heterojunctions. *ACS Nano* **2016**, *10* (5), 4895–4919. https://doi.org/10.1021/acsnano.6b01842

[133] Tung, R. T. The Physics and Chemistry of the Schottky Barrier Height. *Appl. Phys. Rev.* **2014**, *1* (1), 011304. https://doi.org/10.1063/1.4858400

[134] Scaccabarozzi, A. D.; Basu, A.; Aniés, F.; Liu, J.; Zapata-Arteaga, O.; Warren, R.; Firdaus, Y.; Nugraha, M. I.; Lin, Y.; Campoy-Quiles, M.; Koch, N.; Müller, C.; Tsetseris, L.; Heeney, M.; Anthopoulos, T. D. Doping Approaches for Organic Semiconductors. *Chem. Rev.* **2022**, *122* (4), 4420–4492. https://doi.org/10.1021/acs.chemrev.1c00581

[135] Salzmann, I.; Heimel, G.; Oehzelt, M.; Winkler, S.; Koch, N. Molecular Electrical Doping of Organic Semiconductors: Fundamental Mechanisms and Emerging Dopant Design Rules. *Acc. Chem. Res.* **2016**, *49* (3), 370–378. https://doi.org/10.1021/acs.accounts.5b00438

[136] Potje-Kamloth, K. Semiconductor Junction Gas Sensors. *Chem. Rev.* **2008**, *108* (2), 367–399. https://doi.org/10.1021/cr0681086

[137] Pui, W. K.; Yusoff, R.; Aroua, M. K. A Review on Activated Carbon Adsorption for Volatile Organic Compounds (VOCs). *Reviews in Chemical Engineering* **2019**, *35* (5), 649–668. https://doi.org/10.1515/revce-2017-0057

[138] Zhang, Z.; Yates, J. T. Jr. Band Bending in Semiconductors: Chemical and Physical Consequences at Surfaces and Interfaces. *Chem. Rev.* **2012**, *112* (10), 5520–5551. https://doi.org/10.1021/cr3000626

[139] Barsan, N.; Weimar, U. Conduction Model of Metal Oxide Gas Sensors. *Journal of Electroceramics* **2001**, *7* (3), 143–167. https://doi.org/10.1023/A:1014405811371

[140] Zhang, Z.; Qiu, P.; Deng, Y.; Luo, W. Recent Advances in Functionalizing Metal Oxide Semiconductors for Highly Sensitive Gas Sensors. *Small Methods* **2025**, *9* (10), 2500228. https://doi.org/10.1002/smtd.202500228

[141] Zhai, H.; Wu, Z.; Fang, Z. Recent Progress of Ga_2O_3-Based Gas Sensors. *Ceramics International* **2022**, *48* (17), 24213–24233. https://doi.org/10.1016/j.ceramint.2022.06.066

[142] Pargoletti, E.; Cappelletti, G. Breakthroughs in the Design of Novel Carbon-Based Metal Oxides Nanocomposites for VOCs Gas Sensing. *Nanomaterials* **2020**, *10* (8), 1485. https://doi.org/10.3390/nano10081485

[143] Lin, T.; Lv, X.; Hu, Z.; Xu, A.; Feng, C. Semiconductor Metal Oxides as Chemoresistive Sensors for Detecting Volatile Organic Compounds. *Sensors* **2019**, *19* (2), 233. https://doi.org/10.3390/s19020233

[144] Kumar, A.; Meunier-Prest, R.; Bouvet, M. Organic Heterojunction Devices Based on Phthalocyanines: A New Approach to Gas Chemosensing. *Sensors* **2020**, *20*, 4700. https://doi.org/10.3390/s20174700

[145] Ali, S.; Gupta, A.; Shafiei, M.; Langford, S.J. Recent Advances in Perylene Diimide-Based Active Materials in Electrical Mode Gas Sensing. *Chemosensors* **2021**, *9*, 30. https://doi.org/10.3390/chemosensors9020030

[146] Stosic, D.; Zholobenko, V. Application of Zeolite-Based Materials for Chemical Sensing of VOCs. *Sensors* **2025**, *25* (5), 1634. https://doi.org/10.3390/s25051634

[147] Chen, S.; Yuan, B.; Liu, G.; Zhang, D. Electrochemical Sensors Based on Covalent Organic Frameworks: A Critical Review. *Front. Chem.* **2020**, *8*, 601044. https://doi.org/10.3389/fchem.2020.601044

[148] Wang, F.; Hu, S. Electrochemical Sensors Based on Metal and Semiconductor Nanoparticles. *Microchim Acta* **2009**, *165* (1–2), 1–22. https://doi.org/10.1007/s00604-009-0136-4

[149] Kitadai, H.; Yuan, M.; Ma, Y.; Ling, X. Graphene-Based Environmental Sensors: Electrical and Optical Devices. *Molecules* **2021**, *26* (8), 2165. https://doi.org/10.3390/molecules26082165

[150] Gupta, R.K.; Rasheed, T.; Nguyen, T.A.; Bilal, M. (Eds) Metal-Organic Frameworks-Based Hybrid Materials for Environmental Sensing and Monitoring. *CRC Press,* **2022**. https://doi.org/10.1201/9781003188148

[151] Fanti, G.; Borghi, F.; Spinazzè, A.; Rovelli, S.; Campagnolo, D.; Keller, M.; Cattaneo, A.; Cauda, E.; Cavallo, D.M. Features and Practicability of the Next-Generation Sensors and Monitors for Exposure Assessment to Airborne Pollutants: A Systematic Review. *Sensors* **2021**, *21*, 4513. https://doi.org/10.3390/s21134513

[152] Bouvet, M.; Gaudillat, P.; Suisse, J.-M. Phthalocyanine-based hybrid materials for chemosensing. *J. Porphyrins Phthalocyanines* **2013**, *17*, 913–919. https://doi.org/10.1142/S1088424613300073

[153] Kimmel, D. W.; LeBlanc, G.; Meschievitz, M. E.; Cliffel, D. E. Electrochemical Sensors and Biosensors. *Anal. Chem.* **2012**, *84* (2), 685–707. https://doi.org/10.1021/ac202878q

[154] Marín, S.; Merkoçi, A. Nanomaterials Based Electrochemical Sensing Applications for Safety and Security. *Electroanalysis* **2012**, *24* (3), 459–469. https://doi.org/10.1002/elan.201100576

[155] Ramaiyan, K. P.; Mukundan (Mukund), R. Electrochemical Sensors for Air Quality Monitoring. *Electrochem. Soc. Interface* **2019**, *28* (3), 59. https://doi.org/10.1149/2.F08193IF

[156] Sharifi, K.; Pirsa, S. Electrochemical Sensors; Types and Applications in the Food Industry. *Chemical Review and Letters* **2020**, *3* (4), 192–201. https://doi.org/10.22034/crl.2020.240962.1073

[157] Mathew, M.; Sekhar Rout, C. Schottky Diodes Based on 2D Materials for Environmental Gas Monitoring: A Review on Emerging Trends, Recent Developments and Future Perspectives. *Journal of Materials Chemistry C* **2021**, *9* (2), 395–416. https://doi.org/10.1039/D0TC04840B

[158] Daniel, T. T.; Yadav, V. K. S.; Abraham, E. E.; Paily, R. P. Carbon Monoxide Sensor Based on Printed ZnO. *IEEE Sensors J.* **2022**, *22* (11), 10910–10917. https://doi.org/10.1109/JSEN.2022.3166811

[159] Kitai, A. *Principles of Solar Cells, LEDs and Diodes: The Role of the PN Junction*; John Wiley & Sons: Chichester, West Sussex, UK, **2011**.

[160] Zhang, N.; Tan, F.; Qi, L.; An, J.; Che, M.; Shi, Y.; Li, Y.; Shi, Z.; Sun, X.; Li, S.; Li, D. Switchable Operating Modes Enable Low Power Consumption and Improved Gas Sensing Efficiency in MoS2/BP Heterojunction. *Sensors and Actuators B: Chemical* **2023**, *396*, 134620. https://doi.org/10.1016/j.snb.2023.134620

[161] Kim, H.-Y.; Lee, K.; McEvoy, N.; Yim, C.; Duesberg, G. S. Chemically Modulated Graphene Diodes. *Nano Lett.* **2013**, *13* (5), 2182–2188. https://doi.org/10.1021/nl400674k

[162] Terzic, E.; Terzic, J.; Nagarajah, R.; Alamgir, M. Capacitive Sensing Technology. In *A Neural Network Approach to Fluid Quantity Measurement in Dynamic Environments*; Terzic, E., Terzic, J., Nagarajah, R., Alamgir, M., Eds.; Springer: London, 2012; pp 11–37. https://doi.org/10.1007/978-1-4471-4060-3_2

[163] Kopp, T.; Mannhart, J. Calculation of the Capacitances of Conductors: Perspectives for the Optimization of Electronic Devices. *J. Appl. Phys.* **2009**, *106* (6), 064504. https://doi.org/10.1063/1.3197246

[164] Bindra, P.; Hazra, A. Capacitive Gas and Vapor Sensors Using Nanomaterials. *J Mater Sci: Mater Electron* **2018**, *29* (8), 6129–6148. https://doi.org/10.1007/s10854-018-8606-2

[165] Blue, R.; Uttamchandani, D. Chemicapacitors as a Versatile Platform for Miniature Gas and Vapor Sensors. *Meas. Sci. Technol.* **2016**, *28* (2), 022001. https://doi.org/10.1088/1361-6501/28/2/022001

[166] Gonçalves, B. F.; Fernández, E.; Valverde, A.; Gaboardi, M.; Salazar, H.; Petrenko, V.; Porro, J. M.; Cavalcanti, L. P.; Urtiaga, K.; Esperança, J. M. S. S.; Correia, D. M.; Fernandez-Alonso, F.; Lanceros-Mendez, S.; Fernández De Luis, R. Exploring the Compositional Space of a Metal–Organic Framework with Ionic Liquids to Develop Porous Ionic Conductors for Enhanced Signal and Selectivity in VOC Capacitive Sensors. *J. Mater. Chem. A* **2024**, *12* (24), 14595–14607. https://doi.org/10.1039/D4TA00959B

[167] Gründler, P. Conductivity Sensors and Capacitive Sensors. In *Chemical Sensors: An Introduction for scientist and engineers*, **2007**; pp 123−132.

[168] Pejović, M. M.; Pejovic, M. M. *Different Types of Field-Effect Transistors: Theory and Applications*; **2017**. http://dx.doi.org/10.5772/65626

[169] Mao, S.; Chang, J.; Pu, H.; Lu, G.; He, Q.; Zhang, H.; Chen, J. Two-Dimensional Nanomaterial-Based Field-Effect Transistors for Chemical and Biological Sensing. *Chemical Society Reviews* **2017**, *46* (22), 6872–6904. https://doi.org/10.1039/C6CS00827E

[170] Tan, Y.; Cheng, B.; Tang, X.; Zhao, W.; Zhang, Y. Dual-Gate Carbon-Based FET Trace Gas Sensors: Enhancing Sensitivity through Work Function Modulation. *Anal. Chem.* **2025**, *97* (42), 23260–23268. https://doi.org/10.1021/acs.analchem.5c03672

[171] Torsi, L.; Magliulo, M.; Manoli, K.; Palazzo, G. Organic Field-Effect Transistor Sensors: A Tutorial Review. *Chemical Society Reviews* **2013**, *42* (22), 8612–8628. https://doi.org/10.1039/C3CS60127G

[172] Mayarambakam, S.; Bond, C. R.; Katz, H. E.; Solomon, J.; Sobhi, H. F. Incorporation and Electronic Sensing Device Effects of Aniline Functionality in Diketopyrrolopyrrole–Thiophene Semiconducting Polymers. *J. Mater. Chem. C* **2025**, *13* (35), 18176–18186. https://doi.org/10.1039/D5TC01597A

[173] Singh, A. K.; Chowdhury, N. K.; Roy, S. C.; Bhowmik, B. Review of Thin Film Transistor Gas Sensors: Comparison with Resistive and Capacitive Sensors. *J. Electron. Mater.* **2022**, *51* (5), 1974–2003. https://doi.org/10.1007/s11664-022-09485-y

[174] Khojier, K.; Savaloni, H.; Goudarzi, S.; Gholami, M. A Review on Chemiresistive Gas Sensors: Basic Concepts, Evolution, and Perspective. *Challenges in Nano and Micro Scale Science and Technology* **2025**. https://doi.org/10.22111/cnmst.2025.53016.1268

[175] Zeghbroeck, V. Principles of Semiconductor Devices and Heterojunctions; Prentice Hall PTR: 2007.

[176] Vázquez-López, A.; Bartolomé, J.; Cremades, A.; Maestre, D. High-Performance Room-Temperature Conductometric Gas Sensors: Materials and Strategies, *Chemosensors* **2022**, *10*, 227. https://doi.org/10.3390/chemosensors10060227

[177] Korotcenkov, G. The role of morphology and crystallographic structure of metal oxides in response of conductometric-type gas sensors. *Mater. Sci. Eng.* **2008**, *61*, 1–39. https://doi.org/10.1016/j.mser.2008.02.001

[178] Jamnani, S. R.; Moghaddam, H. M.; Leonardi, S. G.; Neri, G.; Ferlazzo, A. VOCs Sensing Properties of Samarium Oxide Nanorods. *Ceramics International* **2024**, *50* (1), 403–411. https://doi.org/10.1016/j.ceramint.2023.10.115

[179] Shaw, S.; White, J. D. Asymmetric Catalysis Using Chiral Salen–Metal Complexes: Recent Advances. *Chem. Rev.* **2019**, *119* (16), 9381–9426. https://doi.org/10.1021/acs.chemrev.9b00074

[180] Abu-Dief, A.M.; Mohamed, I.M.A. A review on versatile applications of transition metal complexes incorporating Schiff bases. *J. basic appl. sci*. **2015**, *4*, 119–133. https://doi.org/10.1016/j.bjbas.2015.05.004

[181] Kaczmarek, M. T. Synthetic Aspects, Crystal Structures and Biological Activities of d- and f-Metal Salen-Type Complexes. *Physical Sciences Reviews 1* (5). https://doi.org/10.1515/psr-2016-0004

[182] Consiglio, G.; Oliveri, I. P.; Failla, S.; Di Bella, S. On the Aggregation and Sensing Properties of Zinc(II) Schiff-Base Complexes of Salen-Type Ligands. *Molecules* **2019**, *24* (13), 2514. https://doi.org/10.3390/molecules24132514

[183] Lamine, W.; Boughdiri, S.; Christ, L.; Morell, C.; Chermette, H. Coordination Chemistry of Zn2+ with Sal(Ph)En Ligands: Tetrahedral Coordination or Penta-Coordination? A DFT Analysis. *Journal of Computational Chemistry* **2019**, *40* (5), 717–725. https://doi.org/10.1002/jcc.25755

[184] Forte, G.; Oliveri, I. P.; Consiglio, G.; Failla, S.; Bella, S. D. On the Lewis Acidic Character of Bis(Salicylaldiminato)Zinc(II) Schiff-Base Complexes: A Computational and Experimental Investigation on a Series of Compounds Varying the Bridging Diimine. *Dalton Trans.* **2017**, *46* (14), 4571–4581. https://doi.org/10.1039/C7DT00574A

[185] Consiglio G.; Failla S.; Fortuna C.G.; D'Urso L.; Forte G. Aggregation of a Zn(II)-salen complex: Theoretical study of structure and spectra. *Comput. Theor. Chem*. **2015**, 1–6. https://doi.org/10.1016/j.comptc.2015.05.014

[186] Kleij, A. W. Zinc-Centred Salen Complexes: Versatile and Accessible Supramolecular Building Motifs. *Dalton Trans.* **2009**, No. 24, 4635–4639. https://doi.org/10.1039/B902866H

[187] Crane, A. K.; MacLachlan, M. J. Portraits of Porosity: Porous Structures Based on Metal Salen Complexes. *European Journal of Inorganic Chemistry* **2012**, *2012* (1), 17–30. https://doi.org/10.1002/ejic.201100786

[188] Wezenberg, S. J.; Kleij, A. W. Material Applications for Salen Frameworks. *Angewandte Chemie International Edition* **2008**, *47* (13), 2354–2364. https://doi.org/10.1002/anie.200702468

[189] Kim, W.-S.; Lee, K. Y.; Ryu, E.-H.; Gu, J.-M.; Kim, Y.; Lee, S. J.; Huh, S. Catalytic Transesterifications by a Zn–BisSalen MOF Containing Open Pyridyl Groups Inside 1D Channels. *European Journal of Inorganic Chemistry* **2013**, *2013* (24), 4228–4233. https://doi.org/10.1002/ejic.201300208

[190] Oliveri, I. P.; Failla, S.; Malandrino, G.; Bella, S. D. New Molecular Architectures by Aggregation of Tailored Zinc(II) Schiff-Base Complexes. *New J. Chem.* **2011**, *35* (12), 2826–2831. https://doi.org/10.1039/C1NJ20618D

[191] Wezenberg, S. J.; Escudero-Adán, E. C.; Benet-Buchholz, J.; Kleij, A. W. Versatile Approach toward the Self-Assembly of Heteromultimetallic Salen Structures. *Inorg. Chem.* **2008**, *47* (8), 2925–2927. https://doi.org/10.1021/ic800033v

[192] Kleij, A. W.; Kuil, M.; Tooke, D. M.; Spek, A. L.; Reek, J. N. H. Metal-Directed Self-Assembly of a ZnII-Salpyr Complex into a Supramolecular Vase Structure. *Inorg. Chem.* **2007**, *46* (15), 5829–5831. https://doi.org/10.1021/ic700408v

[193] Mizukami, S.; Houjou, H.; Nagawa, Y.; Kanesato, M. First Helical Zinc(II) Complex with a Salen Ligand. *Chem. Commun.* **2003**, No. 10, 1148–1149. https://doi.org/10.1039/B301099F

[194] Leoni, L.; Dalla Cort, A. The Supramolecular Attitude of Metal–Salophen and Metal–Salen Complexes. *Inorganics* **2018**, *6* (2), 42. https://doi.org/10.3390/inorganics6020042

[195] Yin, H.-Y.; Tang, J.; Zhang, J.-L. Introducing Metallosalens to Biological Studies: The Renaissance of Traditional Coordination Complexes. *Eur. J. Inorg. Chem.* **2017**, 5085–5093. https://doi.org/10.1002/ejic.201700695

[196] Dalla Cort, A.; Bernardin, P. D.; Forte, G.; Mihan, F. Y. Metal–Salophen-Based Receptors for Anions. *Chem. Soc. Rev.* **2010**, *39* (10), 3863–3874. https://doi.org/10.1039/B926222A

[197] Puglisi, R.; Ballistreri, F. P.; Gangemi, C. M. A.; Toscano, R. M.; Tomaselli, G. A.; Pappalardo, A.; Sfrazzetto, G. T. Chiral Zn–Salen Complexes: A New Class of Fluorescent Receptors for Enantiodiscrimination of Chiral Amines. *New J. Chem.* **2017**, *41* (3), 911–915. https://doi.org/10.1039/C6NJ03592B

[198] Martínez-Rodríguez, L.; Bandeira, N. A. G.; Bo, C.; Kleij, A. W. Highly Efficient Chirality Transfer from Diamines Encapsulated within a Self-Assembled Calixarene–Salen Host. *Chemistry – A European Journal* **2015**, *21* (19), 7144–7150. https://doi.org/10.1002/chem.201500333

[199] Escárcega-Bobadilla, M. V.; Salassa, G.; Martínez Belmonte, M.; Escudero-Adán, E. C.; Kleij, A. W. Versatile Switching in Substrate Topicity: Supramolecular Chirality Induction in Di- and Trinuclear Host Complexes. *Chemistry – A European Journal* **2012**, *18* (22), 6805–6810. https://doi.org/10.1002/chem.201200335

[200] Oliveri, I. P.; Bella, S. D. Lewis Basicity of Relevant Monoanions in a Non-Protogenic Organic Solvent Using a Zinc(II) Schiff-Base Complex as a Reference Lewis Acid. *Dalton Trans.* **2017**, *46* (35), 11608–11614. https://doi.org/10.1039/C7DT02821K

[201] Oliveri, I. P.; Di Bella, S. Sensitive Fluorescent Detection and Lewis Basicity of Aliphatic Amines. *J. Phys. Chem. A* **2011**, *115* (50), 14325–14330. https://doi.org/10.1021/jp2066265

[202] Dalla Cort, A.; Mandolini, L.; Pasquini, C.; Rissanen, K.; Russo, L.; Schiaffino, L. Zinc–Salophen Complexes as Selective Receptors for Tertiary Amines. *New J. Chem.* **2007**, *31* (9), 1633–1638. https://doi.org/10.1039/B700723J

[203] Oliveri, I. P.; Di Bella, S. Highly Sensitive Fluorescent Probe for Detection of Alkaloids. *Tetrahedron* **2011**, *67* (48), 9446–9449. https://doi.org/10.1016/j.tet.2011.09.100

[204] Escudero-Adán, E. C.; Benet-Buchholz, J.; Kleij, A. W. Supramolecular Adsorption of Alkaloids by Metallosalphen Complexes. *Inorg. Chem.* **2008**, *47* (10), 4256–4263. https://doi.org/10.1021/ic702257e

[205] Wezenberg, S. J.; Escudero-Adán, E. C.; Benet-Buchholz, J.; Kleij, A. W. Colorimetric Discrimination between Important Alkaloid Nuclei Mediated by a Bis-Salphen Chromophore. *Org. Lett.* **2008**, *10* (15), 3311–3314. https://doi.org/10.1021/ol801167r

[206] Munzi, G.; Failla, S.; Di Bella, S. Highly Selective and Sensitive Colorimetric/Fluorometric Dual Mode Detection of Relevant Biogenic Amines. *Analyst* **2021**, *146* (7), 2144–2151. https://doi.org/10.1039/D0AN02336A

[207] Wezenberg, S. J.; Anselmo, D.; Escudero-Adán, E. C.; Benet-Buchholz, J.; Kleij, A. W. Dimetallic Activation of Dihydrogen Phosphate by Zn(Salphen) Chromophores. *European Journal of Inorganic Chemistry* **2010**, *2010* (29), 4611–4616. https://doi.org/10.1002/ejic.201000455

[208] Sabaté, F.; Giannicchi, I.; Acón, L.; Dalla Cort, A.; Rodríguez, L. Anion Selectivity of Zn–Salophen Receptors: Influence of Ligand Substituents. *Inorganica Chimica Acta* **2015**, *434*, 1–6. https://doi.org/10.1016/j.ica.2015.04.032

[209] Cano, M.; Rodríguez, L.; Lima, J. C.; Pina, F.; Dalla Cort, A.; Pasquini, C.; Schiaffino, L. Specific Supramolecular Interactions between Zn2+-Salophen Complexes and Biologically Relevant Anions. *Inorg. Chem.* **2009**, *48* (13), 6229–6235. https://doi.org/10.1021/ic900557n

[210] Strianese, M.; Milione, S.; Maranzana, A.; Grassi, A.; Pellecchia, C. Selective Detection of ATP and ADP in Aqueous Solution by Using a Fluorescent Zinc Receptor. *Chem. Commun.* **2012**, *48* (93), 11419–11421. https://doi.org/10.1039/C2CC35730E

[211] Strianese, M.; Lamberti, M.; Pellecchia, C. Interaction of Monohydrogensulfide with a Family of Fluorescent Pyridoxal-Based Zn(II) Receptors. *Dalton Trans.* **2018**, *47* (48), 17392–17400. https://doi.org/10.1039/C8DT03969K

[212] Dalla Cort, A.; De Bernardin, P.; Schiaffino, L. A New Water Soluble Zn-Salophen Derivative as a Receptor for α-Aminoacids: Unexpected Chiral Discrimination. *Chirality* **2009**, *21* (1), 104–109. https://doi.org/10.1002/chir.20614

[213] Jurček, O.; Cametti, M.; Pontini, M.; Kolehmainen, E.; Rissanen, K. A Zinc–Salophen/Bile-Acid Conjugate Receptor Solubilized by CTABr Micelles Binds Phosphate in Water. *Org. Biomol. Chem.* **2013**, *11* (28), 4585–4590. https://doi.org/10.1039/C3OB40724A

[214] Strianese, M.; Guarnieri, D.; Lamberti, M.; Landi, A.; Peluso, A.; Pellecchia, C. Fluorescent Salen-Type Zn(II) Complexes As Probes for Detecting Hydrogen Sulfide and Its Anion: Bioimaging Applications. *Inorg. Chem.* **2020**, *59* (21), 15977–15986. https://doi.org/10.1021/acs.inorgchem.0c02499

[215] Tang, J.; Cai, Y.-B.; Jing, J.; Zhang, J.-L. Unravelling the Correlation between Metal Induced Aggregation and Cellular Uptake/Subcellular Localization of Znsalen: An Overlooked Rule for Design of Luminescent Metal Probes. *Chemical Science* **2015**, *6* (4), 2389–2397. https://doi.org/10.1039/C4SC03824J

[216] Giannicchi, I.; Brissos, R.; Ramos, D.; Lapuente, J. de; Lima, J. C.; Cort, A. D.; Rodríguez, L. Substituent Effects on the Biological Properties of Zn-Salophen Complexes. *Inorg. Chem.* **2013**, *52* (16), 9245–9253. https://doi.org/10.1021/ic4004356

[217] Brissos, R.; Ramos, D.; Lima, J. C.; Mihan, F. Y.; Borràs, M.; Lapuente, J. de; Cort, A. D.; Rodríguez, L. Luminescent Zinc Salophen Derivatives: Cytotoxicity Assessment and Action Mechanism Studies. *New J. Chem.* **2013**, *37* (4), 1046–1055. https://doi.org/10.1039/C3NJ41125G

[218] Hai, Y.; Chen, J.-J.; Zhao, P.; Lv, H.; Yu, Y.; Xu, P.; Zhang, J.-L. Luminescent Zinc Salen Complexes as Single and Two-Photon Fluorescence Subcellular Imaging Probes. *Chem. Commun.* **2011**, *47* (8), 2435–2437. https://doi.org/10.1039/C0CC04113K

[219] Dumur, F.; Contal, E.; Wantz, G.; Gigmes, D. Photoluminescence of Zinc Complexes: Easily Tunable Optical Properties by Variation of the Bridge Between the Imido Groups of Schiff Base Ligands. *European Journal of Inorganic Chemistry* **2014**, *2014* (25), 4186–4198. https://doi.org/10.1002/ejic.201402422

[220] Rout, S. K.; Mohanty, J. S. Continuous Flow Strategies in Organometallic Synthesis: A Critical Review of Oxidative Insertion, Directed Metalation, Halogen–Metal Exchange, and Transmetalation Reactions. *Sustainable Chemistry One World* **2025**, *8*, 100131. https://doi.org/10.1016/j.scowo.2025.100131

[221] Yan, X.; Xi, C. Advances in Transmetalation Reactions Originated from Organozirconium Compounds. *Coordination Chemistry Reviews* **2017**, *350*, 275–284. https://doi.org/10.1016/j.ccr.2017.07.005

[222] Partyka, D. V. Transmetalation of Unsaturated Carbon Nucleophiles from Boron-Containing Species to the Mid to Late d-Block Metals of Relevance to Catalytic C−X Coupling Reactions (X = C, F, N, O, Pb, S, Se, Te). *Chem. Rev.* **2011**, *111* (3), 1529–1595. https://doi.org/10.1021/cr1002276

[223] Solomon, N. S. D.; Keaveney, S. T. Mechanistic Considerations for Transmetalation at Nickel(II) and Palladium(II) Complexes: Towards Improved Catalysis. *Aust J Chem* **2025**, *78* (10), CH25103. https://doi.org/10.1071/CH25103

[224] Osakada, K.; Nishihara, Y. Transmetalation of Boronic Acids and Their Derivatives: Mechanistic Elucidation and Relevance to Catalysis. *Dalton Trans.* **2022**, *51* (3), 777–796. https://doi.org/10.1039/D1DT02986J

[225] Cheng, J.; Ma, X.; Zhang, Y.; Liu, J.; Zhou, X.; Xiang, H. Optical Chemosensors Based on Transmetalation of Salen-Based Schiff Base Complexes. *Inorg. Chem.* **2014**, *53* (6), 3210–3219. https://doi.org/10.1021/ic5000815

[226] Oliveri, I. P.; Attinà, A.; Di Bella, S. A Zinc(II) Schiff Base Complex as Fluorescent Chemosensor for the Selective and Sensitive Detection of Copper(II) in Aqueous Solution. *Sensors* **2023**, *23* (8), 3925. https://doi.org/10.3390/s23083925

[227] Oliveri, I. P.; Consiglio, G.; Munzi, G.; Failla, S.; Di Bella, S. Deaggregation Properties and Transmetalation Studies of a Zinc(II) Salen-Type Schiff-Base Complex. *Dalton Trans.* **2022**, *51* (31), 11859–11867. https://doi.org/10.1039/D2DT01448C

[228] Oliveri, I. P.; Munzi, G.; Di Bella, S. A Simple Approach Based on Transmetalation for the Selective and Sensitive Colorimetric/Fluorometric Detection of Copper(ii) Ions in Drinking Water. *New J. Chem.* **2022**, *46* (37), 18018–18024. https://doi.org/10.1039/D2NJ03695A

[229] Hui, J. K.-H.; MacLachlan, M. J. Metal-Containing Nanofibers via Coordination Chemistry. *Coordination Chemistry Reviews* **2010**, *254* (19), 2363–2390. https://doi.org/10.1016/j.ccr.2010.02.011

[230] Hui, J. K.-H.; Yu, Z.; Mirfakhrai, T.; MacLachlan, M. J. Supramolecular Assembly of Carbohydrate-Functionalized Salphen–Metal Complexes. *Chemistry – A European Journal* **2009**, *15* (48), 13456–13465. https://doi.org/10.1002/chem.200902031

[231] Hui, J. K. H.; Yu, Z.; MacLachlan, M. J. Supramolecular Assembly of Zinc Salphen Complexes: Access to Metal-Containing Gels and Nanofibers. *Angewandte Chemie - International Edition* **2007**, *46* (42), 7980–7983. https://doi.org/10.1002/anie.200702680

[232] Oliveri, I. P.; Malandrino, G.; Bella, S. D. Self-Assembled Nanostructures of Amphiphilic Zinc(II) Salophen Complexes: Role of the Solvent on Their Structure and Morphology. *Dalton Trans.* **2014**, *43* (26), 10208–10214. https://doi.org/10.1039/C4DT00973H

[233] Oliveri, I. P.; Failla, S.; Malandrino, G.; Di Bella, S. Controlling the Molecular Self-Assembly into Nanofibers of Amphiphilic Zinc(II) Salophen Complexes. *J. Phys. Chem. C* **2013**, *117* (29), 15335–15341. https://doi.org/10.1021/jp4038182

[234] Hui, J. K.-H.; MacLachlan, M. J. Fibrous Aggregates from Dinuclear Zinc(II) Salphen Complexes. *Dalton Trans.* **2010**, *39* (31), 7310–7319. https://doi.org/10.1039/C0DT00234H

[235] Chakraborty, S.; Mondal, P.; Krishna Prasad, S.; Shankar Rao, D. S.; Bhattacharjee, C. R. Zinc(II)-Salphen Complexes Bearing Long Alkoxy Side Arms: Synthesis, Solvent Dependent Aggregation, and Spacer Group Substituent Effect on Mesomorphism and Photophysical Property. *Journal of Molecular Liquids* **2017**, *246*, 290–301. https://doi.org/10.1016/j.molliq.2017.09.078

[236] Chakraborty, S.; Mondal, P.; Prasad, S. K.; Rao, D. S. S.; Bhattacharjee, C. R. Induction of Mesomorphism through Supramolecular Assembly in Metal Coordination Compounds of "Salphen"-Type Schiff Bases: Photoluminescence and Solvatochromism. *European Journal of Inorganic Chemistry* **2016**, *2016* (28), 4604–4614. https://doi.org/10.1002/ejic.201600513

[237] Chakraborty, S.; Bhattacharjee, C. R.; Mondal, P.; Prasad, S. K.; Rao, D. S. S. Synthesis and Aggregation Behaviour of Luminescent Mesomorphic Zinc(II) Complexes with 'Salen' Type Asymmetric Schiff Base Ligands. *Dalton Trans.* **2015**, *44* (16), 7477–7488. https://doi.org/10.1039/C4DT03989K

[238] Bhattacharjee, C. R.; Das, G.; Mondal, P.; Prasad, S. K.; Rao, D. S. S. Novel Green Light Emitting Nondiscoid Liquid Crystalline Zinc(II) Schiff-Base Complexes. *European Journal of Inorganic Chemistry* **2011**, *2011* (9), 1418–1424. https://doi.org/10.1002/ejic.201001248

[239] Pyrlin, S. V.; Hine, N. D. M.; Kleij, A. W.; Ramos, M. M. D. Self-Assembly of Bis-Salphen Compounds: From Semiflexible Chains to Webs of Nanorings. *Soft Matter* **2018**, *14* (7), 1181–1194. https://doi.org/10.1039/C7SM02371E

[240] Oliveri, I. P.; Malandrino, G.; Di Bella, S. Phase Transition and Vapochromism in Molecular Assemblies of a Polymorphic Zinc(II) Schiff-Base Complex. *Inorg. Chem.* **2014**, *53* (18), 9771–9777. https://doi.org/10.1021/ic5013632

[241] Mirabella, S.; Oliveri, I. P.; Ruffino, F.; Maccarrone, G.; Di Bella, S. Low-Cost Chemiresistive Sensor for Volatile Amines Based on a 2D Network of a Zinc(II) Schiff-Base Complex. *Applied Physics Letters* **2016**, *109* (14), 143108. https://doi.org/10.1063/1.4963790

[242] Oliveri, I. P.; Malandrino, G.; Mirabella, S.; Bella, S. D. Vapochromic and Chemiresistive Characteristics of a Nanostructured Molecular Material Composed of a Zinc(II)-Salophen Complex. *Dalton Trans.* **2018**, *47* (44), 15977–15982. https://doi.org/10.1039/C8DT03904F

[243] Gaeta, M.; Oliveri, I. P.; Munzi, G.; Lo Presti, F.; Di Bella, S. Stimuli-Responsive Properties of a Zinc(II) Salen-Type Schiff-Base Complex and Vapochromic Detection of Volatile Organic Compounds. *Inorg. Chem.* **2024**, *63* (8), 3850–3858. https://doi.org/10.1021/acs.inorgchem.3c04165

[244] Yan, X.; Song, X.; Mu, X.; Wang, Y. Mechanochromic Luminescence Based on a Phthalonitrile-Bridging Salophen Zinc(II) Complex. *New J. Chem.* **2019**, *43* (40), 15886–15891. https://doi.org/10.1039/C9NJ03704G

[245] Song, X.; Yu, H.; Yan, X.; Zhang, Y.; Miao, Y.; Ye, K.; Wang, Y. A Luminescent Benzothiadiazole-Bridging Bis(Salicylaldiminato)Zinc(II) Complex with Mechanochromic and Organogelation Properties. *Dalton Trans.* **2018**, *47* (17), 6146–6155. https://doi.org/10.1039/C8DT00665B

[246] Clarisse, G.; Riou, M. T. Synthesis and Characterization of Some Lanthanide Phthalocyanines. *Inorganica Chimica Acta* **1987**, *130* (1), 139–144. https://doi.org/10.1016/S0020-1693(00)85943-5

[247] Consiglio, G.; Failla, S.; Finocchiaro, P.; Oliveri, I. P.; Purrello, R.; Di Bella, S. Supramolecular Aggregation/Deaggregation in Amphiphilic Dipolar Schiff-Base Zinc(II) Complexes. *Inorg. Chem.* **2010**, *49* (11), 5134–5142. https://doi.org/10.1021/ic100284r

[248] Yaws, C. L. *The Yaws Handbook of Vapor Pressure: Antoine Coefficients*; Gulf Professional Publishing, **2015**.

[249] Thomson, G. Wm. The Antoine Equation for Vapor-Pressure Data. *Chem. Rev.* **1946**, *38* (1), 1–39. https://doi.org/10.1021/cr60119a001

[250] Wang, X.; Si, Y.; Wang, J.; Ding, B.; Yu, J.; Al-Deyab, S. S. A facile and highly sensitive colorimetric sensor for the detection of formaldehyde based on electro-spinning/netting nano-fiber/nets. *Sens. Actuators B Chem.* **2012**, *163*, 186–193. https://doi.org/10.1016/j.snb.2012.01.033

[251] Chavolla, E.; Zaldivar, D.; Cuevas, E.; Perez, M. A. Color Spaces Advantages and Disadvantages in Image Color Clustering Segmentation. In *Advances in Soft Computing and Machine Learning in Image Processing*; Hassanien, A. E., Oliva, D. A., Eds.; Springer International Publishing: Cham, **2018**; pp 3–22. https://doi.org/10.1007/978-3-319-63754-9_1

[252] Mokrzycki, W. S.; Tatol, M. Colour Difference ΔE - a Survey. *Machine Graphics & Vision International Journal* **2011**, *20* (4), 383–411. https://doi.org/10.5555/3166160.3166161

[253] Currie, L. A. Detection and quantification limits: origins and historical overview. *Anal. Chim. Acta*. **1999**, *391*, 127–134. https://doi.org/10.1016/S0003-2670(99)00105-1

[254] Analytical Methods Committee. Recommendation for the definition, estimation and use of the detection limit. *Analyst* **1987**, *112*, 199–204. https://doi.org/10.1039/AN9871200199

[255] Tonezzer, M.; Van Duy, L. Gas Sensors. In *Encyclopedia of Sensors and Biosensors (First Edition)*; Narayan, R., Ed.; Elsevier: Oxford, **2023**; pp 185–208. https://doi.org/10.1016/B978-0-12-822548-6.00113-8

[256] Bekhit, A.E.-D.A.; Holman, B.W.B.; Giteru, S.G.; Hopkins, D.L. Total volatile basic nitrogen (TVB-N) and its role in meat spoilage: A review. *Trends Food Sci. Technol*. **2021**, *109*, 280–302. https://doi.org/10.1016/j.tifs.2021.01.006

[257] Greim, H.; Bury, D.; Klimisch, H.-J.; Oeben-Negele, M.; Ziegler-Skylakakts, K. Toxicity of Aliphatic Amines: Structure-Activity Relationships. *Chemosphere*. **1998**, *36*, 271–295. https://doi.org/10.1016/S0045-6535(97)00365-2

[258] Roose, P.; Turcotte, M.G. Amines, Lower Aliphatic. Kirk-Othmer Encyclopedia of Chemical Technology. Wiley-VCH: New York, NY, USA, **2016**.

[259] Roose, P.; Eller, K.; Henkes, E.; Rossbacher, P.; Höke, R. Amines, Aliphatic. Ullmann's Encyclopedia of Industrial Chemistry. Wiley-VCH: New York, NY, USA, **2015**.

[260] Astuto, M.C.; Manieu, C. Butylamines. In Encyclopedia of Toxicology (Fourth Edition), *Elsevier*, **2024**, *2*, 343–351.

[261] Gamer, A.O.; van Ravenzwaay, J.H.B. Developmental toxicity of oral n-butylamine hydrochloride and inhaled n-butylamine in rats. *Food Chem. Toxicol*. **2002**, *40*, 1833–1842. https://doi.org/10.1016/S0278-6915(02)00164-3

[262] The National Institute for Occupational Safety and Health, *n*-Butylamine. https://www.cdc.gov/niosh/idlh/109739.html

[263] Occupational Safety and Health Administration, *n*-Butylamine. https://www.osha.gov/chemicaldata/99

[264] Froidevaux, V.; Negrell, C.; Caillol, S.; Pascault, J.P.; Boutevin, B.; Biobased Amines: From Synthesis to Polymers; Present and Future. *Chem. Rev.* **2016**, 116, 14181–14224. https://doi.org/10.1021/acs.chemrev.6b00486

[265] Wu, Y.; An, H. Green Catalytic Synthesis of Ethylenediamine from Ethylene Glycol and Monoethanolamine: A Review. *ACS Omega* **2024**, *9*, 18747–18756. https://doi.org/10.1021/acsomega.4c00709

[266] Kostikov, R.R. 1,2-Diaminoethane. In Encyclopedia of Reagents for Organic Synthesis. *John Wiley & Sons, Ltd.*: Hoboken, NJ, USA, **2001**. https://doi.org/10.1002/047084289X.rd007m

[267] Weissermel, K.; Arpe, H.-J. Industrial Organic Chemistry, 3rd ed. *Wiley-VCH:* Weinheim, Germany, **1997**.

[268] Zuidema, J. Ethylenediamine, profile of a sensitizing excipient. *Pharm. Weekb. Sci. Ed.* **1985**, *7*, 134–140. https://doi.org/10.1007/BF02097249

[269] Hart, J.R. Ethylenediaminetetraacetic Acid and Related Chelating Agents. In Ullmann's Encyclopedia of Industrial Chemistry, (Ed.). *John Wiley & Sons, Ltd*, **2011**, 573–578. https://doi.org/10.1002/14356007.a10_095.pub2

[270] Cary, R.; Dobson, S.; Delic, J. 1,2-Diaminoethane (ethylenediamine). In Concise International Chemical Assessment Documents; *World Health Organization*: Geneva, Switzerland, **1999**, *15*, 1–30.

[271] The National Institute for Occupational Safety and Health, Ethylenediamine (1,2-Diaminoethane). https://www.cdc.gov/niosh/idlh/107153.html

[272] Occupational Safety and Health Administration, Ethylenediamine (1,2-Diaminoethane). https://www.osha.gov/chemicaldata/58

[273] Wójcik, W.; Łukasiewicz, M.; Puppel, K. Biogenic amines: Formation, action and toxicity—A review. *J. Sci. Food Agric.* **2021**, *101*, 2634–2640. https://doi.org/10.1002/jsfa.10928

[274] Ahmad, W.; Mohammed, G.I.; Al-Eryani, D.A.; Saigl, Z.M.; Alyoubi, A.O.; Alwael, H.; Bashammakh, A.S.; O'Sullivan C.K.; El-Shahawi, M.S. Biogenic Amines Formation Mechanism and Determination Strategies: Future Challenges and Limitations. *Crit. Rev. Anal. Chem.* **2019**, *50*, 485–500. https://doi.org/10.1080/10408347.2019.1657793

[275] Natrella, G.; Vacca, M.; Minervini, F.; Faccia, M.; DeAngelis, M. A Comprehensive Review on the Biogenic Amines in Cheeses: Their Origin, Chemical Characteristics, Hazard and Reduction Strategies. *Foods* **2024**, *13*, 2583. https://doi.org/10.3390/foods13162583

[276] Miller, K.; Reichert, C.L.; Schmid, M. Biogenic Amine Detection Systems for Intelligent Packaging Concepts: Meat and Meat Products. *Food Rev. Int.* **2023**, *39*, 2543–2567. https://doi.org/10.1080/87559129.2021.1961270

[277] Biji, K.B.; Ravishankar, C.N.; Venkateswarlu, R.; Mohan, C.O.; Srinivasa Gopal, T.K. Biogenic amines in seafood: a review. *J Food Sci Technol* **2016**, *53*, 2210–2218. https://doi.org/10.1007/s13197-016-2224-x

[278] Guo, Y.-Y.; Yang, Y.-P.; Peng, Q.; Han, Y. Biogenic amines in wine: a review. *IJFST* **2015**, *50*, 1523–1532. https://doi.org/10.1111/ijfs.12833

[279] Saad, B.; Tofalo, R. (Eds.) Biogenic Amines in Food: Analysis Occurrence and Toxicity. *The Royal Society of Chemistry*: Croydon, UK, **2020**.

[280] Tofalo, R.; Schirone, M.; Perpetuini, G.; Suzzi, G. Biogenic amines: Toxicology and health effect. In Encyclopedia of Food and Health; Caballero, B., Finglas, P.M., Toldrá, F., Eds.; *Academic Press:* Cambridge, UK, **2016**, 424–429. http://dx.doi.org/10.1016/B978-0-12-384947-2.00071-4

[281] Ding, T.; Li, Y. Biogenic amines are important indices for characterizing the freshness and hygienic quality of aquatic products: A review. *LWT-Food Science and Technology* **2024**, *194*, 115793. https://doi.org/10.1016/j.lwt.2024.115793

[282] Ruiz-Capillas, C.; Herrero, A.M. Impact of Biogenic Amines on Food Quality and Safety. *Foods* **2019**, *8*, 62. https://doi.org/10.3390/foods8020062

[283] ISO/TS 2610 - Analysis of natural gas. Biomethane; Determination of amines content. **2022**. https://www.iso.org/standard/81454.html

[284] Kabir, A.; Mocan, A.; Piccolantonio, S.; Sperandio, E.; Ulusoyd, H.I.; Locatelli, M. Analysis of amines. *Recent Advances in Natural Products Analysis Elsevier Inc.* **2020**, 569–591 https://doi.org/10.1016/B978-0-12-816455-6.00016-0

[285] ISO 16000–38, Indoor air – Part 38: Determination of amines in indoor and test chamber air; Active sampling on samplers containing phosphoric acid impregnated filters. **2019**. https://www.iso.org/standard/67954.html

[286] ISO 16000–39, Indoor air – Part 39: Determination of amines; Analysis of amines by (ultra-) high-performance liquid chromatography coupled to high resolution or tandem mass spectrometry. **2019**. https://www.iso.org/standard/67958.html

[287] Szulejko, J.E.; Kim, K.-H. A review of sampling and pretreatment techniques for the collection of airborne amines. *Trends Anal. Chem.* **2014**, *57*, 118–134. https://doi.org/10.1016/j.trac.2014.02.010

[288] Liu , P.; Shen, X.; Liu, T.; Liu, J.-J. An electron-deficient viologen metal-organic material for colorimetric and luminescence sensing of organic amines. *J. Solid State Chem*. **2023**, *328*, 124383–124389. https://doi.org/10.1016/j.jssc.2023.124383

[289] Müller, D.G.; Oreste, E.Q.; Heinemann, M.G.; Dias, D.; Kessler, F. Biogenic amine sensors and its building materials: A review. *Eur. Polym. J.* **2022**, *175*, 111221. https://doi.org/10.1016/j.eurpolymj.2022.111221

[290] di Nunzio, M.R.; Gutiérrez, M.; Moreno, J.M.; Corma, A.; Díaz, U.; Douhal, A. Interrogating the Behaviour of a Styryl Dye Interacting with a Mesoscopic 2D-MOF and Its Luminescent Vapochromic Sensing. *Int. J. Mol. Sci*. **2022**, *23*, 330–346. https://doi.org/10.3390/ijms23010330

[291] Bu, L.; Rémond, M.; Colinet, P.; Jeanneau, E.; Le Bahers, T.; Chaput, F.; Andraud, C.; Bretonnière, Y. Sensitive 1,1-dicyanovinyl push-pull dye for primary amine sensing in solution by fluorescence. *Dyes Pigm*. **2022**, *202*, 110258–110266. https://doi.org/10.1016/j.dyepig.2022.110258

[292] Chen, T.-Y.; Cai, Y.-D.; Jiang, S.-Q.; Cai, W.; Tong, M.-L.; Bao, X. Light-and Chemical-Stimuli-Induced Isomerization of Donor. ChemPhotoChem. **2021**, *5,* 559–564. https://doi.org/10.1002/cptc.202100004

[293] Khatua, S.; Biswas, P. Flexible Luminescent MOF: Trapping of Less Stable Conformation of Rotational Isomers, In Situ Guest-Responsive Turn-Off and Turn-On Luminescence and Mechanistic Study. *ACS Appl. Mater. Interfaces* **2020**, *12*, 22335−22346. https://doi.org/10.1021/acsami.0c02891

[294] Flores-Sànchez, R.; Gàmez, F.; Lopes-Costa, T.; Pedrosa, J.M. A Calixarene Promotes Disaggregation and Sensing Performance of Carboxyphenyl Porphyrin Films. *ACS Omega* **2020**, *5*, 6299−6308. https://dx.doi.org/10.1021/acsomega.9b03612?ref=pdf

[295] Danchuk, A.; Komova, N.S.; Mobarez, S.N.; Doronin, S.Y.; Burmistrova, N.A.; Markin, A.V.; Duerkop, A. Optical sensors for determination of biogenic amines in food. *Anal. Bioanal. Chem.* **2020**, *412*, 4023–4036. https://doi.org/10.1007/s00216-020-02675-9

[296] Balijapalli, U.; Manickam, S.; Thirumoorthy, K.; Sundaramurthy, K.N.; Sathiyanarayanan, K.I. (Tetrahydrodibenzo[a,i]phenanthridin-5-yl)phenol as a FluorescentProbe for the Detection of Aniline. *J. Org. Chem*. **2019**, *84*, 11513−11523. https://doi.org/10.1021/acs.joc.9b00709

[297] Sathiskumar, U.; Easwaramoorthi, S. Red-Emitting Ratiometric Fluorescence Chemodosimeter for the Discriminative Detection of Aromaticand Aliphatic Amines. *ChemistrySelect* **2019**, *4*, 7486–749. https://doi.org/10.1002/slct.201901254

[298] Fan, J.; Chang, X.; He, M.; Shang, C.; Wang, G.; Yin, S.; Peng, H.; Fang, Y. Functionality-Oriented Derivatization of Naphthalene Diimide: AMolecular Gel Strategy-Based Fluorescent Film for Aniline VaporDetection. *ACS Appl. Mater. Interfaces* **2016**, *8*, 18584−18592. https://doi.org/10.1021/acsami.6b04915

[299] Dong, L.; Deng, C.; He, C.; Shi, L.; Fu, Y.; Zhu, D.; Cao, H.; He, Q.; Cheng, J. Highly sensitive vapor detection of amines with fluorescent conjugated polymer: A novel lasing turn-on sensory mechanism. *Sens. Actuators B Chem*. **2013**, *180*, 28–34. https://doi.org/10.1016/j.snb.2011.11.046

[300] Zou, H.; Hai, Y.; Ye, H.; You, L. Dynamic Covalent Switches and Communicating Networks for Tunable Multicolor Luminescent Systems and Vapor-Responsive Materials. *J. Am. Chem. Soc*. **2019**, *141*, 16344−16353. http://dx.doi.org/10.1021/jacs.9b07175

[301] Shi, L.; Fu, Y.; He, C.; Zhu, D.; Gao, Y.; Wang, Y.; He, Q.; Cao, H.; Cheng, J. A mild and catalyst-free conversion of solid phase benzylidenemalononitrile/benzylidenemalonate to N-benzylidene-amine and its application for fluorescence detection of primary alkyl amine vapor. *Chem. Commun*. **2014**, *50*, 872–874. https://doi.org/10.1039/C3CC48299E

[302] Oberg, K.I.; Hodyss, R.; Beauchamp, J.L. Simple optical sensor for amine vapors based on dyed silica microspheres. *Sens. Actuators B Chem*. **2006**, *115*, 79–85. https://doi.org/10.1016/j.snb.2005.08.021

[303] Alimohammadi, M.; Sharifi, H.; Tashkhourian, J.; Vazan, M.; Shamsipur, M.; Hemmateenejad, B. An optical nose based on array of metal-doped carbon dots for identification of hazardous amines and assessing meat freshness. *Sens. Actuators B Chem*. **2023**, *393*, 134274–134286. https://doi.org/10.1016/j.snb.2023.134274

[304] Longstreet, A.R.; Chandler, R.R.; Banerjee, T.; Miller, L.Z.; Hanson, K.; McQuade, D.T. Ylidenemalononitrile enamine-coated media as fluorescent "turn-on" probes for volatile primary amines. *Photochem. Photobiol. Sci*. **2017**, *16*, 455–458. https://doi.org/10.1039/C7PP00021A

[305] Venkateswarulu, M.; Gaur, P.; Koner, R.R. Sensitive molecular optical material for signaling primary amine vapors. *Sens. Actuators B Chem*. **2015**, *210*, 144–148. https://doi.org/10.1016/j.snb.2014.12.082

[306] Qin, W.; Parzuchowski, P.; Zhang, W.; Meyerhoff, M.E. Optical Sensor for Amine Vapors Based onDimer-Monomer Equilibrium of Indium(III)Octaethylporphyrin in a Polymeric Film. *Anal. Chem*. **2003**, *75*, 332–340. https://doi.org/10.1021/ac0205356

[307] Roales, J.; Pedrosa, J.M.; Guilléna, M.G.; Lopes-Costa, T.; Pinto, S.M.A.; Calvete, M.J.F.; Pereira, M.M. Optical detection of amine vapors using ZnTriad porphyrin thin films. *Sens. Actuators B Chem*. **2015**, *210*, 28–35. https://doi.org/10.1016/j.snb.2014.12.080

[308] Rochat, S.; Swager, T.M. Fluorescence Sensing of Amine Vapors Using a Cationic Conjugated Polymer Combined with Various Anions. *Angew. Chem. Int. Ed*. **2014**, *53*, 9792–9796. https://doi.org/10.1002/anie.201404439

[309] Ding, X.; Yang, K.-L. Liquid crystal based optical sensor for detection of vaporous butylamine in air. *Sens. Actuators B Chem*. **2012**, *173*, 607–613. http://dx.doi.org/10.1016/j.snb.2012.07.067

[310] Grant, M.J.; Harding, C.R.; Wolfe, K.M.; Welch, G.C. Biogenic amine sensors using organic p-conjugated materials as active sensing components and their commercialization potential. *J. Mater. Chem. C* **2023**, *11*, 9749. https://doi.org/10.1039/d3tc00383c

[311] Wang, S.; Liu, J.; Zhao, H.; Guo, Z.; Xing, H.; Gao, Y. Electrically conductive coordination polymer for highly selective chemiresistive sensing of volatile amines. *Inorg. Chem.* **2018**, *57*, 541–544. https://doi.org/10.1021/acs.inorgchem.7b02464

[312] Zhang, S.; Lin, H.; Sun, P.; Zhou, Y.; Zhang, Q.; Sang, T.; Tuo, A.; Xiong, K.; Gai, Y. Cationic Europium–Organic Framework for Chromatographic Column Separation of Ionic Dyes and Stimuli-Responsive Chromic Properties. *Inorg. Chem.* **2024**, *63*, 9288–9296. https://doi.org/10.1021/acs.inorgchem.4c01035

[313] Saadati, A.; Farshchi, F.; Jafari, M.; Kholafazad, H.; Hasanzadeh, M.; Shadjou, N. Optical discrimination of histamine and ethylenediamine in meat samples using a colorimetric affordable test strip (CATS): Introducing a novel lab-on paper sensing strategy for low-cost ensuring food safety by rapid and accurate monitoring of biogenic amines. *RSC Adv.* **2024**, *14*, 8602–8614. https://doi.org/10.1039/D4RA00101J

[314] Liu, J.-J.; Sun, Z.-L.; Liu, J.; Xia, S.-B. A series of multi-responsive viologen-based alkaline-earth metal coordination complexes: Thermochromism, photochromism, and vapochromism. *J. Mol. Struct*. **2021**, *1238*, 130444. https://doi.org/10.1016/j.molstruc.2021.130444

[315] Jin, Y.-J.; Kwak, G. Detection of biogenic amines using a nitrated conjugated polymer. *Sens. Actuators B Chem*. **2018**, *271*, 183–188. https://doi.org/10.1016/j.snb.2018.05.091

[316] Xia, H.; Liu, G.; Zhao, C.; Meng, X.; Li, F.; Wang, F.; Duana, L.; Chen, H. Fluorescence sensing of amine vapours based on ZnS-supramolecular organogel hybrid films. *RSC Adv.* **2017**, *7*, 17264–17270. https://doi.org/10.1039/C7RA00556C

[317] Zhang, Z.; Ma, W.; Yan, B. Multi-step tandem functionalization assembly of MOFs-based hybrid polymeric films for color tuning luminescence and responsive sensing on organic vapors. *Colloids Surf. A Physicochem. Eng. Asp*. **2022**, *648*, 129416. https://doi.org/10.1016/j.colsurfa.2022.129416

[318] Tunsrichon, S.; Youngme, S.; Boonmak, J. Coexistence of naked-eye mechanochromism, vapochromism, and thermochromism in a soft crystalline layered nickel (II) coordination polymer. *Inorg. Chem*. **2021**, *60*, 18242–18250. https://doi.org/10.1021/acs.inorgchem.1c02875

[319] Klongdee, F.; Leelasubcharoen, S.; Youngme, S.; Boonmak, J. Sonochemical synthesis of a trinuclear Cu (II) complex with open coordination sites for the differentiable optical detection of volatile amines. *RSC Adv.* **2021**, *11*, 12218–12226. https://doi.org/10.1039/D1RA01151K

[320] Li, E.; Jie, K.; Fang, Y.; Cai, P.; Huang, F. Transformation of Nonporous Adaptive Pillar[4]arene[1]quinone Crystals into Fluorescent Crystals via Multi-Step Solid–Vapor Postsynthetic Modification for Fluorescence Turn-on Sensing of Ethylenediamine. *J. Am. Chem. Soc*. **2020**, *142*, 15560–15568. https://doi.org/10.1021/jacs.0c07482

[321] Suebphanpho, J.; Wannapaiboon, S.; Youngme, S.; Boonmak, J. Bifunctional dinuclear complexes based on iminodiacetate and 1,2-di (4-pyridyl) ethylene: Crystal structures, vapochromism, and iodine adsorption. *Cryst. Growth Des.* **2020**, *20*, 7439–7449. https://doi.org/10.1021/acs.cgd.0c01113

[322] Queirós, S.; Ribeiro, S.O.; Silva, A.M.G.; Leite, A. Biogenic Amine Sensing Based on Rosamine a N-Methylpyridinium Derivative Supported on Silica Materials from Rice Husk. *Sensors* **2022**, *22*, 9573. https://doi.org/10.3390/s22249573

[323] Chakraborty, M.; Sivasakthi, P.; Samanta, P.K.; Chakravarty, M. Concentration-tuned diverse response to selective biogenic amines using a reusable fluorophore: Monitoring protein-rich food spoilage. *J. Mater. Chem. B* **2024**, *12*, 2746–2760. https://doi.org/10.1039/D3TB02569A

[324] García-Calvo, V.; García-Calvo, J.; Fernández-Espinosa, I.; Carbayo, A.M.; Rojo, J.; Rodríguez, M.T.; García-Herbosa, G.; Torroba, T.; Cuevas, J.V. Luminescent complexes of iridium(III) with aliphatic amines and detection of biogenic amines. *Inorg. Chim. Acta* **2020**, *50*, 119409. https://doi.org/10.1016/j.ica.2019.119409

[325] Li, L.; Li, W.; Wang, L.; Tang, H.; Cao, D.; Ran, X. Pyrrolopyrrole aza-BODIPY dyes for ultrasensitive and highly selective biogenic diamine detection. *Sens. Actuators B Chem*. **2020**, *312*, 127953. https://doi.org/10.1016/j.snb.2020.127953

[326] Ni, J.; Li, M.-Y.; Liu, Z.; Zhao, H.; Zhang, J.-J.; Liu, S.-Q.; Chen, J.; Duan, C.-Y.; Chen, L.-Y.; Song, X.-D. Discrimination of Various Amine Vapors by a Triemissive Metal-Organic Framework Composite via the Combination of a Three-Dimensional Ratiometric Approach and a Confinement-Induced Enhancement Effect. *ACS Appl. Mater. Interfaces* **2020**, *12*, 12043–12053. https://doi.org/10.1021/acsami.9b22130

[327] Shang, C.; Wang, L.; An, Y.; Chen, P.; Chang, X.; Qi, Y.; Kang, R.; Fang, Y. Langmuir–Blodgett films of perylene bisimide derivatives and fluorescent recognition of diamines. *Phys. Chem. Chem. Phys*. **2017**, *19*, 23898–23904. https://doi.org/10.1039/C7CP04235C

[328] Zhang, J.; Zhou, J.; Zhang, T.; Tang, Y.; Zeng, L. A colorimetric and fluorescent sensor for non-destructive screening of the freshness of shrimp and fish. *Spectrochim. Acta Part A Mol. Biomol. Spectrosc*. **2023**, *296*, 122647. https://doi.org/10.1016/j.saa.2023.122647

[329] Zeng, L.; Xiao, X.; Ye, H.; Ma, D.; Zhou, J. Fast visual monitoring of the freshness of beef using a smart fluorescent sensor. *Food Chem*. **2022**, *394*, 133489. https://doi.org/10.1016/j.foodchem.2022.133489

[330] Ke, Y.; Liu, Y.; Zu, B.; Lei, D.; Wang, G.; Li, J.; Ren, W.; Dou, X. Electronic Tuning in Reaction-Based Fluorescent Sensing for Instantaneous and Ultrasensitive Visualization of Ethylenediamine. *Angew. Chem. Int. Ed.* **2022**, *61*, e202203358. https://doi.org/10.1002/anie.202203358

[331] Roy,R.; Sajeev, N.R.; Sharma, V.; Lal Koner, A. Aggregation induced emission switching based ultrasensitive ratiometric detection of biogenic diamines using a perylenediimide-based smart fluoroprobe. *ACS Appl. Mater. Interfaces* **2019**, *11*, 47207–47217. https://doi.org/10.1021/acsami.9b14690

[332] Consiglio, G.; Failla, S.; Oliveri, I.P.; Purrello, R.; Di Bella, S. Controlling the molecular aggregation. An amphiphilic Schiff-base zinc(II) complex as supramolecular fluorescent probe. *Dalton Trans*. **2009**, 10426–10428. https://doi.org/10.1039/b914930a

[333] Tsukamoto, T.; Aoki, R.; Sakamoto, R.; Toyoda, R.; Shimada, M.; Hattori, Y.; Kitagawa, Y.; Nishibori, E.; Nakano, M.; Nishihara, H. Mechano-, Thermo-, Solvato-, and Vapochromism in Bis(Acetato-K1: O)[4′-(4-(Diphenylamino)Phenyl)](2,2′:6′,2″-Terpyridine-k^{3}N,N′,N″)Zinc(II) and Its Polymer. *Chem. Commun.* **2017**, *53* (70), 9805–9808. https://doi.org/10.1039/c7cc05022d

[334] Platonova, I.; Branchi, A.; Lessi, M.; Ruggeri, G.; Bellina, F.; Pucci, A. Zn(II)-Bisthienylethynylbipyridine Complex: Preparation, Characterization and Vapochromic Behaviour in Polymer Films. *Dyes and Pigments* **2014**, *110*, 249–255. https://doi.org/10.1016/j.dyepig.2014.03.022

[335] Patel, S.; Jamunkar, R.; Sinha, D.; Monisha; Patle, T.K.; Kant, T.; Dewangan, K.; Shrivas, K. Recent development in nanomaterials fabricated paper-based colorimetric and fluorescent sensors: A review. *Trends Environ. Anal. Chem*. **2021**, *31*, e00136–e00148. https://doi.org/10.1016/j.teac.2021.e00136

[336] Tortorich, R.P.; Shamkhalichenar, H.; Choi, J.-W. Inkjet-Printed and Paper-Based Electrochemical Sensors. *Appl. Sci*. **2018**, *8*, 288–303. https://doi.org/10.3390/app8020288

[337] Mahadeva, S.K.; Walus, K.; Stoeber, B. Paper as a Platform for Sensing Applications and Other Devices: A Review. *ACS Appl. Mater. Interfaces* **2015**, *7*, 8345–8362. https://doi.org/10.1021/acsami.5b00373.

[338] Liana, D.D.; Raguse, B.; Gooding, J.J.; Chow, E. Recent Advances in Paper-Based Sensors. *Sensors* **2012**, *12*, 11505–11526. https://doi.org/10.3390/s120911505

[339] Hey, M. The Washing and Aqueous Deacidification of Paper. *Pap. Conserv.* **2010**, *4:1*, 66–80. https://doi.org/10.1080/03094227.1979.9638520

[340] The National Institute for Occupational Safety and Health, Aniline. https://www.cdc.gov/niosh/idlh/62533.html

[341] Ge, X.; Wexler, A. S.; Clegg, S. L. Atmospheric Amines – Part I. A Review. *Atmospheric Environment* **2011**, *45* (3), 524–546. https://doi.org/10.1016/j.atmosenv.2010.10.012

[342] Gal, J.-F. Thermodynamic Treatments of Lewis Basicity. In *Lewis Base Catalysis in Organic Synthesis*; John Wiley & Sons, Ltd, **2016**; pp 55–84. https://doi.org/10.1002/9783527675142.ch3

[343] Hunter, E.P.L.; Lias, S.G. Evaluated Gas Phase Basicities and Proton Affinities of Molecules: An Update, *J. Phys. Chem.* **1998**, Ref. Data 27, 416–456. https://doi.org/10.1063/1.556018

[344] Barzegar, F.; Kamankesh, M.; Mohammadi, A. Heterocyclic Aromatic Amines in Cooked Food: A Review on Formation, Health Risk-Toxicology and Their Analytical Techniques. *Food Chemistry* **2019**, *280*, 240–254. https://doi.org/10.1016/j.foodchem.2018.12.058

[345] Skog, K. I.; Johansson, M. A. E.; Jägerstad, M. I. Carcinogenic Heterocyclic Amines in Model Systems and Cooked Foods: A Review on Formation, Occurrence and Intake. *Food and Chemical Toxicology* **1998**, *36* (9), 879–896. https://doi.org/10.1016/S0278-6915(98)00061-1

[346] Ohgaki, H.; Takayama, S.; Sugimura, T. Carcinogenicities of Heterocyclic Amines in Cooked Food. *Mutation Research/Genetic Toxicology* **1991**, *259* (3), 399–410. https://doi.org/10.1016/0165-1218(91)90130-E

[347] Nadeem, H. R.; Akhtar, S.; Ismail, T.; Sestili, P.; Lorenzo, J. M.; Ranjha, M. M. A. N.; Jooste, L.; Hano, C.; Aadil, R. M. Heterocyclic Aromatic Amines in Meat: Formation, Isolation, Risk Assessment, and Inhibitory Effect of Plant Extracts. *Foods* **2021**, *10* (7), 1466. https://doi.org/10.3390/foods10071466

[348] Rahman, U. ur; Sahar, A.; Khan, M. I.; Nadeem, M. Production of Heterocyclic Aromatic Amines in Meat: Chemistry, Health Risks and Inhibition. A Review. *LWT - Food Science and Technology* **2014**, *59* (1), 229–233. https://doi.org/10.1016/j.lwt.2014.06.005

[349] Sugimura, T.; Wakabayashi, K.; Nakagama, H.; Nagao, M. Heterocyclic Amines: Mutagens/Carcinogens Produced during Cooking of Meat and Fish. *Cancer Science* **2004**, *95* (4), 290–299. https://doi.org/10.1111/j.1349-7006.2004.tb03205.x

[350] Skog, K.; Solyakov, A. Heterocyclic Amines in Poultry Products: A Literature Review. *Food and Chemical Toxicology* **2002**, *40* (8), 1213–1221. https://doi.org/10.1016/S0278-6915(02)00062-5

[351] Knize, M. G.; Salmon, C. P.; Pais, P.; Felton, J. S. Food Heating and the Formation of Heterocyclic Aromatic Amine and Polycyclic Aromatic Hydrocarbon Mutagens/Carcinogens. In *Impact of Processing on Food Safety*; Jackson, L. S., Knize, M. G., Morgan, J. N., Eds.; Springer US: Boston, MA, **1999**; pp 179–193. https://doi.org/10.1007/978-1-4615-4853-9_12

[352] Alaejos, M. S.; Afonso, A. M. Factors That Affect the Content of Heterocyclic Aromatic Amines in Foods. *Comprehensive Reviews in Food Science and Food Safety* **2011**, *10* (2), 52–108. https://doi.org/10.1111/j.1541-4337.2010.00141.x

[353] Cheng, K.-W.; Chen, F.; Wang, M. Heterocyclic Amines: Chemistry and Health. *Molecular Nutrition & Food Research* **2006**, *50* (12), 1150–1170. https://doi.org/10.1002/mnfr.200600086

[354] Sinha, R. An Epidemiologic Approach to Studying Heterocyclic Amines. *Mutation Research/Fundamental and Molecular Mechanisms of Mutagenesis* **2002**, *506–507*, 197–204. https://doi.org/10.1016/S0027-5107(02)00166-5

[355] Felton, J. S.; Malfatti, M. A.; Knize, M. G.; Salmon, C. P.; Hopmans, E. C.; Wu, R. W. Health Risks of Heterocyclic Amines. *Mutation Research/Fundamental and Molecular Mechanisms of Mutagenesis* **1997**, *376* (1), 37–41. https://doi.org/10.1016/S0027-5107(97)00023-7

[356] Sugimura, T. Overview of Carcinogenic Heterocyclic Amines. *Mutation Research/Fundamental and Molecular Mechanisms of Mutagenesis* **1997**, *376* (1), 211–219. https://doi.org/10.1016/S0027-5107(97)00045-6

[357] Allaka, T. R.; Katari, N. K. Chapter 17 - Synthesis of Pyridine Derivatives for Diverse Biological Activity Profiles: A Review. In *Recent Developments in the Synthesis and Applications of Pyridines*; Singh, P., Ed.; Elsevier, 2023; pp 605–625. https://doi.org/10.1016/B978-0-323-91221-1.00005-1

[358] Higasio, Y. S.; Shoji, T. Heterocyclic Compounds Such as Pyrroles, Pyridines, Pyrollidins, Piperdines, Indoles, Imidazol and Pyrazins. *Applied Catalysis A: General* **2001**, *221* (1–2), 197–207. https://doi.org/10.1016/S0926-860X(01)00815-8. https://doi.org/10.1002/14356007.a22_399

[359] Shimizu, S.; Watanabe, N.; Kataoka, T.; Shoji, T.; Abe, N.; Morishita, S.; Ichimura, H. Pyridine and Pyridine Derivatives. In *Ullmann's Encyclopedia of Industrial Chemistry*; John Wiley & Sons, Ltd, **2000**. https://doi.org/10.1002/14356007.a22_399

[360] Zalat, O. A.; Elsayed, M. A. A Study on Microwave Removal of Pyridine from Wastewater. *Journal of Environmental Chemical Engineering* **2013**, *1* (3), 137–143. https://doi.org/10.1016/j.jece.2013.04.010

[361] Buron, G.; Hacquemand, R.; Pourié, G.; Jacquot, L.; Brand, G. Effects of Pyridine Inhalation Exposure on Olfactory Epithelium in Mice. *Experimental and Toxicologic Pathology* **2013**, *65* (1), 159–164. https://doi.org/10.1016/j.etp.2011.08.001

[362] liu, S.; Wu, C.-H.; Huang, H.-J. Toxicity and Anaerobic Biodegradability of Pyridine and Its Derivatives under Sulfidogenic Conditions. *Chemosphere* **1998**, *36* (10), 2345–2357. https://doi.org/10.1016/S0045-6535(97)10203-X

[363] He, F.; Qi, T.; Guo, S.; Wang, H.; Zhang, Z.; Liu, R.; Zong, W. Mechanistic Insights into Pyridine Exposure Induced Toxicity in Model *Eisenia Fetida* Species: Evidence from Whole-Animal, Cellular, and Molecular-Based Perspectives. *Chemosphere* **2023**, *335*, 139139. https://doi.org/10.1016/j.chemosphere.2023.139139

[364] *Some Industrial Chemicals*; International Agency for Research on Cancer, International Agency for Research on Cancer, Eds.; IARC monographs on the evaluation of carcinogenic risks to humans; IARC: Lyon, **1994**.

[365] The National Institute for Occupational Safety and Health, Pyridine. https://www.cdc.gov/niosh/idlh/110861.html

[366] Occupational Safety and Health Administration, Pyridine. https://www.osha.gov/chemicaldata/119

[367] Tarannum, N.; Kumar, D. Chapter 25 - Pyridine: Exposure, Risk Management, and Impact on Life and Environment. In *Hazardous Chemicals*; Chawla, M., Singh, J., Kaushik, R. D., Eds.; Academic Press, 2025; pp 363–374. https://doi.org/10.1016/B978-0-323-95235-4.00036-0

[368] Ajslev, J. Z. N.; Møller, J. L.; Andersen, M. F.; Pirzadeh, P.; Lingard, H. The Hierarchy of Controls as an Approach to Visualize the Impact of Occupational Safety and Health Coordination. *International Journal of Environmental Research and Public Health* **2022**, *19* (5), 2731. https://doi.org/10.3390/ijerph19052731

[369] Ridhi, R.; Saini, G. S. S.; Tripathi, S. K. Study of Sensing Mechanism of Heterocyclic Hazardous Vapors with Metal Phthalocyanines. *Dyes and Pigments* **2023**, *216*, 111328. https://doi.org/10.1016/j.dyepig.2023.111328

[370] Liu, Q.; Zhao, C.; Shao, X.; Wang, W.; Ji, X. High Sensitive Pyridine Chemiresistive Sensors Based on Azacyclobutane Modified Perylene Bisimide Derivatives. *Dyes and Pigments* **2021**, *185*, 108902. https://doi.org/10.1016/j.dyepig.2020.108902

[371] Qin, W.; Parzuchowski, P.; Zhang, W.; Meyerhoff, M. E. Optical Sensor for Amine Vapors Based on Dimer−Monomer Equilibrium of Indium(III) Octaethylporphyrin in a Polymeric Film. *Anal. Chem.* **2003**, *75* (2), 332–340. https://doi.org/10.1021/ac0205356

[372] Kim, J. H.; Kim, S.-H. Sub-Second Pyridine Gas Detection Using a Organometal Halide Perovskite Functional Dye. *Dyes and Pigments* **2016**, *134*, 198–202. https://doi.org/10.1016/j.dyepig.2016.07.015

[373] Haghighi, E.; Zeinali, S. Nanoporous MIL-101(Cr) as a Sensing Layer Coated on a Quartz Crystal Microbalance (QCM) Nanosensor to Detect Volatile Organic Compounds (VOCs). *RSC Adv.* **2019**, *9* (42), 24460–24470. https://doi.org/10.1039/C9RA04152D

[374] Xu, F.; Sun, L.; Huang, P.; Sun, Y.; Zheng, Q.; Zou, Y.; Chu, H.; Yan, E.; Zhang, H.; Wang, J.; Du, Y. A Pyridine Vapor Sensor Based on Metal-Organic Framework-Modified Quartz Crystal Microbalance. *Sensors and Actuators B: Chemical* **2018**, *254*, 872–877. https://doi.org/10.1016/j.snb.2017.07.026

[375] Liu, M.; Chen, L.; Shan, P.; lian, C.; Zhang, Z.; Zhang, Y.; Tao, Z.; Xiao, X. Pyridine Detection Using Supramolecular Organic Frameworks Incorporating Cucurbit[10]Uril. *ACS Appl. Mater. Interfaces* **2021**, *13* (6), 7434–7442. https://doi.org/10.1021/acsami.0c20292

[376] Bairi, P.; Minami, K.; Nakanishi, W.; Hill, J. P.; Ariga, K.; Shrestha, L. K. Hierarchically Structured Fullerene C70 Cube for Sensing Volatile Aromatic Solvent Vapors. *ACS Nano* **2016**, *10* (7), 6631–6637. https://doi.org/10.1021/acsnano.6b01544

[377] Khaing Oo, M. K.; Guo, Y.; Reddy, K.; Liu, J.; Fan, X. Ultrasensitive Vapor Detection with Surface-Enhanced Raman Scattering-Active Gold Nanoparticle Immobilized Flow-Through Multihole Capillaries. *Anal. Chem.* **2012**, *84* (7), 3376–3381. https://doi.org/10.1021/ac300175v

[378] Zhao, K.; Dong, L.; Zheng, Y.; Deng, G.; Li, Z.; Qu, S.; Chen, K.; Wu, J. Optimization of Light-Analyte Interaction in Si_3N_4/Polymer Hybrid Waveguide for Sensitive Sensing of Pyridine Vapor with Ppb-Level Detection Limit. *Sensors and Actuators B: Chemical* **2023**, *377*, 133104. https://doi.org/10.1016/j.snb.2022.133104

[379] Thompson, A. C.; Lee, K. S.; Lewis, N. S. Strain-Based Chemiresistive Polymer-Coated Graphene Vapor Sensors. *ACS Omega* **2022**, *7* (12), 10765–10774. https://doi.org/10.1021/acsomega.2c00543

[380] Younis, M.; Long, J.; Peng, S.-Q.; Wang, X.-S.; Chai, C.; Bogliotti, N.; Huang, M.-H. Reversible Transformation between Azo and Azonium Bond Other than Photoisomerization of Azo Bond in Main-Chain Polyazobenzenes. *J. Phys. Chem. Lett.* **2021**, *12* (14), 3655–3661. https://doi.org/10.1021/acs.jpclett.1c00750

[381] Rochat, S.; Swager, T. M. Fluorescence Sensing of Amine Vapors Using a Cationic Conjugated Polymer Combined with Various Anions. *Angewandte Chemie International Edition* **2014**, *53* (37), 9792–9796. https://doi.org/10.1002/anie.201404439

[382] Dai, Z.-Q.; Song, L.; Chen, J.-E.; Jin, D.-F.; Jin, H.-X.; Guo, X.-L.; Shen, H.-Y.; Chai, W.-X. Smart-Responsive Luminescence and VOC Sensing Application of a Copper(I) Cluster with a Novel $P_2CuI_2CuN_2$ Core. *J. Mater. Chem. C* **2025**, *13* (14), 7234–7244. https://doi.org/10.1039/D4TC05038J

[383] Ermakova, E. V.; Arslanov, V. V.; Bretonnière, Y.; Michel, C.; Bessmertnykh-Lemeune, A. Supramolecular Assembly of Phosphonate-Substituted Porphyrins in Langmuir Layers and Langmuir–Schäfer Films: Structural Studies and Selective Sensing of Pyridine Vapors. *J. Mater. Chem. C* **2025**, *13* (9), 4791–4806. https://doi.org/10.1039/D4TC04449E

[384] Murakami, T.; Homma, T.; Masuno, A.; Okazaki, M.; Ohta, S. Color-Change Behavior of a Bis(Benzimidazole)-Coordinated Nickel-Dichlorido Complex Induced by the Adsorption of Pyridine or Ammonia Vapor. *Transit Met Chem* **2024**, *49* (4), 229–235. https://doi.org/10.1007/s11243-024-00576-9

[385] Kusumoto, S.; Inaba, K.; Suda, H.; Nakaya, M.; Tokunaga, R.; Thuéry, P.; Haruki, R.; Kanazawa, T.; Nozawa, S.; Kim, Y.; Hayami, S.; Koide, Y. Cooperative Spin-State Switching and Vapochromism of Mononuclear Ni(II) Complexes by Pyridine Coordination/Decoordination. *Inorg. Chem.* **2023**, *62* (39), 16222–16227. https://doi.org/10.1021/acs.inorgchem.3c02776

[386] Tang, S.-Y.; Song, L.; Jia, Y.-F.; Xu, W.-Z.; Yang, Y.-X.; Sun, L.-J.; Shen, H.-Y.; Chai, W.-X. Three Heteroleptic Copper(I) Complexes with $[Cu(P^{\wedge}P)N_2]^+$ Structure and Their Fluorescence Sensing for VOCs. *Applied Organometallic Chemistry* **2023**, *37* (11), e7242. https://doi.org/10.1002/aoc.7242

[387] Lv, Y.; Zhang, Y.; Du, Y.; Xu, J.; Wang, J. A Novel Porphyrin-Containing Polyimide Nanofibrous Membrane for Colorimetric and Fluorometric Detection of Pyridine Vapor. *Sensors* **2013**, *13* (11), 15758–15769. https://doi.org/10.3390/s131115758

[388] Elosua, C.; Bariain, C.; Matias, I. R.; Rodriguez, A.; Colacio, E.; Salinas-Castillo, A.; Segura-Carretero, A.; Fernandez-Gutiérrez, A. Pyridine Vapors Detection by an Optical Fibre Sensor. *Sensors* **2008**, *8* (2), 847–859. https://doi.org/10.3390/s8020847

[389] Color Spaces and Color Distances. In *Digital Color Image Processing*; John Wiley & Sons, Ltd, 2008; pp 37–70. https://doi.org/10.1002/9780470230367.ch3

[390] Gao, Y.; Liang, J.; Yang, J. Color Palette Generation From Digital Images: A Review. *Color Research & Application* **2025**, *50* (3), 250–265. https://doi.org/10.1002/col.22975

[391] Rao, P.; Ankam, S.; Ansari, M.; GAVANE, A. G.; Kumar, A.; Pandit, V. I.; Nema, P. Monitoring of Hydrocarbon Emissions in a Petroleum Refinery. *Environ Monit Assess* **2005**, *108* (1), 123–132. https://doi.org/10.1007/s10661-005-3961-x

[392] Oliveri, I. P.; Maccarrone, G.; Di Bella, S. A Lewis Basicity Scale in Dichloromethane for Amines and Common Nonprotogenic Solvents Using a Zinc(II) Schiff-Base Complex as Reference Lewis Acid. *J. Org. Chem.* **2011**, *76* (21), 8879–8884. https://doi.org/10.1021/jo2016218

[393] Ko, I. H.; Park, Y. D. Recent Research Trends for Developing Highly Sensitive, Flexible Organic Field-Effect Transistor-Based Gas Sensors. *ACS Appl. Polym. Mater.* **2025**, *7* (5), 2749–2760. https://doi.org/10.1021/acsapm.4c03902

[394] Xu, X.; Zhao, Y.; Liu, Y. Wearable Electronics Based on Stretchable Organic Semiconductors. *Small* **2023**, *19* (20), 2206309. https://doi.org/10.1002/smll.202206309

[395] Chen, H.; Zhang, W.; Li, M.; He, G.; Guo, X. Interface Engineering in Organic Field-Effect Transistors: Principles, Applications, and Perspectives. *Chem. Rev.* **2020**, *120* (5), 2879–2949. https://doi.org/10.1021/acs.chemrev.9b00532

[396] Zhang, X.; Dong, H.; Hu, W. Organic Semiconductor Single Crystals for Electronics and Photonics. *Advanced Materials* **2018**, *30* (44), 1801048. https://doi.org/10.1002/adma.201801048

[397] Zhang, J.; Liu, X.; Neri, G.; Pinna, N. Nanostructured Materials for Room-Temperature Gas Sensors. *Advanced Materials* **2016**, *28* (5), 795–831. https://doi.org/10.1002/adma.201503825

[398] Morab, S.; Sundaram, M. M.; Pivrikas, A. Review on Charge Carrier Transport in Inorganic and Organic Semiconductors. *Coatings* **2023**, *13* (9), 1657. https://doi.org/10.3390/coatings13091657

[399] Coropceanu, V.; Cornil, J.; Da Silva Filho, D. A.; Olivier, Y.; Silbey, R.; Brédas, J.-L. Charge Transport in Organic Semiconductors. *Chem. Rev.* **2007**, *107* (4), 926–952. https://doi.org/10.1021/cr050140x

[400] Chen, W.; Qi, D.; Huang, H.; Gao, X.; Wee, A. T. S. Organic–Organic Heterojunction Interfaces: Effect of Molecular Orientation. *Adv Funct Materials* **2011**, *21* (3), 410–424. https://doi.org/10.1002/adfm.201000902

[401] Hinderhofer, A.; Schreiber, F. Organic–Organic Heterostructures: Concepts and Applications. *ChemPhysChem* **2012**, *13* (3), 628–643. https://doi.org/10.1002/cphc.201100737

[402] Heremans, P.; Cheyns, D.; Rand, B. P. Strategies for Increasing the Efficiency of Heterojunction Organic Solar Cells: Material Selection and Device Architecture. *Acc. Chem. Res.* **2009**, *42* (11), 1740–1747. https://doi.org/10.1021/ar9000923

[403] Nakano, K.; Tajima, K. Organic Planar Heterojunctions: From Models for Interfaces in Bulk Heterojunctions to High-Performance Solar Cells. *Advanced Materials* **2017**, *29* (25), 1603269. https://doi.org/10.1002/adma.201603269

[404] Street, R. A. Electronic Structure and Properties of Organic Bulk-Heterojunction Interfaces. *Advanced Materials* **2016**, *28* (20), 3814–3830. https://doi.org/10.1002/adma.201503162

[405] Wadsworth, A.; Hamid, Z.; Kosco, J.; Gasparini, N.; McCulloch, I. The Bulk Heterojunction in Organic Photovoltaic, Photodetector, and Photocatalytic Applications. *Advanced Materials* **2020**, *32* (38), 2001763. https://doi.org/10.1002/adma.202001763

[406] Kim, C.-H. Organic Heterojunction Transistors. *ACS Appl. Electron. Mater.* **2022**, *4* (6), 2581–2588. https://doi.org/10.1021/acsaelm.2c00423

[407] Zhang, Z.; Lei, B.; Tan, Y.; Zhang, W.; Fan, Y.; Kalimuthu, R.; Bhat, A. A.; Yang, Y.; Xu, S.; Zhang, H.; Wei, Q.-H.; Gao, S.; Bi, W.; Feng, J. Heterojunctions Based on 2D Materials for Pulse Laser Applications. *ACS Nano* **2025**, *19* (13), 12646–12679. https://doi.org/10.1021/acsnano.4c18849

[408] Armstrong, N. R.; Wang, W.; Alloway, D. M.; Placencia, D.; Ratcliff, E.; Brumbach, M. Organic/Organic′ Heterojunctions: Organic Light Emitting Diodes and Organic Photovoltaic Devices. *Macromolecular Rapid Communications* **2009**, *30* (9–10), 717–731. https://doi.org/10.1002/marc.200900075

[409] Bag, A.; Lee, N.-E. Gas Sensing with Heterostructures Based on Two-Dimensional Nanostructured Materials: A Review. *J. Mater. Chem. C* **2019**, *7* (43), 13367–13383. https://doi.org/10.1039/C9TC04132J

[410] Li, Q.; Ding, S.; Zhu, W.; Feng, L.; Dong, H.; Hu, W. Recent Advances in One-Dimensional Organic p–n Heterojunctions for Optoelectronic Device Applications. *Journal of Materials Chemistry C* **2016**, *4* (40), 9388–9398. https://doi.org/10.1039/C6TC03280J

[411] Balapure, A.; Dutta, J. R.; Ganesan, R. Recent Advances in Semiconductor Heterojunctions: A Detailed Review of the Fundamentals of Photocatalysis, Charge Transfer Mechanism and Materials. *RSC Applied Interfaces* **2024**, *1* (1), 43–69. https://doi.org/10.1039/D3LF00126A

[412] Li, Y.; Zhang, J.; Chen, Q.; Xia, X.; Chen, M. Emerging of Heterostructure Materials in Energy Storage: A Review. *Advanced Materials* **2021**, *33* (27), 2100855. https://doi.org/10.1002/adma.202100855

[413] Li, X.; Wang, Z.; Wang, L. Metal–Organic Framework-Based Materials for Solar Water Splitting. *Small Science* **2021**, *1* (5), 2000074. https://doi.org/10.1002/smsc.202000074

[414] Facchetti, A. π-Conjugated Polymers for Organic Electronics and Photovoltaic Cell Applications. *Chem. Mater.* **2011**, *23* (3), 733–758. https://doi.org/10.1021/cm102419z

[415] Ho, D.; Ozdemir, R.; Kim, H.; Earmme, T.; Usta, H.; Kim, C. BODIPY-Based Semiconducting Materials for Organic Bulk Heterojunction Photovoltaics and Thin-Film Transistors. *ChemPlusChem* **2019**, *84* (1), 18–37. https://doi.org/10.1002/cplu.201800543

[416] Kesters, J.; Verstappen, P.; Kelchtermans, M.; Lutsen, L.; Vanderzande, D.; Maes, W. Porphyrin-Based Bulk Heterojunction Organic Photovoltaics: The Rise of the Colors of Life. *Advanced Energy Materials* **2015**, *5* (13), 1500218. https://doi.org/10.1002/aenm.201500218

[417] Qian, C.; Sun, J.; Gao, Y. Transport of Charge Carriers and Optoelectronic Applications of Highly Ordered Metal Phthalocyanine Heterojunction Thin Films. *Phys. Chem. Chem. Phys.* **2021**, *23* (16), 9631–9642. https://doi.org/10.1039/D1CP00889G

[418] Ferguson, A. J.; Blackburn, J. L.; Kopidakis, N. Fullerenes and Carbon Nanotubes as Acceptor Materials in Organic Photovoltaics. *Materials Letters* **2013**, *90*, 115–125. https://doi.org/10.1016/j.matlet.2012.08.145

[419] Anthony, J. E. Small-Molecule, Nonfullerene Acceptors for Polymer Bulk Heterojunction Organic Photovoltaics. *Chem. Mater.* **2011**, *23* (3), 583–590. https://doi.org/10.1021/cm1023019

[420] Zanotti, G.; Palmeri, F.; Raglione, V. Phthalocyanines Synthesis: A State-of-The-Art Review of Sustainable Approaches Through Green Chemistry Metrics. *Chem. Eur. J.* **2024**, *30*, e202400908. https://doi.org/10.1002/chem.202400908

[421] McKeown, N.B. Phthalocyanine materials: synthesis, structure and function (No. 6). *Cambridge university press*, **1998**.

[422] Lukyanets, E.A.; Nemykin, V.N. The key role of peripheral substituents in the chemistry of phthalocyanines and their analogs. *J. Porphyrins Phthalocyanines* **2010**, *14*, 1–40. https://doi.org/10.1142/S1088424610001799

[423] Nyokong, T. Effects of substituents on the photochemical and photophysical properties of main group metal phthalocyanines. *Coord. Chem. Rev.* **2007**, *251*, 1707–1722. https://doi.org/10.1016/j.ccr.2006.11.011

[424] Wang, M.; Ishii, K. Photochemical properties of phthalocyanines with transition metal ions. *Coord. Chem. Rev*. **2022**, *468*, 214626. https://doi.org/10.1016/j.ccr.2022.214626

[425] Urbani, M.; Ragoussi, M.-E.; Nazeeruddin, M.K.; Torres, T. Phthalocyanines for dye-sensitized solar cells. *Coord. Chem. Rev.* **2019**, *381*, 1–64. https://doi.org/10.1016/j.ccr.2018.10.007

[426] de la Torre, G.; Bottari, G.; Hahn, U.; Torres, T. Functional Phthalocyanines: Synthesis, Nanostructuration, and Electro-Optical Applications. *Struct Bond* 2010, 135, 1–44. https://doi.org/10.1007/978-3-642-04752-71

[427] Gounden, D.; Nombona, N.; E. van Zyl, W. Recent advances in phthalocyanines for chemical sensor, non-linear optics (NLO) and energy storage applications. *Coord. Chem. Rev*. **2020**, *420*, 213359. https://doi.org/10.1016/j.ccr.2020.213359

[428] Melville, O. A.; Lessard, B. H.; Bender, T. P. Phthalocyanine-Based Organic Thin-Film Transistors: A Review of Recent Advances. *ACS Appl. Mater. Interfaces* **2015**, *7* (24), 13105–13118. https://doi.org/10.1021/acsami.5b01718

[429] Oni, J.; Ozoemena, K.I. Phthalocyanines in batteries and supercapacitors. *J. Porphyrins Phthalocyanines* 2012, 16, 754–760. https://doi.org/10.1142/S1088424612300078

[430] Bouvet, M.; Gaudillat, P.; Suisse, J.-M. Lanthanide macrocyclic complexes: from molecules to materials and from materials to devices. *J. Porphyrins Phthalocyanines* **2013**, 17, 1–8. https://doi.org/10.1142/S1088424613300048

[431] Turek, P.; Petit, P.; André, J.-J.; Simon, J.; Even, R.; Boudjema, B.; Guillaud, G.; Maitrot, M. A New Series of Molecular Semiconductors: Phthalocyanine Radicals. *J. Am. Chem. Soc.* 1987, *109*, 17, 5119–5122. https://doi.org/10.1021/ja00251a012

[432] Simon, J.; Andre, J.-J.; Maitrot, M. Lutetium Bisphthalocyanine: The First Molecular Semiconductor. In *Molecules in Physics, Chemistry, and Biology: Physical Aspects of Molecular Systems*; Maruani, J., Ed.; Springer Netherlands: Dordrecht, 1988; pp 599–614. https://doi.org/10.1007/978-94-009-2851-0_20

[433] De Cian, A.; Moussavi, M.; Fischer, J.; M.; Weiss, R. Synthesis, Structure, and Spectroscopic and Magnetic Properties of Lutetium(III) Phthalocyanine Derivatives: $LuPc_2$ CH_2Cl_2 and $[LuPc(OAc)(H_2O)_2]$-H_2O-$2CH_3OH$. *Inorg. Chem.* **1985**, *24*, 3162-3167.

[434] Bouvet, M. Radical Phthalocyanines and Intrinsic Semiconduction. In *The Porphyrin Handbook*; Kadish, K. M.; Smith, K. M.; Guilard, R., Eds.; Academic Press, **2003**; Vol. 19, pp 37– 103.

[435] Bouvet, M.; Parra, V. Semiconductor Tranducer and Its Use in a Sensor for Detecting Electron-Donor or Electron-Acceptor Species. US8450725B2, May 28, **2013**. (accessed 2025-06-03). https://patents.google.com/patent/US8450725B2/en

[436] Parra, V.; Brunet, J.; Pauly, A.; Bouvet, M. Molecular Semiconductor-Doped Insulator (MSDI) Heterojunctions: An Alternative Transducer for Gas Chemosensing. *Analyst* **2009**, *134* (9), 1776. https://doi.org/10.1039/b906786h

[437] King, B.; Moorthy, S. G.; Lesniewska, E.; Meunier-Prest, R.; Bouvet, M.; Lessard, B. H. Modulating the Majority Charge Carrier Type and Performance of Organic Heterojunction Ammonia Sensors by Increasing Peripheral Fluorination of the Silicon Phthalocyanine Sublayer. *Sensors and Actuators B: Chemical* **2024**, *408*, 135507. https://doi.org/10.1016/j.snb.2024.135507

[438] Ganesh Moorthy, S.; King, B.; Kumar, A.; Lesniewska, E.; Lessard, B. H.; Bouvet, M. Molecular Engineering of Silicon Phthalocyanine to Improve the Charge Transport and Ammonia Sensing Properties of Organic Heterojunction Gas Sensors. *Advanced Sensor Research* **2023**, *2* (3), 2200030. https://doi.org/10.1002/adsr.202200030

[439] Di Zazzo, L.; Kumar, A.; Meunier-Prest, R.; Di Natale, C.; Paolesse, R.; Bouvet, M. Electrosynthesized Copper Polycorroles as Versatile Materials in Double Lateral Heterojunctions. *Chemical Engineering Journal* **2023**, *458*, 141465. https://doi.org/10.1016/j.cej.2023.141465

[440] Di Zazzo, L.; Ganesh Moorthy, S.; Meunier-Prest, R.; Lesniewska, E.; Di Natale, C.; Paolesse, R.; Bouvet, M. Ammonia and Humidity Sensing by Phthalocyanine–Corrole Complex Heterostructure Devices. *Sensors* **2023**, *23* (15), 6773. https://doi.org/10.3390/s23156773

[441] Kumar, A.; Meunier-Prest, R.; Lesniewska, E.; Bouvet, M. Interplay of Electrode Geometry and Bias on Charge Transport in Organic Heterojunction Gas Sensors. *Sensors and Actuators B: Chemical* **2022**, *369*, 132313. https://doi.org/10.1016/j.snb.2022.132313

[442] Kumar, A.; Meunier-Prest, R.; Herbst, F.; Heintz, O.; Lesniewska, E.; Bouvet, M. Covalent Grafting of Aryls to Modulate the Electrical Properties of Phthalocyanine-Based Heterostructures: Application to Ammonia Sensing. *Chemical Engineering Journal* **2022**, *436*, 135207. https://doi.org/10.1016/j.cej.2022.135207

[443] Kumar, A.; Alami Mejjati, N.; Meunier-Prest, R.; Krystianiak, A.; Heintz, O.; Lesniewska, E.; Devillers, C. H.; Bouvet, M. Tuning of Interfacial Charge Transport in Polyporphine/Phthalocyanine Heterojunctions by Molecular Geometry Control for an Efficient Gas Sensor. *Chemical Engineering Journal* **2022**, *429*, 132453. https://doi.org/10.1016/j.cej.2021.132453

[444] Ouedraogo, S.; Meunier-Prest, R.; Kumar, A.; Bayo-Bangoura, M.; Bouvet, M. Modulating the Electrical Properties of Organic Heterojunction Devices Based On Phthalocyanines for Ambipolar Sensors. *ACS Sens.* **2020**, *5* (6), 1849–1857. https://doi.org/10.1021/acssensors.0c00877

[445] Kumar, A.; Devillers, C. H.; Meunier-Prest, R.; Sabat, D.; Lesniewska, E.; Bouvet, M. Bias Induced Ambipolar Transport in Organic Heterojunction Sensors. *Advanced Electronic Materials* **2025**, *11* (9), 2400865. https://doi.org/10.1002/aelm.202400865

[446] Ganesh Moorthy, S.; Bouvet, M. Effects of Visible Light on Gas Sensors: From Inorganic Resistors to Molecular Material-Based Heterojunctions. *Sensors* **2024**, *24* (5), 1571. https://doi.org/10.3390/s24051571

[447] Ganesh Moorthy, S.; Ouedraogo, S.; Bouvet, M. Ambipolar Heterojunction Sensors: Another Way to Detect Polluting Gases. *ACS Sens.* **2024**, *9* (7), 3707–3719. https://doi.org/10.1021/acssensors.4c00900

[448] Ganesh Moorthy, S.; Apoubou, A.; Ouedraogo, S.; Vachey, L.; Bayo-Bangoura, M.; Bouvet, M. In-Depth Study of Ambipolar Charge-Transport Regime through External Triggers and Gas Sensing. *ACS Appl. Mater. Interfaces* **2024**, *16* (43), 58991–59003. https://doi.org/10.1021/acsami.4c14619

[449] Kikobo, G. L.; Kumar, A.; Vibhu, V.; Ouedraogo, S.; Deshotel, A.; Mateos, M.; Meunier-Prest, R.; Bouvet, M. Photon Assisted-Inversion of Majority Charge Carriers in Molecular Semiconductor-Based Organic Heterojunctions. *J. Mater. Chem. C* **2021**, *9* (14), 5008–5020. https://doi.org/10.1039/D0TC05828A

[450] Şahin, Z.; Meunier-Prest, R.; Dumoulin, F.; Kumar, A.; Isci, Ü.; Bouvet, M. Tuning of Organic Heterojunction Conductivity by the Substituents' Electronic Effects in Phthalocyanines for Ambipolar Gas Sensors. *Sensors and Actuators B: Chemical* **2021**, *332*, 129505. https://doi.org/10.1016/j.snb.2021.129505

[451] Bouvet, M.; Mateos, M.; Wannebroucq, A.; Navarrete, E.; Llobet, E. A Tungsten Oxide–Lutetium Bisphthalocyanine n–p–n Heterojunction: From Nanomaterials to a New Transducer for Chemo-Sensing. *J. Mater. Chem. C* **2019**, *7* (21), 6448–6455. https://doi.org/10.1039/C8TC06309E

[452] Lamine, W.; Boughdiri, S.; Jeanneau, E.; Sanglar, C.; Morell, C.; Christ, L.; Chermette, H. Unexpected Structure of a Helical N4-Schiff-Base Zn(II) Complex and Its Demetallation: Experimental and Theoretical Studies. *ChemPhysChem* **2018**, *19* (21), 2938–2946. https://doi.org/10.1002/cphc.201800514

[453] Andre, J.-J.; Holczer, K.; Petit, P.; Riou, M.-T.; Clarisse, C.; Even, R.; Fourmigue, M.; Simon, J. Electrical and Magnetic Properties of Thin Films and Single Crystals of Bis(Phthalocyaninato)Lutetium. *Chemical Physics Letters* **1985**, *115* (4), 463–466. https://doi.org/10.1016/0009-2614(85)85171-X

[454] Bredar, A. R. C.; Chown, A. L.; Burton, A. R.; Farnum, B. H. Electrochemical Impedance Spectroscopy of Metal Oxide Electrodes for Energy Applications. *ACS Appl. Energy Mater.* **2020**, *3* (1), 66–98. https://doi.org/10.1021/acsaem.9b01965

[455] Tokmoldin, N.; Deibel, C.; Neher, D.; Shoaee, S. Contemporary Impedance Analyses of Archetypical PM6:Y6 Bulk-Heterojunction Blend. *Advanced Energy Materials* **2024**, *14* (27), 2401130. https://doi.org/10.1002/aenm.202401130

[456] *ZView® For Windows*. Scribner. https://www.scribner.com/software/68-general-electrochemistr376-zview-for-windows/

[457] Lazanas, A. Ch.; Prodromidis, M. I. Electrochemical Impedance Spectroscopy─A Tutorial. *ACS Meas. Sci. Au* **2023**, *3* (3), 162–193. https://doi.org/10.1021/acsmeasuresciau.2c00070

[458] Hirschorn, B.; Orazem, M. E.; Tribollet, B.; Vivier, V.; Frateur, I.; Musiani, M. Determination of Effective Capacitance and Film Thickness from Constant-Phase-Element Parameters. *Electrochimica Acta* **2010**, *55* (21), 6218–6227. https://doi.org/10.1016/j.electacta.2009.10.065

[459] Brug, G. J.; van den Eeden, A. L. G.; Sluyters-Rehbach, M.; Sluyters, J. H. The Analysis of Electrode Impedances Complicated by the Presence of a Constant Phase Element. *Journal of Electroanalytical Chemistry and Interfacial Electrochemistry* **1984**, *176* (1), 275–295. https://doi.org/10.1016/S0022-0728(84)80324-1

[460] Ganesh Moorthy, S.; Arvidson, J.; Meunier-Prest, R.; Wang, H.; Bouvet, M. π-Extended Porphyrin–Phthalocyanine Heterojunction Devices Exhibiting High Ammonia Sensitivity with a Remarkable Light Effect. *ACS Sens.* **2024**, *9* (2), 883–894. https://doi.org/10.1021/acssensors.3c02247

[461] Su, H.; Liu, R.; Shu, M.; Tang, M.; Wang, J.; Zhu, H. Fluorenone-based organogel and self-assembled fibrous film: Synthesis, optical properties and reversible detection of aniline vapor. *Dyes Pigm*. **2019**, *162*, 52–58. https://doi.org/10.1016/j.dyepig.2018.10.006

[462] Debsharma, K.; Santhi, J.; Baire, B.; Prasad, E. Aggregation-Induced Emission Active Donor−Acceptor Fluorophore as a Dual Sensor for Volatile Acids and Aromatic Amines. *ACS Appl. Mater. Interfaces* **2019**, *11*, 48249−48260. https://doi.org/10.1021/acsami.9b17988

[463] Zhang, J.; Liu, K.; Wang, G.; Shang, C.; Peng, H.; Liu, T.; Fang, Y. Detection of gaseous amines with a fluorescent film based on a perylene bisimide-functionalized copolymer. *New J. Chem*. **2018**, *42*, 12737–12744. https://doi.org/10.1039/C8NJ02540A

[464] Jiao, Z.; Zhang, Y.; Xu, W.; Zhang, X.; Jiang, H.; Wu, P.; Fu, Y.; He, Q.; Cao, H.; Cheng, J. Highly Efficient Multiple-Anchored Fluorescent Probe for theD etection of Aniline Vapor Based on Synergistic Effect: Chemical Reaction and PET. *ACS Sens.* **2017**, *2*, 687−694. https://doi.org/10.1021/acssensors.7b00143

[465] Xue, P.; Yao, B.; Wang, P.; Gong, P.; Zhang, Z.; Lu, R. Strong Fluorescent Smart Organogel as a Dual Sensing Material for Volatile Acid and Organic Amine Vapors. *Chem. Eur. J.* **2015**, *21*, 17508–17515. https://doi.org/10.1002/chem.201502401

[466] Zhang, X.; Liu, X.; Lu, R.; Zhang, H.; Gong, P. Fast detection of organic amine vapors based on fluorescent nanofibrils fabricated from triphenylamine functionalized β-diketone-boron difluoride. *J. Mater. Chem*. **2012**, *22*, 1167–1172. https://doi.org/10.1039/C1JM14187B

[467] Shi, L.; He, C.; Zhu, D.; He, Q.; Li, Y.; Chen, Y.; Sun, Y.; Fu, Y.; Wen, D.; Cao, H.; Cheng, J. High performance aniline vapor detection based on multi-branched fluorescent triphenylamine-benzothiadiazole derivatives: branch effect and aggregation control of the sensing performance. *J. Mater. Chem*. **2012**, *22*, 11629–11635. https://doi.org/10.1039/C2JM30933E

[468] Liu, X.; Zhang, X.; Lu, R.; Xue, P.; Xu, D.; Zhou, H. Low-dimensional nanostructures fabricated from bis(dioxaborine)carbazole derivatives as fluorescent chemosensors for detecting organic amine vapors. *J. Mater. Chem.* **2011**, *21*, 8756–8765. https://doi.org/10.1039/C0JM04274A